Fast heating by feedback flow control

Citation for published version (APA):
Lensvelt, R. (2023). *Fast heating by feedback flow control*. [Phd Thesis 1 (Research TU/e / Graduation TU/e), Mechanical Engineering]. Eindhoven University of Technology.

Document status and date:
Published: 09/05/2023

Document Version:
Publisher’s PDF, also known as Version of Record (includes final page, issue and volume numbers)

Please check the document version of this publication:

• A submitted manuscript is the version of the article upon submission and before peer-review. There can be important differences between the submitted version and the official published version of record. People interested in the research are advised to contact the author for the final version of the publication, or visit the DOI to the publisher's website.
• The final author version and the galley proof are versions of the publication after peer review.
• The final published version features the final layout of the paper including the volume, issue and page numbers.

Link to publication

General rights
Copyright and moral rights for the publications made accessible in the public portal are retained by the authors and/or other copyright owners and it is a condition of accessing publications that users recognise and abide by the legal requirements associated with these rights.

- Users may download and print one copy of any publication from the public portal for the purpose of private study or research.
- You may not further distribute the material or use it for any profit-making activity or commercial gain
- You may freely distribute the URL identifying the publication in the public portal.

If the publication is distributed under the terms of Article 25fa of the Dutch Copyright Act, indicated by the “Taverne” license above, please follow below link for the End User Agreement:

www.tue.nl/taverne

Take down policy
If you believe that this document breaches copyright please contact us at:

openaccess@tue.nl

providing details and we will investigate your claim.

Download date: 04. Oct. 2023

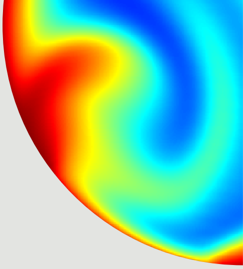

FAST HEATING BY FEEDBACK FLOW CONTROL

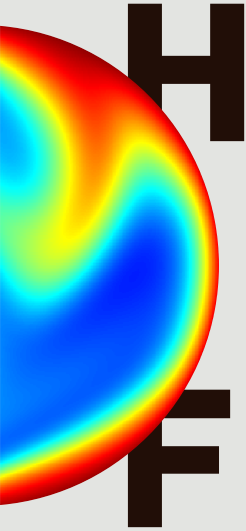

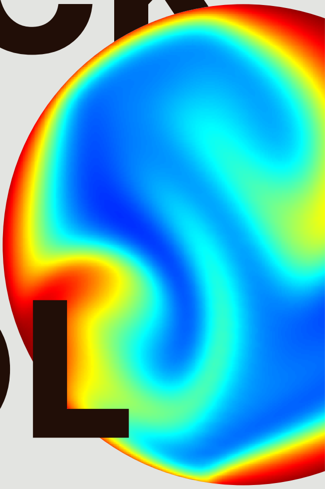

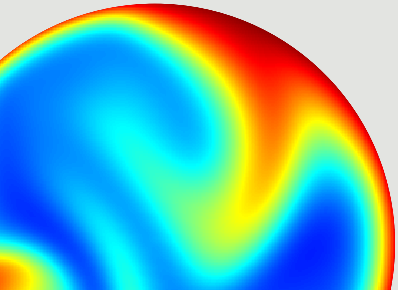

Ruud Lensvelt

2023

Fast heating by feedback flow control

Ruud Lensvelt

The research reported in this thesis is part of the research program of the Dutch Institute of Systems and Control (DISC). The author has successfully completed the educational program of the Graduate School DISC.

This work has been performed within the Computational Sciences for Energy Research (CSER) program from NWO at the Eindhoven University of Technology and was financially supported by NWO, Utrecht, The Netherlands.

A catalogue record is available from the Eindhoven University of Technology Library ISBN: 978-90-386-5728-8.

Typeset using Latex.

Reproduction: Ipskamp Printing, Enschede, The Netherlands
Cover design: R.J. Graafland

©2023 by R. Lensvelt. All Rights reserved.

Fast heating by feedback flow control

PROEFSCHRIFT

ter verkrijging van de graad van doctor aan de Technische Universiteit
Eindhoven, op gezag van de rector magnificus prof.dr.ir. F.P.T. Baaijens, voor
een commissie aangewezen door het College voor Promoties, in het openbaar
te verdedigen op dinsdag 9 mei 2023 om 13:30 uur

door

Ruud Lensvelt

geboren te Oosterhout

Dit proefschrift is goedgekeurd door de promotoren en de samenstelling van de promotiecommissie is als volgt:

voorzitter:	prof.dr.ir. P.D. Anderson
1e promotor:	prof.dr. H. Nijmeijer
2e promotor:	dr.ir. M.F.M. Speetjens
leden:	prof.dr. H.J.H. Clercx
	prof.dr. M.R. de Baar
	prof.dr.ir. B.J. Boersma (Technische Universiteit Delft)
	prof.dr. M. Guay (Queen's University)

Het onderzoek dat in dit proefschrift wordt beschreven is uitgevoerd in overeenstemming met de TU/e Gedragscode Wetenschapsbeoefening.

To Joop, Wil, Lies and Sjaan

Summary

Fast heating by feedback flow control

In fluid heating two aspects need to be optimized simultaneously: i) transfer of heat into a fluid (denoted energization in this thesis) and ii) transport of heat throughout the fluid (homogenization). A proper balance between these competing aspects is crucial for fast heating. This thesis considers systems that transfer heat into a cold fluid by a hot boundary as a representative problem. Heat transport is influenced by stirring the fluid in the considered systems. This immediately raises the question central to this thesis: "How to stir the fluid to heat it up as quickly as possible?". This thesis presents novel active methods to boost fluid heating by stirring.

Promoting transport of heat or other scalars in fluids has received significant attention over the years. Rapid transport of scalars in fluids is important if not vital for various industrial applications. Applications related to polymer and food processing, process intensification and/or micro-fluidics are of particular interest here. Such applications include organ-on-a-chip devices, dispersion in bioreactors or pumping schemes for groundwater remediation or subsurface resource recovery. The fundamental operation of these applications are captured well by a Rotated Arc Mixer (RAM). Therefore, the (control of a) RAM is adopted as a case study and investigated both numerically and experimentally in this thesis.

Conventional stirring methods to accelerate heating have primarily focused on achieving chaotic advection. Chaotic advection can be achieved by activating, or controlling, piecewise steady flow fields. In conventional methods these flow fields are reoriented periodically in either time and/or space. The periodic reorientation results in periodic stirring of the fluid. Typically, it is assumed that chaotic advection, accomplished by periodic stirring, automatically results in rapid heating. However, this reasoning only applies to heat-transfer problems i) with negligible diffusion compared advection (i.e. a Péclet number $\mathcal{O} \gtrsim 10^5$) and/or ii) without heat transfer from a system boundary. Diffusion plays a significant role in fluid heating in systems considered in this thesis. Furthermore, heat is actively transferred from the system boundary into the fluid in the RAM. The presence of both features distinguishes this work from conventional mixing studies.

Periodic stirring protocols are typically designed *a priori* on a model before being applied in practice. This open-loop approach fixes the stirring sequence and thus has some inherent limitations. Periodic stirring lacks any real-time adaptability to perturbation in the instantaneous temperature field. Heating with periodic stirring can also be significantly hampered when model and reality deviate (e.g. parameter perturbations due manufacturing tolerance or ambient effects). Performance results thus often only apply for the conditions/parameters used during design. In addition, “optimal” (periodic) stirring sequences are known to change under varying system conditions. The above pleads for adaptive stirring with stirring based on the instantaneous “state of fluid heating. This closed-loop feedback control approach is known to mitigate the open-loop limitations. Therefore, closed-loop control with feedback based on the temperature field is used in this thesis.

The first contribution of this thesis consists of a flow controller for fluid heating. The fluid flow activation is determined by way of a cost-function prediction. The cost-function contains the difference between the instantaneous and a target fluid temperature. This novel cost-function captures both facets of the heating process (i.e. energization and homogenization). Function analysis reveals that the flow field acts as the thermal actuator that influences both competing facets of heating simultaneously. The controller significantly accelerates heating compared to periodic stirring for a large span of model parameters.

The second contribution of this thesis provides insights to improve existing heating systems. To this end, the above controller is used to obtain stirring sequences that accelerate heating compared to periodic stirring. Fluid heating with circulation in a single direction covers a large range of industrial applications. Therefore, the controller is only allowed to circulate fluids in a single direction. Numerical results reveal improved resilience against parameter deviations with the adaptive sequences, while simultaneously ensuring faster heating. Adaptive sequences achieve this by either i) (slightly) altering periodic stirring sequences or ii) introducing aperiodic transients.

Conventional approaches rely on activating a single flow for discrete time windows. The simultaneous and continuous actuation of flow(s) can potentially achieve even faster fluid heating. In the third contribution of this thesis a general form of the novel cost-function is used to achieve fluid heating. The analogy of these cost functions with thermal energy makes them well suited as Lyapunov functions. This view lies at the foundation of the bang-bang regulator and the quadratic feedback regulator developed in this contribution. Numerical results show that both regulators can heat a fluid faster compared to periodic stirring. Proportionality makes the quadratic regulator particularly well suited for practical application. Furthermore, the quadratic regulator shows improved resilience to perturbations compared to conventional methods.

The flow controllers in this thesis rely on full knowledge of the temperature field. However, in practice the temperature field is only partially available from discretely located sensor data. Therefore, in the final contribution of this thesis an estimator is designed and implemented for temperature field reconstruction. The estimator is investigated both numerically and experimentally to show practical feasibility.

Contents

Summary **i**

Contents **iv**

1 Introduction **1**
- 1.1 Background 1
- 1.2 A representative scalar transport problem 2
- 1.3 Challenges in boosting scalar transport 4
- 1.4 Research objectives and contributions 7
- 1.5 Contributions 9
- 1.6 Thesis outline 10

2 Fast fluid heating by adaptive flow reorientation **13**
- 2.1 Introduction 14
- 2.2 Scalar transport in reoriented flows 16
- 2.3 Dynamics of heating in fluid flows 20
- 2.4 Adaptive flow reorientation 39
- 2.5 Computational performance analysis 43
- 2.6 Conclusions 53

3 Rapid thermalization with restricted adaptive flow reorientation **57**
- 3.1 Introduction 58
- 3.2 Numerical study 58
- 3.3 Conclusions and discussion 65

4 Boosting heating with flow regulation based on Lyapunov functions **67**
- 4.1 Introduction 68
- 4.2 Heat-transfer driven by reoriented flows 70
- 4.3 Flow control to boost heating 72
- 4.4 Numerical methods 80
- 4.5 Performance analysis 81
- 4.6 Conclusions and discussion 100

5 Numerical feasible model and field estimation for scalar transport 103
5.1 Introduction . . . 104
5.2 Scalar transport in Stokes flows . . . 105
5.3 Estimation of scalar transport . . . 114
5.4 Comparative analysis . . . 125
5.5 Conclusions and discussion . . . 137

6 Experimental estimation of scalar transport 141
6.1 Introduction . . . 142
6.2 Field estimation for mere diffusion . . . 143
6.3 Field estimation for the base flow . . . 147
6.4 Field estimation for a periodic flow . . . 151
6.5 Conclusions and discussion . . . 154

7 Conclusions and recommendations 157
7.1 Conclusions . . . 158
7.2 Recommendations . . . 161

A Evolution of metric J_1 165

B Laplacian eigenfunctions 167

C Well-posedness of the bang-bang controller 169
C.1 Hybrid automaton definitions . . . 169
C.2 Analysis of the bang-bang controller . . . 172

D Local identifiability of model parameters 175

E Reorientation invariance of the discrete algebraic Ricatti equation 177

F Error dynamics for a periodic flow 179

G Impact sensor placement on field estimation for the base flow 181

Bibliography 185

List of publications 197

Dankwoord 199

About the author 201

CHAPTER 1

Introduction

1.1 Background

According to recent estimates, heating accounted to 50 % of the worlds' energy consumption. Moreover, heat transport, as part of industrial processes, accounts for around 50 % of this global heat consumption [1]. Heat is a scalar quantity, which, like mass, can be transported by fluids. Flows can be used to influence the rate of fluid heating/cooling. The rapid transportation of scalar quantities such as, e.g., heat or chemical species by flows is key to many industrial activities. The industrial applications of interest range from viscous mixing of polymers and foodstuffs [2, 3] via process intensification and micro-fluidic devices [4, 5, 6] to subsurface resource recovery [7, 8, 9] and groundwater remediation [10, 11]. Boosting the efficiency of scalar transport can potentially result in faster and, consequently, more (energy) efficient operation of these applications.

Central to this thesis is a practical scalar transport system that is representative for the applications of interest: the two-dimensional ($2D$) Rotated Arc Mixer (RAM). The $2D$ RAM is a fluid heating system, which heats (cools) an initially cold (hot) fluid by fluid stirring through a hot (cold) boundary. The experimental $2D$ RAM, shown in Figure 1.1, is a $2D$ experimental representation of an inline mixer studied for heating/mixing of foodstuffs [16, 17]. The relative simple experimental configuration of the $2D$ RAM, i.e., compared to the other applications in Figure 1.1, means that strategies, devised to boost scalar transport, can be studied in practice as well. Practical feasibility of these strategies is key to their adoption by industry and is, therefore, an important rationale to adopt the (experimental) $2D$ RAM as a case-study. In addition, there are several key similarities, schematically summarized in Figure 1.1, between the applications of interest and the RAM, that forms the motivation for its adoption as a *representative* case-study

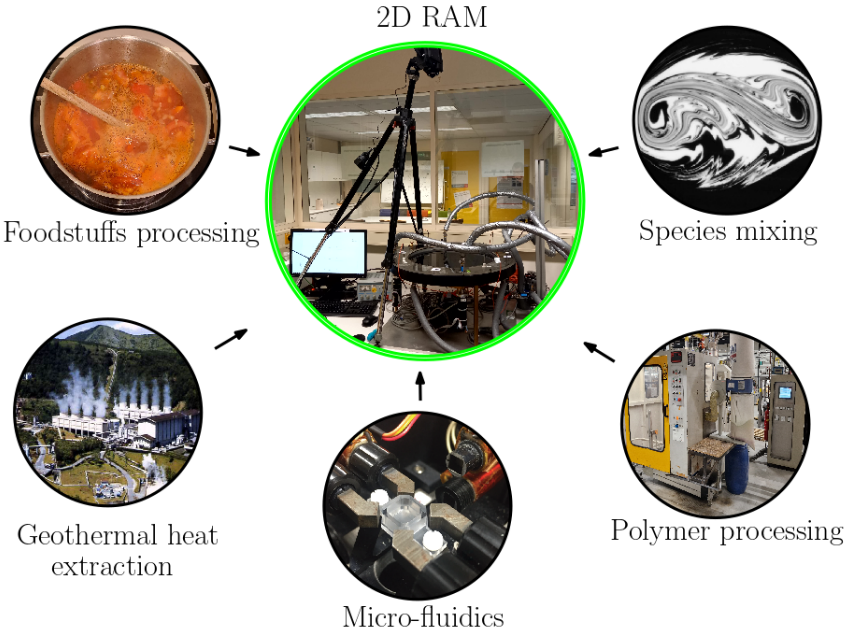

Figure 1.1: Various applications of interest that typically employ reorienting flow fields for fluid stirring in a similar fashion as the case-study central to this thesis; the two-dimensional ($2D$) Rotated Arc Mixer (RAM). Adopted pictures are, starting from the upper right corner in clock-wise order around the $2D$ RAM , from Baskan et al. [12], Roto-art [13], van Pelt et al. [14] and DiPippo [15].

throughout this thesis. These similarities will be summarized/explained next.

1.2 A representative scalar transport problem

The various applications in Figure 1.1 intend to transport heat or chemical species (in)to the fluid as fast as possible. In the $2D$ RAM, fluid stirring is used to promote heat transport (in)to the fluid as fast as possible. Hence, they share the same goal; boost scalar transport (in)to a fluid as much as possible. In addition, in both the applications and the RAM a non-adiabatic boundary condition is present, which provides a scalar influx across the system boundary that “drives” scalar transport. In addition, diffusion is present in both the applications and the RAM, which significantly impacts scalar transport behaviour. The top view of the experimental $2D$ RAM and the schematic configuration, used throughout this thesis, are shown in Figure 1.2 to clarify the implementation of the non-adiabatic boundary condition in the $2D$ RAM in Figure 1.1. The fluid is contained inside a circular fluid container $\mathcal{D}$ with radius R. The circular fluid container $\mathcal{D}$ is enclosed

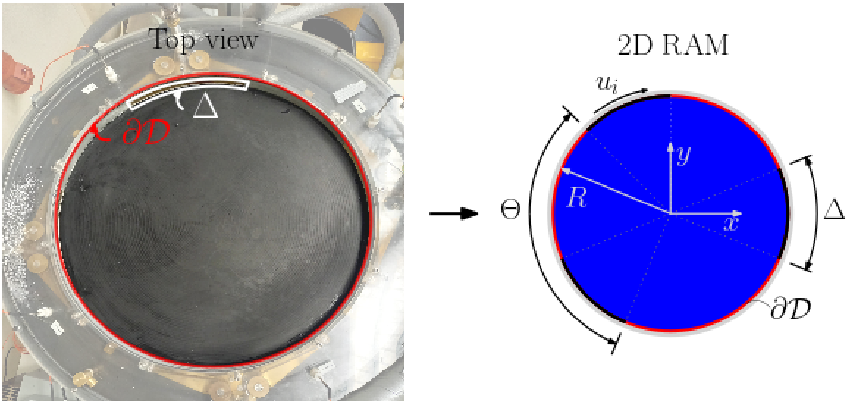

Figure 1.2: The top view and the schematic configuration of the $2D$ RAM. The schematic configuration that shows that the three apertures of arc-length Δ reorient by an angle Θ along the boundary $\partial\mathcal{D}$. The hot (red) boundary temperature and cold (blue) initial fluid temperature are indicated as well.

by a hot boundary $\partial\mathcal{D}$ implemented by circulating a hot fluid through the annulus encircling the fluid container. Heat is transferred from the hot boundary, which encloses the fluid container, into an initially cold fluid.

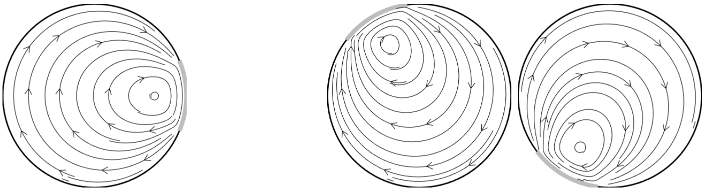
(a) Base flow.

(b) Reoriented flows.

(c) Temperature field evolution.

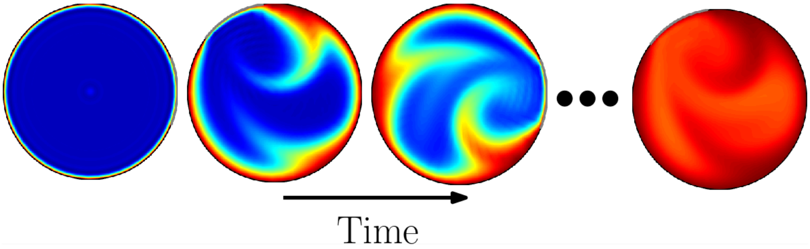

Figure 1.3: The streamlines of (a) base flow and (b) the reoriented flows of a $2D$ RAM with three apertures. The typical evolution of the (c) temperature field evolution for an open-loop periodic reorientation scheme that step-wise activates of the base flow and reoriented flows (blue: cold; red: hot).

Scalar transport is “driven” by reorienting laminar base flows in both the applications of interest and the RAM. Such laminar flows occur in the flow system under consideration as a result of high fluid viscosities, low flow velocities and/or small length scales. Here, reorientations of the laminar base flow are implemented in the applications of interest via flow forcing, e.g., by moving impellers or alternating pumps, and serve to enhance scalar transport. In the $2D$ RAM, moving boundary segments induce a fluid flow by viscous drag. To do so, the hot boundary contains apertures along the azimuth, which are covered by belts. The fluid inside this container is set into motion by viscous drag due to the tangential motion of a belt-pulley system. These moving boundary segments are indicated in Figure 1.2 as well. The (reoriented) fluid flow fields induced, by the moving boundary segments, are shown in Figure 1.3. Flow fields merely reorient by, say, an angle Θ as can be seen in Figure 1.3a,b. The activation of each aperture, following the periodic activation of apertures in Figure 1.3a,b, in the presence of the hot boundary results in a temperature field evolution as shown Figure 1.3c. Figure 1.3c shows that the activation of a moving boundary results in the formation of a plume that transfers heat from the hot boundary into the colder fluid. Various other (a)periodic reorientation sequences can be envisioned for the activation of the fluid flows shown in Figure 1.3a,b. This immediately raises the question that is central to this thesis:

- How to stir the fluid to heat it up as quickly as possible?

1.3 Challenges in boosting scalar transport

This thesis concentrates on the representative scalar transport problem presented in the previous section; heating/cooling of an initially cold/hot fluid in the presence of diffusion through a hot/cold boundary. Boundary heating of a fluid, in the presence of diffusion, involves transporting the scalar quantity in(to) the fluid. This inherently means that scalar transport (and, in particular, fluid heating) is governed by *two* processes. Namely, scalar transfer from the boundary into the fluid and transport of said scalar throughout the fluid. In this study these two processes are, respectively, referred to as energisation and homogenisation hereafter. This section provides an overview of various research challenges currently encountered throughout literature.

1.3.1 Challenges of conventional flow forcing control

The question central to this thesis has been the topic of numerous transport studies. The majority of these transport studies solely concentrate on transport of the scalar *throughout* the fluid and is commonly referred to as *mixing* [18]. In such transport studies, the scalar field typically has a constant (or zero) mean value owing to the presence of an adiabatic boundary condition (i.e. no scalar transport across the system boundary). This means that the majority of transport studies are primarily focussed on homogenization. Effective heat transport in the presence of a non-adiabatic boundary condition requires the optimization of both competing mechanisms involved in fluid heating, however.

The conventional approach towards enhancing scalar transport consists of assuming that enhanced scalar transport, regardless of the nature of the problem, is automatic with efficient fluid mixing and utilising periodic flow reorientations either in space or time to accomplish such mixing in laminar flows via so-called “chaotic advection” [19, 18, 20]. This leans on the intuitive notion that stirring a fluid results in rapid scalar transport. However, a reoriented flow so designed, even if effectively accomplishing chaotic advection, has important limitations for enhancing scalar transport. First, it substantially restricts permissible flow reorientations and thus potentially excludes more optimal scenarios. Second, it discounts the actual scalar transport relevant to the system. Third, it lacks resilience to any unforeseen disturbances and changing process conditions. Fourth, it omits diffusive transport both internally and across non-adiabatic boundaries. Numerous studies have delved into any number of these limitations leading to various solutions such as (a)periodic flow forcing [21], optimized periodic flow forcing [12, 22] or optimized (aperiodic) flow forcing [23, 24] to name a few. Cortelezzi et al. [24] showed that flow forcing protocols designed for fast homogenisation can only enhance scalar transport in the absence of significant diffusion (i.e. for high Pèclet numbers $Pe \gtrsim \mathcal{O}(10^3)$). However, adopting an open-loop flow forcing approach – viz. real-time actuation of the fluid flow without any knowledge of the underlying evolution of the scalar field – inherently results in the abovementioned limitations.

These limitations can be mitigated by basing flow forcing on the current scalar field with a controller. Thusfar, the roll-out based optimal controller proposed by Dolk et al. [25] remains one of the only closed-loop methods that uses *flow forcing* to boost homogenization. In addition, boosting scalar transport with a flow forcing controller in the presence of both diffusion *and* non-adiabatic boundary conditions has remained an open issue.

1.3.2 Scalar field estimation

Knowledge of the *complete* scalar field (or state) is of vital importance to perform (closed-loop) flow forcing control to boost scalar transport. However, in practical (industrial) applications, information about the scalar field is, typically, only partially available through measurements with a finite set of sensors. To obtain the complete field and, consequently, track scalar transport, a state estimator (or observer) can be used. Estimator (or observer) design for state reconstruction is a well-established field within the control community (see reviews [26, 27] and the references therein). The majority of these designs require states that only evolve in time (i.e. their dynamics are described by ordinary differential equations (ODEs)). Estimating states that also evolve in space – viz. scalar fields governed by partial differential equations (PDEs) – requires more elaborate techniques for estimator/observer design. Several techniques for state estimation in PDEs are available in literature, which include backstepping observers [28, 29], optimal observers [30], nonlinear observers [31, 32, 33], (extended) Kalman filters [34, 35] or Luenburger observers [36, 37, 38, 39, 40]. However, the majority of estimator design studies only focus on the theoretical and numerical development of said designs. Moreover, the developed observers are often designed for one-dimensional ($1D$) systems, which are governed by PDEs without space-varying coefficients. In addition, PDEs are usually discretized, by various numerical methods to obtain a set of ODEs, to perform numerical simulations [41]. Regardless of the method employed, fluid heating in two-dimensional ($2D$) systems typically contains a significantly large number of states (i.e. all nodal elements of a scalar field). The computational burden associated with estimation in such large scale systems (i.e. in terms of the state dimension) renders most of the abovementioned techniques computationally too slow/complex for real-time state reconstruction. Furthermore, estimator designs for systems without space-varying coefficients are not necessarily applicable to systems with more intricate transport dynamics (e.g. such as heat transport with a $2D$ flow field shown in Figure 1.3c). Nonetheless, Gunder et al. [34] successfully applied an extended Kalman filter for $2D$ velocity field reconstruction based on a discretely sampled field from a CFD model. Lausterer et al. [42] performed experimental $2D$ temperature field reconstruction of a heated steel ingot. However, (experimental) $2D$ scalar field estimation in fluids with a (laminar) flow field has remained an open challenge.

1.3.3 Scalar transport measure

The question central to this thesis has been the subject of several studies. In these studies a variety of measures has been proposed to gauge the effectiveness of scalar transport. For example, Danckwerts [43] introduced the intensity of segregation as the variance of a scalar field with respect to its equilibrium value. Mix-norms – defined separately by Mathew et al. [44] and Doering and Thiffeault [45] – are equivalent to Sobolev space norms of negative indices. These norms can be viewed as the power spectral density of the scalar field [44]. D'Alessandro et al. [46] gauged mixedness of a dynamical system by its entropy. Numerous other measures have been investigated, which are very effective to determine the “state” of the scalar field in measure-preserving systems [18, 47, 48, 49, 50]. However, the flow velocities, length scales and (thermal) diffusivity considered here, are such that diffusion plays a significant role in scalar transport. Moreover, scalar influx across a system boundary occurs due to the presence of a non-adiabatic boundary condition in the applications of interest. For flow systems where scalar transport occurs in the presence of both i) diffusion and ii) a non-adiabatic boundary condition, a different, more appropriate measure, needs to be devised to track scalar transport. The effectiveness of scalar transport for systems with significant diffusion and a non-adiabatic boundary condition has been determined by L^p norms [51] or (several) statistical properties of the scalar field [52, 53]. However, how fluid flow relates to the two competing aspects that control fluid heating remains an open challenge.

1.4 Research objectives and contributions

In this thesis, closed-loop flow controllers and field estimators are used to solve the challenges inherently associated with rapid fluid heating by conventional flow control strategies as introduced in Section 1.2. In Section 1.4.1, the essential components of the closed-loop used to boost scalar transport are briefly introduced. The research objectives of this thesis are presented in Section 1.4.2. Finally, the research contributions of this thesis are presented in Section 1.5.

1.4.1 Closed-loop flow forcing control

The objective of a controller is to ensure the output of a system behaves as intended by manipulating the input [54]. In this thesis, the goal of a flow controller is to boost scalar transport by stirring. In that case, the scalar field can be viewed as the output or, in case the field is measured with only a discrete sensor set, parts of the scalar field can be viewed as the output. Moreover, the fluid flow field(s) can be viewed as the input that can manipulate/influence the scalar field. Boosting scalar transport, in the context of this thesis, refers to reaching a desired (homogeneous) scalar field at steady-state which can thus be viewed as a reference r such that $\widetilde{T} = T - r$. This allows a closed-loop flow controller for boosting scalar transport to be schematically represented as in Figure 1.4.

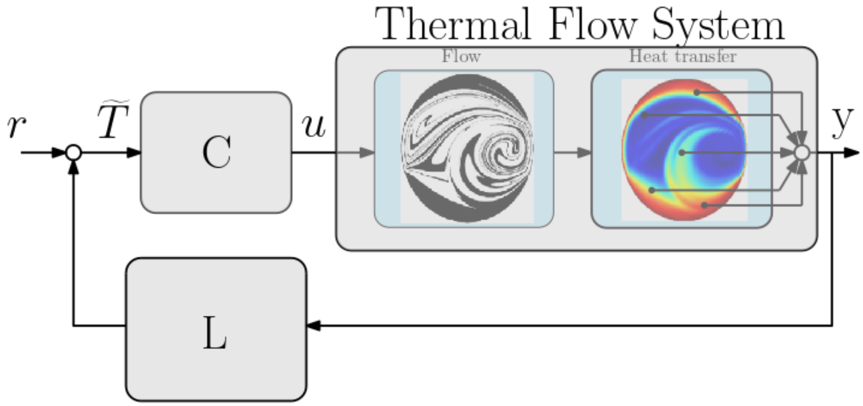

Figure 1.4: A schematic of the closed-loop feedback controller C with estimator L considered in this thesis.

Figure 1.4 shows a simplified version of the closed-loop flow controllers central to this thesis. The flow controller C in Figure 1.4 requires a *control error* $\widetilde{T}$ to devise an appropriate input (or fluid flow field) with which to adjust the scalar field. For the $2D$ RAM, and likewise for the applications of interest in this thesis (see Figure 1.1), the control error is defined as the difference between the desired (homogeneous) scalar field at steady-state (i.e. the scalar field as time $t \to \infty$) and the instantaneous scalar field. For the $2D$ RAM, the instantaneous scalar field of interest is the temperature field. The controller requires this instantaneous scalar field to determine the control error $\widetilde{T}$. The complete temperature distribution inside $\mathcal{D}$ is available in the (experimental) $2D$ RAM (like Figure 1.3c). However, in many practical applications the scalar field is only partially available by measurements with a discrete sensor set. Hence, the instantaneous field needs to be reconstructed based on the available measurement data. The reconstruction or estimation of the instantaneous field requires the inclusion of an estimator L (or observer) in the feedback loop as shown in Figure 1.4.

1.4.2 Research objectives

The methods, developed throughout this thesis, are numerically and/or experimentally investigated on a representative case-study, i.e., the $2D$ RAM, presented in Section 1.2. The case-study consists of a two-dimensional fluid container, which is enclosed by a circular boundary. The schematic configuration of the studied system is shown in Figure 1.2. A closed-loop flow forcing controller is used to tackle the inherent challenges associated with boosting fluid heating with open-loop flow forcing control (e.g. such as periodic flow reorientation shown in Figure 1.3c).

The principal objective of this thesis is to gain theoretical and experimental insight into the design of closed-loop flow forcing controllers that can boost scalar transport by stirring. The intermediate objectives of this thesis can be listed as:

Objective 1. Gain insights into heating dynamics that can be used to structurally boost fluid heating in practice.

Objective 2. Develop a flow forcing controller that significantly enhances fluid heating in the presence of both diffusion and a non-adiabatic boundary condition.

Objective 3. Develop a method that is able to accurately capture/reconstruct the scalar field from discrete sensor data in practice.

The first two objective directly relate to the question raised at the end of Section 1.2. Moreover, achieving the first objective can, for example, improve scalar transport of existing systems or helps in the redesign/improvement of novel applications. The third objective directly relates to the closed-loop presented in Figure 1.4 as field estimation is of particular interest in the development of a practical closed-loop flow forcing controller.

1.5 Contributions

There are four contributions in this thesis that directly address the three research objectives presented in the previous section. These contributions are:

Contribution 1. The first main contribution of this thesis consists of a flow controller for fluid heating. The fluid flow activation is determined by way of a cost-function prediction. The cost-function contains the difference between the instantaneous and a target fluid temperature. Moreover, the complete temperature field is available for feedback flow control. Therefore, the estimator in Figure 1.4 is absent in the closed-loop considered in this contribution. A rigorous and in-depth analysis reveals that the cost-function captures both facets of the heating process (i.e. energization and homogenization). Function analysis reveals that the flow field acts as the “thermal actuator” that simultaneously influences both competing facets of heating. The flow controller is investigated for the representative case-study presented in Section 1.2. The controller significantly accelerates heating compared to a conventional periodic stirring protocol for a large span of model parameters.

Contribution 2. The second main contribution of this thesis provides insights to improve existing heating systems. To this end, the flow controller of the first main contribution is analysed further. The flow controller is used to obtain stirring sequences that accelerate heating compared to periodic stirring. The flow controller is only allowed to circulate the fluid in a single direction in these stirring sequences. Fluid heating with circulation in a single direction covers a large range of industrial applications. Numerical results reveal improved resilience against deviations in model parameter (i.e. Péclet number and activation time) with the found stirring sequences, while simultaneously ensuring faster heating, compared to the periodic stirring sequences. The adaptive sequences achieve this by either i) (slightly) altering periodic stirring sequences or ii) introducing aperiodic transients.

Contribution 3. Conventional (periodic) stirring approaches rely on activating a single flow for discrete time windows. The simultaneous and continuous actuation of flow(s) can potentially achieve even faster fluid heating. In the third contribution of this thesis a general form of the novel cost-function is used to achieve fluid heating. The analogy of these cost functions with thermal energy makes them well suited as control Lyapunov functions. This view lies at the foundation of the bang-bang controller and the quadratic feedback controller developed in this contribution. The designed flow controllers use the simultaneous and continuous actuation of flow(s) to boost heating. The flow controllers are numerically and theoretically investigated for the representative case-study presented in Section 1.2. Well-posedness of the bang-bang controller is proven to assure existence and uniqueness of the closed-loop system. Again, the complete temperature field is available for flow control. Hence, the estimator in Figure 1.4 is absent in the closed-loop considered in this contribution. Numerical results show that both flow controllers can heat a fluid faster than mere diffusion, fluid circulation by a single flow and a conventional periodic stirring sequence. Scaling of the inputs with the instantaneous scalar field makes the quadratic controller particularly well suited for practical applications. An in-depth analysis of the improved heating behaviour reveals an effective mechanism for fluid heating. Moreover, this heating behaviour and, consequently, its improvement in fluid heating possesses at least some resilience to perturbations.

Contribution 4. The flow controllers in the main contributions of this thesis rely on the full knowledge of the temperature field. However, in practice the temperature field is only partially available from discretely located sensor data. Therefore, in the final contribution of this thesis a Luenburger estimator is designed and implemented for temperature field reconstruction. The estimator requires only a small part of the scalar field, available through measurements by discrete sensors that sample the scalar field, to reconstruct the field. A sensor placement method and parameter identification method are presented here as well. The developed estimators are investigated both numerically and experimentally on the representative case-study presented in Section 1.2. The estimator is investigated both numerically and experimentally to gauge practical feasibility in the closed-loop in Figure 1.4. Numerical results show that the estimator is able to accurately capture the scalar field for mere diffusion, a single flow or a periodic stirring sequence. Moreover, experiments show that the estimator can still accurately reconstruct the scalar field even in the presence of noise.

1.6 Thesis outline

This thesis consists of 7 chapters including the introduction. In Chapter 2, the first main contribution of this thesis is presented. The main results in Chapter 2 are based on Lensvelt et al. [55] and preliminary results appear in Lensvelt et al. [56]. The evolution of the cost-function in this chapter is presented in Appendix A. Chapter 3 encompasses the second main contribution of this thesis of which preliminary results can be found in Lensvelt et al. [57]. In Chapter 4, the two flow controllers, which represent the third main contribution of this thesis, are presented and analyzed. The numerical results in this chapter are based on the preliminary results presented in Lensvelt et al. [58]. The eigenfunctions, used to model heat-transfer in Chapter 4, and a well-posedness result for the bang-bang flow controller are presented in Appendix B and Appendix C, respectively. Chapter 5 and Chapter 6 contain the fourth and final contribution of this thesis. The derivations required to determine local identifiability during parameter identification are presented in Appendix D. Reorientation invariance of the discrete algebraic Ricatti equation (DARE) and the evolution of the estimation error for a periodic flow are presented in Appendix E and Appendix F, respectively. The impact of sensor placement on scalar field estimation in with heat transport driven by the base flow is presented in Appendix G. Finally, Chapter 7 provides a summary of the main results and conclusions of this thesis combined with several recommendations for future research. Note that Chapters 2, 4 and 5 are standalone by design such that these chapters can be read individually. This can introduce some repetition in the introductions and/or system descriptions amongst these chapter. Chapter 3 and Chapter 6 are extension to Chapter 2 and Chapter 5, respectively.

CHAPTER 2

Fast fluid heating by adaptive flow reorientation

Transport of scalar quantities such as e.g. heat or chemical species in laminar flows is key to many industrial activities and stirring of the fluid by flow reorientation is a common way to enhance this process. However, "How best to stir?" remains a major challenge. The present study aims to contribute to existing solutions by the development of a dedicated flow-control strategy for the fast heating of a cold fluid via a hot boundary in a representative case study. In-depth analysis of the dynamics of heating in fluid flows serves as foundation for the control strategy and exposes fluid deformation as the "thermal actuator" via which the flow affects the heat transfer. This link is non-trivial, though, in that fluid deformation may both enhance and diminish local heat exchange between fluid parcels and a fundamental "conflict" between local heat transfer and thermal homogenisation tends to restrict the beneficial impact of flow to short-lived episodes. Moreover, the impact of fluid deformation on the global fluid heating is primarily confined to the direct proximity of the moving boundary that drives the flow. These insights imply that incorporation of the thermal behaviour is essential for effective flow-based enhancement strategies and efficient fluid mixing, the conventional approach adopted in industry for this purpose, is potentially sub-optimal. The notion that global heating encompasses two concurrent processes, i.e. increasing energy content ("energising") and thermal homogenisation, yields the relevant

---

The contents of this chapter is based on: R. Lensvelt, M.F.M. Speetjens and H. Nijmijer "Fast fluid heating by adaptive flow reorientation", In: *International Journal of Thermal Sciences*, (180), 107720, 2022. Related preliminary results are reported in: R. Lensvelt, M.F.M. Speetjens and H. Nijmijer "Heat-transfer enhancement by adaptive reorientation of flow fields". In: *5th Thermal and Fluids Engineering Conference.*, New-Orleans, pages 411-420, 2020.

metrics for the global dynamics and thus enables formulation of the control problem as the minimisation of a dedicated cost function. This facilitates step-wise determination of the "best" flow reorientation from predicted future evolutions of actual intermediate states and thereby paves the way to (real-time) regulation of scalar transport by flow control in practical applications. Performance analyses reveal that this "adaptive flow reorientation" significantly accelerates the fluid heating throughout the considered parameter space and thus is superior over conventional periodic schemes (designed for efficient fluid mixing) both in terms of consistency and effectiveness. The controller in fact breaks with conventions by, first, never selecting these periodic schemes and, second, achieving the same superior performance for all flow conditions irrespective of whether said mixing occurs. The controller typically achieves this superiority by thermal plumes that extend from the hot wall into the cold(er) interior and are driven by two alternating and counter-rotating circulations.

2.1 Introduction

Transport of scalar quantities such as e.g. heat or chemical species in laminar flows is key to many industrial activities ranging from viscous mixing of polymers and foodstuffs [2, 3] via process intensification and micro-fluidic devices [4, 5, 6] to subsurface resource recovery [7, 8, 9] and groundwater remediation [10, 11]. Such systems often employ reorientations of a laminar base flow via the flow forcing (e.g. moving impellers or alternating pumps) to enhance scalar transport and thus lean on the intuitive notion that stirring of a fluid benefits this transport. However, design and engineering of such reoriented flows faces a major challenge, namely "How best to stir?" and, intimately related to this, "What defines efficient transport?" in a given system.

The conventional approach towards tackling this challenge consists of assuming that enhanced scalar transport, regardless of the nature of the problem, is automatic with efficient fluid mixing and utilising periodic flow reorientations either in space or time to accomplish such mixing in laminar flows via so-called "chaotic advection" [19, 18, 20]. Numerous studies adopt this approach for a variety of configurations and design strategies ranging from parametric optimisation of activation times to maximising entropy [46, 16, 59, 5, 60]. However, a reoriented flow so designed, even if effectively accomplishing chaotic advection, has important limitations for enhancing scalar transport. First, it substantially restricts permissible flow reorientations and thus potentially excludes more optimal scenarios. Second, it is non-dedicated by discounting the actual scalar transport relevant to the system. Third, it lacks robustness to unforeseen disturbances and changing process conditions. Fourth, it omits diffusive transport both internally and across non-adiabatic boundaries.

The above limitations motivated a host of efforts to design and create flows for enhancing scalar transport by way of optimal control [49, 23, 61, 62, 24, 63, 64, 65, 66, 67, 25]. This overwhelmingly concerns scalar homogenisation in adiabatic systems and the control strategy essentially consists of *a priori* determining the flow (forcing) that maximally accelerates said homogenisation in terms of an optimality criterion. To this end various measures for scalar transport have successfully been employed, primarily the mix-norm [61, 24, 64, 60, 66, 67, 68] yet also e.g. stretching rates of fluid interfaces [49] or the intensity of segregation [25]. Reference [23] thus designed a control law for a four-point vortex flow that maximizes the scalar flux across certain fluid interfaces via low-frequency modulation of the vortex motion. Reference [68] thus determined the motion of stirrers to accomplish maximum scalar homogenisation inside a circular domain using the mix-norm by [44].

However, these control strategies generally concern scalar transport only by (chaotic) advection and are often restricted to highly-idealised configurations and/or forcing mechanisms with limited practical relevance. Several studies address the effect of diffusion (characterised by the well-known Péclet number Pe) by demonstrating that control laws and measures designed for advective transport (i.e. limit $Pe \to \infty$) may remain effective for finite Pe. Flow forcing optimised for advective transport in Reference [24] e.g. proved effective for $Pe \gtrsim \mathcal{O}(10^4)$ and Reference [66] e.g. successfully applied the mix-norm down to $Pe \sim \mathcal{O}(10^3)$. Furthermore, Reference [24] introduces some degree of robustness by performing step-wise optimal control using the intermediate state. However, existing studies nonetheless primarily address the first and second limitations mentioned above; limited robustness and omission of diffusion remain two important shortcomings in most optimal-control approaches. Moreover, goals other than homogenisation such as e.g. enhanced scalar flux across non-adiabatic boundaries receive scant attention to date.

The above findings motivate the present study, which aims at contributing to the development of dedicated flow-control strategies for enhancement of advective-diffusive scalar transport in realistic flow systems with non-adiabatic boundaries. To this end the present study adopts heating of an initially cold fluid via an isothermal hot boundary in the 2D unsteady Rotated Arc Mixer (RAM) according to [17] as representative case study. Control target is accomplishing “fast” fluid heating in a robust manner by a control strategy that step-wise determines the most effective reorientation of the RAM base flow from predicted future evolutions of the actual intermediate state. This expands the exploratory study in [56] by, first, foundation of the control strategy on insights into the dynamics of heating in fluid flows and, second, an extensive performance analysis.

The study contributes to existing work in literature in several ways. First, it involves advective-diffusive scalar transport including flux across a non-adiabatic boundary in a realistic configuration. The RAM namely is experimentally realisable and admits laboratory studies both on (chaotic) advection and thermal transport [17, 69]. Second, the control problem is of great (practical) relevance yet, contrary to scalar homogenisation in adiabatic systems, scarcely investigated. Third, the control strategy paves the way to (real-time) regulation of scalar transport in practical applications. This sets the present study apart from related studies on realistic boundary-driven flows in [49, 25, 68]. The latter namely concern enhancement of scalar homogenisation. Moreover, References [49, 68] again employ optimal control for this purpose; only Reference [25] (to the best of our knowledge) adopts prediction-based state-feedback control akin to the present study.

The study is organised as follows. Section 2.2 introduces the problem of interest and the general control strategy including the (to this end relevant) structure of the temperature field in reoriented flows. The dynamics of heating in fluid flows are investigated in Section 2.3 and insights thus gained are employed to develop the control strategy in Section 2.4. The performance of adaptive flow reorientation is examined in Section 2.5 by a computational analysis and reconciled with flow and thermal physics. Conclusions and recommendations for future work are presented in Section 2.6.

2.2 Scalar transport in reoriented flows

2.2.1 Flow configuration

The flow configuration of the $2D$ unsteady RAM is given in Figure 2.1a and consists of a circular container $\mathcal{D} = \left\{ (r,\theta) \in \mathbb{R}^2 \middle| r \leq R, -\pi \leq \theta \leq \pi \right\}$ enclosed by a circular boundary $\Gamma = \partial\mathcal{D}$ of unit radius R (red circle). The circumference of the RAM contains N apertures (black arcs in Figure 2.1a) with arc length Δ and angular offset $\Theta = 2\pi/N$ (i.e. the centerline of arc $1 \leq k \leq N$ is located at angle $\theta_k = (k-1)\Theta$). Sliding wall segments along these apertures (practically realizable by belts [17]) via viscous drag drive the flow inside the RAM. Activation of the first arc (i.e. centred on the x-axis) in clockwise direction at an angular velocity Ω thus sets up a steady flow $\mathbf{v}_1$ with streamline pattern following Figure 2.1b. This constitutes the *base flow* of the RAM. Assumed are an instantaneous fluid response and negligible inertia, implying that the base flow is a steady Stokes flow symmetric about the x-axis and admitting an analytical solution following [70]. These properties have the important consequence that other activations of the arcs result in flows that are direct transformations of base flow $\mathbf{v}_1$. Reversal of the motion of the first arc simply reverses the base flow, yielding a flow $\mathbf{v}(r,\theta) = -\mathbf{v}_1(r,\theta)$, while maintaining the streamline portrait following Figure 2.1c. Activation of arc $k > 1$ rotates the base flow and yields a flow following $\mathbf{v}\left(r,\theta\right) = \mathbf{v}_1\left(r, \theta + \left(k-1\right)\Theta\right)$, resulting in reoriented flows as shown in Figure 2.1d for $k = 2$ (left) and $k = 3$ (right) for reorientation angle $\Theta = 2\pi/3$.

Systematic reorientation of a base flow by the flow forcing as exemplified in Figure 2.1 for the RAM can be accomplished in many industrial applications by similar wall activations yet also via mechanic stirrers, electro-magnetic stirring and an array of (micro-fluidic) body forcings such as e.g. electro-osmosis, acoustic streaming or electro-wetting [20]. Moreover, recent studies demonstrated that subsurface flows in e.g. enhanced geothermal systems, *in situ* mining or groundwater remediation admit similar flow reorientation via unsteady pumping schemes for injection and production wells [71, 9]. Thus the RAM indeed captures the essence of a wide range of systems.

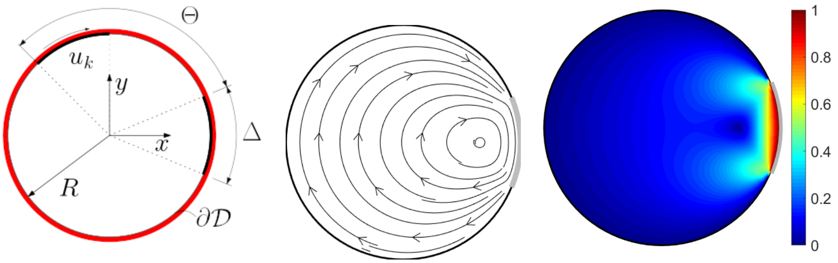
(a) Geometry (b) Base flow

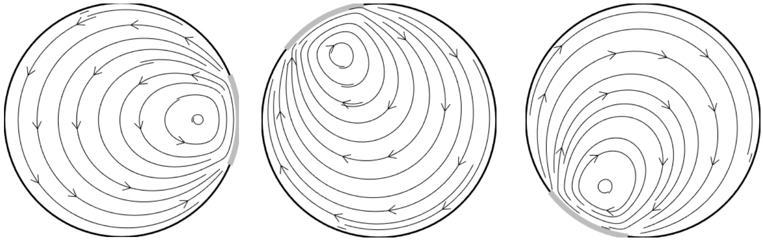
(c) Reversed flow (d) Reoriented flows

Figure 2.1: Flow configuration of 2D unsteady RAM: (a) geometry bounded by circular wall of radius R containing apertures of arc length $\Delta = \pi/4$ and offset by angle Θ; (b) streamline pattern (left) and magnitude (right) of base flow driven by arc at $-\Delta/2 \leq \theta \leq \Delta/2$; (c) reversed base flow; (d) reorientations of the base flow.

2.2.2 Thermal problem and general control strategy

Scalar transport in the RAM is investigated in terms of the heating of an initially cold fluid at uniform temperature T_0 inside $\mathcal{D}$ via the hot boundary Γ with constant temperature $T_\infty > T_0$ (red circle in Figure 2.1a). The evolution of the corresponding temperature field $T(\mathbf{x}, t)$ is described by the advection-diffusion equation (ADE), which in non-dimensional form is given by

$$\frac{\partial T}{\partial t} = -\mathbf{v} \cdot \boldsymbol{\nabla} T - \nabla \cdot \mathbf{q} = -\mathbf{v} \cdot \boldsymbol{\nabla} T + \frac{1}{Pe} \boldsymbol{\nabla}^2 T, \qquad \mathbf{q} = -\frac{1}{Pe} \boldsymbol{\nabla} T, \tag{2.1}$$

with $\mathbf{v}(\mathbf{x}, t)$ the unsteady flow, $Pe = UR/\nu$ the well-known Pèclet number (determined by characteristic length and velocity scales R and $U = \Omega R$, respectively, and thermal diffusion ν) and $\mathbf{q}$ the diffusive heat flux according to Fourier's law [17, 56]. (Geometry and flow forcing rescale to unit radius $R = 1$ and unit angular velocity $\Omega = 1$, respectively). The initial and boundary conditions corresponding with the above heating problem are $T(\mathbf{x}, 0) = T_0$ and $T(\mathbf{x}, t)|_\Gamma = T_\infty$ for all $\mathbf{x} \in \mathcal{D}$ and $t \geq 0$. Thermal problems within the scope of our study typically have $Pe \sim \mathcal{O}(10^2 - 10^4)$, implying advection-dominated heat transfer yet with significant diffusion. Presence of diffusion has the important consequence that, regardless of the flow $\mathbf{v}$, any initial temperature field $T(\mathbf{x}, 0)$ *always* evolves towards the uniform final state $\lim_{t\to\infty} T(\mathbf{x}, t) = T_\infty$ (Section 2.3.4). Thus the dynamic behaviour induced by a particular flow $\mathbf{v}$ is entirely incorporated in the transient temperature

$$\widetilde{T}(\mathbf{x}, t) \equiv T(\mathbf{x}, t) - T_\infty \tag{2.2}$$

which is governed by the ADE

$$\frac{\partial \widetilde{T}}{\partial t} = -\mathbf{v} \cdot \boldsymbol{\nabla} \widetilde{T} + \frac{1}{Pe} \boldsymbol{\nabla}^2 \widetilde{T}, \qquad \widetilde{T}(\mathbf{x}, 0) = T_0 - T_\infty, \qquad \widetilde{T}(\mathbf{x}, t)\Big|_\Gamma = 0. \tag{2.3}$$

as readily follows from substitution of (2.2) into (2.1). Heating of the fluid then becomes equivalent to progression of the transient temperature towards the final state $\widetilde{T}_\infty = \lim_{t\to\infty} \widetilde{T} = 0$. Initial and boundary conditions can be set to $T_0 = 0$ and $T_\infty = 1$ hereafter without loss of generality and thus give $\widetilde{T}(\mathbf{x}, 0) = -1$ for the initial condition in (2.3).

The flow $\mathbf{v}(\mathbf{x}, t)$ in (2.3) plays a crucial role in the evolution of $\widetilde{T}$ towards $\widetilde{T}_\infty$. It is namely well-known that stirring of a fluid has a major impact on its heating and thereby on the duration of the transient. However, the central question is: "How best to stir to obtain the fastest fluid heating?" The RAM (and reoriented flows in general) aims at achieving optimal stirring in this sense via an unsteady flow $\mathbf{v}$ generated by switching between steady flows $\mathbf{v}_u$ following

$$\mathbf{v}(\mathbf{x}, t) = \mathbf{v}_{u_n}(\mathbf{x}) \tag{2.4}$$

with $\mathcal{U} = \{u_0, u_1, \dots u_n, \dots\}$ the "reorientation scheme" that activates a selected flow $\mathbf{v}_u$ with reorientation u at time step $t_n = n\tau$ ($n \in \{0, 1, \dots\}$) for a time interval $t_n \leq t \leq t_n + \tau$ of duration τ. The activated flow $\mathbf{v}_u$ can for a RAM with N arcs at each t_n be selected from the set of $2N + 1$ flows $\mathbf{v}_k$ defined by transformations of the base flow $\mathbf{v}_1$ according to

$$\mathbf{v}_u(\mathbf{x}) = \begin{cases} sign(u)\mathbf{v}_1(\mathcal{R}_u(\mathbf{x})) & u \neq 0 \\ \mathbf{0} & u = 0, \end{cases} \tag{2.5}$$

with $u \in \{-N, \dots, N\}$. Here operators $\mathcal{R}_u : (r, \theta) \to (r, \theta - (|u| - 1)\Theta)$ and $sign(u)$ determine rotation and flow direction, respectively, for a given $u \neq 0$. For example: $u = 3$ rotates the base flow by angle 2Θ by activation of aperture $u = 3$ in clockwise direction; $u = -3$ in addition reverses aperture motion and flow; $u = 0$ deactivates the flow and heat is transferred by diffusion only. Reorientation scheme $\mathcal{U} = \{1, -3, 2\}$ e.g. subsequently activates apertures $(1, 3, 2)$, each for a duration τ and with clockwise $(1, 2)$ and counter-clockwise (3) motion.

Determining the "best" reorientation scheme $\mathcal{U}$ to achieve the control target, i.e. accomplishing the "fastest" fluid heating, is a major challenge. Existing approaches employ reorientation schemes consisting of *ad infinitum* periodic repetitions of a fixed sequence such as e.g. $\mathcal{U} = \{1, 2, \ldots, N\}$ or sequences determined *a priori* via optimal control. However, both approaches have important conceptual shortcomings and current optimal-control schemes are in general dedicated to homogenisation (Section 2.1). This limits the suitability of these approaches for the present control problem. Section 2.4 resolves this by a dedicated control strategy that identifies the "best" $\mathcal{U}$ specifically for fast fluid heating by step-wise determining the most effective flow reorientation from predicted future evolutions of the actual intermediate state (denoted "adaptive flow reorientation" hereafter). Crucial to this end is an adequate definition and quantification of what constitutes "best" and "fastest" in the present context. This is to be specified in Section 2.4.1.

2.2.3 Reorientation of the temperature field

Key for realizing a control strategy for advective-diffusive transport using reorientations of a base flow for actuation is the property that flow reorientations (2.4) and (2.5) carry over to the temperature field. This hinges on the spectral decomposition of the Perron-Frobenius evolution operator $\mathcal{P}_t$ governing the temperature evolution for the base flow $\mathbf{v}_1$, given by

$$\begin{aligned} \widetilde{T}(\mathbf{x}, t) = \mathcal{P}_t \widetilde{T}(\mathbf{x}, 0) = \sum_{m=0}^{\infty} \alpha_m \phi(\mathbf{x}) e^{\lambda_m t}, \\ \widetilde{T}(\mathbf{x}, 0) = \sum_{m=0}^{\infty} \alpha_m \phi(\mathbf{x}), \end{aligned} \tag{2.6}$$

with $\{\phi_m, \lambda_m\}$ the eigenfunction-eigenvalue pairs defined by the eigenvalue problem

$$Pe^{-1} \boldsymbol{\nabla}^2 \phi_m - \mathbf{v}_1 \cdot \boldsymbol{\nabla} \phi_m = \lambda_m \phi_m, \quad \phi_m\left(\mathbf{x}\right)|_{\Gamma} = 0, \tag{2.7}$$

corresponding with the advection-diffusion operator in (2.1) and α_m the expansion coefficients determined by the initial condition [16, 17]. The terms in (2.6) constitute fundamental dynamic states (commonly denoted "eigenmodes") and are ordered by increasing decay rate according to $\cdots < Re(\lambda_1) < Re(\lambda_0) < 0$, where $m = 0$ is the slowest-decaying (or "dominant") mode with characteristic decay time $\tau_0 = -1/Re(\lambda_0)$.

The spectral decomposition of reoriented flows is governed by eigenvalue problem (2.7) upon substitution of $\mathbf{v}_1$ by $\mathbf{v}_u$ following (2.5) and directly relates to the base-flow decomposition (2.6) via

$$\widetilde{T}(\mathbf{x},t) = \mathcal{P}_t^{(u)}\widetilde{T}(\mathbf{x},0) = \sum_{m=0}^{\infty} \alpha_m^{(u)}\psi_m^{(u)}(\mathbf{x})e^{\lambda_m t}, \qquad \widetilde{T}(\mathbf{x},0) = \sum_{m=0}^{\infty} \alpha_m^{(u)}\psi_m^{(u)}(\mathbf{x}), \tag{2.8}$$

with $\mathcal{P}_t^{(u)}$ the corresponding Perron-Frobenius operator and

$$\mu_m = \left\{ \begin{array}{ll} \lambda_m & u \neq 0 \\ \lambda_m^0 & u = 0 \end{array} \right. , \qquad \psi_m^{(u)}(\mathbf{x}) = \left\{ \begin{array}{ll} \phi_m\left(\mathcal{G}_u\left(\mathbf{x}\right)\right) & u \neq 0 \\ \phi_m^0(\mathbf{x}) & u = 0 \end{array} \right. , \tag{2.9}$$

where $\{\phi_m^0, \lambda_m^0\}$ are the eigenfunction-eigenvalue pairs for the diffusion-only case $u = 0$ governed by (2.7) for deactivated base flow $\mathbf{v}_1 = \mathbf{0}$, and

$$\mathcal{G}_u : (r,\theta) \rightarrow \left\{ \begin{array}{ll} \mathcal{R}_u(r,\theta) & u > 0 \\ \mathcal{S}\left(\mathcal{R}_u(r,\theta)\right) & u < 0 \end{array} \right. , \tag{2.10}$$

the transformation operator for the eigenfunctions and $\mathcal{S} : (r,\theta) \rightarrow (r,-\theta)$ a reflection about the symmetry axis $\theta = 0$ of the base flow. Thus flow reorientation (and reversal) results in the same reorientation (and reflection) of the eigenfunction basis ϕ_m of the base flow while maintaining the eigenvalue spectrum λ_m and, inherently, the decay rates. Flow deactivation results in a projection onto to the eigenfunction basis ϕ_m^0 and corresponding eigenvalues λ_m^0 of the diffusion-only case.

Spectral decomposition (2.8) admits direct expression of the evolution of the transient temperature $\widetilde{T}$ for any flow reorientation (including deactivation) in terms of the base-flow decomposition (2.6) and its diffusion-only counterpart for $\mathbf{v}_1 = \mathbf{0}$. This facilitates efficient prediction of $\widetilde{T}$ for arbitrary flow reorientations and is an essential element for the control strategy proposed in Section 2.4.

2.3 Dynamics of heating in fluid flows

A further essential element for the control strategy, besides the reorientation property of Section 2.2.3, is adequately capturing the system dynamics and in particular the impact of the (base) flow on the heating process. To this end the dynamics of this process are investigated below.

2.3.1 Fluid deformation as “thermal actuator”

The main reasoning behind the belief that fluid mixing and chaotic advection automatically enhance heat transfer is that this tends to expand fluid interfaces and increase scalar gradients via exponential stretching of fluid parcels and thereby yields faster scalar exchange over larger areas [20]. Fluid deformation may thus indeed act as a “thermal actuator” yet the underlying mechanisms and resulting behaviour are rather delicate and, contrary to said belief, not necessarily conducive to efficient heat transfer. This is investigated below and leans on the so-called “Lagrangian representation” of fluid flow and heat transfer (i.e. relative to the fluid parcels).

2.3.1.1 Lagrangian dynamics of fluid motion

The Lagrangian representation of fluid motion expresses the Eulerian flow field $\mathbf{v}$ in (2.1) in terms of the evolution of the current positions $\mathbf{x}(t)$ of fluid parcels released at initial position $\mathbf{x}(0) = \mathbf{x}_0$. This Lagrangian motion is governed by the kinematic equation

$$\frac{d\mathbf{x}(t)}{dt} = \mathbf{u}\left(\mathbf{x}(t), t\right), \quad \mathbf{x}(0) = \mathbf{x}_0 \quad \Rightarrow \quad \mathbf{x}(t) = \mathbf{\Phi}_t(\mathbf{x}_0), \tag{2.11}$$

with flow $\mathbf{\Phi}_t$ as its formal solution [19]. Relevant in the present context of heat transfer is, besides the displacement of fluid parcels, in particular also their deformation due to viscous stresses. Classical continuum mechanics describes this deformation in terms of the so-called “Lagrangian coordinates”, which are defined by the initial parcel positions $\mathbf{x}_0$ and via inversion of (2.11), i.e.

$$\mathbf{x}_0 = \mathbf{\Phi}_t^{-1}(\mathbf{x}). \tag{2.12}$$

relate to the Eulerian coordinates $\mathbf{x}$ [72]. The Eulerian representation shows the momentary situation at time t in fixed positions $\mathbf{x}$ in physical space as actually seen by an observer; the Lagrangian representation gives this situation relative to the moving fluid parcels (labelled by initial positions $\mathbf{x}_0$) and thus enables description of the corresponding material behaviour. Key to this are the deformation gradient tensor and right Cauchy-Green deformation tensor, given by

$$\begin{aligned} F_0 &= \partial\mathbf{x}/\partial\mathbf{x}_0 = (\nabla_0\mathbf{x})^\dagger, \\ C_0 &= F_0^\dagger F_0 = \lambda_1\mathbf{v}_1^0\mathbf{v}_1^0 + \lambda_2\mathbf{v}_2^0\mathbf{v}_2^0 = \Lambda^{-1}\mathbf{v}_1^0\mathbf{v}_1^0 + \Lambda\mathbf{v}_2^0\mathbf{v}_2^0, \end{aligned} \tag{2.13}$$

respectively, where F_0 describes the motion of initial material line segments $d\mathbf{x}_0$ in the reference frame co-moving with a parcel released at $\mathbf{x}_0$ via $d\mathbf{x} = F_0 d\mathbf{x}_0$ and C_0 describes its corresponding material deformation via $|d\mathbf{x}|^2 = d\mathbf{x}^\dagger \cdot d\mathbf{x} = d\mathbf{x}_0^\dagger \cdot C_0 \cdot d\mathbf{x}_0$ († indicates transpose). Relation (2.13) gives C_0 in terms of its eigenvalue-eigenvector pairs $(\lambda_i, \mathbf{v}_i^0)$ and thus exposes the principal compression axis $\mathbf{v}_1^0$ (factor $\lambda_1 = \Lambda^{-1} < 1$) and principal stretching axis $\mathbf{v}_2^0 \perp \mathbf{v}_1^0$ (factor $\lambda_2 = \Lambda > 1$) of the deforming fluid parcel in question. ($|C_0| = \lambda_1\lambda_2 = 1$ for the 2D flow of an incompressible fluid.) The associated left Cauchy-Green deformation tensor

$$B_0 = F_0 F_0^\dagger = R_0 C_0 R_0^\dagger = \Lambda^{-1}\mathbf{v}_1\mathbf{v}_1 + \Lambda\mathbf{v}_2\mathbf{v}_2, \quad \mathbf{v}_i = R_0\mathbf{v}_i^0, \tag{2.14}$$

describes the material deformation in terms of the principal deformation axes $\mathbf{v}_{1,2}$ in current position $\mathbf{x}$ in the Eulerian frame. These axes are simply rotations of their companions $\mathbf{v}_{1,2}^0$ in the Lagrangian frame by R_0 from the well-known polar decomposition $F_0 = R_0 U_0$ [72]. Further relevant tensors are the counterparts of (2.13) and (2.14) in the reversed flow $\mathbf{x}_0 = \mathbf{\Phi}_t^{-1}(\mathbf{x})$, i.e.

$$\begin{gathered} F = (\nabla \mathbf{x}_0)^\dagger = F_0^{-1}, \quad C = B_0^{-1} = \Lambda \mathbf{v}_1 \mathbf{v}_1 + \Lambda^{-1} \mathbf{v}_2 \mathbf{v}_2, \\ B = C_0^{-1} = \Lambda \mathbf{v}_1^0 \mathbf{v}_1^0 + \Lambda^{-1} \mathbf{v}_2^0 \mathbf{v}_2^0, \end{gathered} \tag{2.15}$$

constituting inverses of the tensors of the forward flow following (2.11) and revealing that the principal contraction and stretching axes interchange. The stretching rate Λ introduced above admits alternative expression as the so-called "Finite-time Lyapunov exponent" (FTLE), i.e.

$$\sigma(\mathbf{x}_0, t) \equiv \frac{\log \Lambda(\mathbf{x}_0, t)}{2t}, \tag{2.16}$$

which sets the upper bound for the material stretching rate of parcel $\mathbf{x}_0$ in the finite time span up to t: $|\mathbf{x}(t)|/|\mathbf{x}_0| \leq \exp(\sigma t)$. Positive FTLEs (i.e. $\sigma > 0$) signify exponential stretching and, if persistent for all t, are regarded as "fingerprints" of chaotic advection [19].

Figure 2.2a illustrates typical Lagrangian dynamics in the base flow $\mathbf{v}_1$ (Figure 2.1b) by the evolution of a fluid element (blue) of initially circular shape released at $\mathbf{x}_0$ (cyan dot). This reveals a gradual deformation into an elliptical shape during its excursion from $\mathbf{x}_0$ to current position $\mathbf{x}$ (cyan star) via the Lagrangian path (cyan) along the streamlines (black concentric curves). This deformation ensues from the shear flow between the streamlines and is dictated by the principal contraction ($\mathbf{v}_1$; gray bar) and stretching ($\mathbf{v}_2$; red bar) axes of B_0. Figure 2.2b gives the corresponding FTLE (2.16) and reveals an increase to a maximum about halfway the high-shear region near the moving arc (entry and exit demarcated by the dashed lines) that is followed by a sharp decline upon transiting into the domain interior towards a minimum at around $t \approx 3$ and a subsequent increase to a moderate level. FTLE $\sigma > 0$ everywhere implies an overall net stretching yet with a partial reversal of earlier deformation in the interval between local maximum and minimum due to strong and "unfavourable" velocity gradients near the exit of the arc region (bottom/left dashed line).

The orientation angle ρ of the principal stretching axis $\mathbf{v}_2$ relative to the streamlines, defined as $\cos\rho = \mathbf{v}_2^\dagger \mathbf{u}/|\mathbf{v}_2||\mathbf{u}|$, is shown in Figure 2.2c and exhibits non-monotonic behaviour consistent with the FTLE: rapid alignment of $\mathbf{v}_2$ with streamlines (i.e. diminishing ρ) within the high-shear region, followed by rapid misalignment upon exiting this region and renewed alignment while further migrating into the domain interior. Fluid elements released at other locations exhibit essentially the same behaviour upon passing through the arc region. Multiple passages of this region while circulating along closed streamlines results in progressively weaker fluctuations and eventually causes convergence on the asymptotic limit

$\lim_{t\to} \rho = 0$. This exposes the stream lines as “attractors” for the fluid deformation in the sense that fluid parcels ultimately align with these entities. Compare this with unstable manifolds of hyperbolic points in chaotic flows and their finite-time counterparts in generic aperiodic flows, viz. attracting LCSs [20].

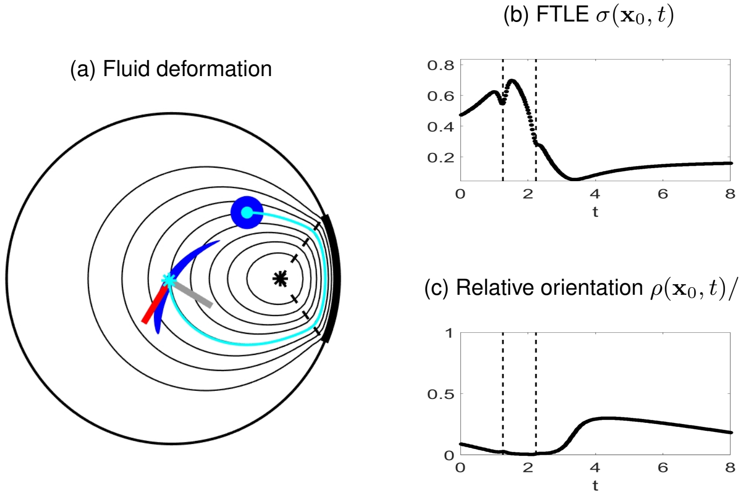
(a) Fluid deformation

(b) FTLE $\sigma(\mathbf{x}_0, t)$

(c) Relative orientation $\rho(\mathbf{x}_0, t)/\pi$

Figure 2.2: Lagrangian dynamics in base flow: (a) deformation of fluid element (blue) along streamlines (black) versus principal stretching (red) and compression (gray) axes; (b) quantitative deformation in terms of FTLE following (2.16); (c) orientation of principal stretching axis relative to streamlines.

2.3.1.2 Lagrangian dynamics of heat transfer

Transformation of the energy balance (2.3) from Eulerian ($\mathbf{x}$) to Lagrangian ($\mathbf{x}_0$) coordinates via (2.12) yields the Lagrangian representation of heat transfer

$$\begin{aligned} &\frac{\partial \widetilde{T}}{\partial t} = -\boldsymbol{\nabla}_0 \cdot \mathbf{q}_0, \\ &\qquad \mathbf{q}_0 = F\mathbf{q} = -F\frac{1}{Pe}\nabla T = -F\frac{1}{Pe}F^{\dagger}\nabla_0 T = -B\frac{1}{Pe}\nabla_0 T, \end{aligned} \tag{2.17}$$

with $\mathbf{q}_0$ the Lagrangian representation of the diffusive heat flux $\mathbf{q} = -Pe^{-1}\nabla T$ according to (2.1) and B the left Cauchy-Green tensor of the reversed flow following (2.15) [73]. Energy balance (2.17) describes the actual heat transfer between a moving fluid parcel at current position $\mathbf{x} = \boldsymbol{\Phi}_t(\mathbf{x}_0)$ with its neighbouring parcels. This occurs solely via diffusive flux $\mathbf{q}_0$; the advective term $\mathbf{v} \cdot \nabla T$ in the Eulerian form has vanished from (2.17) due to vanishing velocity in the (co-moving) Lagrangian frame. Relation (2.17) reveals that the momentary isotropic diffusive flux $\mathbf{q} = -Pe^{-1}\nabla T$ in a fixed position $\mathbf{x}$ in Eulerian space translates into a momentary anisotropic diffusive flux $\mathbf{q}_0$, with B the corresponding diffusion tensor, at the fluid parcel passing through $\mathbf{x}$ and originating from $\mathbf{x}_0 = \mathbf{\Phi}_t^{-1}(\mathbf{x})$. This anisotropy is a direct consequence of fluid deformation; $B = I$ for a non-deforming fluid and yields $\mathbf{q}_0 = \mathbf{q}$.

The Lagrangian heat flux $\mathbf{q}_0$ in (2.17) constitutes the fundamental link between heat transfer and fluid motion and enables further investigation of the impact of the latter on the former. Expression in terms of the principal deformation axes $\mathbf{v}_{1,2}$ of tensor B following (2.15) yields

$$\mathbf{q}_0 = -B\frac{1}{Pe}\nabla_0 T = -\left[\frac{\Lambda}{Pe}(\mathbf{v}_1^0 \cdot \nabla_0 T)\mathbf{v}_1^0 + \frac{1}{\Lambda Pe}(\mathbf{v}_2^0 \cdot \nabla_0 T)\mathbf{v}_2^0\right], \quad (2.18)$$

and reveals that enhancement (by factor Λ) and diminution (by factor Λ^{-1}) of heat transfer occurs in the principal contraction ($\mathbf{v}_1^0$) and stretching ($\mathbf{v}_2^0$) directions, respectively, compared to isotropic heat diffusion $\mathbf{q}_0^{\mathrm{iso}} = -Pe^{-1}\nabla_0 T$ between non-deforming fluid parcels subject to the same flow and temperature field [73]. (Symbol † is for brevity omitted for inner products as in (2.18).) However, the net effect of fluid deformation depends on the orientation of the principal axes $\mathbf{v}_{1,2}^0$ relative to the temperature gradient $\nabla_0 T$ and this may enhance yet also diminish heat transfer between fluid parcels. This highly non-trivial process is investigated further in Section 2.3.2.

Lagrangian energy balance (2.17) admits a formal solution according to

$$\begin{aligned}\widetilde{T}_D(\mathbf{x}_0, t) &= \widetilde{T}(\mathbf{x}_0, 0) + \frac{1}{Pe}\int_0^t \nabla_0 \cdot \left(B|_{\mathbf{\Phi}_\xi(\mathbf{x}_0)}\nabla_0 T(\mathbf{x}_0, \xi)\right) d\xi \\ &\equiv \mathcal{D}_t[\mathbf{x}_0]\widetilde{T}(\mathbf{x}_0, 0),\end{aligned} \quad (2.19)$$

with diffusion operator $\mathcal{D}_t$ as Lagrangian counterpart to the Perron-Frobenius operator $\mathcal{P}_t$ in (2.6). This enables representation of simultaneous advective-diffusive heat transfer governed by (2.3) as a composition of two successive operations: (i) anisotropic diffusion between fluid parcels at fixed positions $\mathbf{x}_0$ via (2.19) and (ii) passive redistribution of fluid parcels to positions $\mathbf{x} = \mathbf{\Phi}_t(\mathbf{x}_0)$, i.e.

$$\widetilde{T}(\mathbf{x}, t) = \widetilde{T}\left(\mathbf{\Phi}_t(\mathbf{x}_0), t\right) = \widetilde{T}_D(\mathbf{x}_0, t). \quad (2.20)$$

which, upon defining an advection operator $\widetilde{T}(\mathbf{x}, t) = \widetilde{T}\left(\mathbf{\Phi}_t^{-1}(\mathbf{x}), 0\right) \equiv \mathcal{A}_t\widetilde{T}(\mathbf{x}, 0)$, translates into

$$\widetilde{T}(\mathbf{x}, t) = \mathcal{A}_t\mathcal{D}_t[\mathbf{x}]\widetilde{T}(\mathbf{x}, 0) = \mathcal{D}_t\left[\mathbf{\Phi}_t^{-1}(\mathbf{x})\right]\mathcal{A}_t\widetilde{T}(\mathbf{x}, 0), \quad (2.21)$$

as two equivalent formulations in terms of Eulerian evolution operators. Thus the Perron-Frobenius operator $\mathcal{P}_t$ following (2.6) decomposes into an advective ($\mathcal{A}_t$) and diffusive ($\mathcal{D}_t$) factor following

$$\mathcal{P}_t = \mathcal{A}_t\mathcal{D}_t[\mathbf{x}] = \mathcal{D}_t\left[\mathbf{\Phi}_t^{-1}(\mathbf{x})\right]\mathcal{A}_t, \quad (2.22)$$

providing a link between the Eulerian and Lagrangian representations of heat transfer.

Figure 2.3 shows the temperature evolution $\widetilde{T}(\mathbf{x},t)$ in the Eulerian frame $\mathbf{x}$ subject to the base flow $\mathbf{v}_1$, with blue and red indicating $\min(\widetilde{T}) = -1$ and $\max(\widetilde{T}) = 0$, respectively. (This colour coding is used throughout the remainder of this study unless noted otherwise.) Shown evolution reveals a thermal plume emanating from the bottom edge of the moving arc and propagating along the streamlines (bright closed curves) into the domain interior. The plume thus "wraps" itself around the center of circulation and creates a hot annular region encircling a cold "core". This behaviour is a direct consequence of the fluid motion: the material stretching along streamlines demonstrated in Figure 2.2 promotes steepening and flattening of the temperature gradient transverse and parallel to the streamlines, respectively. This gradient steepening enhances transverse heat flux in the fluid heated during passage along the arc and thereby promotes its transverse thermal homogenisation while propagating and shearing along the streamlines and thus creates a thermal front (i.e. said plume). The underlying local mechanisms and corresponding impact on the global heating dynamics are investigated in Secs. 2.3.2–2.3.3 and Section 2.3.5, respectively.

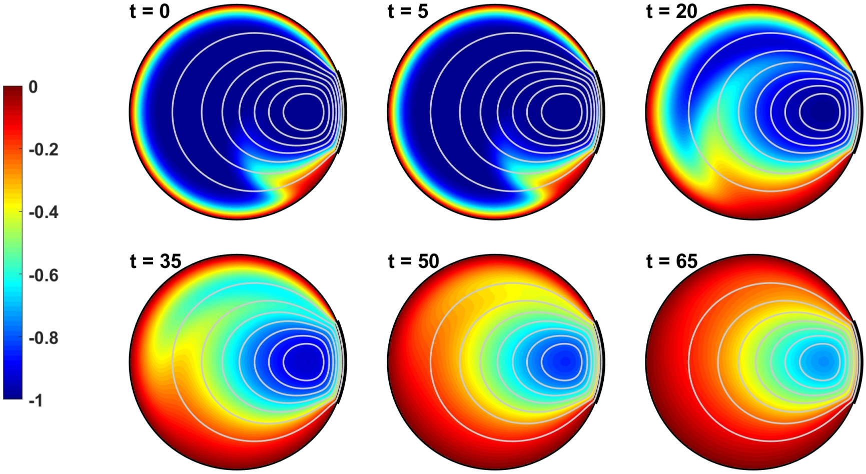

Figure 2.3: Evolution of transient temperature $\widetilde{T}(\mathbf{x},t)$ in Eulerian frame $\mathbf{x}$ subject to base flow (blue: $\min(\widetilde{T}) = -1$; red: $\max(\widetilde{T}) = 0$; closed curves: streamlines).

2.3.2 Local impact of fluid deformation

Relations (2.17) and (2.18) reveal that fluid deformation has a twofold impact on heat transfer $\mathbf{q}_0$ between fluid parcels:

1. Change in flux density. Consider the heat flux $\widetilde{\mathbf{q}}_0 = q_1^0\mathbf{v}_1^0 + q_2^0\mathbf{v}_2^0$ at an undeformed rectangular $dx_1^0 \times dx_2^0$ fluid parcel in the Lagrangian frame and the corresponding heat flux $\widetilde{\mathbf{q}} = q_1\mathbf{v}_1 + q_2\mathbf{v}_2$ at the deformed rectangular $dx_1 \times dx_2$ fluid parcel in the Eulerian frame. (The normals of interfaces $dx_{1,2}^0$ coincide with $\mathbf{v}_{2,1}^0$ and likewise for $dx_{1,2}$ versus $\mathbf{v}_{2,1}$.) The net heat exchange across the entire interface is conserved due to $|F_0| = |C_0| = 1$, i.e. $dQ = dx_1^0 q_2^0 + dx_2^0 q_2^1 = dx_1 q_2 + dx_2 q_2$, yet the heat-flux *density* at the *individual* interfaces changes as

$$\frac{q_1^0}{q_1} = \frac{dx_2}{dx_2^0} = \sqrt{\Lambda} > 1, \qquad \frac{q_2^0}{q_2} = \frac{dx_1}{dx_1^0} = \frac{1}{\sqrt{\Lambda}} < 1, \tag{2.23}$$

due to deformation $\widetilde{\mathbf{q}} = F_0\widetilde{\mathbf{q}}_0$ and $d\mathbf{x} = F_0 d\mathbf{x}_0$. Deformation thus augments (reduces) the spatial contact area dx_2 (dx_1) between fluid parcels for heat exchange in $\mathbf{v}_1$ ($\mathbf{v}_2$) direction, in Eulerian space; for given Eulerian heat-flux density $\widetilde{\mathbf{q}}$ this increases (decreases) the heat-flux density $\widetilde{\mathbf{q}}_0$ at fluid interface dx_2^0 (dx_1^0) in $\mathbf{v}_1^0$ ($\mathbf{v}_2^0$) direction. The net effect on the heat exchange between fluid parcels depends on the relative orientation between heat flux and principal deformation axes. The extremal cases $\widetilde{\mathbf{q}}_0 = q_1\mathbf{v}_1^0$ and $\widetilde{\mathbf{q}}_0 = q_2\mathbf{v}_2^0$ give maximum augmentation ($|\widetilde{\mathbf{q}}_0|/|\widetilde{\mathbf{q}}| = \sqrt{\Lambda} > 1$) and reduction ($|\widetilde{\mathbf{q}}_0|/|\widetilde{\mathbf{q}}| = 1/\sqrt{\Lambda} < 1$), respectively; generic cases give $1/\sqrt{\Lambda} \leq |\widetilde{\mathbf{q}}_0|/|\widetilde{\mathbf{q}}| \leq \sqrt{\Lambda}$.

2. Change in temperature gradient. A similar analysis for the temperature gradients $\nabla_0\widetilde{T} = (\partial\widetilde{T}/\partial x_1^0)\mathbf{v}_1^0 + (\partial\widetilde{T}/\partial x_2^0)\mathbf{v}_2^0$ and $\nabla\widetilde{T} = (\partial\widetilde{T}/\partial x_1)\mathbf{v}_1 + (\partial\widetilde{T}/\partial x_2)\mathbf{v}_2$ across the rectangular fluid parcels introduced above yields

$$\frac{\partial\widetilde{T}}{\partial x_1} = \frac{dx_1^0}{dx_i}\frac{\partial\widetilde{T}}{\partial x_1^0} = \sqrt{\Lambda}\frac{\partial\widetilde{T}}{\partial x_1^0}, \qquad \frac{\partial\widetilde{T}}{\partial x_2} = \frac{dx_2^0}{dx_i}\frac{\partial\widetilde{T}}{\partial x_2^0} = \frac{1}{\sqrt{\Lambda}}\frac{\partial\widetilde{T}}{\partial x_2^0}, \tag{2.24}$$

due to deformation $\nabla\widetilde{T} = F^\dagger\nabla_0\widetilde{T}$ and $d\mathbf{x} = F_0 d\mathbf{x}_0$. Deformation in $\mathbf{v}_1$ and $\mathbf{v}_2$ directions thus steepens (i.e. $(\partial\widetilde{T}/\partial x_1)/(\partial\widetilde{T}/\partial x_1^0) = \sqrt{\Lambda} > 1$) and flattens (i.e. $(\partial\widetilde{T}/\partial x_2)/(\partial\widetilde{T}/\partial x_2^0) = 1/\sqrt{\Lambda} < 1$) the temperature gradient, respectively, in Eulerian space; for given temperature difference dT between fluid parcels this increases (decreases) the gradient-driven heat-flux density $\widetilde{\mathbf{q}} = -Pe^{-1}\nabla\widetilde{T}$ in Eulerian space in $\mathbf{v}_1$ ($\mathbf{v}_2$) direction. The net effect depends on the relative orientation between temperature gradient and principal deformation axes. The extremal cases $\nabla_0\widetilde{T} = (\partial\widetilde{T}/\partial x_1^0)\mathbf{v}_1^0$ and $\nabla_0\widetilde{T} = (\partial T/\partial x_2^0)\mathbf{v}_2^0$ give maximum augmentation ($|\nabla\widetilde{T}|/|\nabla_0\widetilde{T}| = \sqrt{\Lambda} > 1$) and reduction ($|\nabla\widetilde{T}|/|\nabla_0\widetilde{T}| = 1/\sqrt{\Lambda} < 1$), respectively; generic cases give $1/\sqrt{\Lambda} \leq |\nabla\widetilde{T}|/|\nabla_0\widetilde{T}| \leq \sqrt{\Lambda}$.

The anisotropic heat flux $\widetilde{\mathbf{q}}_0$ between fluid parcels according to (2.17) results from the combined effect of (2.23) and (2.24). This yields a momentary net change in heat-flux density by a factor

$$\beta(\mathbf{x}_0) \equiv \frac{|\widetilde{\mathbf{q}}_0|}{|\widetilde{\mathbf{q}}_0^{\mathrm{iso}}|} = \sqrt{\frac{(\nabla_{\mathbf{0}}\widetilde{T})^\dagger \cdot B^2 \cdot (\nabla_{\mathbf{0}}\widetilde{T})}{(\nabla_{\mathbf{0}}\widetilde{T})^\dagger \cdot (\nabla_{\mathbf{0}}\widetilde{T})}}, \ \Lambda(\mathbf{x}_0)^{-1} \leq \beta(\mathbf{x}_0) \leq \Lambda(\mathbf{x}_0), \tag{2.25}$$

compared to isotropic heat transfer $\widetilde{\mathbf{q}}_0^{\mathrm{iso}} = -Pe^{-1}\nabla_0\widetilde{T}$ between non-deforming fluid parcels (i.e. $B = I$) for a given flow and temperature field. Relative heat-flux densities $\beta > 1$ and $\beta < 1$ signify relative enhancement and diminution, respectively, of momentary heat transfer between neighbouring fluid parcels at position $\mathbf{x}_0$ and time t. The actual β, similar as before, depends essentially on the relative orientation between temperature gradient and principal deformation axes and is bounded by $\beta = \Lambda > 1$ for $\nabla_0\widetilde{T} = (\partial\widetilde{T}/\partial x_1^0)\mathbf{v}_1^0$ and $\beta = 1/\Lambda < 1$ for $\nabla_0\widetilde{T} = (\partial\widetilde{T}/\partial x_2^0)\mathbf{v}_2^0$.

Fluid deformation, besides the heat-flux *density* following (2.25), also impacts the heat-flux *direction*: $\Lambda > 1$ namely increases and decreases the leading and trailing terms in (2.18), respectively, and thus promotes alignment of $\widetilde{\mathbf{q}}_0$ with the principal contraction axis $\mathbf{v}_1^0$. This, in turn, promotes thermal homogenisation in $\mathbf{v}_1^0$-direction and, inherently, alignment of the temperature gradient $\nabla_0\widetilde{T}$ with the principal stretching axis $\mathbf{v}_2^0$. The net result is the emergence of a thermal front propagating in $\mathbf{v}_2^0$-direction as e.g. the thermal plume in Figure 2.3. These counter-acting mechanisms, viz. enhancement of the $\mathbf{v}_1^0$-component of $\nabla_0\widetilde{T}$ in $\widetilde{\mathbf{q}}_0$ versus diminution of this same component by said thermal homogenisation, suggest a fundamental "conflict" between heat transfer and homogenisation in that the latter opposes the former. Angles ϱ_q and ϱ_T defined as

$$\begin{aligned} \tan\,\varrho_q(\mathbf{x}_0) \equiv \frac{|\mathbf{v}_2^0\cdot\widetilde{\mathbf{q}}_0|}{|\mathbf{v}_1^0\cdot\widetilde{\mathbf{q}}_0|} = \frac{|\mathbf{v}_2^0\cdot\nabla_0\widetilde{T}|}{\Lambda^2(\mathbf{x}_0)|\mathbf{v}_1^0\cdot\nabla_0\widetilde{T}|}, \\ \tan\,\varrho_T(\mathbf{x}_0) \equiv \frac{|\mathbf{v}_1^0\cdot\nabla_0\widetilde{T}|}{|\mathbf{v}_2^0\cdot\nabla_0\widetilde{T}|}, \end{aligned} \tag{2.26}$$

express the orientation of heat flux and temperature gradient relative to principal axes $\mathbf{v}_1^0$ and $\mathbf{v}_2^0$, respectively, and enable examination of this process ($\varrho_{q,T} = 0$ means coincidence with axes $\mathbf{v}_{1,2}^0$).

The analysis below investigates the interplay between fluid deformation and thermal phenomena for three fluid parcels with initial conditions $\mathbf{x}_0$ (coloured stars) and corresponding trajectories (coloured curves) shown in Figure 2.4a relative to the streamline pattern (black curves) and central stagnation point (black star). The FTLEs in Figure 2.4b reveal a fluid deformation that is qualitatively similar to Figure 2.2a: peaking of the FTLE upon passage through the high-shear arc region and a subsequent decline upon entering the domain interior via the sharply deflecting streamlines at the lower arc edge. However, intensities and variations depend strongly on the initial positions. Moreover, peaks progressively weaken with multiple passages through the arc region, as demonstrated by the only minor second peak of the cyan parcel around $t \approx 7$.

The evolution of the temperature $\widetilde{T}(\mathbf{x}_0, t)$ and corresponding gradient $\nabla_0\widetilde{T}$ along the trajectories using the temperature field at $t = 20$ in Figure 2.3 as initial condition are shown in Figure 2.4c and Figure 2.4d, respectively, and reveal a significant thermal heterogeneity. The impact of the fluid deformation on heat

(a) Trajectories (b) FTLE

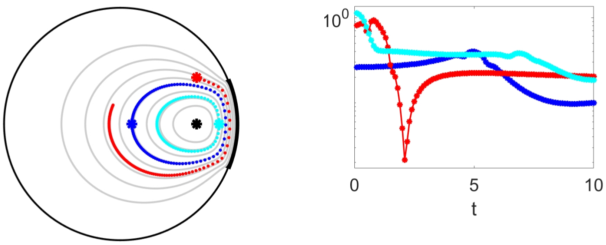

(c) $\widetilde{T}(\mathbf{x}_0, t)$ (d) $\nabla_0 \widetilde{T}$ (e) $\ln \beta$

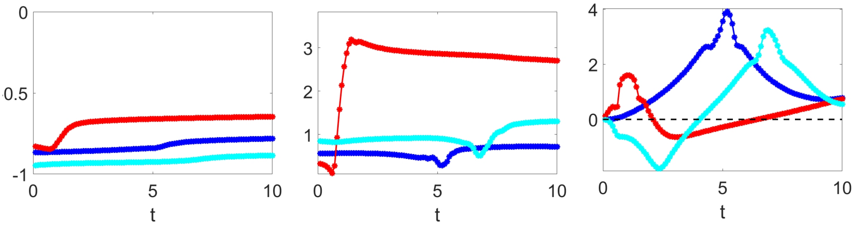

(f) β_Λ (g) ϱ_T/π (h) ϱ_q/π

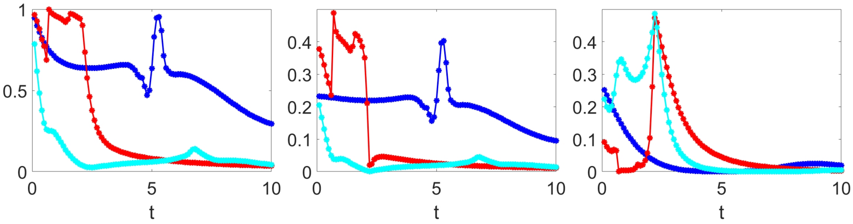

Figure 2.4: Local heating dynamics due to interplay between fluid deformation and temperature field in base flow: (a) representative fluid trajectories distinguished by red/blue/cyan (stars indicate initial positions $\mathbf{x}_0$; dots indicate positions $\mathbf{x}(t)$ at time levels $t = k\Delta t$ for $\Delta t = 0.1$) versus streamlines (black); (b-d) FTLE following (2.16) and temperature (gradient) of fluid parcels; (e) relative heat-flux density β following (2.25); (f) normalised heat-flux density $\beta_\Lambda = \beta/\Lambda$; (g) orientation of temperature gradient with principal stretching axis ϱ_T following (2.26); (h) orientation of heat flux with principal compression axis ϱ_q following (2.26).

transfer is shown in Figure 2.4e in terms of the momentary change in heat-flux density β following (2.25) (expressed as $\ln \beta$ for greater legibility). This exposes peaks $\beta > 1$ ($\ln \beta > 0$) that coincide with the FTLE-peaks in Figure 2.4b and thus signify momentary heat-transfer enhancement due to passage through the arc region. (The β-peak for the cyan parcel corresponds with the beforementioned second passage of the arc region around $t \approx 7$.) However, the quantitative correlations are non-trivial in that the weak FTLE-peaks of the blue/cyan parcels yield pronounced β-peaks of comparable magnitude while the high FTLE-peak of the red parcel yields a substantially smaller β-peak. Moreover, both cyan and red parcels exhibit significant heat-transfer diminution ($\beta < 1$ or $\ln \beta < 0$) during the transition from arc region to flow interior, signifying an unfavourable orientation of fluid deformation versus temperature gradient $\nabla_0 \widetilde{T}$.

Normalised heat-flux density $\beta_\Lambda \equiv \beta/\Lambda$ quantifies to what extent heat-transfer enhancement reaches its (theoretical) ceiling $\max \beta = \Lambda$ following (2.25) and the corresponding evolutions of this measure are shown in Figure 2.4f. This reveals short episodes of β_Λ close to unity – signifying maximum beneficial impact of fluid deformation – that closely correlate with the (first) FTLE-peaks in Figure 2.4b followed by a dramatic breakdown. The breakdown in β_Λ reflects a sudden reduction of the impact of fluid deformation on heat transfer and ensues from the diminution of heat flux $\mathbf{q}_0$ by thermal homogenisation due to the abovementioned conflict between heat transfer and homogenisation. Such local thermal homogenisation, once reached, strongly diminishes the impact of future fluid deformation and thus explains why the second FTLE peak of the cyan parcel around $t \approx 7$, in contrast with the pronounced β-peak in Figure 2.4e, induces an only weak second peak in β_Λ. This has the fundamental implication that significant impact of fluid deformation on heat transfer and thermal homogenisation is for a given fluid parcel primarily restricted to the first passage of the arc region. These phenomena are further examined in Section 2.3.3.

The dynamics of angles ϱ_q and ϱ_T of the heat flux $\widetilde{\mathbf{q}}_0$ and temperature gradient $\nabla_0 \widetilde{T}$, respectively, with the principal axes $\mathbf{v}^0_{1,2}$ following (2.26) substantiate the above findings. Figure 2.4g gives ϱ_T and exposes highly dynamic and non-monotonic behaviour during episodes/peaks of β_Λ close to unity followed by a rapid decline – signifying progressive alignment of $\nabla_0 \widetilde{T}$ with principal stretching axis $\mathbf{v}^0_2$ and, inherently, thermal homogenisation in $\mathbf{v}_1$-direction – during the breakdown of β_Λ. The relative orientation angle ϱ_q of heat flux $\widetilde{\mathbf{q}}_0$ in Figure 2.4h overall exhibits the same correlation with β_Λ in that also here progressive alignment sets in upon breakdown of β_Λ.

2.3.3 Local breakdown of heat-transfer enhancement

The breakdown of maximum heat-transfer enhancement after the first FTLE peak demonstrated with the normalised heat-flux density β_Λ in Figure 2.4f ensues from the beforementioned conflict between heat transfer and homogenisation and signifies a highly non-trivial role of fluid deformation in the thermal transport. Consider for a generic analysis the simplified case of a constant FTLE σ in (2.16), resulting in $\Lambda(t) = \exp(2\sigma t)$, and temperature gradient $\nabla_0 \widetilde{T} = c_1 \exp(-\sigma_T t)\mathbf{v}^0_1 + c_2 \mathbf{v}^0_2$, with (c_1, c_2) the initial temperature gradient and $\sigma_T > 0$ the thermal-homogenisation rate. Substitution in (2.18) gives

$$\widetilde{\mathbf{q}}_0(\mathbf{x}_0, t) = -\frac{1}{Pe} e^{(2\sigma - \sigma_T)t} \left[c_1 \mathbf{v}^0_1 + c_2 e^{(\sigma_T - 4\sigma)t} \mathbf{v}^0_2 \right], \tag{2.27}$$

and restricts the thermal-homogenisation rate to $2\sigma < \sigma_T < 4\sigma$ to maintain bounded $\mathbf{q}_0$. Through

$$\begin{gathered} \tan\,\varrho_q = \frac{c_2}{c_1}e^{(\sigma_T-4\sigma)t}, \quad \tan\,\varrho_T = \frac{c_1}{c_2}e^{-\sigma_T t}, \\ \beta_\Lambda \equiv \frac{\beta}{\Lambda} = \sqrt{\frac{c_1^2\exp(-2\sigma_T t) + c_2^2\exp(-8\sigma t)}{c_1^2\exp(-2\sigma_T t) + c_2^2}}, \end{gathered} \tag{2.28}$$

this indeed yields the conjectured alignment of heat flux and temperature gradient with principal contraction ($\mathbf{v}_1^0$) and stretching ($\mathbf{v}_2^0$) axes, respectively, i.e. $\lim_{t\to\infty}\varrho_{q,T} = 0$ and, in consequence,

$$\lim_{t\to\infty}\widetilde{\mathbf{q}}_0(\mathbf{x}_0,t) = -\frac{\Lambda}{Pe}(\mathbf{v}_1^0\cdot\nabla_0\widetilde{T})\mathbf{v}_1^0, \qquad \lim_{t\to\infty}\nabla_0\widetilde{T} = (\mathbf{v}_2^0\cdot\nabla_0\widetilde{T})\mathbf{v}_2^0, \tag{2.29}$$

thus demonstrating the generic mechanisms behind said conflict. Relations $\nabla\widetilde{T} = F\nabla_0\widetilde{T} = \exp(-\sigma t)\,[c_1\exp((2\sigma-\sigma_T)t)\mathbf{v}_1 + c_2\mathbf{v}_2]$ and $2\sigma - \sigma_T < 0$ imply that the $\mathbf{v}_1^0$-wise thermal homogenisation in the Lagrangian frame causes corresponding $\mathbf{v}_1$-wise thermal homogenisation in the Eulerian frame and, despite the non-zero limit (2.29) for $\nabla_0\widetilde{T}$, subsequent full thermal homogenisation $\lim_{t\to\infty}\nabla\widetilde{T} = \mathbf{0}$. This results in rapid convergence of β_Λ on the intermediate state

$$\beta_\Lambda \approx \beta_\Lambda^* \equiv \sqrt{\frac{c_1^2\exp(-2\sigma_T t)}{c_1^2\exp(-2\sigma_T t) + c_2^2}} = \frac{|\mathbf{v}_1^0\cdot\nabla_0\widetilde{T}|}{|\nabla_0\widetilde{T}|}, \tag{2.30}$$

for $t \gtrsim \mathcal{O}(\tau_\beta)$ and subsequent progression to limit $\lim_{t\to\infty}\beta_\Lambda = 0$. Here

$$\tau_\beta = 1/2(4\sigma - \sigma_T), \tag{2.31}$$

is the characteristic decay time of ratio $\exp(-t/\tau_\beta) = \exp(-8\sigma t)/\exp(-2\sigma_T t)$ between the "fast" and "slow" unsteady terms in β_Λ. Decay rate $d\beta_\Lambda^*/dt = \sigma_T\beta_\Lambda^*({\beta_\Lambda^*}^2 - 1) \ll 0$ due to $\sigma_T \gg 1$ around the first FTLE peaks and $\beta_\Lambda^* < 1$ causes a rapid diminution of β_Λ^* and thus explains the dramatic breakdown from $\beta_\Lambda \sim \mathcal{O}(1)$ to $\beta_\Lambda \ll 1$ in Figure 2.4f upon reaching the intermediate state β_Λ^* at $t \sim \mathcal{O}(\tau_\beta)$. Figure 2.5 overlays shown β_Λ with the generic form of β_Λ^* following (2.30) (dashed black curve) and the close agreement beyond the first FTLE peaks – as well as during the build-up towards these peaks for the red and blue parcels – indeed substantiates these findings.

The above exposes the local breakdown of heat-transfer enhancement observed in Section 2.3.2 as generic (and consistent with the "diffusive relaxation" during chaotic advection observed in [73]). This renders the common belief of efficient heat transfer being automatic with fluid mixing and chaotic advection fallacious. Fluid deformation namely plays a dual role by, on the one hand, enhancing heat transfer and thermal homogenisation between/of fluid parcels (provided

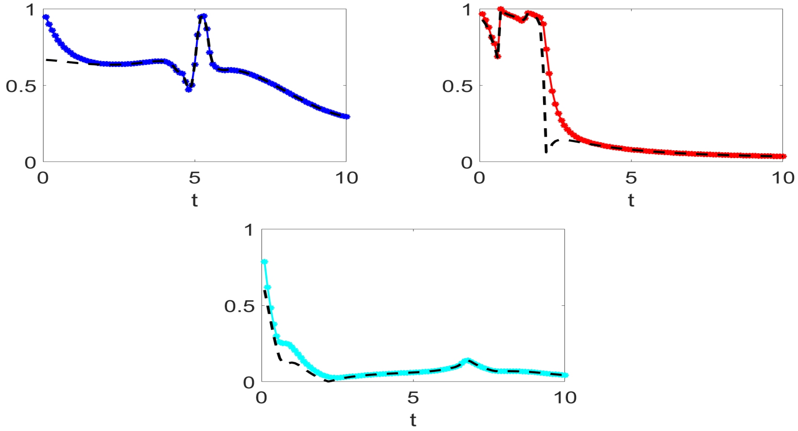

Figure 2.5: Local breakdown of heat-transfer enhancement during transition from $\beta_\Lambda \sim \mathcal{O}(1)$ to $\beta_\Lambda \ll 1$ of normalised heat-flux density $\beta_\Lambda = \beta/\Lambda$ (solid) versus intermediate state β^*_Λ (dashed) for fluid trajectories in Figure 2.4a.

favourable orientations with the temperature gradient) yet, on the other hand, restricting its beneficial impact to short-lived episodes in the transient. Their specific occurrence, duration and intensity for a given fluid parcel may vary greatly, though (Figure 2.5). However, the local thermal equilibration of fluid parcels progressively lagging behind with faster fluid deformation strongly suggests that σ_T and, consequently, τ_β tend towards their lower bounds $\min \sigma_T = 2\sigma$ and $\min \tau_\beta = 1/4\sigma$, respectively, with increasing σ. This advances $\tau_\beta \simeq \mathcal{O}(0.3 - 3)$ as estimated duration of said episodes for fluid parcels passing through the high-shear arc region using $\sigma \simeq \mathcal{O}(0.1 - 1)$ from Figure 2.2b. The arc region is to emerge as dominant for the global behaviour in Section 2.3.5.

2.3.4 Global metrics for heating and their general dynamics

Essential for effective control is an adequate description of the global dynamics associated with the above local behaviour. Key to this is that the control target, viz. fast heating of the cold fluid towards the hot equilibrium $\widetilde{T}_\infty = 0$, entails concurrent accomplishment of two goals: (i) fast increase of the total energy content (denoted “energising” hereafter) and (ii) fast homogenisation of the internal temperature distribution. Decomposition of the transient temperature as

$$\widetilde{T}(\mathbf{x},t) = \bar{T}(t) + T'(\mathbf{x},t), \quad \bar{T}(t) = \frac{1}{A}\int_{\mathcal{D}} \widetilde{T}(\mathbf{x},t)d^2\mathbf{x}, \\ T'(\mathbf{x},t) \equiv \widetilde{T}(\mathbf{x},t) - \bar{T}(t), \tag{2.32}$$

with here $A = \pi$, isolates the temperature contributions corresponding with these goals. Average temperature $\bar{T}(t) = \widetilde{E}(t)/\pi$ represents the total energy content

$\widetilde{E}$ of field $\widetilde{T}$ (here $\widetilde{E} \leq 0$); "heterogeneity" $T'(\mathbf{x},t)$ represents the departure of $\widetilde{T}$ from the momentary homogeneous state $\bar{T}$.

Decomposition (2.32) exposes the far greater dynamic complexity of the current heating problem compared to homogenisation problems commonly considered in literature (Section 2.1). The latter generically concern adiabatic domains, implying $\bar{T}(t) = 0$, and thus depend solely on the single field $\widetilde{T} = T'$. Fluid heating, on the other hand, encompasses two processes, viz. energising and homogenisation, and relevant to its dynamics are therefore the total transient field $\widetilde{T}$ as well as its individual components $\bar{T}(t)$ and T' according to (2.32).

The above advances 3 measures for the global dynamic behaviour of the heating process, viz.

$$J_1(t) \equiv \frac{1}{\pi}\int_{\mathcal{D}} \widetilde{T}^2(\mathbf{x},t)d^2\mathbf{x}, \quad J_2(t) \equiv \frac{1}{\pi}\int_{\mathcal{D}} \widetilde{T}(\mathbf{x},t)d^2\mathbf{x}, \\ J_3(t) \equiv \frac{1}{\pi}\int_{\mathcal{D}} {T'}^2(\mathbf{x},t)d^2\mathbf{x}, \tag{2.33}$$

with J_1 the global departure from equilibrium, $J_2 = \bar{T}$ the normalised energy content of the transient state and J_3 the global heterogeneity. These measures via (2.32) and $\int_{\mathcal{D}} T'(\mathbf{x},t)d^2\mathbf{x} = 0$ relate as

$$J_1(t) = {J_2}^2(t) + J_3(t), \tag{2.34}$$

and thus effectively constitute two independent degrees of freedom.

The evolution of J_2 is governed by the integral energy balance corresponding with (2.3). Property $\mathbf{v}\cdot\boldsymbol{\nabla}\widetilde{T} = \boldsymbol{\nabla}\cdot(\mathbf{v}\widetilde{T})$ for $\boldsymbol{\nabla}\cdot\mathbf{v} = 0$ upon elimination of time derivative $\partial\widetilde{T}/\partial t$ with (2.3) and application of Gauss' divergence theorem [74] yields

$$\begin{aligned} \frac{dJ_2}{dt} &= \frac{1}{\pi}\int_{\mathcal{D}} \frac{\partial\widetilde{T}}{\partial t} d^2\mathbf{x} = -\frac{1}{\pi}\int_{\mathcal{D}} \boldsymbol{\nabla}\cdot(\mathbf{v}\widetilde{T} + \widetilde{\mathbf{q}})d^2\mathbf{x} \\ &= -\frac{1}{\pi}\int_{\Gamma} (\mathbf{v}\widetilde{T} + \widetilde{\mathbf{q}})\cdot\mathbf{n}ds, \end{aligned} \tag{2.35}$$

with $\widetilde{\mathbf{q}} = -Pe^{-1}\nabla\widetilde{T}$. Here the convective flux $\mathbf{v}\cdot\mathbf{n}\widetilde{T}$ vanishes by virtue of both the impenetrable boundary ($\mathbf{v}\cdot\mathbf{n} = 0$) and the homogeneous Dirichlet condition $\widetilde{T}|_\Gamma = 0$. This reveals that energising effectively occurs only by the diffusive flux $\widetilde{\mathbf{q}}$ normal to the boundary, i.e.

$$\frac{dJ_2}{dt} = -\frac{1}{\pi}\int_{\Gamma} \widetilde{\mathbf{q}}\cdot\mathbf{n}ds = \frac{1}{\pi Pe}\int_{\Gamma} \mathbf{n}\cdot\boldsymbol{\nabla}\widetilde{T}ds, \tag{2.36}$$

and flow $\mathbf{v}$ only indirectly affects the heat-flux density and temperature gradient via motion and deformation of fluid parcels by the mechanisms from Section 2.3.2. The evolution of J_1 is governed by

$$\frac{dJ_1}{dt} = \frac{2}{\pi}\int_{\mathcal{D}} \widetilde{\mathbf{q}}\cdot\boldsymbol{\nabla}\widetilde{T}d^2\mathbf{x} = -\frac{2}{\pi Pe}\int_{\mathcal{D}} |\boldsymbol{\nabla}\widetilde{T}|^2 d^2\mathbf{x}, \tag{2.37}$$

which follows in a similar way as (2.36) from the energy equation (A). The evolution of J_3 via relation (2.34) depends on (2.36) and (2.37) according to $dJ_3/dt = dJ_1/dt - 2J_2(dJ_2/dt)$.

Relation (2.37) via inequality $|\nabla\widetilde{T}| > 0$ in at least one non-zero subset $\mathbf{x} \in \mathcal{D}$ for any non-uniform $\widetilde{T}$ implies $dJ_1/dt < 0$ and thus a monotonic decay of measure J_1 from $J_1(0) > 0$ to $\lim_{t\to\infty} J_1(t) = 0$. This is a consequence of the Second Law of Thermodynamics, which dictates that diffusive heat flux always acts against the temperature gradient, i.e. $\widetilde{\mathbf{q}} = -Pe^{-1}\nabla\widetilde{T}$, and thereby yields the particular RHS of (2.37). This implies that *any* non-zero transient temperature $\widetilde{T}\,(\mathbf{x}, t)$, irrespective of the flow, always evolves towards the final equilibrium $\widetilde{T}_\infty = 0$ and the system is intrinsically stable. The decay *rate* of J_1 depends essentially on the flow, however. The principal goal of the control strategy in Section 2.4 is finding the *fastest* route towards this equilibrium.

Measure J_3, on the other hand, is inherently *non-monotonic* due to identical initial and asymptotic conditions $J_3(0) = \lim_{t\to\infty} J_3(t) = 0$ and this constitutes a further essential departure from the beforementioned homogenisation problems (where $J_3 = J_1$ implies monotonic behaviour). Said conditions namely dictate an initial growth of heterogeneity ($dJ_3/dt|_{t=0} > 0$) that through an inevitable $J_3(t) > 0$ at intermediate times t settles on an eventual decline ($dJ_3/dt < 0$) towards the final state. Through relation (2.34) this in principle admits non-monotonic evolutions from $J_2(0) < 0$ to $\lim_{t\to\infty} J_2(t) = 0$ for measure J_2 as well. However, here the uniform boundary condition $\widetilde{T}|_\Gamma = 0$ together with the uniform initial condition $\widetilde{T}(\mathbf{x}, 0) = -1$ implies $\widetilde{T}(\mathbf{x}, t) \leq 0$ for all $\mathbf{x}$ and t and thus $\partial\widetilde{T}/\partial r|_\Gamma > 0$ and, in consequence, monotonic $dJ_2/dt > 0$.

2.3.5 Global impact of fluid deformation

The evolution of metrics J_2 and J_1 – and, via relation (2.34), indirectly also of J_3 – is determined by (2.36) and (2.37), respectively. Lagrangian coordinates admit, similar as in Section 2.3.2, investigation of the impact of fluid flow on these evolutions. Consider to this end said metrics for a material region with current Eulerian position $\mathcal{D}(t)$ and its boundary $\Gamma(t)$, i.e.

$$J_2^0(t) = \frac{1}{\pi}\int_{\mathcal{D}_0} \widetilde{T}(\mathbf{x}_0, t) d^2\mathbf{x}_0, \qquad J_1^0(t) = \frac{1}{\pi}\int_{\mathcal{D}_0} \widetilde{T}^2(\mathbf{x}_0, t) d^2\mathbf{x}_0, \tag{2.38}$$

with $\mathcal{D}_0$ and Γ_0 the corresponding initial (fixed) position in the Eulerian (Lagrangian) frame. The evolutions of (2.38) are in Lagrangian coordinates described by

$$\begin{aligned} \frac{dJ_2^0}{dt} &= -\frac{1}{\pi}\int_{\Gamma_0} \widetilde{\mathbf{q}}_0 \cdot \mathbf{n}_0 ds_0, \\ \frac{dJ_1^0}{dt} &= \frac{2}{\pi}\int_{\mathcal{D}_0} \widetilde{\mathbf{q}}_0 \cdot \nabla_0 \widetilde{T} d^2\mathbf{x}_0 - \frac{2}{\pi}\int_{\Gamma_0} \widetilde{T}\widetilde{\mathbf{q}}_0 \cdot \mathbf{n}_0 ds_0, \end{aligned} \tag{2.39}$$

where the boundary integral in dJ_1^0/dt emerges for generic material interfaces $\Gamma(t)$ evolving with the flow. This integral can be omitted in the present analysis for reasons explained below.

The impact of the flow on the global dynamics is investigated via the rates-of-change of the metric evolutions (2.39), which, upon omitting said boundary integral, are governed by

$$\begin{aligned}\frac{d^2J_2^0}{dt^2} &= \frac{1}{\pi Pe}\int_{\Gamma_0}\left(\frac{\partial B}{\partial t}\nabla_0\widetilde{T}\right)\cdot\mathbf{n}_0 ds_0 \\ &\qquad + \frac{1}{\pi Pe}\int_{\Gamma_0}\left(B\nabla_0\left(\frac{\partial\widetilde{T}}{\partial t}\right)\right)\cdot\mathbf{n}_0 ds_0 \\ \frac{d^2J_1^0}{dt^2} &= -\frac{2}{\pi Pe}\int_{\mathcal{D}_0}\left(\frac{\partial B}{\partial t}\nabla_0\widetilde{T}\right)\cdot\nabla_0\widetilde{T}d^2\mathbf{x}_0 \\ &\qquad - \frac{4}{\pi Pe}\int_{\mathcal{D}_0}(B\nabla_0\widetilde{T})\cdot\nabla_0\left(\frac{\partial\widetilde{T}}{\partial t}\right)d^2\mathbf{x}_0,\end{aligned} \tag{2.40}$$

using $\widetilde{\mathbf{q}}_0 = -Pe^{-1}B\nabla_0\widetilde{T}$. The link with the corresponding behaviours of global metrics J_2 and J_1 in (2.33) in the Eulerian frame is established via leading-order approximations of (2.40). This embarks on considering (i) an initial material boundary Γ_0 of circular shape with radius $r_0 = 1 - \epsilon_r$ very close to the circular boundary Γ of radius $r = 1$ (i.e. $\epsilon_r \ll 1$) and (ii) incremental Lagrangian motion from $\mathbf{x}(t)$ to $\mathbf{x}(t+dt) = \mathbf{x}(t) + d\mathbf{x} = \mathbf{x}(t) + \mathbf{u}dt$. Thus $\mathcal{D}(t) \approx \mathcal{D}_0 \approx \mathcal{D}$ and $\Gamma(t) \approx \Gamma_0 \approx \Gamma$, which via $\widetilde{T}|_{\Gamma(t)} \approx \widetilde{T}|_\Gamma = 0$ indeed to good approximation implies vanishing of the boundary integral in the evolution of J_1^0 in (2.39). The leading-order approximations of the relevant quantities and variables, i.e. $J_2^0 = J_2$ and $J_1^0 = J_1$, $F = F_0 = I$, $B = I$, $d\mathbf{x} = d\mathbf{x}_0$, $\mathbf{n} = \mathbf{n}_0$ and $ds = ds_0$, combined with the rate-of-change $\partial B/\partial t \equiv \dot{B} = -2D$ of the left Cauchy-Green tensor as per [72] subsequently yield

$$\begin{aligned}\frac{d^2J_2}{dt^2} &= \frac{1}{\pi Pe}\int_\Gamma(\dot{B}\nabla\widetilde{T})\cdot\mathbf{n}ds + \frac{1}{\pi}\int_\Gamma\mathbf{n}\cdot\nabla\left(\frac{\partial\widetilde{T}}{\partial t}\right)ds \\ \frac{d^2J_1}{dt^2} &= -\frac{2}{\pi Pe}\int_\mathcal{D}(\dot{B}\nabla\widetilde{T})\cdot\nabla\widetilde{T}d^2\mathbf{x} - \frac{4}{\pi Pe}\int_\mathcal{D}\nabla\widetilde{T}\cdot\nabla\left(\frac{\partial\widetilde{T}}{\partial t}\right)d^2\mathbf{x},\end{aligned} \tag{2.41}$$

with $D = 1/2[\nabla\mathbf{u} + (\nabla\mathbf{u})^\dagger]$ the strain-rate tensor.

Relations (2.41) describe the rates-of-change of the metric evolutions (2.36) and (2.37) and via the leading integrals incorporate the momentary impact of fluid deformation on the heating dynamics for given temperature $T(\mathbf{x},t)$. The corresponding integrands describe the rate-of-change of integrands $\bar{f} \equiv \mathbf{n}\cdot\nabla\widetilde{T}|_\Gamma =$

$\partial\widetilde{T}/\partial r|_\Gamma$ and $\widetilde{f} \equiv |\nabla\widetilde{T}|^2$ in (2.36) and (2.37), respectively, via

$$\begin{aligned}
\bar{g}(\mathbf{x},t) &\equiv \left.\frac{d\bar{f}}{dt}\right|_{\widetilde{T}} = (\dot{B}\nabla\widetilde{T})\cdot\mathbf{n} = 2\mu\left[(\mathbf{w}_1\cdot\nabla\widetilde{T})\mathbf{w}_1\cdot\mathbf{n} - (\mathbf{w}_2\cdot\nabla\widetilde{T})\mathbf{w}_2\cdot\mathbf{n}\right] \\
\widetilde{g}(\mathbf{x},t) &\equiv \left.\frac{d\widetilde{f}}{dt}\right|_{\widetilde{T}} = (\dot{B}\nabla\widetilde{T})\cdot\nabla\widetilde{T} = 2\mu\left[(\mathbf{w}_1\cdot\nabla\widetilde{T})^2 - (\mathbf{w}_2\cdot\nabla\widetilde{T})^2\right], \qquad (2.42)
\end{aligned}$$

with $\mu > 0$ ($-\mu < 0$) the stretching (contraction) rate along principal axis $\mathbf{w}_2$ ($\mathbf{w}_1$) of tensor $D = \mu\mathbf{w}_2\mathbf{w}_2 - \mu\mathbf{w}_1\mathbf{w}_1$. Here the impact of fluid deformation on heat transfer, analogous to (2.18), again depends on the relative orientation between principal deformation axes and temperature gradient. The qualitative global impact is determined by the sign of the leading integrals in (2.41):

- $\boldsymbol{\bar{G}(t) \equiv \int_\Gamma \bar{g}(\mathbf{x},t)ds > 0}$ momentarily accelerates the growth from $J_2 < 0$ to $\lim_{t\to\infty} J_2(t) = 0$ compared to a non-deforming fluid (i.e. $d^2J_2/dt^2|_{\mu>0} > d^2J_2/dt^2|_{\mu=0}$) and thus accomplishes faster energising. Conversely, $\bar{G}(t) < 0$ delays global energising.

- $\boldsymbol{\widetilde{G}(t) \equiv \int_{\mathcal{D}} \widetilde{g}(\mathbf{x},t)d^2\mathbf{x} > 0}$ momentarily accelerates the decay from $J_1 > 0$ to $\lim_{t\to\infty} J_1(t) = 0$ compared to a non-deforming fluid (i.e. $d^2J_1/dt^2|_{\mu>0} < d^2J_1/dt^2|_{\mu=0}$) and thus accomplishes faster equilibration. Conversely, $\widetilde{G}(t) < 0$ delays global equilibration.

Integrals $\bar{G}(t)$ and $\widetilde{G}(t)$ incorporate the net impact on global energising and equilibration, respectively, by local enhancement (i.e. $\bar{g}(\mathbf{x},t) > 0$ and $\widetilde{g}(\mathbf{x},t) > 0$) or diminution (i.e. $\bar{g}(\mathbf{x},t) < 0$ and $\widetilde{g}(\mathbf{x},t) < 0$). However, the local contributions to the global behaviour may, consistent with Figure 2.4, vary significantly. This admits investigation via the corresponding relative change rates

$$\begin{aligned}
\bar{\beta} \equiv \frac{\bar{g}}{\bar{f}} &= \mathbf{e}_r^\dagger\cdot\dot{B}\cdot\mathbf{e}_r = -2\mathbf{e}_r^\dagger\cdot D\cdot\mathbf{e}_r = -2\frac{\partial v_r}{\partial r}, \\
\widetilde{\beta} \equiv \frac{\widetilde{g}}{\widetilde{f}} &= \mathbf{e}_T^\dagger\cdot\dot{B}\cdot\mathbf{e}_T = -2\mathbf{e}_T^\dagger\cdot D\cdot\mathbf{e}_T,
\end{aligned} \qquad (2.43)$$

with $\mathbf{e}_T = \nabla T/|\nabla T|$, and constitute Eulerian counterparts to β following (2.25). Here $\bar{\beta}$ follows from uniformity of the wall temperature, which implies $\nabla\mathbf{T} = (\partial T/\partial r)\mathbf{e}_r$ at boundary Γ and to leading-order approximation on the beforementioned circles Γ_0. This furthermore implies $\mathbf{e}_T = \mathbf{e}_r$ and thus $\widetilde{\beta} = \bar{\beta}$ at Γ. Moreover, both measures are bounded as $-2\mu \leq \bar{\beta} \leq 2\mu$ and $-2\mu \leq \widetilde{\beta} \leq 2\mu$.

Incompressibility $\nabla\cdot\mathbf{v} = 0$ yields $\partial v_r/\partial r = -r^{-1}\partial v_\theta/\partial\theta$ and via (2.43) links the energising dynamics to the boundary velocity $\mathbf{v}_1|_\Gamma = v_\theta\mathbf{e}_\theta$. Through $v_\theta = H(\theta - \Delta/2) - H(\theta + \Delta/2)$ this gives $\bar{\beta} = 2\delta(\theta - \Delta/2) - 2\delta(\theta + \Delta/2)$ as singular limit for $\bar{\beta}$ on Γ, with H and δ the well-known Heaviside and Dirac

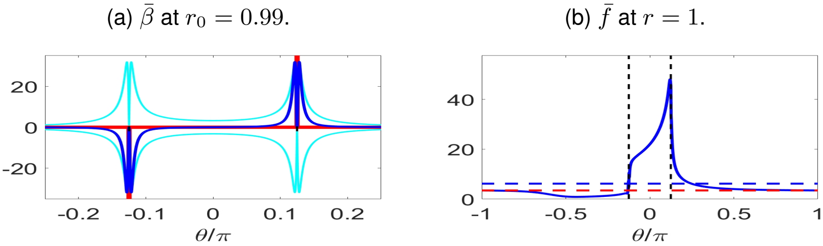
(a) $\bar{\beta}$ at $r_0 = 0.99$.

(b) $\bar{f}$ at $r = 1$.

(c) $\bar{g}/\max|\bar{g}|$ at $r_0 = 0.99$.

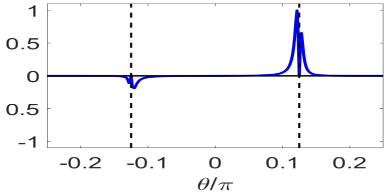

Figure 2.6: Impact of fluid deformation on energising for temperature at $t = 20$ in Figure 2.3: (a) relative change rate $\bar{\beta} = \bar{g}/\bar{f}$ on circle $r_0 = 0.99$ (blue) including limit on $r = 1$ (red) and bounds (cyan); (b) wall temperature gradient $\bar{f} = \partial\widetilde{T}/\partial r|_\Gamma$ (blue) including average (blue dashed) and diffusive limit (red dashed); (c) change rate $\bar{g}$ at $r_0 = 0.99$ (blue). Vertical dashed lines indicate leading ($\theta = \Delta/2$) and trailing ($\theta = -\Delta/2$) arc edges.

functions, respectively. This, in turn, yields

$$\bar{G}(t) = r_0 \int_0^{2\pi} \bar{\beta}(\theta; r_0) \frac{\partial \widetilde{T}}{\partial r} d\theta \overset{r_0=1}{=} 2 \left\{ \left. \frac{\partial \widetilde{T}}{\partial r} \right|_{\theta=\Delta/2} - \left. \frac{\partial \widetilde{T}}{\partial r} \right|_{\theta=-\Delta/2} \right\}, \qquad (2.44)$$

as leading-order approximation for integral $\bar{G}$ on said Γ_0 and its corresponding limit on Γ. Figure 2.6a shows $\bar{\beta}$ for $r_0 = 0.99$ (blue) including its limit (red) and bounds (cyan) and reveals that significant contributions to $\bar{G}$ are indeed restricted to the direct proximity of the arc edges $\theta = \pm\Delta/2$ (dashed lines). The rapid material stretching along streamlines and subsequent relaxation near arc edges $\theta = \Delta/2$ and $\theta = -\Delta/2$, respectively, demonstrated in Figure 2.2 causes a relative steepening (flattening) of wall temperature gradient $\bar{f} = \partial\widetilde{T}/\partial r|_\Gamma$ – or equivalently, a local rate of change $\bar{\beta} > 0$ ($\bar{\beta} < 0$) – near former (latter) arc edge by the mechanism according to Section 2.3.2. This implies

$$0 < \left. \frac{\partial \widetilde{T}}{\partial r} \right|_{\theta=-\Delta/2, t>0} < \left. \frac{\partial \widetilde{T}}{\partial r} \right|_{\Gamma, t=0} < \left. \frac{\partial \widetilde{T}}{\partial r} \right|_{\theta=\Delta/2, t>0}, \qquad (2.45)$$

due to the uniform initial gradient $\partial\widetilde{T}/\partial r|_{\Gamma,t=0} > 0$ for the initial/boundary conditions in (2.3) and via (2.44) thus always accelerates energising ($\bar{G} > 0$). This behaviour is demonstrated in Figure 2.6b by $\partial\widetilde{T}/\partial r|_{\Gamma}$ (blue curve) and corresponding integrand $\bar{g}$ in Figure 2.6c for the temperature field at $t = 20$ in Figure 2.3 and, in accordance with $\bar{G} > 0$, yields an average temperature gradient (blue dashed line in Figure 2.6b) and associated boundary heat flux that is significantly larger than the diffusive limit (red dashed line). However, consistent with the local behaviour exposed in Section 2.3.2, unfavourable orientations of fluid deformation versus temperature gradient may via (2.44) also cause $\bar{G} < 0$ and thus (temporary) diminution of global energising.

Global equilibration shows similar characteristics due to the fact that significant fluid deformation within the interior also concentrates primarily around the arc edges. Figure 2.7a demonstrates this by the stretching rate μ (shown as $\mu_{\log} = \log_{10}(\mu/\max\mu)$ to enhance contrast) and reveals a rapid decay from its peaks near said edges by several orders of magnitude within a confined boundary region. Typical corresponding magnitudes of $\widetilde{\beta}$ are shown in Figure 2.7b for $t = 20$ and $t = 50$ and Figure 2.7c distinguishes subregions of different impact levels using $\widetilde{\beta}_{\rm rel} \equiv \widetilde{\beta}/\max|\widetilde{\beta}|$ and thresholds $(\epsilon_1, \epsilon_2) = (5\times10^{-3}, 5\times10^{-2})$: strong enhancement ($\widetilde{\beta}_{\rm rel} \geq \epsilon_2$; red) versus strong diminution ($\widetilde{\beta}_{\rm rel} \leq -\epsilon_2$; blue); moderate enhancement ($\epsilon_1 \leq \widetilde{\beta}_{\rm rel} < \epsilon_2$; yellow) versus moderate diminution ($-\epsilon_2 < \widetilde{\beta}_{\rm rel} \leq -\epsilon_1$; cyan); insignificant ($|\widetilde{\beta}_{\rm rel}| < \epsilon_1$; green). (Regions $\widetilde{\beta} > 0$ and $\widetilde{\beta} < 0$ correspond with local enhancement and diminution, respectively, of equilibration due to $\widetilde{f} > 0$ and thus fully capture the equilibration dynamics.) This reveals that the confinement of significant fluid deformation to the arc region carries over to its impact on the equilibration dynamics. The red/blue regions in Figure 2.7c with the strongest enhancement/diminution of equilibration remain largely stationary and closely correlate with μ. Significant temporal changes in $\widetilde{\beta}$ occur mainly in the yellow/cyan regions and for the present temperature field manifest themselves in the diminishing banana-shaped region emerging from arc edge $\theta = \Delta/2$. However, their intensity is 1-2 orders of magnitude smaller compared to the arc region and thus of secondary importance only.

The relative rate of change $\widetilde{\beta}$ for a reorientation of the temperature field at $t = 20$ following Figure 2.7d is shown in Figure 2.7e and exposes high-impact regions (red/blue) at the arc edges that are basically reorientations of their base-flow counterparts in Figure 2.7b – and thus (nearly) independent of the momentary $\widetilde{T}$ – coexisting with interior regions (yellow/cyan) that depend significantly on $\widetilde{T}$ yet have an only moderate impact. This behaviour is typical of any reorientation and diminishes the (potential) impact of internal fluid mixing and chaotic advection, thereby further eroding the beforementioned common belief of an invariably beneficial role of these conditions.

The rapid alignment of isothermals with streamlines in the arc region (Figure 2.3) suggests that $\widetilde{\beta}$ here approximately behaves as $\widetilde{\beta}^* = -2\mathbf{e}_v^\dagger \cdot D \cdot \mathbf{e}_v$, with $\mathbf{e}_v = (v_y, -v_x)/|\mathbf{v}_1|$ the normal to the streamlines. (Property $\mathbf{e}_v|_\Gamma = \mathbf{e}_r|_\Gamma$

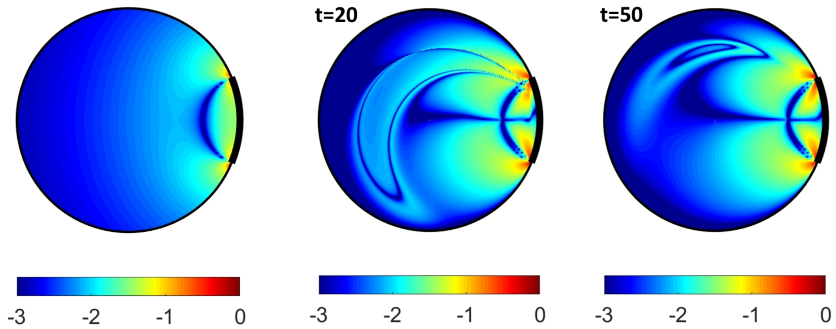

(a) $\mu_{\text{ log}}$

(b) $\widetilde{\beta}_{\text{ log}}$

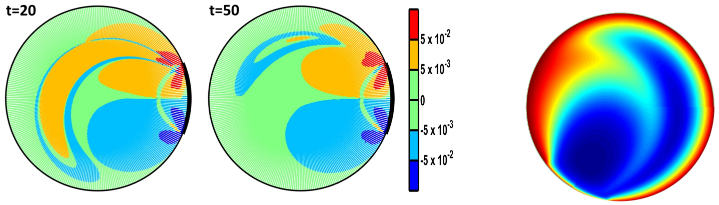

(c) Partition of $\widetilde{\beta}$ into impact levels.

(d) Reoriented $\widetilde{T}$.

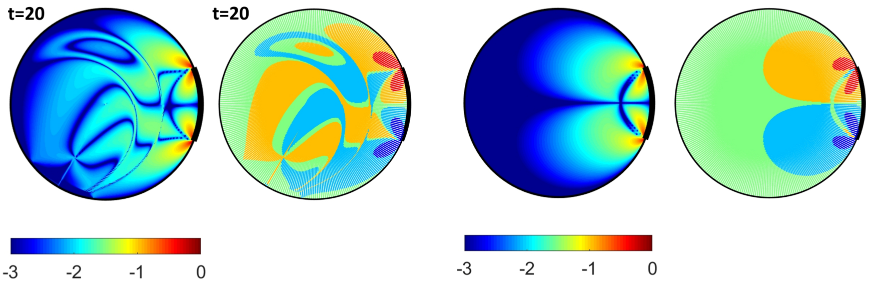

(e) $\widetilde{\beta}_{\text{ log}}$ for reoriented $\widetilde{T}$.

(f) $\widetilde{\beta}^*_{\text{log}}$

Figure 2.7: Impact of fluid deformation on equilibration: (a) stretching rate μ of fluid parcels expressed as $\mu_{\text{ log}} = \log_{10}(\mu/\max\mu)$; (b) relative change rate $\widetilde{\beta} = \widetilde{g}/\widetilde{f}$ expressed as $\widetilde{\beta}_{\text{ log}} = \log_{10}(|\widetilde{\beta}|/\max|\widetilde{\beta}|)$; (c) partition of $\widetilde{\beta}$ via $\widetilde{\beta}_{\text{ rel}} \equiv \widetilde{\beta}/\max|\widetilde{\beta}|$ into regions with strong enhancement ($\widetilde{\beta}_{\text{ rel}} \geq \epsilon_2$; red) versus strong diminution ($\widetilde{\beta}_{\text{ rel}} \leq -\epsilon_2$; blue), moderate enhancement ($\epsilon_1 \leq \widetilde{\beta}_{\text{ rel}} < \epsilon_2$; yellow) versus moderate diminution ($-\epsilon_2 < \widetilde{\beta}_{\text{ rel}} \leq -\epsilon_1$; cyan) and insignificant impact ($|\widetilde{\beta}_{\text{ rel}}| < \epsilon_1$; green) using thresholds $(\epsilon_1, \epsilon_2) = (5 \times 10^{-3}, 5 \times 10^{-2})$; (d) reoriented $\widetilde{T}$ at $t = 20$; (e) $\widetilde{\beta}_{\text{ log}}$ for reoriented $\widetilde{T}$; (f) approximation $\widetilde{\beta}^*$ expressed as $\widetilde{\beta}^*_{\text{log}} = \log_{10}(|\widetilde{\beta}^*|/\max|\widetilde{\beta}^*|)$.

ensures consistency with the previous relation $\widetilde{\beta}|_\Gamma = \bar{\beta}|_\Gamma$.) Figure 2.7f gives the magnitude of $\widetilde{\beta}^*$ (left) and corresponding partition by impact levels (right).

This indeed reveals a close agreement of the approximated strong-impact regions (red/blue) with their actual counterparts in figures 2.7c and 2.7d; deviations are restricted to the moderate-impact regions (yellow/cyan). Thus $\widetilde{G}$ to good approximation collapses on a form akin to (2.44), i.e.

$$\widetilde{G}(t) \approx \int_{(r,\theta)\in\mathcal{D}^+} \widetilde{\beta}^*(r,\theta)\left[|\nabla\widetilde{T}|^2_{(r,\theta)} - |\nabla\widetilde{T}|^2_{(r,-\theta)}\right] rdrd\theta \qquad (2.46)$$

with $\mathcal{D}^+$ the strong-enhancement region (red) in Figure 2.7f (right) and using the anti-symmetry $\widetilde{\beta}^*(r,\theta) = -\widetilde{\beta}^*(r,-\theta)$ about the centerline $\theta = 0$ of the arc. Similar reasoning as that underlying (2.45) gives $0 < |\nabla\widetilde{T}|^2_{(r,-\theta),t>0} < |\nabla\widetilde{T}|^2_{(r,\pm\theta),t=0} < |\nabla\widetilde{T}|^2_{(r,\theta),t>0}$ and in conjunction with $\widetilde{\beta}^*|_{\mathcal{D}^+} > 0$ implies $\widetilde{G} > 0$. So fluid deformation for (at least) base flow $\mathbf{v}_1$ and given initial/boundary conditions in (2.3) always accelerates, besides energising, also equilibration. However, unfavourable reorientations may, as before, also cause (temporary) diminution of global equilibration ($\widetilde{G} < 0$).

2.4 Adaptive flow reorientation

2.4.1 Control strategy revisited

Section 2.3 reveals that the impact of flow on thermal transport is highly nontrivial and depends essentially on the interplay between fluid deformation and temperature field. This may benefit as well as deteriorate said transport and thus conclusively demonstrates that efficient fluid mixing by chaotic advection does not imply enhanced thermal performance. Decomposition (2.22) of the Perron-Frobenius operator $\mathcal{P}_t$ clearly illustrates this: the temperature evolution depends on factors $\mathcal{A}_t$ (advection) and $\mathcal{D}_t$ (diffusion) yet mixing/advection-based optimisation effectively omits $\mathcal{D}_t$. Moreover, significant impact of fluid deformation is restricted to the active arc region (figures 2.6 and 2.7) and the underlying processes become exponentially complex and intractable with consecutive flow reorientations. These issues render (i) optimisation of heat transfer based solely on mixing/advection characteristics inefficient and potentially ineffective and (ii) control strategies based directly on fundamental thermal mechanisms as exposed in Secs. 2.3.1 and 2.3.2 impractical.

The global metrics for heating defined in Section 2.3.4 incorporate the global impact of the flow (Section 2.3.5) and thus offer a workable alternative to determine the "best" reorientation scheme $\mathcal{U}$ in the general control strategy in Section 2.2.2. Such metrics namely admit its formulation as the minimisation of a cost function $J(t)$ from $J(0) > 0$ to $J(t_\epsilon) \leq \epsilon$ in the shortest possible time $t_\epsilon > 0$, with $\epsilon > 0$ a preset tolerance. The control action consists of step-wise activating flow $\mathbf{v}_{u_k}$ in (2.4) at t_n that minimises J for the finite horizon $t_{n+1} = t_n + \tau$, i.e.

$$\begin{aligned} &\arg\min_k J_k\left(t_{n+1}\right), \quad J_k(t) \equiv J\left(\widetilde{T}_k(\mathbf{x},t)\right), \\ &\widetilde{T}_k(\mathbf{x},t) \equiv \widetilde{T}(\mathbf{x},t;\mathbf{v}_{u_k}(\mathbf{x}),\widetilde{T}(\mathbf{x},t_n)), \end{aligned} \tag{2.47}$$

from predicted future states $\widetilde{T}_k(\mathbf{x},t_{n+1})$ of the momentary temperature $\widetilde{T}(\mathbf{x},t_n)$. The schematic in Figure 2.8 shows this control loop, which, by relying on (real-time) feedback from the actual state at t_n and its evolution, enables control that is robustness to disturbances accumulated up to t_n.

Critical for an effective controller is an adequate cost function J in (2.47). The dynamics of global metrics (2.33) (Section 2.3.4) advance metric J_1 as the most suitable candidate, i.e. $J \equiv J_1$, for the following reasons. First, J_1 incorporates both energising (represented by J_2) and homogenisation (represented by J_3) by virtue of relation (2.34) and thus accounts for the two fundamental processes in the heating process. Second, the fundamental conflict between heat transfer and homogenisation (Section 2.3.2) precludes an overall effective controller based on either J_2 (energising) or J_3 (homogenisation). Third, the invariably monotonic decay of J_1 dictated by (2.37) ensures convergence and regularity of the minimisation procedure (2.47). The inherently (potentially) non-monotonic behaviour of J_3 (J_2), on the other hand, may compromise this procedure.

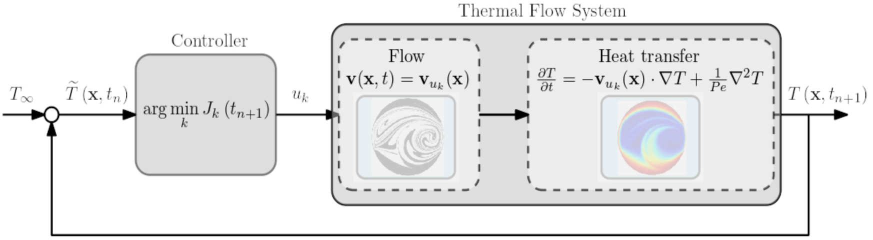
Thermal Flow System
Controller
Flow
$\mathbf{v}(\mathbf{x},t) = \mathbf{v}_{u_k}(\mathbf{x})$
Heat transfer
$\frac{\partial T}{\partial t} = -\mathbf{v}_{u_k}(\mathbf{x}) \cdot \nabla T + \frac{1}{Pe}\nabla^2 T$
T_∞
$\widetilde{T}\left(\mathbf{x},t_n\right)$
$\arg\min_k J_k\left(t_{n+1}\right)$
u_k
$T\left(\mathbf{x},t_{n+1}\right)$

Figure 2.8: Schematic of control loop for adaptive flow reorientation in the RAM.

The above effectively yields the step-wise optimal control adopted in [56] including metric J_1 as cost function. However, the study in [56] thus followed standard practice in control theory by using the well-known L^2-norm of state $\widetilde{T}$ (identifying with J_1) [75]. The present study provides the hitherto missing scientific support for adopting J_1 as cost function in the current thermal context. The practical control action involves repetition of the following steps at time levels t_n:

Step 1 Predict future temperature $\widetilde{T}_k(\mathbf{x},t_{n+1})$ from $\widetilde{T}\left(\mathbf{x},t_n\right)$ for each flow $\mathbf{v}_{u_k}$.

Step 2 Select flow $\mathbf{v}_{u_k}(\mathbf{x})$ that minimises cost function $J = J_1$ according to (2.47).

Step 3 Activate the selected aperture k for time interval $t_n \leq t \leq t_{n+1}$.

This procedure is terminated at time level t_{n+1} for which $J_{n+1} = J(t_{n+1}) < \epsilon$. The corresponding transient time t_ϵ, defined as $J(t_\epsilon) = \epsilon$, is interpolated via $t_\epsilon = t_n + \tau(J_n - \epsilon)/(J_n - J_{n+1})$. Prediction using the actual intermediate state $\widetilde{T}(\mathbf{x}, t_n)$ provides robustness to disturbances accumulated up to t_n and this positions the control strategy within the realm of Model Predictive Control (MPC) [76]. A difference compared to common MPC is that here the prediction horizon coincides with the duration of the control action (prediction horizons usually are far ahead into the future). A strong point is that the current strategy involves the full spatio-temporal state described by the conservation laws (MPC of thermo-fluidic systems usually concerns global behaviour of bulk quantities described by integral models [77]).

Moreover, cost functions J in (2.47), instead of solely including the state $\widetilde{T}$ in the current $J = J_1$, generically also account for the effort required to execute the control action [77]. In the RAM this consists of the energy consumption $E(t)$ for driving the arcs. However, given reorientation schemes U here always concern step-wise activation of a single arc at constant speed, said energy consumption for any $\mathcal{U}$ always increases linearly in time following $E(t) = Wt$, with W the constant power consumption by the flow forcing. Hence $E(t)$ is irrelevant for the minimisation procedure (2.47) and reaching the control target (i.e. the minimum transient time t_ϵ) automatically yields the minimum energy consumption in the present approach. Advanced control strategies involving e.g. simultaneous activations of multiple arcs at variable speeds, on the other hand, result in energy consumption that depends explicitly on the activation scheme and must therefore generically be taken into account through cost function J for an overall optimal performance.

2.4.2 Compact model for fast predictions

Essential for a useful controller is sufficiently fast prediction of the $2N + 1$ future states $\widetilde{T}_k(\mathbf{x}, t_{n+1})$ in (2.47) at each t_n with an acceptable computational effort. Backbone for this fast predictor is the property that spectral decomposition (2.8) for the temperature evolution in the reoriented flow $\mathbf{v}_u$ is a linear transformation from spectral decomposition (2.6) of the base flow following (2.9). This enables a fact predictor via the numerical approximation of Perron-Frobenius operator $\mathcal{P}_t$ in (2.6) and embarks on spatial discretisation of ADE (2.3) for $\mathbf{v} = \mathbf{v}_1$, i.e.

$$\frac{d\widetilde{\mathbf{T}}(t)}{dt} = \mathbf{A}\widetilde{\mathbf{T}}(t), \tag{2.48}$$

with $\widetilde{\mathbf{T}}(t) = [\widetilde{T}(\mathbf{x}_0, t), \ldots, \widetilde{T}(\mathbf{x}_M, t)]^\dagger$ the temperatures in the nodes of the computational grid $\mathbf{X} = [\mathbf{x}_0, \ldots, \mathbf{x}_M]^\dagger$ and system matrix $\mathbf{A}$ the discrete approximation of the advection-diffusion operator. Steady base flow $\mathbf{v}_1$ implies a constant $\mathbf{A}$ and thus admits

$$\widetilde{\mathbf{T}}\left(t\right)=\mathbf{P}_t\widetilde{\mathbf{T}}_0=\sum_{m=0}^{M}\alpha_m\boldsymbol{\phi}_m e^{\lambda_m t},\quad \boldsymbol{\alpha}=\mathbf{V}^{-1}\widetilde{\mathbf{T}}_0,\quad \mathbf{P}_t=\mathbf{V}e^{\mathbf{\Lambda}_1 t}\mathbf{V}^{-1},\tag{2.49}$$

as semi-analytical solution for (2.48) using the spectral decomposition $\mathbf{A}=\mathbf{V}\mathbf{\Lambda}\mathbf{V}^{-1}$, with $\mathbf{V}=[\boldsymbol{\phi}_0,\ldots,\boldsymbol{\phi}_M]$ and $\mathbf{\Lambda}=\text{diag}(\lambda_0,\ldots,\lambda_M)$ the eigenvector and eigenvalue matrices, respectively.

Relation (2.49) constitutes the discrete approximation of spectral decomposition (2.6) of the Perron-Frobenius operator $\mathcal{P}_t$. The reorientation property of the continuous system following Section 2.2.3 carries over to its discrete approximation and yields

$$\begin{aligned}\widetilde{\mathbf{T}}\left(t\right)&=\mathbf{P}_t^{(u)}\widetilde{\mathbf{T}}_0=\sum_{m=0}^{M}\alpha_m^{(u)}\boldsymbol{\psi}_m^{(u)}e^{\mu_m t},\\ \boldsymbol{\alpha}^{(u)}&=\mathbf{V}_u^{-1}\widetilde{\mathbf{T}}_0,\quad \mathbf{P}_t^{(u)}=\mathbf{V}_u e^{\mathbf{\Omega}_u t}\mathbf{V}_u^{-1},\end{aligned}\tag{2.50}$$

as discrete approximation of (2.8). Eigenvalues $\mathbf{\Omega}_u=\text{diag}(\mu_0,\ldots,\mu_M)$ and eigenvectors $\mathbf{V}_u=[\boldsymbol{\psi}_0^{(u)},\ldots,\boldsymbol{\psi}_M^{(u)}]$ are following (2.9) given by $(\mathbf{\Omega}_u,\mathbf{V}_u)=(\mathbf{\Lambda},\mathbf{G}_u\mathbf{V})$ and $(\mathbf{\Omega}_u,\mathbf{V}_u)=(\mathbf{\Lambda}^0,\mathbf{V}^0)$ for $u\neq 0$ and $u=0$, respectively. The reorientation operator is following (2.10) composed of the discrete rotation ($\mathbf{R}_u$) and reflection ($\mathbf{S}$) operators: $\mathbf{G}_u=\mathbf{R}_u$ for $u>0$ and $\mathbf{G}_u=\mathbf{S}\mathbf{R}_u$ for $u<0$.

The above discrete approximation translates the evolution and reorientation into standard matrix-vector multiplications using pre-constructed system matrices and thus tremendously reduces the computational effort compared to a conventional time-marching scheme for (2.48) and its counterpart for reoriented flows. Further substantial reduction relies on the exponential decay with characteristic time scale $\tau_m=-1/Re(\mu_m)$ of the individual modes m in (2.50). This renders contributions by modes m for which $\tau_m/\tau\ll 1$ insignificant and admits close approximation of the temperature evolution by a truncation of expansion (2.50) at $Q\ll M$, i.e.

$$\begin{aligned}\widetilde{\mathbf{T}}(t)\approx&\widehat{\mathbf{T}}(t)\equiv\widehat{\mathbf{P}}_t^{(u)}\widetilde{\mathbf{T}}_0=\sum_{m=0}^{Q}\widehat{\alpha}_m^{(u)}\boldsymbol{\psi}_m^{(u)}\exp(\mu_m t),\\ &\widehat{\boldsymbol{\alpha}}^{(u)}=\widehat{\mathbf{V}}_u^{*}\widetilde{\mathbf{T}}_0,\quad \widehat{\mathbf{P}}_t^{(u)}=\widehat{\mathbf{V}}_u e^{\widehat{\mathbf{\Omega}}_u t}\widehat{\mathbf{V}}_u^{*},\end{aligned}\tag{2.51}$$

with $\widehat{\mathbf{V}}_u^{*}$ the Moore-Penrose inverse of the reduced eigenvector basis $\widehat{\mathbf{V}}_u=[\boldsymbol{\psi}_0^{(u)},\ldots,\boldsymbol{\psi}_Q^{(u)}]$.

The total reduction in computational effort afforded by compact model (2.51) amounts to 3-4 orders of magnitude compared to conventional time-marching of (2.48) [56]. Moreover, system matrix $\mathbf{A}$ can be constructed from any spatial discretisation method including e.g. FEM and FVM (and even directly exported from some commercial CFD packages) and decomposed by linear-algebra tools as e.g. `MATLAB`. Thus the compact model enables the fast temperature predictions necessary to make the control strategy in Section 2.4.1 viable for practical applications.

2.5 Computational performance analysis

2.5.1 Performance of minimisation procedure and predictor

The general performance and robustness of the minimisation procedure (2.47) and the compact model (2.50) are investigated for a typical RAM consisting of $N = 3$ apertures at $Pe = 500$ and $\tau = 5$ and involves the following steps. First, simulation of both the actual temperature evolution $\widetilde{T}(\mathbf{x}, t)$ and the stepwise predictions $\widetilde{T}_k(\mathbf{x}, t)$ by full resolution of ADE (2.3) using the dedicated spectral scheme for the RAM of [16]. This serves as reference for the performance analysis. Second, simulation of $\widetilde{T}(\mathbf{x}, t)$ by full resolution of ADE (2.3) using a conventional FVM scheme [78] and predictions $\widetilde{T}_k(\mathbf{x}, t)$ via approximation (2.50) based on truncation of the spectral decomposition of the FVM system matrix $\mathbf{A}$ in (2.48). This emulates a predictor-based minimisation in a practical implementation. The FVM grid consists of a cylindrical mesh with equidistant inter-nodal spacings $(\Delta r, \Delta\theta)$ and here includes $M = 51,121$ elements (convergence verified by mesh-refinement tests); truncation is at $Q = 500$ according to typical reductions $Q/M \sim \mathcal{O}(10^{-1})$ and thus accomplishes the total reduction in computational effort as estimated in Section 2.4.2 [56].

The temperature evolution $\widetilde{T}(\mathbf{x}, t)$ and adaptive reorientation scheme $\mathcal{U}$ (here restricted to $u \geq 0$) determined via (2.3) by simulation with the spectral method are shown in Figure 2.9a and Figure 2.9b, respectively. This results in sequential activation of the apertures reminiscent of periodic reorientation, i.e. $\mathcal{U} = \{1, 2, 3, 1, 2, 3, \dots\}$, yet with variable duration, i.e. $t_{\text{active}} = \tau$ or $t_{\text{active}} = 2\tau$, signifying an essentially aperiodic reorientation scheme. The reorientation is clearly visible in the temperature field via the emergence of multiple thermal plumes. Figure 2.9c gives the evolution of the cost function $J = J_1$ as $\log_{10} J$ and reveals, consistent with (2.37), a monotonic and exponential decay that reaches the termination criterion $J(t_\epsilon) \leq \epsilon$ at transient time $t_\epsilon \approx 140$ for $\epsilon = 10^{-2}$. Simulations for different (Pe, τ) yield reorientation schemes that comprise of switching between apertures akin to Figure 2.9b and cost functions that exponentially converge similar to Figure 2.9c and terminate the control action at comparable transient times t_ϵ. This demonstrates an overall functioning control strategy that converges and identifies an effective reorientation scheme.

The reorientation scheme $\mathcal{U}$ obtained with the FVM-based method is included in Figure 2.9b (red solid) and coincides with the reference scheme (black dashed) found via the spectral method. The corresponding evolution of the cost function in

(a) Reference temperature $\widetilde{T}(\mathbf{x}, t)$

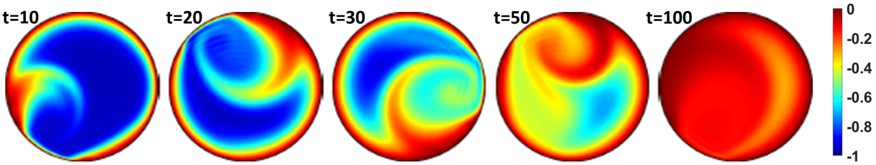

(b) Adaptive reorientation scheme $\mathcal{U}$.

(c) $\log_{10} J$

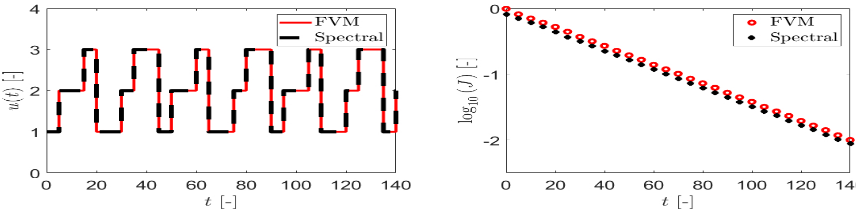

Figure 2.9: Performance of minimisation procedure and FVM-based predictor for RAM with three apertures ($N = 3$) at $(Pe, \tau) = (500, 5)$: (a) reference temperature $\widetilde{T}(\mathbf{x}, t)$ simulated by spectral method; (b) adaptive reorientation scheme $\mathcal{U} = \{u_0, u_1, \dots\}$ accomplishing switching between reorientations u_n of the base flow following (2.4) at time levels $t_n = n\tau$ for spectral versus FVM-based method; (c) cost function J for spectral versus FVM-based method.

Figure 2.9c (red circle) slightly deviates from its reference (black cross), though, yet this must be attributed to different characteristics of the numerical schemes. (FVMs are e.g. known to suffer from numerical diffusion [78].) However, attainment of identical $\mathcal{U}$ implies that the controller is insensitive to (at least) disturbances of this magnitude, caused by numerical effects or otherwise. Simulations for different cases consolidate these findings. This demonstrates that the FVM-based predictor admits reliable and robust performance of minimisation (2.47) and the control strategy indeed is viable for practical applications.

2.5.2 Performance of adaptive flow reorientation for process enhancement

The effectiveness of adaptive flow reorientation is determined by comparing the transient time t_ϵ required to reach equilibrium $\widetilde{T}_\infty$ with that for conventional periodic reorientation consisting of repetition of the sequence $\mathcal{U} = \{1, 2, \dots, N\}$ at given (Pe, τ). The performance indicator

$$\chi(Pe, \tau) = \frac{t_{\varepsilon,p}(Pe, \tau)}{t_{\varepsilon,a}(Pe, \tau)}, \tag{2.52}$$

where subscripts “p” and “a” denote periodic and adaptive schemes, respectively, quantifies this effectiveness as follows: $\chi > 1$ indicates a shorter transient and, inherently, a faster equilibration rate – and thus superior performance – of the adaptive scheme compared to the periodic scheme; $\chi < 1$ indicates a relatively inferior performance of the adaptive scheme.

The performance analysis is carried out for aperture configurations $N = 2, 3, 4$ and involves evaluation of χ in (Pe, τ)-space for $5 \times 10^2 \leq Pe \leq 5 \times 10^3$ and $3 \leq \tau \leq 30$ using tolerance $\varepsilon = 10^{-2}$ introduced above. The range for Pe encompasses the values $Pe \sim \mathcal{O}(10^3)$ typical of practical systems within the present scope (Section 2.1); the range for τ captures the transition from regular towards chaotic advection with conventional periodic reorientation schemes in the RAM for given N [12]. Performance indicator χ is computed on an equidistant grid of $50 \times 50 = 2500$ points inside the considered parameter range using the spectral method of Section 2.5.1.

Figure 2.10 gives χ versus (Pe, τ) for $N = 2$ (left), $N = 3$ (center) and $N = 4$ (right) using a logarithmic scale for τ to enhance contrast. This yields $\chi > 1$ everywhere and thus exposes – at least in the considered parameter range – the adaptive scheme as superior to the conventional periodic scheme. The difference in performance exhibits substantial variation, however. Peak performance is for cases $N = 2$ and $N = 3$ confined to relatively narrow bands near the lower bound $\tau = 3$ ($\log_{10} \tau = 0.5$) and within this regime reaches $\max \chi = 3.5$ for $N = 2$ and $\max \chi = 3.9$ for $N = 3$ at the upper bound $Pe = 5 \times 10^3$; performance rapidly declines to $\chi \simeq \mathcal{O}(1)$ upon increasing τ. Case $N = 4$ is devoid of pronounced high-performance bands and exhibits more erratic behaviour with a considerably lower $\max \chi = 1.5$. Section 2.5.4 reconciles shown performance with the advection characteristics and fluid deformation.

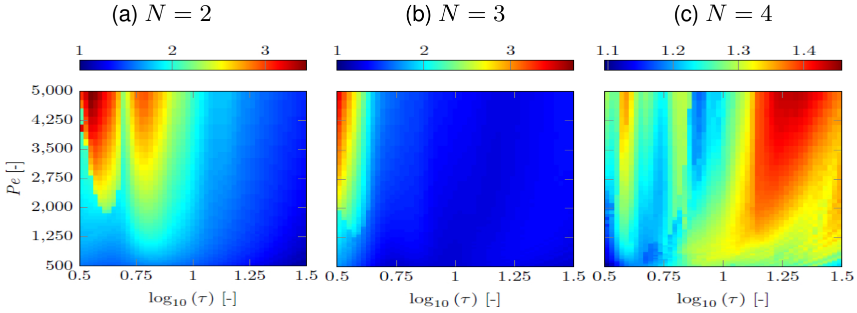
(a) $N = 2$ (b) $N = 3$ (c) $N = 4$

Figure 2.10: Performance indicator χ versus (Pe, τ) for RAM with number of apertures N as indicated.

Important for practical purposes is that the adaptive scheme also in regions $\chi \simeq \mathcal{O}(1)$ outside the high-performance bands significantly outperforms the conventional periodic scheme. Figure 2.11 highlights this by partition of parameter space into regions with a relative acceleration of the fluid heating $\chi_{\text{rel}} = (\chi - 1) \times 100\%$ of $0 < \chi_{\text{rel}} \leq 15\%$ (blue), $15\% < \chi_{\text{rel}} \leq 20\%$ (green), $20\% < \chi_{\text{rel}} \leq 25\%$ (yellow), $25\% < \chi_{\text{rel}} \leq 30\%$ (orange) and $\chi_{\text{rel}} > 30\%$

(red). This reveals accelerations by at least 15% in nearly the entire parameter range (save some localised regions for $N = 2$ and $N = 4$) and 25% or more in large areas. This has the major (practical) implication that adaptive flow reorientation enables the same process with the same device yet at considerably lower effort compared to conventional operation (energy consumption for flow forcing is proportional to t_ϵ). Process enhancement of this magnitude namely constitutes a dramatic reduction in energy and (potentially also) resource consumption in industries as those highlighted in Section 2.1.

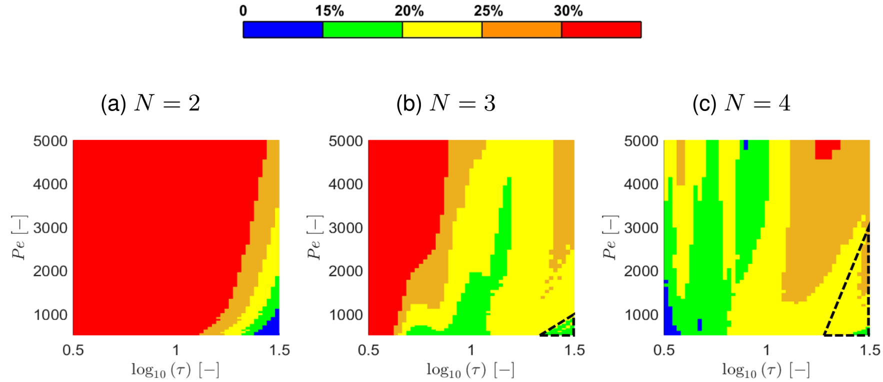

Figure 2.11: Relative acceleration of fluid heating $\chi_{\text{rel}} = (\chi - 1) \times 100\%$ by adaptive flow reorientation for RAM with number of apertures N as indicated: $0 < \chi_{\text{rel}} \leq 15\%$ (blue), $15\% < \chi_{\text{rel}} \leq 20\%$ (green), $20\% < \chi_{\text{rel}} \leq 25\%$ (yellow), $25\% < \chi_{\text{rel}} \leq 30\%$ (orange), $\chi_{\text{rel}} > 30\%$ (red). Dashed black triangles in panels (b) and (c) approximately outline regions with adaptive schemes consisting of periodic repetitions of $\mathcal{U} = \{1, 3, 2\}$ and $\mathcal{U} = \{1, 4, 3, 2\}$, respectively.

2.5.3 Optimal reorientation schemes and heating dynamics

Control actions in the considered parameter range invariably involve aperture activation and frequent switching ($u \neq 0$); intermediate diffusion-only steps ($u = 0$) are non-existent in the adaptive reorientation schemes. This implies that flow reorientation, despite inevitable local diminution (Section 2.3.2), on a global scale always enhances the heating process. Striking, though, is that the controller never selects the conventional periodic reorientation scheme introduced in Section 2.5.2 or, generically, repetitions of other systematic progressions along all apertures such as e.g. $\mathcal{U} = \{-1, -2, \ldots, -N\}$ or $\mathcal{U} = \{N, N-1, \ldots, 1\}$. The sole exceptions are periodic repetitions of $\mathcal{U} = \{1, 3, 2\}$ for $N = 3$ and $\mathcal{U} = \{1, 4, 3, 2\}$ for $N = 4$ found in the localised parameter regimes approximately bounded by the dashed black triangles in Figure 2.11b and Figure 2.11c, respectively. Figure 2.9b demonstrates that the adaptive scheme, even upon restriction to $u > 0$, exhibits aperiodic deviation from said conventional scheme.

Adaptive reorientation schemes generically are essentially aperiodic and Figure 2.12 shows typical cases for $N = 2$ (red), $N = 3$ (black) and $N = 4$ (blue) yielding $\chi = 2.49$, $\chi = 2.15$ and $\chi = 1.25$, respectively. However, adaptive reorientation schemes in a significant portion of the parameter space encompass prolonged periodic episodes (including some cases that are entirely periodic) as illustrated in Figure 2.12b for $(Pe, \tau) = (3275, 4.2)$. Here the reorientation schemes settle on the periodic sequence

$$\begin{gathered} \mathcal{U}_{N=2} = \{1, -2, 1, -2, \dots\}, \quad \mathcal{U}_{N=3} = \{1, -3, 1, -3, \dots\}, \\ \mathcal{U}_{N=4} = \{2, -3, 2, -3, \dots\}, \end{gathered} \tag{2.53}$$

either directly from the start ($N = 2$) or after a short transient ($N = 3, 4$) and for given (Pe, τ) yield $\chi_{N=2} = 2.81$, $\chi_{N=3} = 2.15$ and $\chi_{N=4} = 1.31$.

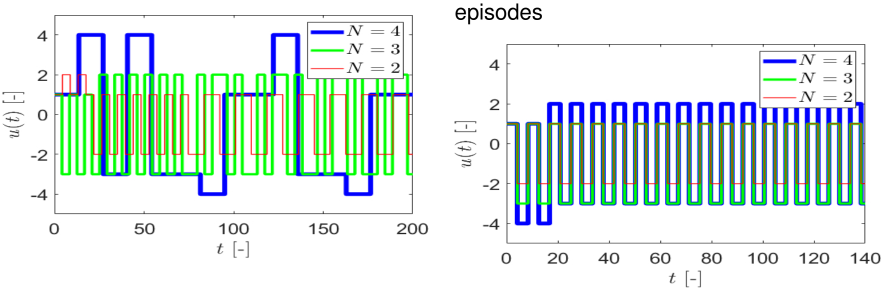
(a) Essentially aperiodic schemes

(b) Schemes with prolonged periodic episodes

Figure 2.12: Typical adaptive reorientation schemes $\mathcal{U} = \{u_0, u_1, \dots\}$ accomplishing switching between reorientations u_n of the base flow following (2.4) at time levels $t_n = n\tau$: (a) essentially aperiodic schemes for $(Pe, \tau)_{N=2} = (2471, 4.4)$, $(Pe, \tau)_{N=3} = (3125, 4.2)$ and $(Pe, \tau)_{N=4} = (1012, 13.6)$; (b) schemes with prolonged periodic episodes for $(Pe, \tau) = (3275, 4.2)$ and N as indicated.

Key difference between said periodic sequences and the conventional periodic schemes is that the former always consist of switching between two adjacent arcs that move in opposite directions. This sets up two alternating and counter-rotating circulations and, depending on the relative arc movement, results in the following thermal behaviour. Arcs moving *towards* each other create a single thermal plume between the arcs that sways back and forth with the alternating circulations as demonstrated by the temperature evolutions in Figure 2.13a corresponding with case $N = 2$ (top) and $N = 3$ (bottom) in (2.53). Arcs moving *away from* each other create two thermal plumes, emanating from the leading edges of the arcs, that are periodically reinvigorated by the alternating circulations as demonstrated in Figure 2.13b for case $N = 4$ in (2.53).

Aperiodic and (largely) periodic schemes as illustrated in Figure 2.12 may emerge throughout parameter space yet the controller generally tends towards aperiodic (periodic) schemes for “lower” (“higher”) τ. Such aperiodic schemes often exhibit intermittent behaviour by comprising of plume-forming periodic episodes interspersed with aperiodic intervals; this e.g. occurs typically in the high-performance regions for $N = 2$ and $N = 3$ in Figure 2.10. Moreover, persistent single plumes as shown in Figure 2.13a mainly emerge for $N = 2$ and $N = 3$; case $N = 4$ overall tends more towards aperiodic behaviour. However, a direct link between type of adaptive reorientation and parameter regimes appears absent yet generic correlations with the advection characteristics exist (Section 2.5.4).

(a) Single thermal plume for $N = 2$ (top) and $N = 3$ (bottom).

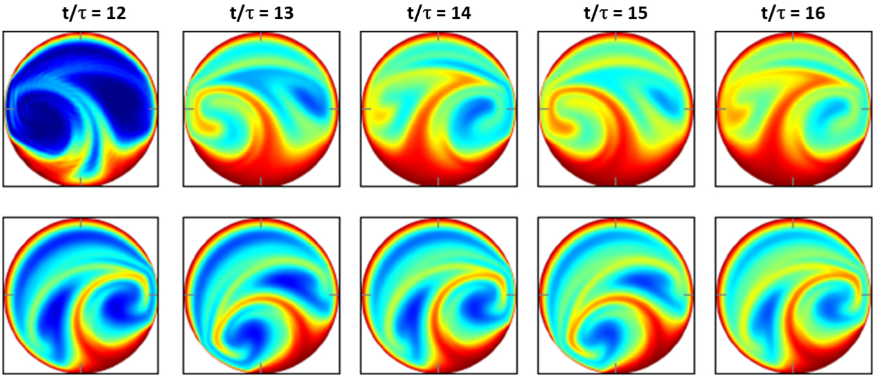

(b) Pair of thermal plumes for $N = 4$.

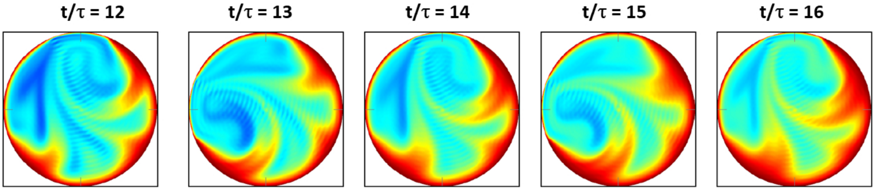

Figure 2.13: Formation of thermal plumes due to periodic (episodes of) reorientation schemes selected by adaptive flow reorientation demonstrated for case $(Pe, \tau) = (3275, 4.2)$ in Figure 2.12b: (a) single thermal plume driven by two adjacent arcs alternately moving towards each other for $N = 2$ (top) and $N = 3$ (bottom); (b) pair of thermal plumes driven by two adjacent arcs alternately moving away from each other for $N = 4$.

The dependence of performance indicator χ on parameters (Pe, τ) shown in Figure 2.10 is inextricably linked to that of the transient times for the adaptive ($t_{\varepsilon,a}$) and conventional periodic ($t_{\varepsilon,p}$) schemes. Figure 2.14 gives $t_{\varepsilon,a}$ (dashed) and $t_{\varepsilon,p}$ (solid) for $N = 2$ and $N = 3$ at the indicated Pe and reveals a significant decline of $t_{\varepsilon,p}$ with increasing τ that grows more pronounced with larger Pe versus a nearly uniform $t_{\varepsilon,a}$ in τ-direction that increases moderately with Pe. Case $N = 4$ (not shown) exhibits similar behaviour yet with a mildly-fluctuating (instead of significantly declining) $t_{\varepsilon,p}$. These observations imply that variation of χ in Figure 2.10 stems primarily from variable $t_{\epsilon,p}$ and, inherently, variable performance of the conventional periodic scheme.

Uniform $t_{\epsilon,a}$ dependent only on Pe in Figure 2.14, on the other hand, signifies a consistent performance of the adaptive scheme that (save the localised spike at the lower bound for τ at $Pe = 5000$ in Figure 2.14a) is virtually independent of both τ and N. This implies that the controller systematically identifies the (on average) optimal orientation between deformation and temperature gradient at the fluid parcels and heat transfer is limited primarily by the thermophysical conditions at the molecular level for given Pe. Heat transfer between fluid parcels namely occurs at time scales proportional to the diffusive time scale $t_{\text{ diff}} = R^2/\nu$, which in the non-dimensional formulation of Section 2.2.2 (i.e. relative to the advective time scale $t_{\text{ adv}} = R/U$) depends linearly on Pe via $t'_{\text{diff}} = t_{\text{ diff}}/t_{\text{ adv}} = Pe$. Linear correlation $t_{\epsilon,a} \propto Pe$, for (at least) $N = 2$ and $N = 3$ in Figure 2.10 implies that the controller (within the constraint of the stepwise optimisation of Section 2.4.1) consistently identifies the "best" reorientation scheme for molecular transfer rates at given Pe.

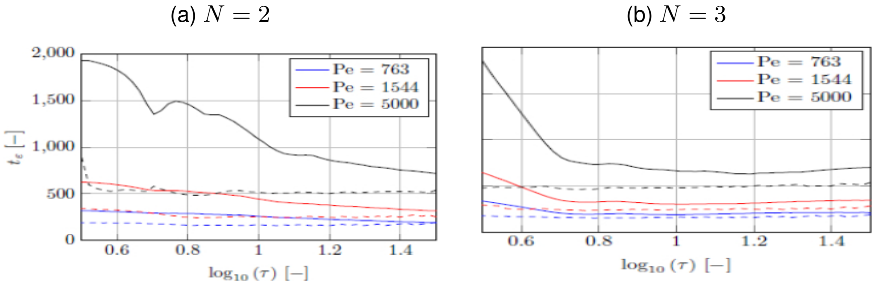

Figure 2.14: Transient time $t_{\varepsilon,a}$ (dashed) and $t_{\varepsilon,p}$ (solid) of adaptive and conventional periodic schemes, respectively, versus τ for selected Pe and RAM with number of apertures N as indicated.

2.5.4 Role of fluid deformation and chaotic advection

Fluid deformation impacts the global heat transfer by changing the rates of global energising (quantified by metric J_2) and equilibration (quantified by metric J_1) via the leading integrals in (2.41) represented by functions $\bar{G}$ and $\widetilde{G}$ according to (2.44) and (2.46), respectively. The spatial distribution of the corresponding integrands $\bar{g}$ ($\widetilde{g}$), shown in Figure 2.6 (Figure 2.7) in terms of $\bar{\beta}$ ($\widetilde{\beta}$) following (2.43), reveals that this impact is primarily restricted to the direct vicinity of the arc edges and (at least) for temperature evolutions in the base flow $\mathbf{v}_1$ from the uniform initial condition T_0 accelerates energising and equilibration. The generality of this behaviour is investigated below.

Key to energising is the wall temperature gradient $\bar{f} = \partial\widetilde{T}/\partial r|_{\Gamma}$. Figure 2.15 shows $\bar{f}$ for the adaptive (red) versus conventional periodic (blue) scheme at time levels t_{n+1} during an intermediate episode of the transient for the typical case $N = 3$ and $Pe = 1000$ at given τ. (The adaptive scheme corresponds with $\mathcal{U}_{N=3} = \{1, -3, 1, -3, \dots\}$ following (2.53).) Gradient $\bar{f}$ significantly steepens at the active arc during step $t_n \leq t \leq t_{n+1}$, with corresponding leading (trailing) edges indicated by dashed (solid) vertical lines, and peaks at the trailing egde. This reveals that fluid deformation, despite considerable changes in initial conditions at t_n, step-wise creates essentially the same situation as for the base flow in Figure 2.6b and – upon identifying $\theta = \Delta/2$ ($\theta = -\Delta/2$) in (2.44) with the trailing (leading) edge of the active arc – implies $\bar{G} > 0$ and thus accelerated energising compared to a non-deforming fluid. Both schemes accomplish this yet the consistently higher peaks at the trailing edges for the adaptive scheme render this effect more pronounced and thereby signify a systematically superior performance over the conventional scheme.

The step-wise impact of fluid deformation on equilibration for the above case is shown in Figure 2.16 in terms of $\widetilde{\beta}$ and is also reminiscent of that of the base flow in Figure 2.7: emergence of localised high-impact regions (red/blue) near the arc edges and larger moderate-impact regions (yellow/cyan) in the interior. Moreover, these high-impact regions again vary only marginally in time and with flow reorientation; significant spatio-temporal variation occurs only in the moderate-impact regions. Thus the simplified $\widetilde{G}$ following (2.46) to good approximation holds in general and in conjunction with the wall temperature gradients in Figure 2.15 implies $\widetilde{G} > 0$ and, inherently, acceleration of equilibration by the same reasoning as for the base flow in Section 2.3.5.

The above behaviour is representative for the entire transient in arbitrary cases and demonstrates that fluid deformation generically indeed enhances energising and equilibration. However, as clearly demonstrated in Figure 2.16, this primarily relies on the high-shear regions near the arc edges and their interaction with the temperature gradient; fluid deformation in the flow interior only plays a secondary role in this process due to its relative weakness compared to said regions. This has the major implication that the adaptive scheme attains its superior and consistent performance mainly from step-wise optimal orientation between arc edges and wall temperature gradient. The adaptive scheme thus creates peaks of comparable magnitude close to an upper limit set by the beforementioned thermo-physical conditions for all τ, as e.g. demonstrated by the profiles at $t_{n+1} = 20$ in Figure 2.15, yielding the nearly uniform $t_{\varepsilon,a}$ in Figure 2.14. The conventional scheme, on the other hand, sequentially creates peaks at the consecutive arcs that grow with τ (again demonstrated by the profiles at $t_{n+1} = 20$ in Figure 2.15) due to the increasing fluid deformation associated with longer arc activation and approach said upper limit only for sufficiently large τ. Reaching this limit is intimately related to the local breakdown of heat-transfer enhancement at $t \sim \mathcal{O}(\tau_\beta)$, with τ_β according to (2.31), where $\tau_\beta \simeq \mathcal{O}(0.3 - 3)$ for the degree of fluid deformation in the arc region (Section 2.3.3). The significant decline and subsequent flattening of $t_{\varepsilon,p}$ exactly at step durations τ of this magnitude in Figure 2.14 support this scenario.

(a) $\tau = 2$

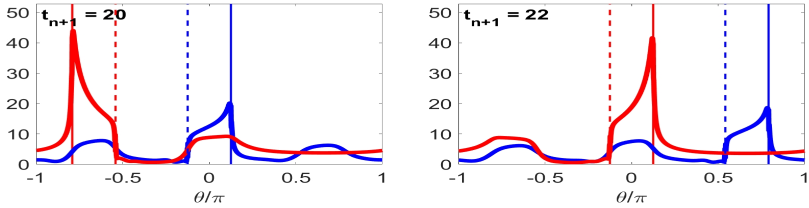

(b) $\tau = 5$

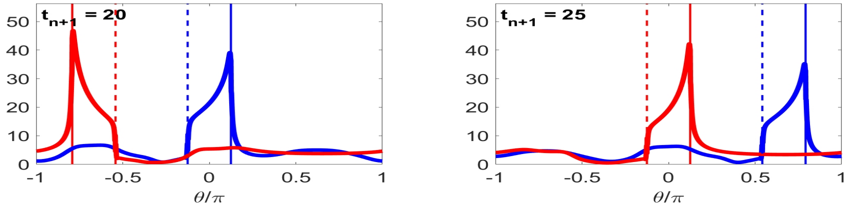

(c) $\tau = 10$

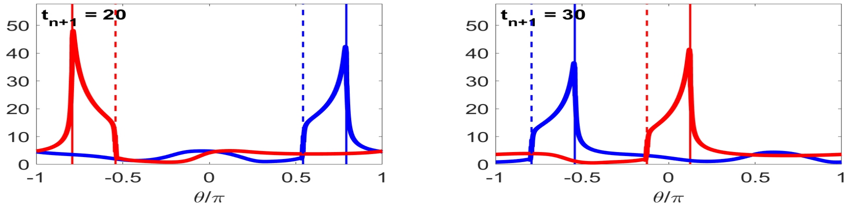

Figure 2.15: Impact of fluid deformation on energising demonstrated by wall temperature gradient $\bar{f} = \partial\widetilde{T}/\partial r|_\Gamma$ for adaptive (red) versus conventional periodic (blue) scheme at time levels t_{n+1} for $N = 3$ and $Pe = 1000$ at given τ. Dashed (solid) vertical lines indicate leading (trailing) edges of active arc.

The relative weakness of fluid deformation in the domain interior suggests that global advection mainly serves as mechanism for exchanging (to be) heated fluid parcels between the arc regions and said interior and makes whether this fluid transport is chaotic or not of secondary importance. The following considerations substantiate this subordinate role of chaotic advection for the heating performance of the RAM. Lagrangian transport within the flow interior associated with the frequently-emerging periodic plume-forming schemes such as e.g. (2.53) transits from regular to chaotic with increasing τ, as demonstrated in Figure 2.17 by the stroboscopic map of 100 tracers released on the x-axis. However, the corresponding transient time $t_{\varepsilon,a}$ in Figure 2.14 remains uniform, signifying a thermal performance of the adaptive scheme that is consistent for all τ and, in

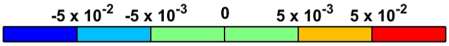

(a) Adaptive scheme $\tau = 2$ (b) Conventional scheme $\tau = 2$

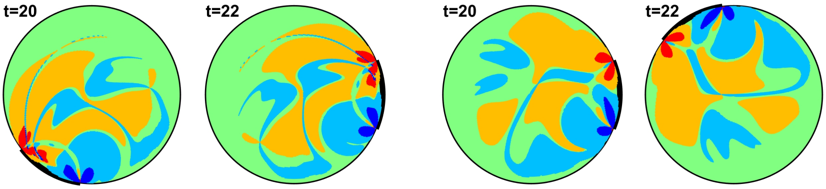

(c) Adaptive scheme $\tau = 5$ (d) Conventional scheme $\tau = 5$

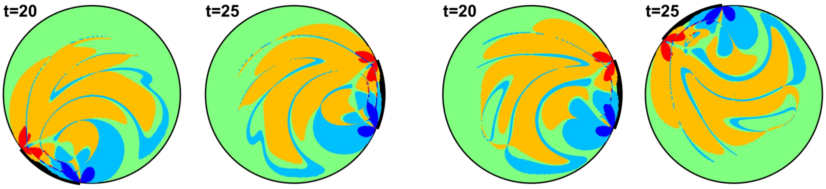

(e) Adaptive scheme $\tau = 10$ (f) Conventional scheme $\tau = 10$

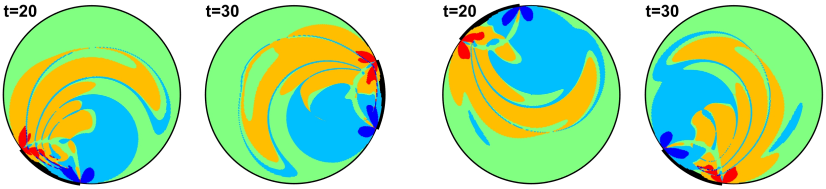

Figure 2.16: Impact of fluid deformation on equilibration demonstrated by partition of relative change rate $\widetilde{\beta} = \widetilde{g}/\widetilde{f}$ via $\widetilde{\beta}_{\,\mathrm{rel}} \equiv \widetilde{\beta}/\max|\widetilde{\beta}|$ into regions with strong enhancement ($\widetilde{\beta}_{\,\mathrm{rel}} \geq \epsilon_2$; red) versus strong diminution ($\widetilde{\beta}_{\,\mathrm{rel}} \leq -\epsilon_2$; blue), moderate enhancement ($\epsilon_1 \leq \widetilde{\beta}_{\,\mathrm{rel}} < \epsilon_2$; yellow) versus moderate diminution ($-\epsilon_2 < \widetilde{\beta}_{\,\mathrm{rel}} \leq -\epsilon_1$; cyan) and insignificant impact ($|\widetilde{\beta}_{\,\mathrm{rel}}| < \epsilon_1$; green) using thresholds $(\epsilon_1, \epsilon_2) = (5 \times 10^{-3}, 5 \times 10^{-2})$ for $N = 3$ and $Pe = 1000$ at given τ. Heavy boundary segments indicate active arc during step $[t - \tau, t]$ prior to given time level t.

consequence, independent of the emergence of chaos.

The conventional scheme results in a similar transition from regular to chaotic advection in the ranges $1 \lesssim \tau \lesssim 6$ ($0 \lesssim \log_{10}\tau \lesssim 0.8$), $2 \lesssim \tau \lesssim 5$ ($0.3 \lesssim \log_{10}\tau \lesssim 0.7$) and $2 \lesssim \tau \lesssim 5$ ($0.3 \lesssim \log_{10}\tau \lesssim 0.7$) for $N = 2$, $N = 3$ and $N = 4$, respectively, and yields stroboscopic maps as shown in [12]. (Stroboscopic maps in [12] in fact concern companion schemes for $\Theta' = -\Theta$ and $\Omega') = -\Omega$ and on grounds of symmetry are identical to maps of the current schemes.) The transition and fully-chaotic zones correlate with the regimes of declining and flat profiles of $t_{\varepsilon,p}$ in Figure 2.14, respectively, and this may thereby suggest a significant role of the interior (chaotic) advection in the thermal performance. However, increasing τ and N simultaneously changes the conditions near the active arc by two effects: (i) circulation of more fluid parcels through the N arc regions (thus promoting greater heat exchange between wall and interior) and (ii) larger fluid deformation (thus promoting a steeper wall temperature gradient at the arc). This, together with the flattening of $t_{\varepsilon,p}$ at $\tau \sim \mathcal{O}(\tau_\beta)$ established above, advances the conditions at the active arc that drives the interior (chaotic) advection – rather than the nature of this interior transport itself – as the primary cause for the decline in $t_{\varepsilon,p}$ and corresponding enhancement in thermal performance.

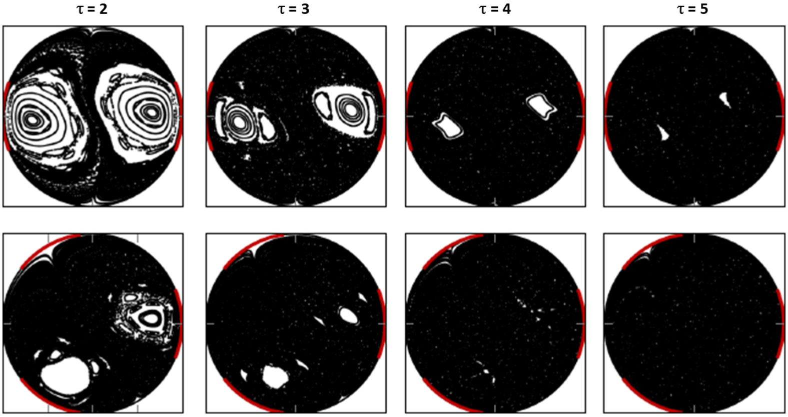

Figure 2.17: Lagrangian transport associated with periodic plume-forming schemes (2.53) versus τ demonstrated by stroboscopic map of 100 tracers released on x-axis for RAM with $N = 2$ (top) and $N = 3$ (bottom) apertures.

2.6 Conclusions

The present study aims to contribute to existing solutions for enhancement of scalar transport in laminar flows through flow reorientation. To this end a dedicated flow-control strategy is developed (i.e. “adaptive flow reorientation”) that systematically determines the “best” flow reorientation for the fast heating of a cold fluid via a hot boundary in a representative case study.

The control strategy is founded on an in-depth analysis of the dynamics of heating in fluid flows. This exposes fluid deformation as the “thermal actuator” via which the flow affects the heat transfer. The link between former and latter is non-trivial, though. Fluid deformation may, depending on its orientation relative to the temperature gradient, both enhance and diminish local heat exchange between fluid parcels. Moreover, enhanced heat transfer promotes local thermal homogenisation and, by reducing temperature gradients, thus effectively counteracts itself. This fundamental “conflict” between local heat transfer and thermal homogenisation tends to restrict the beneficial impact of flow to short-lived episodes. The impact of fluid deformation on the global fluid heating is primarily confined to the direct proximity of the moving boundary that drives the flow. Fluid deformation in the flow interior only plays a secondary role in this process due to its relative weakness compared to said regions. These insights imply that incorporation of the thermal behaviour is essential for effective flow-based enhancement strategies and efficient fluid mixing, the conventional approach adopted in industry for this purpose, is potentially sub-optimal.

Global heating encompasses two concurrent processes, i.e. increasing energy content (“energising”) and thermal homogenisation, and this fundamentally differentiates the current problem from the thermal homogenisation in adiabatic systems usually considered in related studies. Moreover, this notion yields the relevant metrics for the global dynamics and thus enables formulation of the control problem as the minimisation of a dedicated cost function that naturally emerges from the dynamic analyses and adequately incorporates both processes. This facilitates step-wise determination of the “best” flow reorientation from predicted future evolutions of actual intermediate states and, in tandem with an efficient predictor, paves the way to (real-time) regulation of scalar transport by flow control in practical applications. Key enablers for this predictor are (i) the property that flow reorientations carry over to the temperature field (ii) a compact reduced-order model for the Perron-Frobenius evolution operator that rapidly maps initial to final temperature fields for each step duration and flow reorientation.

Performance analyses reveal that adaptive flow reorientation significantly accelerates the fluid heating throughout the considered parameter space and thus is superior over conventional periodic schemes (designed for efficient fluid mixing) both in terms of consistency and effectiveness. Fluid heating is accelerated by at least 14% everywhere and 24% or more in large areas and process enhancement of this magnitude constitutes a dramatic reduction in energy and (potentially also) resource consumption in industries motivating the present study. The controller in fact breaks with conventions by, first, never selecting these periodic schemes and, second, achieving the same superior performance for all flow conditions irrespective of whether said mixing occurs. The controller typically achieves this superiority by creating an essentially heterogeneous situation comprising of thermal plumes that extend from the hot wall into the cold(er) interior and are driven by two alternating and counter-rotating circulations. The performance analyses furthermore substantiate the primary and secondary roles of fluid deformation near the driving boundary segments and in the flow interior, respectively, in the heating enhancement by the flow.

Ongoing efforts concern, first, more advanced and precise regulation of the thermal process by continuous actuation of all moving boundary segments and, second, experimental validation and testing of the control strategy. Future studies aim at further paving the way to practical applications by development of observers for full state estimation from discrete sensor data and data-based construction of compact models as well as realisation of advanced control targets such as e.g. thermal fronts or heterogeneous temperature fields for promotion of chemical reactions.

CHAPTER 3

Rapid thermalization with restricted adaptive flow reorientation

Abstract - *The aim of this chapter is to provide insights into accelerating scalar transport (e.g. of heat or chemical species) in flow systems where transport is "driven" by reorientations of a laminar base flow. In the previous chapter, an adaptive flow reorientation approach, which determines the best flow field reorientation and circulation direction to boost fluid heating, is presented. The applications of interest in this chapter encompass applications that allow a reorientation of the base flow as in Chapter 2. However, fluid is only allowed to circulate in a single direction here. Such limitations are frequently imposed by the geometric/mechanical configuration in, e.g., (inline) mixers or stirring tanks in the foodstuffs, medical and/or (petro)chemical industry. The conventional heating/mixing approach for rapid scalar transport in these applications entails the periodic reorientation (in space) of the base flow to promote fluid mixing (e.g. by baffles or rotating beaters). As discussed in Chapter 2, the homogenisation rate of the scalar field is not necessarily accelerated with these periodic approaches in the presence of i) substantial diffusion and/or chemical reactions and/or ii) a non-adiabatic boundary condition. In the present study, heat transport enhancement with the adaptive reorientation protocol is again investigated on a case-study, the Rotated Arc Mixer (RAM), for an entire parameter space of fluid and flow properties. However, fluid*

The contents of this chapter is an extension of: R. Lensvelt, M.F.M. Speetjens, and H. Nijmeijer. "Rapid thermalization by adaptive flow reorientation". In: *Journal of Physics: Conference Series.* (2116), Lisbon, 012114.

circulation is only allowed in a single direction in this chapter. Numerical results show that the adaptive approach is still able to significantly enhance heat transport compared to the conventional periodic heating/mixing approach designed for efficient mixing.

3.1 Introduction

In Chapter 2, an adaptive approach is presented for "optimal" selection of the flow field reorientation and fluid circulation direction based on a L^2 norm of a predicted scalar field. In Chapter 2, a compact predictor model is developed that allows for real-time selection of the flow field reorientation and fluid circulation direction in the presence of both significant diffusion and a non-adiabatic boundary condition.

In this chapter, reorientation schemes obtained with the adaptive reorientation protocol are analysed further in order to gain insights relevant to improving existing fluid stirring applications. Fluids can, in some of the applications of interest, only be stirred in a single direction (e.g. due to geometrical and/or mechanical configuration of the stirring application). Hence, the adaptive reorientation protocol is only permitted to circulate the fluid in a single direction in this chapter. This constrains the fluid circulation direction – and thus the analysis – compared to Chapter 2. However, the limitation ensures that the obtained reorientation schemes are directly applicable to heating/mixing system where fluids circulate in a single direction and where Stokes flows reorient in either space or time.

The primary focus of this chapter is to enhance scalar transport on a case-study, which is representative for the applications of interest; heating of an initially cold fluid by stirring in the presence of a hot boundary. Hence, the Rotated Arc Mixer (RAM) studied in Chapter 2 is investigated here as well. The work in this chapter extends the analysis of the adaptive reorientation protocol in Chapter 2 by performing an in-depth analysis of the reorientation schemes that result in improved heat transport on the RAM. To this end, fluid heating in the case-study is investigated for flow forcing based on the adaptive reorientation protocol and compared to flow forcing by the conventional periodic protocol in Section 3.2. Numerical results are investigated for a similar range of practically relevant fluid and flow parameters as in Chapter 2. Finally, conclusions and recommendations for future research are presented in Section 3.3.

3.2 Numerical study

In this section, the adaptive reorientation protocol is employed to determine "optimal" reorientation schemes for the same case-study that was investigated in Chapter 2: the $2D$ Rotated Arc Mixer (RAM). The adaptive approach and the compact model – required for fast numerical simulations – used in this chapter are presented in Section 2.4.

3.2.1 Performance measure

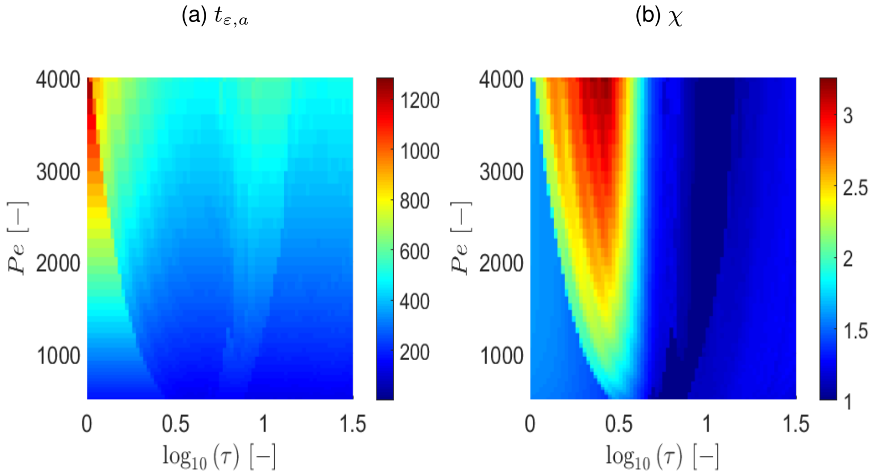

Figure 3.1: (a) Homogenisation times ($t_{\varepsilon,a}$) for the reorientation schemes obtained with the adaptive flow reorientation protocol presented in Section 2.4 and (b) homogenisation ratios (χ) for various Péclet numbers and activation times.

Here, fluid heating with each protocol is investigated for a range of Péclet numbers where both advection and diffusion significantly impact heat transport. The effectiveness to produce homogeneity is defined by the amount of non-dimensional time steps (t_ε) required for the transient field to be within a certain threshold ε (i.e. $\int_{\mathcal{D}} \widetilde{T}^2(\boldsymbol{x}, t_\varepsilon)\,\mathrm{d}^2\boldsymbol{x} \leq \varepsilon^2$ where $\widetilde{T}(\boldsymbol{x}, t) = T(\boldsymbol{x}, t) - 1$ as in Chapter 2). The homogenisation rate for each protocol is investigated by comparing the transient times of reorientation schemes to reach ε. Therefore, the measure χ presented in (2.52) is used here. Protocols are investigated on their ability to generate 99 % homogeneity $\varepsilon = 10^{-2}$. The homogenisation time is obtained from an interpolation of J_n when the temperature field reaches the threshold ε within the activation interval of span τ (i.e. $t_{\varepsilon,a/p} = n\tau + (J_{n+1} - J_n)/\tau\,(\varepsilon - J_n)$). Ratios (2.52) that exceed unity ($\chi > 1$) denote accelerated thermal homogenisation rates by the adaptive reorientation protocol, which are faster than the conventional periodic one. The protocols are studied for a physically interesting parameter range with Péclet numbers and activation times between $500 \leq Pe \leq 4000$ and $10^0 \leq \tau \leq 10^{1.5}$, respectively [79, 4]. We consider a RAM with three apertures in which a fluid can only circulate in clock-wise direction. This constraint to fluid circulation represents a key difference with respect to the analysis in Chapter 2. This limitation in the circulation direction means the adaptive reorientation protocol can only alter the order of flow field activation and its duration. However, this makes observations potentially useful for better design of reorientation schemes in (existing) applications without requiring adaptations for feedback control (e.g. due to the absence of sensors to obtain $\widetilde{T}$).

3.2.2 Heating dynamics

Numerical results of homogenisation times and ratios according to (2.52) are shown in Figure 3.1. Heating rates for the periodic scheme match numerical results previously obtained with reorientation schemes that periodically activate flow fields (i.e.
$u_n \in \{\mathcal{U}_\mathcal{T}, \mathcal{U}_\mathcal{T}, \ldots\}$ where $\mathcal{U}_\mathcal{T} = \{1, 2, 3\}$ [16]).

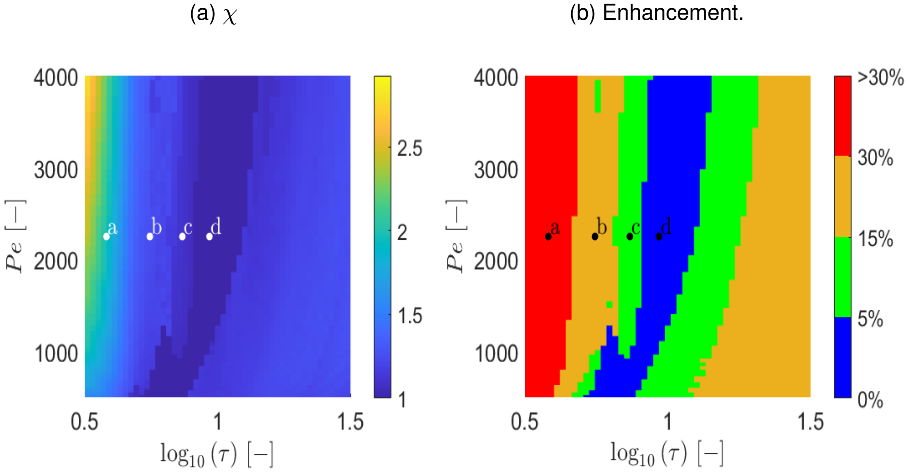
(a) χ

(b) Enhancement.

Figure 3.2: Zoom of (a) homogenisation ratios (χ) and (b) enhancement percentage with $\chi_r = (\chi^{-1} - 1) \times 100$ %, into regions where $0 \leq \chi_r < 5\%$ (blue), $5 \leq \chi_r < 15\%$ (green), $15 \leq \chi_r < 30\%$ (orange) and $\chi_r \geq 30\%$ (red) for various Péclet numbers and activation times with points of interest A through B.

Figure 3.1b shows improved heating rates ($\chi \geq 1$) with the adaptive schemes throughout the investigated parameter domain. A plateau with more or less constant improvement (i.e. $\chi \approx 1.6$) can be found for small activation times in Figure 3.1b. Homogenisation times grow proportionately with Pe for the adaptive schemes in this region as can be seen in Figure 3.1a. Examination of the adaptive reorientation schemes in this region reveals that they activate only a single flow field. Periodic reorientations schemes rapidly reorient individual flows for such small activation times. The rapid activation of the different flow fields in the periodic scheme results in an average flow field governing heat transport [22] (i.e. a small τ results in $\boldsymbol{v}(\mathbf{x}, t) \approx 1/3 \sum_i \boldsymbol{v}_i(\mathbf{x})$). Note that this characteristic behaviour of the adaptive reorientation schemes remains the same, even if the number of parameters in the model's parameter space is refined (i.e. the protocols are evaluated for more model parameters Pe, τ inside the considered domain). The plateau has a distinct boundary of which activation times are related by a reciprocal of the Péclet number (i.e. $\tau \propto Pe^{-0.5}$).

The prediction horizons are too short to produce any significant changes in the cost-to-go function (i.e. J_n) of the adaptive protocol for parameters inside the plateau. This renders activation of a single flow more beneficial than a periodic scheme for certain Péclet numbers according to J_n in (2.47). Therefore, (adaptive) reorientation of flows, with a one-step ahead prediction horizon, is only investigated further for activation times beyond the aforementioned boundary that marks the edge of this plateau. This is further illustrated by the significant drop in homogenisation times for the adaptive reorientation schemes beyond this boundary (in Figure 3.1a).

Following the plateau, a "transition zone" can be observed for increasing activation times in Figure 3.1b. In this region, heating shows a drastic improvement with the adaptive schemes compared to the periodic schemes. The adaptive schemes depart from single flow activations and transition into more complex (a)periodic schemes as activation times increase. Immediately after the transition (around $\tau \approx 2.2$ (or $\log_{10}(\tau) = 0.34$) is a region where adaptive schemes consist of an initial aperiodic window followed by periodic reorientation. Fluid is circulated in the exact opposite direction in these adaptive schemes as the periodic schemes (i.e. one finds $u_n \in \mathcal{U} = \{3, 2, 1, 3, 2, \ldots\}$). Heating rates can be improved by more then three times ($\chi > 3$) with the adaptive schemes compared to the periodic ones for large Péclet numbers and medium sized activation times ($\tau \approx 3.2$). Mixing studies on a RAM with $\Theta = 2\pi/3$ show that the transition to chaotic advection – signifying efficient laminar mixing – occurs in the considered periodic schemes beyond the peak value for χ observed in Figure 3.1b [12]. The transition towards "good mixing" performance is numerically estimated around $\tau \approx 3.2$ ($\log_{10}(3.2) \approx 0.5$) for a RAM with $\Theta = 2\pi/3$. Heating rates drastically improve with the periodic protocol beyond this point [16]. This is confirmed by Figure 3.1a, where homogenisation times of the adaptive schemes vary only slightly throughout the parameter domain. The observed decrease of χ in Figure 3.1b is therefore only due to improved heating rates of the periodic schemes.

The region after $\tau \approx 3.2$ in Figure 3.1b is investigated more closely in Figure 3.2a since heating rates significantly deteriorate with the periodic scheme before this threshold. Note the difference in magnitudes between Figure 3.2a and Figure 3.1b. Better heating with the periodic scheme marks a sharp decrease in homogenisation ratios as can be seen in Figure 3.2a. The adaptive schemes in this region consist of an aperiodic transient followed by periodic reorientation. Homogenisation ratios keep decreasing until both adaptive and periodic schemes converge in terms of homogenisation time. Examination of Figure 3.2a reveals a narrow strip without any heating rate enhancement with the adaptive scheme. The adaptive reorientation protocol identifies the periodic schemes inside this strip, resulting in the same homogenisation rates (i.e. $\chi = 1$). This implies that the periodic schemes are “optimal” (according to (2.47)) inside the narrow strip. Identification of periodic schemes by the adaptive reorientation protocol shows that the periodic reorientation schemes also have some (limited) resilience to parameter perturbations in both τ and Pe. The same periodic reorientation protocol is namely found for different τ and Pe.

Heating is significantly promoted outside the strip by the adaptive schemes. To clarify this enhancement in homogenisation rate, the parameter space is partitioned, based on the relative improvement of the homogenisation ratio defined by $\chi_r = (1-\chi^{-1}) \times 100$ %, into regions where $0 \leq \chi_r < 5\%$ (blue), $5 \leq \chi_r < 15\%$ (green), $15 \leq \chi_r < 30\%$ (orange) and $\chi_r \geq 30\%$ (red). Results are shown in Figure 3.2b. A narrow band without any improvement ($0 \leq \chi_r < 5\%$; blue) is clearly visible in Figure 3.2b. This band coincides with the aforementioned strip where both the adaptive and periodic reorientation schemes are the same, which yields the same homogenisation time (i.e. $\chi = 1$ and thus $\chi_r = 0$ %). Here the adaptive protocol fails to accelerate the homogenisation rate while it significantly enhances heating by more then 15 % in a large portion of the considered parameter space. Homogenisation rates χ progressively improve for increasing τ as the adaptive reorientation schemes start to diverge from the periodic reorientation schemes.

Four parameter sets are selected (each associated with a χ_r subspace in Figure 3.3) to investigate the dependence of dynamic behaviour on τ (labelled a through d in Figure 3.2). A relative improvement in homogenisation rate of $\chi_{r,a} = 50.1$ %, $\chi_{r,b} = 20.4$ %, $\chi_{r,c} = 9.6$ % and $\chi_{r,d} = 0$ % can be found in a, b, c and d, respectively. Note that even the (relatively) small improvement in c can translate into a potentially significant reduction of the fluid heating time in (industrial) applications of interest. For example, the adaptive scheme accelerates heating by several hours relative to the periodic scheme. The periodic scheme typically achieves homogenisation in several tens of hours on the experimental RAM in [17]. Heating with a typical micro-mixer (i.e. having a characteristic length of $100\ \mu m$ with characteristic fluid velocity $1\ mm/s$ according to Reference [80]) would be accelerated by several seconds relative to the several tens of seconds in which a periodic reorientation scheme would achieve homogenisation. Figure 3.3a shows that adaptive schemes with $\chi_r \geq 15$ % (i.e. parameter set a and b) activate the exact opposite sequence of (periodic) reorientations (e.g. $\mathcal{U}_{\mathcal{T}} = \{3, 2, 1\}$). In addition, both schemes for set a and b show an initial transient that deviates from the rest of the reorientation scheme. This behaviour characterizes most adaptive schemes, with high relative improvements, found outside the strip in Figure 3.2a. Prolonged activation of the same flow field for consecutive activation steps in reorientation schemes, associated with sets a and b, decreases as the activation time τ increases.

The reorientation schemes associated with both c and d are completely periodic. However, the reorientation scheme associated with set c shows a minor deviation in its reorientation scheme (i.e. $\mathcal{U}_{\mathcal{T}} = \{1, 2, 2, 3, 1, 2, 3, 3\}$) compared to the periodic scheme. This small deviation has a relatively small impact on the ho-

(a) Reorientation schemes.

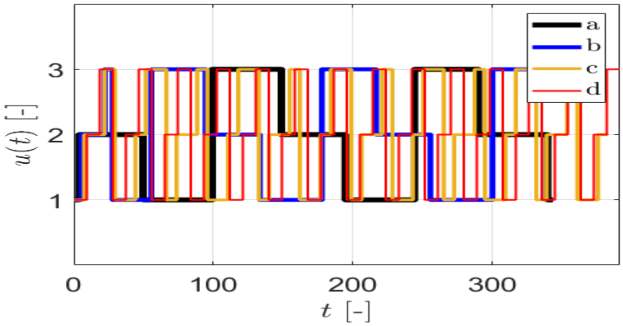

(b) Cost function.

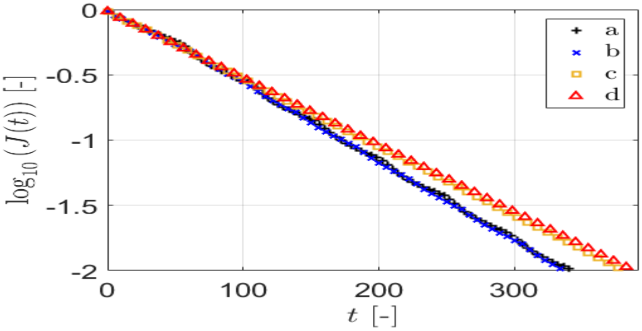

Figure 3.3: The (a) adaptive reorientation schemes and (b) the transient field associated with the selected points a, b, c and d in Figure 3.2.

mogenisation rate. This is clearly seen in Figure 3.3b as the adaptive scheme in c reaches 99 % homogeneity after $t_{\varepsilon,a} = 380$ time units as opposed to $t_{\varepsilon,a} = 388$ time units (only a 2 % deviation with respect to the adaptive (periodic) scheme in d). Furthermore, the similar $t_{\varepsilon,a}$ for a and b in Figure 3.3b implies that the deterioration of χ in the transition zone (observed in Figure 3.1b) is due to improved heating with the periodic scheme as homogenisation times for adaptive schemes vary only slightly.

The four parameter sets (indicated in Figure 3.2a) are studied further by investigating the temporal snapshots of the temperature field in Figure 3.4 to understand the dynamic behaviour associated with the schemes. The difference in homogenisation rate primarily occurs at the start of an activation. Hence, the initial transient temperature snapshots are of particular interest (i.e. for $t_n \leq 100$). Snapshots for the adaptive scheme in Figure 3.4(a)-(d) reveal why heat transfer from the boundary is promoted for sets a and b compared to sets c and d. Heat is circulated less effectively into the cold flow interior for prolonged activation of

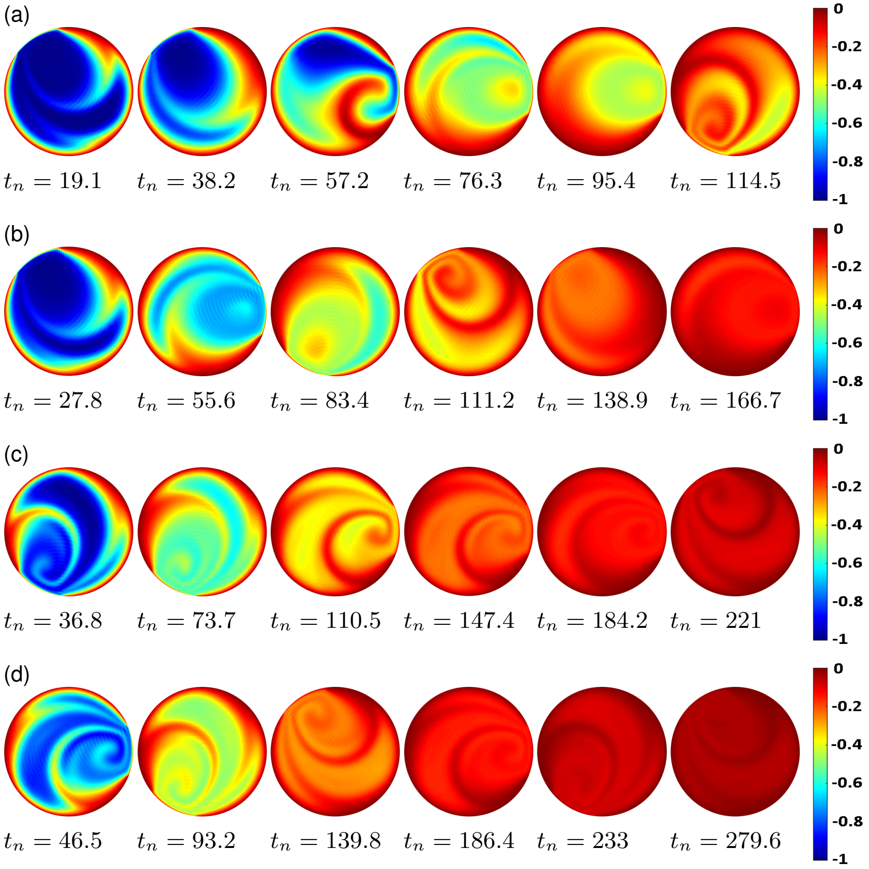

Figure 3.4: Temporal snapshots of the transient temperature field $\widetilde{T}(\boldsymbol{x}, t)$ for an advection dominated flow with $Pe = 2249$ at points a (top row), b (second row), c (third row) and d (fourth row) in Figure 3.2 (blue: $\min(\widetilde{T}(\boldsymbol{x}, t)) = -1$; red: $\max(\widetilde{T}(\boldsymbol{x}, t)) = 0$).

the flow fields in sets c and d. Heat transport seems to remain confined at the circumference, for sets a and b, as the fluid temperature remains lower in the flow interior than in close proximity to the boundary, compared to sets c and d. This is especially visible in the first few transient temperature field snapshots in Figure 3.4. Prolonging the aperture activation – viz. beyond d – has a detrimental effect on the homogenisation times as can be seen in Figure 3.1a. This observation is in line with the observations made in Chapter 2 (i.e. effective heat transport by flow circulation is confined to short-lived time windows after flow activation). The snapshots for d (i.e. the periodic scheme) in Figure 3.4(d) reveal a "pattern", which is described by the dominant eigenmode in the spectral decomposition of the temperature field analogous to (2.6) [17], that reorients with the activated flow field. This spatial pattern for set d remains mostly preserved in c despite a minor alteration in its reorientation scheme compared in Figure 3.4(c). The persistence of this pattern regardless of this minor alteration in the reorientation scheme explains the relatively small improvement in homogenisation rate from set c to set d observed in Figure 3.3b.

3.3 Conclusions and discussion

Heat transfer into an initially cold fluid from a hot boundary is influenced by both fluid and flow parameters. The numerical study of heat transport in Chapter 2 has shown that flow field reorientations, obtained with an adaptive flow reorientation protocol, can significantly improve heat transport compared to a conventional periodic reorientation protocol for a large span of these parameters. This chapter again investigates the adaptive reorientation protocol on the same case-study as in Chapter 2; the Rotated Arc Mixer (RAM). However, the adaptive reorientation protocol is restricted in the numerical study in this chapter to circulation of the fluid in a single direction. This is contrary to the study in Chapter 2, where the adaptive reorientation protocol can circulate the fluid in two direction. Numerical results show that the adaptive reorientation protocol can still accomplish a systematic improvement over a large span of fluid and flow parameters despite the restriction. Numerical results reveal improved resilience against parameter deviations with the adaptive schemes, while simultaneously ensuring faster heating. Adaptive schemes achieve this by either i) (slightly) altering the conventional periodic reorientation scheme or ii) introducing an aperiodic transient.

Future work should extend the analysis in this chapter by evaluating homogenisation rates for different numbers of apertures. Such an extension can determine the impact of fluid circulation in a single direction on scalar transport with the adaptive protocol. Future efforts should be directed towards experimental investigations of the adaptive reorientation protocol, determination of the spectral decomposition from CFD/experimental data using e.g. Dynamic Mode Decomposition (DMD), dedicated observer design for transient field estimation in experiments and control synthesis for further enhancement of scalar transport.

CHAPTER 4

Boosting heating with flow regulation based on Lyapunov functions

Abstract - *Transport of scalars, in the form of heat or chemicals, by fluid flow is a key feature for the effective operation of applications that range from thermal processing of foodstuffs via chemical species mixing to subsurface resource extraction. Therefore, enhancing the transport of these scalars in(to) a fluid will prove beneficial to a large variety of industries. The industrial applications of interest involve scalar transfer from the boundary and have a substantial influence of diffusion and/or chemical reactions which can both significantly influence heat/-chemical transport. In this chapter we propose a bang-bang controller and a nonlinear quadratic feedback controller to rapidly heat and homogenize a scalar field by reorienting a laminar Stokes flow. The general idea of these controllers is that influencing heating rates by fluid flow is analogous to controlling the flow based on a suitable Lyapunov function. The heating rates obtained by the two controllers are theoretically and numerically investigated for a heat-transfer case-study that is representative for the applications of interest; boosting boundary heating of a cold fluid by stirring. Numerical results show that the proposed controllers improve heating rates in the case-study by upto* 78 *% compared to mere diffusive heating and* 13 *% compared to an optimized conventional periodic scheme.*

The contents of this chapter is an extension of: R. Lensvelt, M.F.M. Speetjens and H. Nijmeijer "Lyapunov-based temperature regulation by flow reorientation". In: *19th European Control Conference*, Delft, The Netherlands. Supplementary material is provided in Appendices B and C.

4.1 Introduction

Transport of scalars, as either heat or chemicals, by fluid flows is a key feature to the effective operation of various applications. These applications are diverse and range from bioreactors for pollutant treatment [81], (micro)fluidic devices for fluid heating/mixing [82] or thermal processing of foodstuffs [2]. A common feature amongst the mentioned applications is that fluids are stirred (e.g. induced by rotating baffels or pumps) to accelerate scalar transport. This immediately raises the key question central to this chapter: “How to stir a fluid to accelerate transport?”.

The conventional approach to accelerate scalar transport relies heavily on periodic stirring strategies. Such strategies are tailored towards efficient fluid mixing by achieving “chaotic advection” [6]. The rationale for periodic stirring approaches is that fluid mixing automatically accelerates scalar transport. Numerous computational studies have been performed, which attempt to boost heating/mixing for periodic approaches. For example, DAllesandro et al. [83] determined which periodic sequence of flows maximizes entropy in the egg-batter flow. Omari and Guer [59] determined which periodic stirring protocol maximizes heating in a two-rod mixer. Lester et al. [16] optimized a periodic stirring protocol based on the decay rate of the dominant eigenmode of the Rotated Arc Mixer (RAM). Results showed that heating rates of periodic flows depend on both the stirring sequence and the system parameters. Gubanov and Cortelezzi [60] showed that periodic stirring is highly susceptible to perturbations in the initial conditions (ICs). Periodic stirring protocols, which are optimized for effective mixing, were found to be effective only if diffusion is negligible (i.e. for sufficiently high Péclet numbers $Pe \gtrsim \mathcal{O}(10^4)$) [24]. Moreover, aperiodic fluid forcing has been found to boost heating/mixing rates beyond those accomplished with periodic stirring protocols [21, 23]. However, transport studies for (a)periodic stirring have typically focussed on systems without scalar flux across the boundary (i.e. the scalar remains conserved due to an adiabatic boundary) [21, 83, 23, 61, 16, 24]. Scalar transport in systems that contain scalar boundary fluxes (via a non-adiabatic boundary condition) have received considerably less attention [59, 58, 55]. The above highlights the inherent issues associated with (a)periodic stirring. First, *a priori* design limits the amount of stirring sequences and can thus lead to suboptimal transport enhancement. Moreover, open-loop flow control using an *a priori* designed (a)periodic protocol makes fluid heating sensitive to disturbances if they were not considered during the design. Second, periodic stirring protocols are typically designed without considering either diffusion or scalar transport via a non-adiabatic boundary.

Scalar transport is typically described by the advection-diffusion equation (ADE) in the abovementioned applications. The ADE represents an infinite dimensional bilinear system for which numerous control techniques are available. They range from optimal control [61, 81, 84, 85, 86], backstepping control [87, 88, 89, 90] and Lyapunov-based boundary control [32] to (quadratic) state feedback control [91, 92]. However, scalar transport can only directly be influenced by the fluid flow in the applications of interest. The bilinear nature of the ADE makes flow control based on quadratic state feedback control of particular interest here. Quadratic feedback control of (in)finite dimensional bilinear systems has been well researched since the late 70s [93]. Such feedback laws, with(out) input constraints, have been studied to ensure weak or strong stability in bilinear systems with bounded input operators of finite [94, 95, 96] and infinite dimension [93, 97, 98]. Quadratic feedback has also been used to stabilize the unstable heat equation with scalar control [99, 98]. However, control of bilinear systems has primarily focussed on finding sufficient conditions to ensure stabilization. In this chapter we use quadratic feedback and/or bang-bang control to boost scalar transport of heat transfer/mixing problems. In [58], we designed a bang-bang controller and nonlinear controller based on a Lyapunov function containing the instantaneous temperature field. The controllers actuate the flow fields based on the temperature field (gauged through a Lyapunov function) in order to boost fluid heating. The proposed flow controllers showed i) rapid transfer of a scalar into a fluid via a non-adiabatic boundary and ii) the spread of the scalar distribution throughout the fluid.

The main objective of this chapter is to boost fluid heating with closed-loop flow control. In [55], Chapter 2 and Chapter 3, we proposed a flow controller that selects the optimal fluid stirring over a single time step from among a finite set of stirring options. This makes heating rates dependant on both the considered stirring options and the prediction time step. The controllers in this chapter do not possess such dependencies since the fluid flows are controlled on the basis of a (quadratic) feedback law. Moreover, the controllers in this chapter can continuously and simultaneously stir the fluid. In this chapter, we numerically investigate the dynamic behaviour associated with improved heat transport by these methods. In addition, a theoretical analysis is performed to determine what improvements in heating rate can be expected with these controllers. Performance of these controllers is investigated on a $2D$ thermal flow system: the $2D$ Rotated Arc Mixer [12]. In the RAM, fluids are heated from an initially low temperature to a homogeneous higher temperature. Heat transport is “driven” by steady laminar fluid flows, which differ from each another by at most a reorientation. Heat (or scalar) transport driven by reorienting flow fields make the RAM a representative system to the abovementioned applications of interest. Two features that distinguish the investigated system from those in conventional mixing studies are the presence of both i) significant diffusion ($Pe \sim \mathcal{O}(10^3)$) and ii) scalar transfer from the boundary into the domain.

This chapter is structured as follows. In Section 4.2, the model and resulting system description we use to study heat-transfer regulated by fluid flows is presented. In Section 4.3, we express the control objective and formulate two controllers to accomplish it based on a Lyapunov function. In Section 4.5, we present the simulated behaviour of the case study and discuss the characteristic behaviour associated with control. Finally, conclusions and recommendations for further design and practical implementation are presented in Section 4.6.

4.2 Heat-transfer driven by reoriented flows

4.2.1 Representative case study

In this work, heat transport in a fluid is investigated in a two-dimensional (2D) circular container $\mathcal{D}$ with a radius R. Three-dimensional effects are therefore neglected and thus limit the current study. The proposed controllers (see Section 4.3.4) are investigated on the $2D$ Rotated Arc Mixer (RAM) [12]. The RAM consists of a $2D$ circular container $\mathcal{D} = \left\{(r, \theta) \in \mathbb{R}^2 | r \leq R, -\pi \leq \theta \leq \pi\right\}$ of radius $R = 1$ that contains a fluid. This container holds an initially cold fluid. The fluid is enclosed by a hot boundary $\partial\mathcal{D}$ at constant temperature. There are I apertures in the circumference $\partial\mathcal{D}$. Each of these apertures has an opening angle Δ. The apertures have an angular offset along the circumference of $\Theta = 2\pi/I$. A schematic representation of the RAM is shown in Figure 4.1.

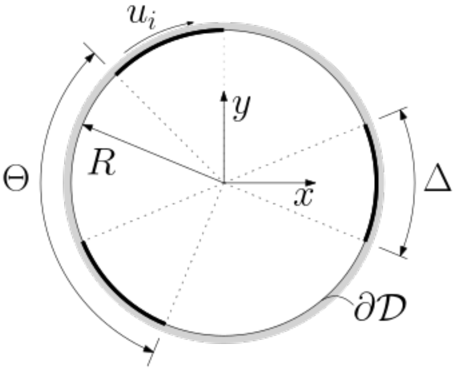

Figure 4.1: Schematic representation of the 2D Rotating Arc Mixer (RAM) used to study the proposed heating methods.

The apertures are covered by sliding belts in the $2D$ RAM. Belt motion along the apertures thus creates moving boundary segments or “moving arcs”. These moving arcs induce a flow inside the container by viscous drag. The fluid is assumed viscous enough such that inertia can be neglected. Numerical simulation times are sufficiently large to ensure that the fluid’s response to a moving boundary segment can be considered instantaneous. Therefore, activation of each moving arc results in a Stokes flow. In addition, the rotation symmetry between apertures directly transfers to the fluid flow. This means each flow is a mere reorientation of the base flow (at $\Theta = 0$) following (4.2). The analytical expression for the base flow can be found in Hwu [70].

4.2.2 Thermal flow problem

Control of fluid heating inside the fluid container would typically involve influencing the temperature field by either adjusting the boundary temperature of the container or controlling heating/cooling actuators inside the fluid. However, our interest is in heat-transfer problems without any sources/sinks inside the container or at the boundary to directly influence the temperature field. Heat transport throughout the container is captured by the non-dimensional advection-diffusion equation (ADE) defined as [55]

$$\frac{\mathrm{d}T(\boldsymbol{x},t)}{\mathrm{d}t} = -\sum_{i=1}^{I} \boldsymbol{v}_i(\boldsymbol{x},t)\cdot\boldsymbol{\nabla}T(\boldsymbol{x},t) - \boldsymbol{\nabla}\cdot\boldsymbol{q}(\boldsymbol{x},t), \quad \boldsymbol{q} = -Pe^{-1}\boldsymbol{\nabla}T(\boldsymbol{x},t), \tag{4.1}$$

with T the temperature field, $\boldsymbol{v}_i$ the ith fluid flow field of in total I flow fields, $\boldsymbol{\nabla}$ the gradient operator and $Pe = UR/\nu$ the Péclet number (with U the characteristic velocity and ν the thermal diffusivity of the fluid). The right hand side terms in (4.1) describe (from left to right) heat transport by advection (or convection) and diffusion (or conduction). Heating and, more importantly, heat transport can thus only be influenced in (4.1) by altering the fluid flow(s) $\boldsymbol{v}_i$. Flows $\boldsymbol{v}_i$ are considered solenoidal as mass is conserved and density is independent of T inside the container (i.e. the considered flow fields are divergence-free and satisfy $\boldsymbol{\nabla}\cdot\boldsymbol{v}_i = 0$). We consider sufficiently slow flow velocities and negligible fluid inertia so that the flow field approaches the Stokes limit and instantaneously starts upon activation of a wall. The considered Stokes flows consist of reorientations of a normalized base flow $\boldsymbol{w}$ which is defined as

$$\boldsymbol{v}_i(\boldsymbol{x},t) = u_i(t)\boldsymbol{w}(\mathcal{R}_i(\boldsymbol{x})) = u_i(t)\boldsymbol{w}(r,\theta+(i-1)\Theta), \quad i = 1,\ldots,I, \tag{4.2}$$

with (r,θ) the polar coordinates, $\Theta = 2\pi/I$ the rotation angle of each flow and $u_i(t)$ the inputs. The sign of these inputs indicates the direction of fluid circulation while the magnitude determines the scaling with respect to base flow $\boldsymbol{w}$. The individual inputs are constrained to $u_i(t) \in [-1,1]$. Moreover, these Stokes flows can be defined according to (4.2) due to the presence of rotation symmetries between each fluid flow $\boldsymbol{v}_i$. The cold fluid inside the container is heated by a hot circumference $\partial\mathcal{D}$ at a constant temperature T_∞ captured by

$$T(\boldsymbol{x},0) = T_0(\boldsymbol{x}) \qquad T(\boldsymbol{x},0)|_{\partial\mathcal{D}} = T_\infty, \tag{4.3}$$

with $\boldsymbol{x}$ a position inside the container $\mathcal{D}$. The initial condition is limited to $T_0(\boldsymbol{x}) < T_\infty$ for all $\boldsymbol{x} \in \mathcal{D}$ to ensure heating occurs. The fluid temperature (T) is normalized between the initial (T_0) and the boundary temperature (T_∞) such that $0 \leq T(\boldsymbol{x},t) \leq 1$.

4.2.3 Bilinear state-space representation of heating

The ADE in (4.1) is discretized in space in order to numerically investigate heat transport inside the container. To this end we employ the spectral method by Lester et al [16]. The transient temperature field can be approximated by the L

most dominant Laplacian eigenfunctions as [16]

$$\widetilde{T}\left(\boldsymbol{x},t\right) \equiv T\left(\boldsymbol{x},t\right) - T_{\infty} \approx \sum_{\ell=1}^{L} \phi_{\ell}\left(\boldsymbol{x}\right)\eta_{\ell}(t), \tag{4.4}$$

with $\widetilde{T}\left(\boldsymbol{x},t\right)$ the transient temperature field and $(\phi_{\ell},\lambda_{\ell})$ the eigenfunction-eigenvalue pairs to $-\boldsymbol{\nabla}^2\phi_{\ell} = \lambda_{\ell}\phi_{\ell}$ for all ℓ on $\mathcal{D}$ (see (B.1)). The evolution of the spectral coefficients associated with these eigenfunctions can then be described as [16]

$$\frac{\mathrm{d}\boldsymbol{\eta}(t)}{\mathrm{d}t} = \left(\sum_{i=1}^{I} u_i\left(t\right)\boldsymbol{H}_i + \frac{1}{Pe}\boldsymbol{D}\right)\boldsymbol{\eta}(t), \tag{4.5}$$

with $\boldsymbol{\eta}\left(t\right) \in \mathbb{R}^{L}$ the spectral coefficient vector, $\boldsymbol{D} \in \mathbb{R}^{L\times L}$ a diagonal matrix and $\boldsymbol{H}_i \in \mathbb{R}^{L\times L}$ a skew-symmetric matrix (i.e. ${\boldsymbol{H}_i}^{\dagger} = -\boldsymbol{H}_i$) associated with each flow field $i \in \{1,\ldots,I\}$ with inputs u_i from (4.2) indicated by subscripts i. Note that orthonormality of ϕ_{ℓ} under the L^2 norm combined with the second law of thermodynamics assures that $\boldsymbol{D}$ is a diagonal Hurwitz matrix containing the Laplacian eigenvalues $\lambda_{\ell} \leq 0$. Heat transport dynamics expressed in the spectral coefficients accommodate real-time thermal control by enabling fast computation. The obtained state-space description in (4.5) is known as a bilinear system, because of the linear combination of the inputs $u_i(t)$ with the states $\boldsymbol{\eta}$. The description in (4.5) provides access to a large variety of control methodologies [100]. However, the presented fluid container limits heat-transfer studies to a circular $2D$ domain. This geometry is encountered in a wide range of applications in practice though (e.g. in $3D$ RAM [101] or stirred reactor tanks [102]). In addition, the state-space description in (4.5) applies to other simple $2D$ container geometries as well [16].

4.3 Flow control to boost heating

The main objective of this work is to heat an initially cold fluid $T_0\left(\boldsymbol{x}\right)$ to a homogeneous hot temperature field at T_{∞} as fast as possible. To this end stirring methods that accelerate fluid heating are investigated below.

4.3.1 Metrics for fluid heating

The bilinear representation in (4.5) enables fast computation of the temperature field. Fast numerical simulations are important to reduce delays due to computation. A sufficiently fast computation therefore allows for real-time control. The difference between the current fluid temperature and the hot boundary temperature is gauged from the transient temperature field defined according to (4.4). The L^2 norm of this transient temperature $\widetilde{T}$ is expressed in the spectral coefficients by

$$\begin{aligned} J_1(\boldsymbol{\eta}(t)) &= \frac{1}{\pi}\int_{\mathcal{D}} \widetilde{T}^2(\boldsymbol{x},t)\mathrm{d}\boldsymbol{x} = \frac{1}{\pi}\int_{\mathcal{D}} \boldsymbol{\eta}^\dagger(t)\boldsymbol{\varphi}^\dagger(\boldsymbol{x})\boldsymbol{\varphi}(\boldsymbol{x})\boldsymbol{\eta}(t)\mathrm{d}\boldsymbol{x}, \\ &= \frac{1}{\pi}\boldsymbol{\eta}^\dagger(t)\boldsymbol{P}_1\boldsymbol{\eta}(t) = \frac{1}{\pi}\|\boldsymbol{\eta}(t)\|_2^2, \end{aligned} \tag{4.6}$$

with $\boldsymbol{P}_1 = \boldsymbol{I}$ due to orthonormality of the eigenfunctions and where $\boldsymbol{I} \in \mathbb{R}^{L\times L}$ the identity matrix and $\|\boldsymbol{\eta}(t)\|_2^2 = \eta_1^2(t) + \eta_2^2(t) + \ldots$ the vector 2-norm of $\boldsymbol{\eta}$. Time-dependency of $\boldsymbol{\eta}$ is hereafter omitted for notational convenience.

Fluids are considered sufficiently heated when $J_1(\boldsymbol{\eta})$ satisfies

$$J_1(\boldsymbol{\eta}) \leq \sigma, \tag{4.7}$$

where $\sigma = \varepsilon^2$. Relation (4.6) captures the "thermal distance" till equilibrium inside $\mathcal{D}$. In Chapter 2, the cost function $J_1(\boldsymbol{\eta})$ was shown to capture the two key aspects relate fluid heating. Fluid heating requires, first, heat to be transferred into a fluid (denoted as energization). And second heat needs to be transported throughout the fluid (homogenization).

Minimizing $J_1(\boldsymbol{\eta})$ as fast as possible requires a minimization of its decay rate. The decay rate $\mathrm{d}J_1(\boldsymbol{\eta})/\mathrm{d}t$ can readily be obtained from a time derivative of (4.6). The decay rate of $J_1(\boldsymbol{\eta})$ combined with (4.1) results in

$$\begin{aligned} \frac{\mathrm{d}J_1(\boldsymbol{\eta})}{\mathrm{d}t} &= -\frac{1}{\pi}\left(\dot{\boldsymbol{\eta}}^\dagger\boldsymbol{\eta} + \boldsymbol{\eta}^\dagger\dot{\boldsymbol{\eta}}\right) \\ &= \frac{2}{\pi Pe}\boldsymbol{\eta}^\dagger\boldsymbol{D}\boldsymbol{\eta} + \frac{1}{\pi}\sum_{i=1}^{I} u_i\boldsymbol{\eta}^\dagger\left(\boldsymbol{H}_i{}^\dagger\boldsymbol{P}_1 + \boldsymbol{P}_1\boldsymbol{H}_i\right)\boldsymbol{\eta}. \end{aligned} \tag{4.8}$$

The advection matrices $\boldsymbol{H}_i$ are skew-symmetry, which means that the inputs u_i therefore disappear from (4.8) for $\boldsymbol{P}_1 = \boldsymbol{I}$. In this case the heating rate in (4.12) reduces to

$$\frac{\mathrm{d}J_1(\boldsymbol{\eta})}{\mathrm{d}t} = \frac{2}{\pi Pe}\boldsymbol{\eta}^\dagger\boldsymbol{D}\boldsymbol{\eta}. \tag{4.9}$$

Relation (4.9) expresses (2.37) in spectral coefficients $\boldsymbol{\eta}$. Rate J_1 in (4.9) in spectral coefficients is negative due to negative definiteness of $\boldsymbol{D}$. Negative definiteness of $\boldsymbol{D}$ implies that (4.5) is stable regardless of the fluid flow. As a consequence the state $\boldsymbol{\eta}$ converges to the origin as $t \to \infty$. This implies that (4.5) is asymptotically stable in that case. The decay rate of the thermal energy in (4.9) reveals that i) (4.1) is always stable for $Pe > 0$ and ii) fluid flow indirectly influences (4.6). The former is a direct consequence of the Second law of Thermodynamics. Heat transfer $\boldsymbol{q}$ always acts in the opposite direction to a temperature gradient for $Pe \geq 0$. As a consequence, the transient temperature is ensured to decay along state trajectories $\widetilde{T}$. This occurs for arbitrary inputs since $\mathrm{d}J_1(\boldsymbol{\eta})/\mathrm{d}t < 0$ for any $\widetilde{T} \neq 0$ based on (4.9). Thermal control therefore only focusses on accelerating the transition towards a homogeneous hot fluid in this work. However, a direct relation between the fluid flow and the heating rate $\mathrm{d}J_1(\boldsymbol{\eta})/\mathrm{d}t$ is absent in (4.9). Further analysis of (4.6) revealed that fluid deformation by induced flow fields serve as the "thermal actuators" [55]. Fluid flows accelerate/decelerate fluid heating (i.e. $u_i(t)$ influences $\mathrm{d}^2J_1(\boldsymbol{\eta})/\mathrm{d}t^2$ directly). Direct influence of the heating rate $\mathrm{d}J_1(\boldsymbol{\eta})/\mathrm{d}t$ is preferred for control, however. A methodology that ensures the direct influence of the fluid flow on the heating rate is presented next.

4.3.2 Heating metrics as Lyapunov function candidates

The cost-function $J_1(\boldsymbol{\eta})$ in (4.6) is convex in $\boldsymbol{\eta}$ since $J_1(\boldsymbol{\eta})$ can be expressed as the vector 2-norm of $\boldsymbol{\eta}$. A generic heating metric, other than $J_1(\boldsymbol{\eta})$, should also possess this property, since convex cost functions simplify the analysis of optimal heating considerably. The rationale for this is that local minima are absent in a convex function [103]. Showing the cost function decays relies solely on a functions' decay rate in this case (e.g. $\mathrm{d}J_1/\mathrm{d}t < 0$ for any $\boldsymbol{\eta} \neq \mathbf{0}$ means that $J_1(\boldsymbol{\eta})$ always decreases). The general form of these convex functions is defined as

$$J_4(\boldsymbol{\eta}) = \frac{1}{\pi}\boldsymbol{\eta}^\dagger \boldsymbol{P}_4 \boldsymbol{\eta}, \tag{4.10}$$

for $\boldsymbol{P}_4$ a positive definite matrix. Positive definiteness of the matrix is denoted by $\boldsymbol{P}_4 \succ 0$ in this work. Functions of the form (4.10) can be regarded as potential Lyapunov function candidates if they satisfy [75]

$$J_4(0) = 0 \text{ iff } \boldsymbol{\eta} \equiv \mathbf{0}, \quad J_4(\boldsymbol{\eta}) = \frac{1}{\pi}\boldsymbol{\eta}^\dagger \boldsymbol{P}_4 \boldsymbol{\eta} > 0 \text{ in } \mathcal{H} - \{\mathbf{0}\}, \tag{4.11}$$

for $\mathcal{H} \subset \mathbb{R}^L$. The cost functions in (4.10) clearly satisfy (4.11) for $\boldsymbol{P}_4 \succ 0$. The substitution of $\boldsymbol{P}_4 = \boldsymbol{I}$ following (4.10) reveals that $J_1(\boldsymbol{\eta})$ is also of the form (4.10). It therefore satisfies the condition in (4.11) as well. The cost function J_1 can thus be regarded as a Lyapunov function. Functions of the form (4.10) are radially unbounded for positive definite $\boldsymbol{P}_4$ (i.e. $J_4(\boldsymbol{\eta}) \to \infty$ as $\|\boldsymbol{\eta}\|_2 \to \infty$). Radial unbounded functions are typically used to ensure global asymptotic convergence.

The utility of J_4 becomes clear upon evaluating its evolution. The time derivative of (4.10), combined with (4.5), is expressed as

$$\begin{aligned} \frac{\mathrm{d}J_4(\boldsymbol{\eta})}{\mathrm{d}t} &= \frac{1}{\pi}\left(\dot{\boldsymbol{\eta}}^\dagger \boldsymbol{P}_4 \boldsymbol{\eta} + \boldsymbol{\eta}^\dagger \boldsymbol{P}_4 \dot{\boldsymbol{\eta}}\right) \\ &= \frac{1}{\pi Pe}\boldsymbol{\eta}^\dagger \left(\boldsymbol{D}^\dagger \boldsymbol{P}_4 + \boldsymbol{P}_4 \boldsymbol{D}\right)\boldsymbol{\eta} + \frac{1}{\pi}\sum_{i=1}^{I} u_i \boldsymbol{\eta}^\dagger \boldsymbol{Q}_i \boldsymbol{\eta} \end{aligned} \tag{4.12}$$

where

$$\boldsymbol{Q}_i = \boldsymbol{H}_i{}^\dagger \boldsymbol{P}_4 + \boldsymbol{P}_4 \boldsymbol{H}_i, \tag{4.13}$$

with $\boldsymbol{Q}_i$ an indefinite matrix. Matrix $\boldsymbol{Q}_i$ is neither positive definite nor negative definite and thus $\boldsymbol{\eta}^\dagger \boldsymbol{Q}_i \boldsymbol{\eta}$ can be either positive *or* negative. The switching functions $\boldsymbol{\eta}^\dagger \boldsymbol{Q}_i \boldsymbol{\eta}$ can thus change sign due to the indefiniteness of $\boldsymbol{Q}_i$ (i.e. $\boldsymbol{\eta}^\dagger \boldsymbol{Q}_i \boldsymbol{\eta}$ can be either positive or negative for non-trivial $\boldsymbol{\eta}$). The indefiniteness of $\boldsymbol{Q}_i$ plays a crucial role in the controllers designed in this work (see Section 4.3.4 and Section 4.5.3). The advection matrices $\boldsymbol{H}_i$ are skew-symmetry, which means that $\boldsymbol{Q}_i = \boldsymbol{0}$ if $\boldsymbol{P}_4 = \boldsymbol{P}_1 = \boldsymbol{I}$. The inputs u_i therefore vanish in (4.12) (see Section 4.3.1). However, inputs u_i remains explicitly present in heating rate $\mathrm{d}J_4(\boldsymbol{\eta})/\mathrm{d}t$ for $\boldsymbol{P}_4 \neq \boldsymbol{I}$. Inputs u_i and $\boldsymbol{P}_4$ that render $\mathrm{d}J_4(\boldsymbol{\eta})/\mathrm{d}t$ negative imply that (4.5) are asymptotically stable. In such a case, $J_4(\boldsymbol{\eta})$ represents a Lyapunov function. Inputs u_i and $\boldsymbol{P}_4$ that yield a positive heating rate ($\mathrm{d}J_4(\boldsymbol{\eta})/\mathrm{d}t > 0$) imply instability of (4.5). This would imply that the fluid flow transports heat from the cold fluid to the hot boundary and thus violates the Second Law of Thermodynamics. Hence, inputs u_i and $\boldsymbol{P}_4$ that render (4.12) positive are meaningless to adequately describe heating.

4.3.3 Link with boosting heat transport

The design the matrix $\boldsymbol{P}_4$ with $\boldsymbol{P}_4 \neq \boldsymbol{I}$ allows for the *direct* influence of the heating rate by inputs u_i according to (4.12). Solutions to the Lyapunov inequality (i.e. $\boldsymbol{D}^\dagger \boldsymbol{P}_4 + \boldsymbol{P}_4 \boldsymbol{D} \preceq -\boldsymbol{Q}$) exist if and only if $\boldsymbol{D}$ is Hurwitz [75]. Matrix $\boldsymbol{D}$ contains the eigenvalues of the Laplacian and is thus Hurwitz. The solution to the Lyapunov equation is diagonal for the diagonal $\boldsymbol{D}$ if $\boldsymbol{Q}$ is also diagonal. The matrix $\boldsymbol{Q}$ can be arbitrarily *chosen* as long as it is positive definite. Therefore, the simple matrix $\boldsymbol{Q} = \boldsymbol{I}$ is adopted here. Solving the Lyapunov equality results in a unique solution for $\boldsymbol{P}_4$ as

$$\boldsymbol{P}_4 = -\frac{1}{2}\boldsymbol{D}^{-1}, \tag{4.14}$$

The inequality is used to design a $\boldsymbol{P}_4$ based on a $\boldsymbol{Q}$. The above solution provides the link between $J_4(\boldsymbol{\eta})$ and $J_1(\boldsymbol{\eta})$. This can be observed by combining the cost function in (4.10) with (4.14) such that

$$J_4(\boldsymbol{\eta}) = \frac{1}{\pi}\boldsymbol{\eta}^\dagger \boldsymbol{P}_4 \boldsymbol{\eta} = \sum_{\ell=1}^{L} -\frac{1}{2\pi D_{\ell\ell}}\eta_\ell^2 = \frac{1}{\pi}\int_{\mathcal{D}} \Gamma^2(\boldsymbol{x},t)\mathrm{d}^2\boldsymbol{x}, \tag{4.15}$$

where

$$\Gamma(\boldsymbol{x},t) = \sum_{\ell=0}^{L} \alpha_\ell \phi_\ell(\boldsymbol{x})\eta_\ell(t), \tag{4.16}$$

for $\alpha_\ell = \sqrt{-1/\left(2\pi D_{\ell\ell}\right)}$. The “temperature” field Γ in (4.15) consists of eigenfunctions, which are scaled by their associated decay rate. Scaling each spectral coefficient according to (4.14) means the energy of each eigenfunction is weighed in $J_4(\boldsymbol{\eta})$. The solution (4.14) also implies that $J_4(\boldsymbol{\eta}) \leq J_1(\boldsymbol{\eta})$ since $|D_{\ell\ell}| > 1$.

Moreover, (4.15) reveals that (4.10) represents a similar, but not the same, measure as (4.6).

The abovementioned design of $\boldsymbol{P}_4$ ensures that the influence of the inputs on $\mathrm{d}J_4(\boldsymbol{\eta})/\mathrm{d}t$ is maintained. Proper design of $u_i(t)$ therefore needs to enforce $\mathrm{d}J_4(\boldsymbol{\eta})/\mathrm{d}t \leq 0$ for any non-trivial $\boldsymbol{\eta}$. Again, positive decay rates simply imply that cost function $J_4(\boldsymbol{\eta})$ is inadequate to describe heating. The heating rate in (4.12), with $\boldsymbol{P}_4$ according to (4.14), is described by

$$\frac{\mathrm{d}J_4(\boldsymbol{\eta})}{\mathrm{d}t} = -\frac{1}{\pi Pe}\|\boldsymbol{\eta}\|_2^2 + \frac{1}{\pi}\sum_{i=1}^{I} u_i \boldsymbol{\eta}^\dagger \boldsymbol{Q}_i \boldsymbol{\eta}, \tag{4.17}$$

for all $\boldsymbol{\eta}$ and where

$$\boldsymbol{Q}_i = \frac{1}{2}\left(\boldsymbol{H}_i{}^\dagger \boldsymbol{D}^{-1} + \boldsymbol{D}^{-1}\boldsymbol{H}_i\right), \tag{4.18}$$

following the substitution of (4.14) in (4.13). In the absence of any fluid flow (i.e $u_i = 0$) heat transport is governed by mere diffusion. In this case the heating rate (4.17) reduces to

$$\frac{\mathrm{d}J_{4,d}(\boldsymbol{\eta})}{\mathrm{d}t} = -\frac{1}{\pi Pe}\|\boldsymbol{\eta}\|_2^2, \tag{4.19}$$

where subscript “d” indicates diffusion. The design of u_i, viz. developing inputs that ensure $\mathrm{d}J_4(\boldsymbol{\eta})/\mathrm{d}t \leq 0$, needs to boost fluid heating compared to diffusion. Conditions for u_i that can boost heating are obtained by evaluating the difference between (4.17) and (4.19). The difference between $J_4(\boldsymbol{\eta})$ and $J_{4,d}(\boldsymbol{\eta})$ is called the Lyapunov control function and is defined as

$$E(\boldsymbol{\eta}) \equiv J_4(\boldsymbol{\eta}) - J_{4,d}(\boldsymbol{\eta}), \tag{4.20}$$

and its evolution is described by

$$\frac{\mathrm{d}E(\boldsymbol{\eta})}{\mathrm{d}t} = \frac{\mathrm{d}J_4(\boldsymbol{\eta})}{\mathrm{d}t} - \frac{\mathrm{d}J_{4,d}(\boldsymbol{\eta})}{\mathrm{d}t} = \frac{1}{\pi}\sum_{i=1}^{I} u_i \boldsymbol{\eta}^\dagger \boldsymbol{Q}_i \boldsymbol{\eta}. \tag{4.21}$$

Fluid heating is as fast as possible if u_i minimizes (4.17) as much as possible (i.e. u_i make $\mathrm{d}E(\boldsymbol{\eta})/\mathrm{d}t$ as small as possible). Rendering the evolution of the Lyapunov control function in (4.20) negative definite enforces negative definiteness of (4.17) as well. A proper design of u_i can guarantee that each component in the evolution of the Lyapunov control function remains negative definite. This will ensure that (4.21) is negative definite and thus that fluid heating is boosted with respect to diffusion (i.e. since $J_4(\boldsymbol{\eta})$ decays faster than $J_{4,d}(\boldsymbol{\eta})$). However, each $\boldsymbol{\eta}^\dagger \boldsymbol{Q}_i \boldsymbol{\eta}$ can change sign since each $\boldsymbol{Q}_i$ is indefinite. The property will prove vital in developing controllers that boost heating as will be shown in Section 4.3.4. In addition, the matrix $\boldsymbol{Q}_i$ is Hermitian (i.e. $\boldsymbol{Q}_i = \boldsymbol{Q}_i^\dagger$). This follows immediately from its definition and the abovementioned solution for $\boldsymbol{P}_4$ combined with the skew-symmetry of $\boldsymbol{H}_i$.

In practice, the combined flow field $\boldsymbol{v}$ will be driven externally by actuators. As a result, the inputs u_i are constrained. The kinetic energy associated with the fluid flow $\boldsymbol{v}$ depends on the scaling (u_i) of each $\boldsymbol{u}_i$ in (4.2). This energy contribution, due to fluid flow $\boldsymbol{v}$, is constrained by a threshold β. Most applications of interest circulate fluid by activating only a single flow at a time. Therefore, the kinetic energy associated with $\boldsymbol{v}$ is constrained by the kinetic energy of a single flow field. The kinetic energy of the combined flow field $\boldsymbol{v}\left(\boldsymbol{x}, t\right)$ is defined as

$$\begin{aligned}\frac{1}{2}\int_{\mathcal{D}} \boldsymbol{v}\left(\boldsymbol{x}, t\right)^{\dagger} \boldsymbol{v}\left(\boldsymbol{x}, t\right)\mathrm{d}^2\boldsymbol{x} &= \frac{1}{2}\int_{\mathcal{D}} \left(\sum_{i=1}^{I} \boldsymbol{v}_i\left(\boldsymbol{x}, t\right)\right)^{\dagger} \left(\sum_{i=1}^{I} \boldsymbol{v}_i\left(\boldsymbol{x}, t\right)\right)\mathrm{d}^2\boldsymbol{x}, \\ &\overset{(4.2)}{=} \frac{1}{2}\widetilde{\boldsymbol{u}}^{\dagger}\boldsymbol{R}\widetilde{\boldsymbol{u}} \leq \frac{1}{2}\int_{\mathcal{D}} \boldsymbol{w}\left(\boldsymbol{x}\right)^{\dagger} \boldsymbol{w}\left(\boldsymbol{x}\right)\mathrm{d}^2\boldsymbol{x} = \frac{1}{2}\beta,\end{aligned} \tag{4.22}$$

where $\widetilde{\boldsymbol{u}}^{\dagger} = \begin{bmatrix} u_1(t) & \cdots & u_I(t)\end{bmatrix}$ the input vector and $\boldsymbol{R} \in \mathbb{R}^{I\times I}$ the input weighing matrix. Constraint (4.22) will also ensure a fair comparison of heating rates for various amounts of active flow fields. The coefficients of the input weighing matrix $\boldsymbol{R}$ are defined as

$$R_{ij} = \int_{\mathcal{D}} \boldsymbol{w}\left(\mathcal{R}_i(\boldsymbol{x})\right)^{\dagger}\boldsymbol{w}\left(\mathcal{R}_j(\boldsymbol{x})\right)\mathrm{d}^2\boldsymbol{x}. \tag{4.23}$$

The weighing matrix $\boldsymbol{R}$ is a symmetric matrix with coefficients dependent on the angle Θ between flow fields. Moreover, the weighing matrix is positive definite by definition (i.e. kinetic energy is positive regardless of the input vector).

4.3.4 Controllers for boosting heating

4.3.4.1 Bang-bang controller

The above shows that inputs u_i should render (4.21) sufficiently negative in order for the fluid flow to improve heating with respect to diffusion (i.e. $\mathrm{d}E/\mathrm{d}t < 0$). A straightforward choice that ensures this strict requirement is bang-bang control defined as

$$u_i = \begin{cases} -k & \text{if } \boldsymbol{\eta}^{\dagger}\boldsymbol{Q}_i\boldsymbol{\eta} \geq 0, \\ k & \text{if } \boldsymbol{\eta}^{\dagger}\boldsymbol{Q}_i\boldsymbol{\eta} \leq 0 \end{cases} \tag{4.24}$$

where $k > 0$ the maximum actuation magnitude. The inputs in (4.24) enforce fluid circulation (i.e. $u_i \neq 0$ since $k \neq 0$). Such inputs ensure that $\mathrm{d}J_4/\mathrm{d}t < 0$ is satisfied until reaching the control objective (i.e. convergence to the origin $\boldsymbol{\eta} = \boldsymbol{0}$).

The discrete inputs of the bang-bang controller naturally raise questions on existence and uniqueness (or well-posedness) of the closed-loop state trajectories. Well-posedness is essential for the reliable operation of the controller in practice. Numerical solutions are shown to be well-posed by considering the closed-loop as a hybrid automaton. A detailed well-posedness analysis of a closed-loop with the bang-bang controller is provided in Appendix C.

The evolution of the Lyapunov control function associated with bang-bang control is investigated to judge its impact on heating. Combining (4.21) with (4.24) results in the evolution of the Lyapunov control function as

$$\frac{\mathrm{d}E(\boldsymbol{\eta})}{\mathrm{d}t} = -\frac{k}{\pi}\sum_{i=1}^{I}\left|\boldsymbol{\eta}^{\dagger}\boldsymbol{Q}_i\boldsymbol{\eta}\right|. \tag{4.25}$$

for the bang-bang controller. The Lyapunov control function (4.25) is negative semi definite for any positive actuation magnitude $k > 0$. Moreover, (4.25) shows that a high actuation magnitude maximizes the decay rate of Lyapunov control function most and thus accelerates heating most for this Lyapunov control function as a result. However, the maximum allowable actuation magnitude is limited to enforce the beforementioned constraint on kinetic energy. The constraint on kinetic energy therefore also limits the maximum heating rate. Finding the maximum actuation magnitude based on the constraint requires i) $\boldsymbol{v}_i$ in order to obtain each element of $\boldsymbol{R}$ and ii) the input vector $\widetilde{\boldsymbol{u}}$. The latter requires knowledge of the spectral coefficients, or likewise the temperature field, based on (4.24). Kinetic energy will be maximized by maximizing $\|\widetilde{\boldsymbol{u}}\|_2$ according to (4.22) though. Consequently, a conservative maximum actuation magnitude can be obtained from (4.22) by considering the simultaneous circulation of all flows in a single direction (i.e. $\widetilde{\boldsymbol{u}}^{\dagger} = \begin{bmatrix} k \cdots k \end{bmatrix}$). This maximizes both $\|\widetilde{\boldsymbol{u}}\|_2$ and $1/2\widetilde{\boldsymbol{u}}^{\dagger}\boldsymbol{R}\widetilde{\boldsymbol{u}}$ simultaneously. Evaluation of (4.22) reveals that actuation magnitudes should satisfy

$$k \leq \sqrt{\frac{\beta}{\sum_{i=1}^{I}\sum_{j=1}^{I} R_{ij}}}, \tag{4.26}$$

in that case. Elements of the input weighing matrix $\boldsymbol{R}$ depend on the (number of) flow fields as mentioned above. Maximum allowable actuation magnitudes thus depend on both the flow field implemented by a particular system and the amount of flow fields available for control. The controller actuation magnitudes considered in this work will be discussed in more detail in Section 4.5.

Finally, the matrix $\boldsymbol{Q}_i$ (and $\boldsymbol{H}_i$) is (are) rank deficient and therefore has (have) a non-trivial null space. For $\mathrm{d}E(\boldsymbol{\eta})/\mathrm{d}t = 0$ to occur for non-trivial $\boldsymbol{\eta}$, the linear combination of switching functions $\boldsymbol{\eta}^{\dagger}\boldsymbol{Q}_i\boldsymbol{\eta}$ needs to vanish. In that case, the evolution of (part of) the Lyapunov control function could vanish for such a non-trivial $\boldsymbol{\eta}$. Note that this is caused by the indefiniteness of $\boldsymbol{Q}_i$ (or $\boldsymbol{H}_i$). Heat transport is merely as fast as diffusion according to (4.17) in that case, even with fluid flow(s). The non-trivial null space of $\boldsymbol{H}_i$ can be physically understood from (4.1). The space describes the alignment between the streamlines of flow field $\boldsymbol{v}$ and the isotherms (i.e. such that $\sum_{i=1}^{I} u_i(t)\boldsymbol{u}_i \cdot \boldsymbol{\nabla} T = 0$). Alignment between the isotherms and streamlines is expected to be highly improbable in practice though. Even if alignment occurs, it will be short-lived due to the continuous evolution of the temperature field.

4.3.4.2 Quadratic feedback controller

Bang-bang control is well-known for causing undesirable high-frequency switching which can be detrimental to real-life actuators [104]. Therefore, we propose a less restrictive input law that allows for a more proportionate response to deviations from thermal homogenisation as

$$u_i(t) = \begin{cases} -c\boldsymbol{\eta}^\dagger \boldsymbol{Q}_i \boldsymbol{\eta} & \text{if } c|\boldsymbol{\eta}^\dagger \boldsymbol{Q}_i \boldsymbol{\eta}| \leq u_{max}, \\ -u_{max}\text{sign}\left(\boldsymbol{\eta}^\dagger \boldsymbol{Q}_i \boldsymbol{\eta}\right) & \text{if } c|\boldsymbol{\eta}^\dagger \boldsymbol{Q}_i \boldsymbol{\eta}| \geq u_{max}, \end{cases} \tag{4.27}$$

where $c > 0$ the quadratic controller gain and $u_{max} > 0$ the maximum allowable input. Input laws like (4.27) are known as quadratic feedback which have received significant attention in (weak) stabilization and control of both SISO [93, 91, 105] and, to a lesser extent, MIMO [84] (in)finite dimensional bilinear systems. The non-linear controller uses a quadratic feedback law according when the first condition in (4.27) is satisfied. The state feedback law saturates upon reaching u_{max}. In that case the controller behaves similar to the bang-bang controller according to the second condition in (4.27). The evolution of the Lyapunov control function according to (4.21) for inputs (4.27) is described as

$$\frac{\mathrm{d}E(\boldsymbol{\eta})}{\mathrm{d}t} = \begin{cases} -\frac{c}{\pi}\sum_{i=1}^{I}\left(\boldsymbol{\eta}^\dagger \boldsymbol{Q}_i \boldsymbol{\eta}\right)^2 & \text{if } c|\boldsymbol{\eta}^\dagger \boldsymbol{Q}_i \boldsymbol{\eta}| \leq u_{max}, \\ -\frac{u_{max}}{\pi}\sum_{i=1}^{I}\left|\boldsymbol{\eta}^\dagger \boldsymbol{Q}_i \boldsymbol{\eta}\right| & \text{if } c|\boldsymbol{\eta}^\dagger \boldsymbol{Q}_i \boldsymbol{\eta}| \geq u_{max}. \end{cases} \tag{4.28}$$

The evolution of the Lyapunov control function in (4.28) shows that heating is accelerated most if both c and u_{max} and maximized. The bound on u_{max} can be obtained analogously to the bound on k for the bang-bang regulator. The total kinetic energy satisfies (4.22) for the second condition of (4.27) when

$$u_{max} \leq \sqrt{\frac{\alpha}{\sum_i \sum_j R_{ij}}}. \tag{4.29}$$

for fluid circulation in a single direction (i.e. $\widetilde{\boldsymbol{u}}^\dagger = \begin{bmatrix} u_{max} & \cdots & u_{max} \end{bmatrix}$). Both (4.29) and (4.26) thus bound the inputs in a similar fashion. The second condition in (4.28) is negative definite for any $c \geq 0$. Inputs will still satisfies (4.22) even for sufficiently high gain feedback. However, controller gain c cannot be increased indefinitely even though the second condition in (4.28) suggests so. Only the second condition of (4.28) will be active for sufficiently high gain feedback, thereby reducing (4.29) to (4.24). In addition, high-gain feedback can result in undesirable noise amplification in a practical application. The controller gain c should therefore be tuned to avoid unnecessary amplification of noise in practice.

4.4 Numerical methods

4.4.1 Regularization of the bang-bang controller

The discontinuity in the bang-bang controller makes (numerically) solving the state trajectory of $\boldsymbol{\eta}$ accurately in (4.5) for (4.24) complex. Therefore, the inputs (4.24) are regularized in close proximity to the discontinuity by

$$u_i(t) = -k \tanh\left(\frac{\boldsymbol{\eta}^\dagger \boldsymbol{Q}_i \boldsymbol{\eta}}{\delta}\right), \tag{4.30}$$

for $\delta = \gamma / \operatorname{arctanh}(k)$ inside the threshold (i.e. for $|\boldsymbol{\eta}^\dagger \boldsymbol{Q}_i \boldsymbol{\eta}| \leq \gamma$). An input $u_i(t)$ according to (4.30) is schematically shown in Figure 4.2 for clarification. The regularization ensures that the input u_i is described by (4.24) as long as $|\boldsymbol{\eta}^\dagger \boldsymbol{Q}_i \boldsymbol{\eta}| \gg \gamma$ for a threshold $\gamma > 0$ where $\gamma = 10^{-10}$. This regularization of the inputs means $u_i(t)$ is smooth, which allows numerical simulations to be performed with regular ODE-solvers (e.g. like a Runge-Kutta method). However, the threshold γ needs to be sufficiently small for $u_i(t)$ to approximate (4.24). As a result, numerical solutions can become exceedingly hard to obtain for the bang-bang controller. This is caused by the regularization resulting in high stiffness of the ODE [106]. Therefore, a fixed time step of $\Delta\tau = 0.05$ is adopted to ensure reasonable computation times. This time step is below the smallest characteristic time scale that governs heat transport by a single flow (i.e. $\Delta\tau \ll \tau_m = -1/Re(\mu_m)$ where μ_m an eigenvalue of $\boldsymbol{H}_i + Pe^{-1}\boldsymbol{D}$). Such small time steps result in only small increments of $\boldsymbol{\eta}$ and, consequently, ensure that input switches are accurately captured during numerical simulation. Numerical simulations for time steps smaller than Δt remain unaltered, which confirms that results are independent of the time step (i.e. $u_i(t)$ remains unaltered for $\Delta\tau \ll 0.05$). Practical implementation of the bang-bang controller can require exact regularization (e.g. by applying the augmented Lagrangian method) to allow for real-time computation of the input. The non-dimensional fixed time step translates to a sample time of $31.25\ s$ for the RAM (with $Pe = 10^3$) presented in Baskan et al. [12]. The Strouhal number

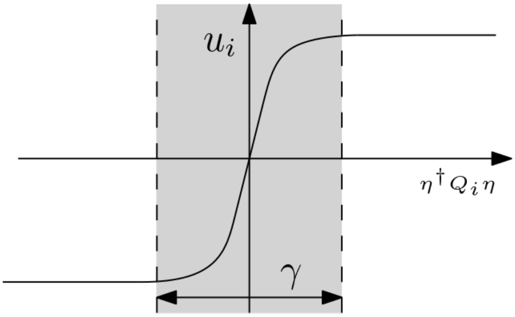

Figure 4.2: Schematic representation of the regularized inputs (4.24) in (4.30).

(defined as $Sr = T_\nu/T_s$ with T_ν the viscous time scale and T_s the sampling time) increases to $Sr \approx 0.2$ in this work. This increase means fluid inertia can have an impact on the fluid flow. To investigate the impact of fluid inertia, the bang-bang controller is investigated for a RAM with three apertures and $Pe = 10^3$ (see Figure 4.4c). The obtained inputs are used in a CFD model that includes inertia to determine the influence of fluid inertia on heat transport. The difference between the temperature fields with both models is negligible. Therefore, inertia remains negligible even for this increased Strouhal number.

4.4.2 Spill-over effects

The Laplacian eigenvalue-eigenfunctions pairs $(\lambda_\ell, \phi_\ell)$ can be obtained analytically for the RAM [16]. Their expression is included in (B.1) for completeness. Feasible numerical simulation requires a finite number of Laplacian eigenmodes in (4.4). However, truncation to a finite number of Laplacian eigenmodes can result in spill-over effects by the uncontrolled higher order modes [107]. The uncontrolled higher order modes can influence behaviour of the lower order modes. In addition, both controllers require the spectral coefficients $\boldsymbol{\eta}$ in order to provide an input u_i. Spill-over effects can therefore potentially influence closed loop control with the proposed controllers as well. However, relation (4.14) reveals that the higher order modes contribute less to $J_4(\boldsymbol{\eta})$ by definition (i.e. $Re(\mu_\ell) \geq Re(\mu_{\ell+1})$ for all ℓ). As a result, including higher order modes will have small impact on $u_i(t)$ with $\boldsymbol{P}_4$ in (4.14). Retaining a sufficient number of eigenmodes in the truncation means that the highest order mode, which is still retained in the truncation, decays fastest. This means that undesirable spill-over effects are diminished/absent when the highest order eigenmode's decay rate is faster than the characteristic time-scale of the system [107]. To determine the number of eigenmodes that need to be retained, we investigate the bang-bang controller for various numbers of Laplacian eigenmodes. The temperature fields are compared to those obtained from a finite volume method (FVM). The domain is discretized into a mesh of 11381 elements. This mesh size is sufficiently fine to ensure accurate temperature fields based on a convergence analysis by mesh refinement. The comparison should reveal negligible deviations for a sufficient number of modes in (4.4). A convergence study reveals that $L = 3067$ Laplacian eigenmodes is a sufficient number of modes to accurately capture the temperature field for $Pe = 10^3$ [16].

4.5 Performance analysis

The conventional method to fluid heating periodically activates flow fields. In the RAM flow fields periodically reorient as a consequence. Periodic activation of u_i

follows [108]

$$u_i(l\tau) = \begin{cases} 1 & \text{if } i = \text{mod}(l-1, L) + 1, \\ 0 & \text{otherwise.} \end{cases} \tag{4.31}$$

where $l = 0, 1, \ldots$ and τ the activation time of an aperture. Heating with inputs according to (4.31) depends on both τ and Pe [109]. Furthermore, heating rates associated with an "optimal" τ and Pe in (4.31) lack resilience to perturbations. For example, mixing efficiency is known to be highly susceptible to perturbations in the initial configuration of the mixture and operating conditions [5]. The dependency of heating on τ and Pe makes comparisons challenging however. This means global conclusions require a large amount of simulations. Therefore, comparisons between heating rates from the periodic protocol and the controllers are only made locally (i.e. for a specific Pe and τ). Heating by the controllers is also compared to mere diffusion and continuous circulation by a single flow. Furthermore, resilience against IC perturbations is gauged by numerical simulation. The performance of the quadratic controller is compared to a periodic scheme where the activation time τ is optimized on a RAM with four apertures with $Pe = 10^3$ (see Reference [16]). Fluids are considered sufficiently heated in this work when J_1 reaches the threshold $\varepsilon = 10^{-4}$.

Table 4.1: Maximum allowable controller gains u_{max} and actuation magnitudes k that satisfy constraint (4.26) for various flow fields available for control.

Flow field I	1	2	3	4
Maximum u_{max} and k	1	0.70405	0.56985	0.48689

Finally, both k and c need to be positive. This ensures that $\boldsymbol{Q}_i$ inherits the same fluid circulation direction as $\boldsymbol{H}_i$ in (4.5). Furthermore, in a physical system low-gain feedback is required to prevent noise propagation. That is, if (part of) $\boldsymbol{\eta}$ is measured and used in output feedback. However, accelerated heating requires high-gain feedback as seen in (4.28) and (4.25). The maximum allowable gains and actuation magnitudes that satisfy (4.22) in both controllers are presented in Table 4.1. The obtained values follow directly from considering (4.22) for the RAM.

4.5.1 Heating by bang-bang control

Heating with the bang-bang controller is investigated for various actuation magnitudes k. The effect of the number of inputs (i.e. number of apertures I) on heating with the bang-bang controller is considered as well. Numerical results are shown in Figure 4.3. Figure 4.4 shows the evolution of $||\boldsymbol{\eta}||_2$ rather than the evolution of J_4. The rationale for this measure is that the relation of $||\boldsymbol{\eta}||_2$ with J_1 in (4.6) allows for a direct comparison with previous results obtained in [55]. The inputs associated with the results in Figure 4.3 are shown in Figure 4.4. They serve to

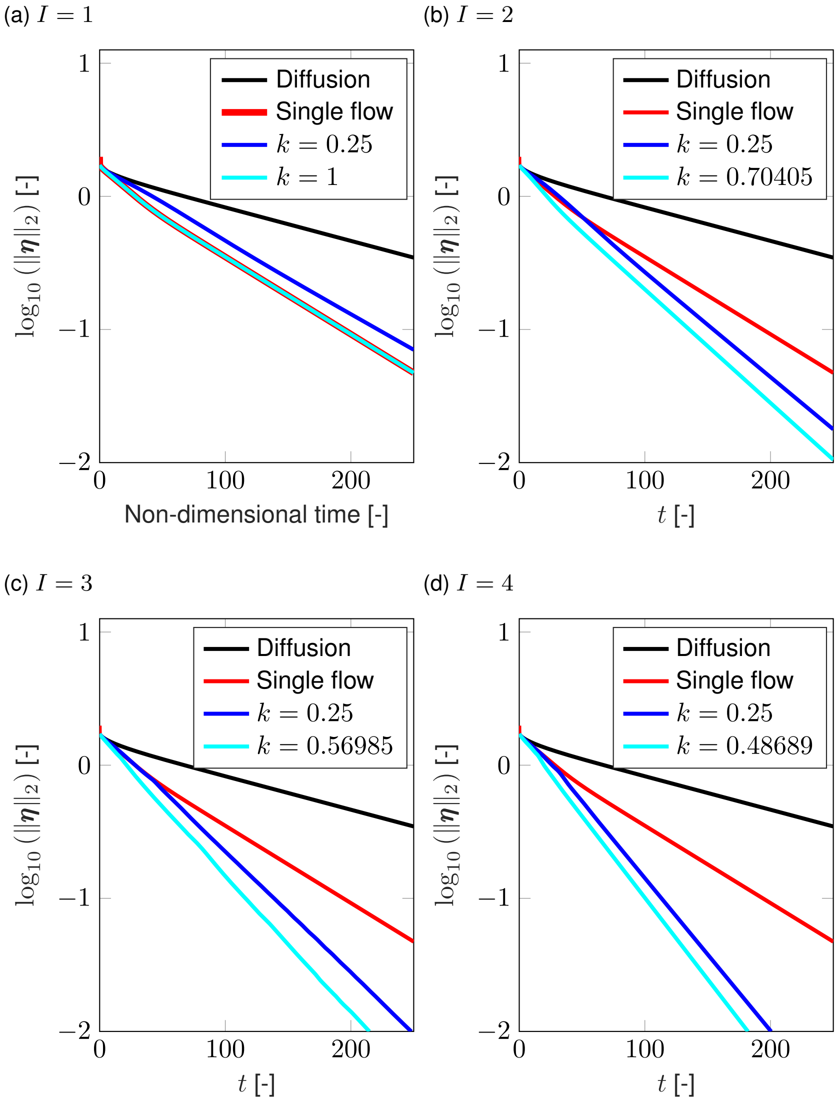

Figure 4.3: Evolution of the spectral coefficients $\|\boldsymbol{\eta}\|_2$ for various controller gains k of the bang-bang controller on RAMs with different apertures numbers I where transport is dominated by advection at $Pe = 10^3$.

clarify the flow field actuation that results in the heating behaviour observed in Figure 4.3.

The results in Figure 4.3 reveal that fluid flow improves heating compared to

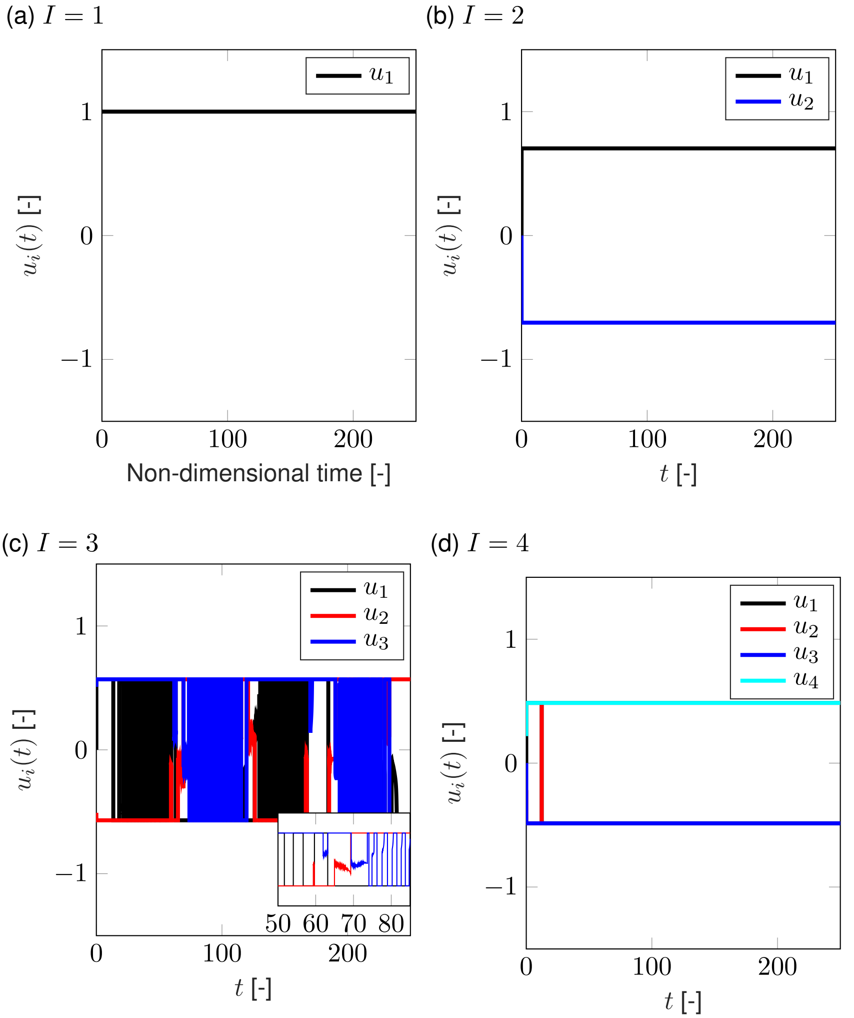
(a) $I = 1$ (b) $I = 2$ (c) $I = 3$ (d) $I = 4$

Figure 4.4: Time evolution of the inputs $u_i(t)$ associated with $\|\boldsymbol{\eta}\|_2$ in Figure 4.3 for $k = 1$ on RAMs with different apertures numbers I where transport is dominated by advection at $Pe = 10^3$.

mere diffusion. Moreover, fluid circulation by a *single* flow already significantly improves heating rates. The threshold ε is reached in 323.3 time units when heat transport is driven by a single flow. This an improvement of 58 % compared to the 764 time units required by mere diffusion to heat the fluid. Figure 4.3 shows little improvements in heating by the bang-bang controller with a single flow. Reduction of the actuation magnitude inevitably decelerates heating rates with the bang-bang controller compared to continuous circulation. Even the maximum allowable actuation magnitude (see Table 4.1) fails to improve heating rates with the bang-bang controller compared to continuous circulation by a single flow. Figure 4.4a reveals that the bang-bang controller circulates the fluid in only a single direction. This shows that the bang-bang controller with a single flow is, unsurprisingly, at most as fast as continuous fluid circulation by just a single flow.

However, considering multiple flows for the bang-bang controller yield improvements in heating rate according to Figure 4.3. Results show improved heating compared to both diffusion and continuous circulation. Heating is accelerated by a maximum of 31%, 41% and 49 % by the controller compared to continuous circulation by a single flow for a RAM with two, three and four apertures, respectively. Likewise, a comparison with diffusion reveals that heating is accelerated by upto 78 % with the bang-bang controller for the considered parameters. Figures 4.3b and 4.3d reveal monotonic exponential heating for high actuation magnitudes. This monotonic decay of $\|\boldsymbol{\eta}\|_2$ is caused by the continuous and (nearly) time-invariant fluid circulation by the bang-bang controller as can be seen in Figures 4.4b and 4.3d. As a result of this continuous and time-invariant circulation, heating dynamics according to (4.5) become time-invariant as well. This allows for a quantitative comparison of the heating rate for the controller and diffusion.

Heating rates associated with continuous circulation are approximated by $\|\boldsymbol{\eta}(t)\|_2 \leq \alpha e^{-\lambda t}\|\boldsymbol{\eta}(0)\|_2$. This inequality typically bounds the temperature evolution $\|\boldsymbol{\eta}\|_2$ from above. However, continuous circulation by the bang-bang controller implies this inequality to be exact. Numerical approximation of λ, based on the results in Figure 4.3, yields $\lambda_2 = 0.0203$ and $\lambda_4 = 0.0276$ for $I = 2$ and $I = 4$, respectively. The heating rate for diffusion is known as $\lambda_d = 0.0058$ on the RAM [16]. Furthermore, the heating rate for an optimized periodic input as shown in (4.31) on a RAM with four apertures for $Pe = 10^3$ is known at $\lambda_p = 0.0134$ [16]. Heating is thus accelerated by at most a factor $\lambda_4/\lambda_d \approx 4.76$ with the bang-bang controller compared to mere diffusion. Heating is also accelerated by at most a factor $\lambda_4/\lambda_p \approx 2.06$ compared to an optimized conventional periodic reorientation scheme. A similar analysis for RAMs with an odd number of apertures is less insightful. Heating rates show "time" windows with non-monotonous decay of $\|\boldsymbol{\eta}\|_2$ in these cases. Therefore, the heating rate estimates are far too conservative. Figure 4.4c reveals that the time windows with non-monotonic behaviour coincide with the high frequent switching. This behaviour is characteristic for bang-bang controllers. However, it only occurs for RAMs with an odd number of apertures (e.g. similar behaviour is found for $I = 5$). This rapid switching between constraints can be detrimental to actuators in real-life. The cause of this rapid switching in RAMs with an odd number of apertures is investigated further in Section 4.5.3.

The bang-bang controller improves heating compared to mere diffusion as is shown in Figure 4.3. These results also show that proximity to the maximum allowable actuation magnitude (see Table 4.1) maximizes heating for current conditions. Maximizing of the actuation magnitude can ensure the bang-bang controller outperforms a single flow, provided that i) more than a single flow is actuated and ii) actuation magnitudes are sufficiently high. Heating rates are not guaranteed to accelerate compared to continuous single flow circulation for every actuation magnitude k though. Namely, Figure 4.3b shows a brief initial transient (i.e. $t < 50$) where continuously circulation with a single flow outperforms bang-bang control for $k = 0.25$. Heating by the bang-bang controller resembles continuous circulation by a single flow for such low actuation magnitudes. Heating slows down for such low actuation magnitudes regardless of the number of apertures studied in this work. In fact, control with small actuation magnitudes ensures heating is primarily driven by diffusion. This observation is to be expected based on (4.25) (i.e. $\mathrm{d}J_4(\boldsymbol{\eta})/\mathrm{d}t$ is dominated by $\|\boldsymbol{\eta}\|_2$ for insufficient k).

Performance of the bang-bang controller is compared to our adaptive reorientation controller presented in chapters 2 and 3. Notable differences between this controller and the bang-bang controller are i) the activation of a single flow ii) for a discrete time iii) based on the minimization of J_1 instead of J_4. For a RAM with three apertures ($I = 3$) either controller suffices to accelerate heating. Heating rates are only slightly slower with the bang-bang controller (i.e. by only 2 %). This heating rate cannot be improved by increasing the actuation magnitudes k due to the additional constraint on the inputs in (4.22). The constraint limits any additional improvement of increasing actuation magnitudes. This could be resolved by allowing the bang-bang controller to turn off fluid circulation and adjusting the maximum actuation magnitude that satisfies (4.26) for the remaining inputs (viz. all inputs in (4.24) circulate fluid in a single direction in order to determine the maximum allowable actuation magnitude for k in Table 4.1). Turning off fluid circulation means higher maximum actuation magnitudes are permitted – such that (4.22) is still satisfied – for inputs that keep circulating a fluid. However, making the input constraint depending on the number of activated inputs is excessively cumbersome. Note, however, that the heating rates obtained with the bang-bang controller become comparable to those obtained with the adaptive reorientation controller if both are considered on a RAM with four apertures ($I = 4$).

4.5.2 Heating by quadratic feedback control

The quadratic controller is studied in a similar fashion as the bang-bang controller (see Section 4.5.1). The numerical results in the previous section show that the number of apertures in the RAM is instrumental to accelerate heating. Therefore, heating with the quadratic controller for various numbers of apertures is studied as well. Numerical results are shown in Figure 4.5. The effect of the gain c on heating rates is shown in Figure 4.5 too.

Numerical results in Figure 4.5 reveal that quadratic feedback can boost heating. Heating accelerates by at most 71 %, 74 % and 78 % compared to diffusion on a RAM with two, three and four apertures, respectively. Furthermore, fluid heating with the quadratic controller on a RAM with a single aperture is at most

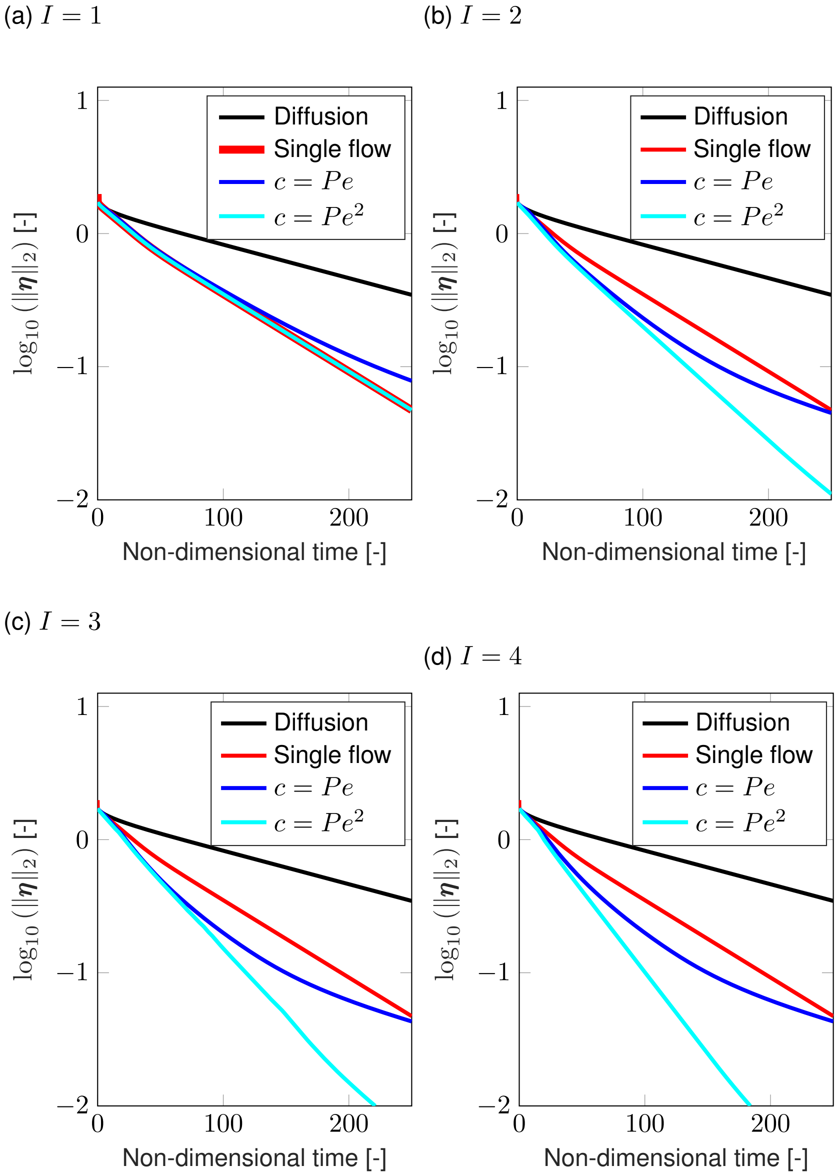

(a) $I = 1$

(b) $I = 2$

(c) $I = 3$

(d) $I = 4$

Figure 4.5: Time evolution of the spectral coefficients $\|\boldsymbol{\eta}\|_2$ for various controller gains c of the nonlinear controller on RAMs with different amounts of apertures I where transport is dominated by advection at $Pe = 10^3$.

as fast as continuous circulation by a single flow. Moreover, monotonous heating rates appear on RAMs with an even number of apertures. The RAM with three apertures shows nonmonotonous heating rates for sufficiently high gains.

This can be understood by examining the inputs in Figure 4.6. The inputs are associated with the high-gain feedback case, chosen at $c = Pe^2$, in Figure 4.5. The quadratic controller responds exactly the same as the bang-bang controller on a RAM with a single aperture (e.g. compare Figure 4.4a with Figure 4.6a). Most inputs on RAMs with more than one aperture reach their respective constraints in the early stage of heating (i.e. within the time window $t \in [0, 70]$). Thereafter inputs remain at the same value for a relatively long time for RAMs with an even number of apertures. The input remains at the same value after an initial transient for a RAM with four apertures (i.e. after $t \geq 15.1$). This is exemplified in both Figure 4.6b and Figure 4.6d. The constant inputs have a profound effect on the fluid temperature evolution. Figure 4.5 shows a monotonous exponential heating rate sets in on RAMs with an even number of apertures. The inputs (4.24) behave vastly different for a RAM with three apertures than for a RAM with one, two and four apertures. Moreover, in a RAM with three apertures heating rates are nonmonotonous as shown in Figure 4.5. The above observations strongly suggest that this can be attributed to the rapidly switching inputs shown in Figure 4.6. This follows since the rapid switching is the only discerning difference in actuation behaviour.

The inputs start to diminish as time progresses beyond a certain time. This diminishing of the inputs is observed for one or multiple apertures in the quadratic controller. The decrease of the inputs is proportional to $\|\boldsymbol{\eta}\|_2$ in the controller. Proportionality makes the quadratic controller dependent on both current state and gain. Examining Figure 4.5 reveals that this input decay is associated with slower heating rates. Inputs diminish in proportion with $\|\boldsymbol{\eta}\|_2$ as the system approaches thermal homogenisation for $t \to \infty$. The proportionality of the inputs implies that the inputs u_i according to (4.28) can become smaller than the input constraints (i.e. $|u_i| < u_{max}$). This means that activating more apertures can result in deteriorating heating rates with the quadratic controller compared to the bang-bang controller (i.e. $\mathrm{d}J_4(\boldsymbol{\eta})/\mathrm{d}t$ becomes less negative even when more apertures are activated). This effect is found to become less pronounced for higher controller gains (i.e. the inputs diminishes proportionately with the state at a later stage of the heating for higher gains).

The quadratic controller requires sufficiently large gains to boost heating. Figure 4.5 reveals that the quadratic controller can outperform continuous circulation with a single flow. However, heating rates can deteriorate with the quadratic controller for a too small gain. Increasing the gains sufficiently accelerates heating compared to single flow circulation for any number of apertures. Notable exception is quadratic control on a RAM with a single aperture. In this case heating is at most as fast as continuous circulation by a single flow. This can be seen clearly in Figure 4.5a. Relatively low gains (i.e. below $c = Pe$) combined with diminishing states can thus slow heating as heating progresses. This implies that

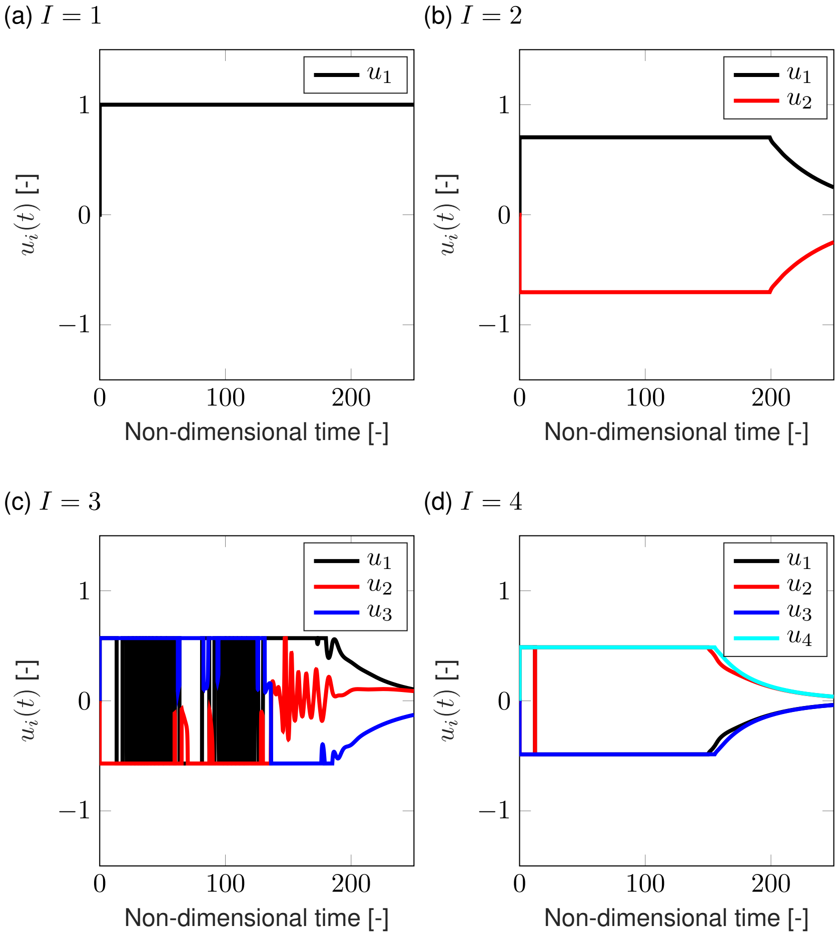

Figure 4.6: Time evolution of the inputs $u_i(t)$ associated with $\|\boldsymbol{\eta}\|_2$ in Figure 4.5 for $c = Pe^2$ on RAMs with different apertures numbers I where transport is dominated by advection at $Pe = 10^3$.

tuning is vital for fast heating with quadratic feedback.

Heating is found to significantly accelerate for large gains upto $c = Pe^2$. These high gains force the inputs into their respective constraints (see Figure 4.6). Figure 4.5d reveals that the threshold is reached in 165.9 time units with the controller on a RAM with four apertures. Furthermore, the associated monotonous heating rate is only maintained for these high gains. Such monotonous heating rates are caused by constant fluid circulation here. Gains that are too low, fail to force the inputs into their respective constraints. As a consequence, the inputs are unsteady throughout the entire time window resulting in nonmonotonous heating rates. Large controller gains also result in rapid switching inputs on a RAM with three apertures for the quadratic controller similar as for bang-bang controller. The high-frequency switching for a RAM with three apertures (see Figure 4.6c) decreases for smaller gains. These results suggests that proper tuning of controller gain c can simultaneously boost heating *and* minimize unnecessary switching behaviour.

Figure 4.6c shows that rapid switching behaviour is confined to the early stages of heating. The bang-bang controller showed rapid switching throughout the entire time domain. The reduced number of switches makes the quadratic controller less demanding compared to the bang-bang controller. Furthermore, the quadratic controller is only slightly slower than the bang-bang controller (i.e. a maximum of 0.05 % for the considered parameters). This means that the quadratic controller is also slightly slower than the adaptive reorientation controller considered in chapters 2 and 3. Likewise, the closed-loop response of the quadratic controller resembles the bang-bang controller for high-gain feedback. Increasing gains ensures heating rates similar to those observed in the bang-bang controller can be obtained. These features make the quadratic controller preferable to the bang-bang controller in practice.

4.5.3 Thermal plume formation for effective heating

The inputs in Figure 4.4 and Figure 4.6 show that both controllers circulate fluids in opposing directions between apertures. Opposing fluid circulation is known to boost heating in open-loop. For example, Omari and Guer [59] have shown that heating was accelerated by sinusoidal flow modulation between the rods and the boundary of a two-rod stirring system. In the RAM, opposing circulation between neighbouring apertures can produce a hot plume between said apertures. These neighbouring apertures need to be separated by an arc-length Θ. In that case, the opposing circulation results in the formation of a hot plume between the neighbouring apertures, which enhances fluid heating very effectively. Such heating characteristics were observed for the discrete adaptive reorientation scheme presented in [55]. Both controllers follow similar characteristic behaviour here as well (see Figure 4.4 and Figure 4.6). Namely, the inputs of the controllers lead to plume formation via a similar mechanism as mentioned above. However, plume behaviour differs significantly from previously observed results (e.g. due to invariant or rapidly switching inputs). This warrants a thorough analysis of the dynamics involved in heating. Both controllers show close resemblance for high gain feedback. Hence the analysis is limited to the quadratic controller with large gains.

Bang-bang control continuously circulates the fluid for RAMs with one or two apertures. The quadratic controller shows similar behaviour for large gains. To understand the impact of continuous circulation, the transient temperature field is investigated. Figure 4.7 shows transient temperature field snapshots at different

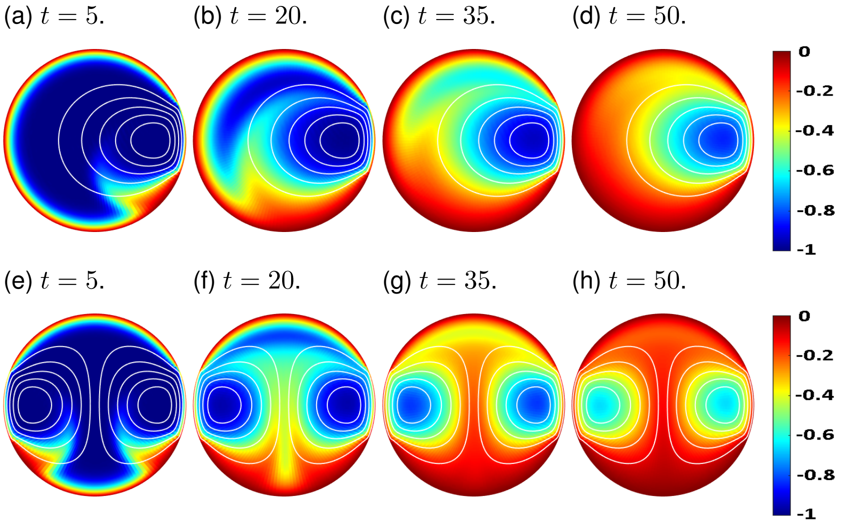
(a) $t = 5.$ (b) $t = 20.$ (c) $t = 35.$ (d) $t = 50.$

(e) $t = 5.$ (f) $t = 20.$ (g) $t = 35.$ (h) $t = 50.$

Figure 4.7: Evolution of transient temperature fields for quadratic feedback for a RAM with a single aperture (top row) and two apertures (bottom row) (blue: $\min(\widetilde{T}) = -1$; red: $\max(\widetilde{T}) = 0$; closed curves: streamlines).

times during heating. The snapshots in Figures 4.7a and 4.7d result from applying the inputs shown in Figure 4.6a. Similarly, snapshots in Figure 4.7c,d follow from applying the inputs shown in Figure 4.6b. The streamlines are indicated to clarify the underlying flow field.

Figure 4.7a shows the results of continuously circulating a single flow. The induced flow generates a hot plume that heats up the fluid. Figure 4.7d shows that the cold interior heats up as time progresses. The impact of continuous circulation on heating is limited though. Heating acceleration is constrained to only a brief time window following flow activation [55]. Prolonged circulation thus drastically reduces the potential to accelerate heating. Figure 4.7d shows the effect of prolonged activation of a single flow; the isotherms and streamlines align as heating progresses. Similar behaviour was also observed in Chapter 2. This progressive alignment reduces the contribution of advection to heating (i.e. $\boldsymbol{u}_1 \cdot \boldsymbol{\nabla} T \to 0$ in (4.1) or, likewise, $\boldsymbol{\eta} \to \mathcal{N}(\boldsymbol{H}_1)$ with $\mathcal{N}(\boldsymbol{H}_1)$ the non-trivial null-space of $\boldsymbol{H}_1$ as both align). LaSalle's invariance principle can potentially be used to investigate the impact of the alignment on heating further.

Figure 4.7e shows multiple plumes. Both apertures continuously circulate the fluid in opposing directions (see Figure 4.6c). These plumes merge due to the simultaneous circulation between two apertures. The merged plume arises exactly between these two apertures since both flows are induced by the same input magnitudes with opposite circulation directions. The transient temperature field therefore becomes symmetric under the considered conditions. Fig-

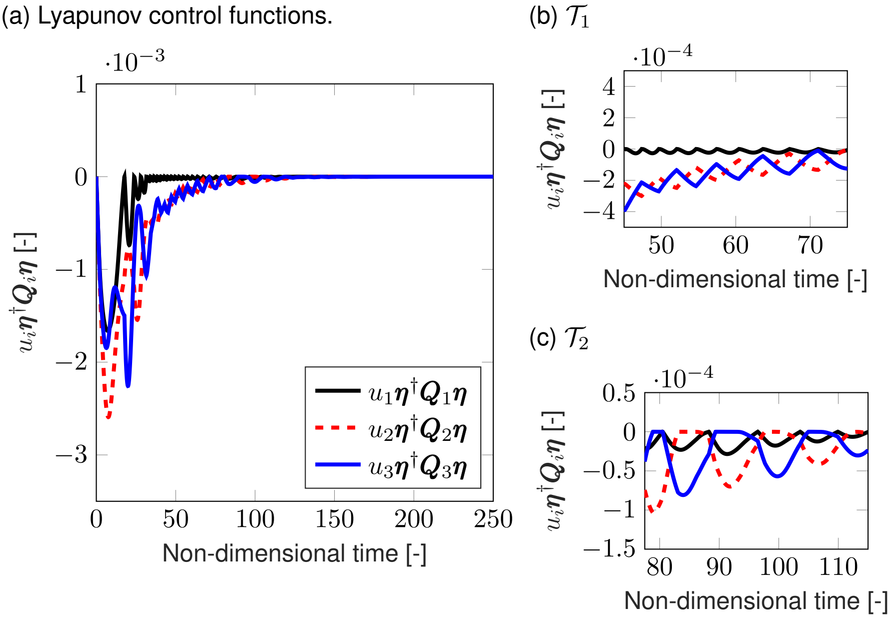
(a) Lyapunov control functions.

(b) $\mathcal{T}_1$

(c) $\mathcal{T}_2$

Figure 4.8: The (a) Lyapunov control functions for the quadratic controller with $c = Pe^2$ on a RAM with $I = 3$. Magnification of the Lyapunov control functions inside time intervals (b) $\mathcal{T}_1$ and (c) $\mathcal{T}_2$.

ure 4.7e shows that the merged plumes possess a reflection symmetry along the y-axis. This symmetry axis coincides with the symmetry axis of the streamlines. Circulation by both flows progressively heats up the cold interior. Heating is again hampered by the alignment between the isothermals and streamlines. These isotherms and streamlines differ from those for a single flow though (e.g. $\sum_{i=1}^{2} \boldsymbol{v}_i \cdot \boldsymbol{\nabla} T \to 0$ in (4.1) or $\boldsymbol{\eta} \to \mathcal{N}\left(\sum_{i=1}^{2} u_i \boldsymbol{H}_i\right)$ with $\mathcal{N}\left(\sum_{i=1}^{2} u_i \boldsymbol{H}_i\right)$ the non-trivial null-space of $\sum_{i=1}^{2} u_i \boldsymbol{H}_i$). Hence, heating by advection is hampered when the isothermals align with the linear *combination* of the activated flow fields. The alignment ensures that advective heat transport diminishes as heating progresses (see discussion below Figure 2.7). Furthermore, continuous circulation leaves undesirable “cold spots” inside the fluid as seen in Figure 4.7h.

Flow forcing control responds in a vastly different fashion on a RAM with three apertures than on a RAM with two or less apertures. High-frequency switching is observed in the inputs of both controllers for RAMs with uneven numbers of apertures (see both Figure 4.4c and Figure 4.6c). This behaviour is linked to the evolution of the respective Lyapunov control functions associated with each input i. Their evolution partly depends on the geometry of the system at hand (e.g. the number of inputs is defined by the number of apertures of the RAM). Each component of the Lyapunov control function is investigated further here. Their analysis will reveal the reason for the fundamental difference between flow control on a RAM with two and three apertures. The individual components of the Lyapunov control function are shown in Figure 4.8. Each component i is associated with the respective contribution of each flow field to heating. Figure 4.8a reveals that these components converge to the origin. Rapid oscillations can be seen throughout the considered time span. Two time windows (indicated by $\mathcal{T}_1$ and $\mathcal{T}_2$ in Figure 4.8a) are of particular interest to heating. Figure 4.8b and Figure 4.8c show the Lyapunov control functions inside these windows. The origin is intermittently approached by $u_1\boldsymbol{\eta}^\dagger\boldsymbol{Q}_1\boldsymbol{\eta}$ throughout $\mathcal{T}_1$. Similar behaviour can be observed for $u_1\boldsymbol{\eta}^\dagger\boldsymbol{Q}_1\boldsymbol{\eta}$ throughout $\mathcal{T}_2$. Both magnifications show fundamentally different oscillating behaviour of the other Lyapunov control functions (i.e. $u_2\boldsymbol{\eta}^\dagger\boldsymbol{Q}_2\boldsymbol{\eta}$ and $u_3\boldsymbol{\eta}^\dagger\boldsymbol{Q}_3\boldsymbol{\eta}$). These Lyapunov control functions eventually converge to the origin in both windows. However, throughout $\mathcal{T}_1$ these remaining control functions oscillate in opposite phases without actually reaching the origin. Throughout $\mathcal{T}_2$ all control functions reach the origin intermittently, albeit never simultaneously. Moreover, the control functions $u_2\boldsymbol{\eta}^\dagger\boldsymbol{Q}_2\boldsymbol{\eta}$ and $u_3\boldsymbol{\eta}^\dagger\boldsymbol{Q}_3\boldsymbol{\eta}$ stay close to the origin for prolonged time windows. Figure 4.6c reveals that the inputs are non-zero throughout $\mathcal{T}_2$ (i.e. both u_2 and u_3 are non-zero throughout $\mathcal{T}_2$). This suggests the switching functions approach the origin as $u_i\boldsymbol{\eta}^\dagger\boldsymbol{Q}_i\boldsymbol{\eta}$ approaches the origin. The transition between the two behaviours occurs towards the end of $\mathcal{T}_1$. Figure 4.8b shows that both $u_2\boldsymbol{\eta}^\dagger\boldsymbol{Q}_2\boldsymbol{\eta}$ and $u_3\boldsymbol{\eta}^\dagger\boldsymbol{Q}_3\boldsymbol{\eta}$ remain close to the origin near the end of $\mathcal{T}_1$.

Notably different behaviour can be observed in both time-windows; the behaviour inside $\mathcal{T}_1$ is reminiscent of limit-cycling behaviour. This behaviour can be visualized in the following fashion. The oscillating Lyapunov control functions inside $\mathcal{T}_1$ result in oscillations in their associated inputs. These oscillating inputs are, naturally, directly related to the oscillations in the switching functions. Figure 4.9 therefore shows the phase-space of the switching functions inside $\mathcal{T}_1$. The trajectory is indicated in black and flow reversal moments are indicated by red squares. The direction of the trajectory inside the time window is indicated by a blue arrow. The trajectory in Figure 4.9 converges towards the origin as heating progresses. Near the end of $\mathcal{T}_1$ both $\boldsymbol{\eta}^\dagger\boldsymbol{Q}_2\boldsymbol{\eta}$ and $\boldsymbol{\eta}^\dagger\boldsymbol{Q}_3\boldsymbol{\eta}$ converge to the origin as well. Both approach the origin alternately. Heating by advection is severely hampered when the Lyapunov control functions approach the origin (i.e. $\boldsymbol{\eta}^\dagger\boldsymbol{Q}_i\boldsymbol{\eta}$ approaches the origin such that $u_i\boldsymbol{\eta}^\dagger\boldsymbol{Q}_i\boldsymbol{\eta}$ reaches the origin). In that case, the advective contribution to $\mathrm{d}J_4/\mathrm{d}t$ diminishes significantly according to (4.12). The controller consequently adjusts the inputs to promote heating by advection again. Numerical results thus suggest that the transition from the behaviour in $\mathcal{T}_1$ to the behaviour in $\mathcal{T}_2$ occurs, because advective heat transport by circulating fluid no longer contributes significantly to heating (see discussion below Figure 4.7). Furthermore, oscillations of the switching functions follow a very distinct pattern inside $\mathcal{T}_1$ according to Figure 4.9. This indicates limit cycling behaviour.

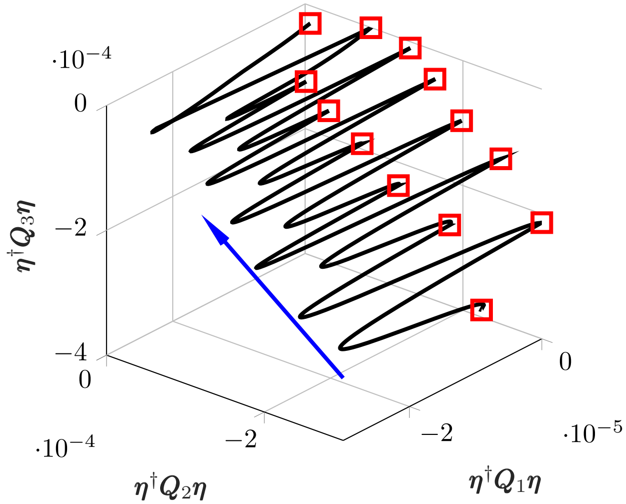

Figure 4.9: Phase-space of the switching functions for the quadratic controller associated inside $\mathcal{T}_1$. Trajectories are indicated in black with flow reversal moments (i.e. as $\boldsymbol{\eta}^\dagger \boldsymbol{Q}_i \boldsymbol{\eta}$ passes through zero) indicated in red. The blue arrow indicates direction of motion.

The relationship between oscillating control/switching functions and heating can be understood from the associated transient temperature fields. Figure 4.10 shows snapshots of the transient temperature field inside both time windows. These snapshots are sampled at the flow reversal moments indicated in Figure 4.9. Transient temperature fields associated with flow control on a RAM with three apertures show vastly different behaviour than those observed in Figure 4.7. Transient temperature fields inside $\mathcal{T}_1$ (top row in Figure 4.10) and inside $\mathcal{T}_2$ (bottom row in Figure 4.10) also contain a plume between two neighbouring apertures. This plume is formed around the x-axis, which corresponds to the symmetry axis of the base flow in this case (indicated by $\mathcal{I}_1$). The oscillation of the inputs results in a plume that sways across the x-axis. The resulting back-and-forth motion of the plume aids heat transport throughout the fluid. Similar heating behaviour was observed for the adaptive reorientation scheme in [55]. However, a key difference with the results presented here is that fluid flows are activated simultaneously and sometimes even constantly rather than sequentially by a(n) (a)periodic reorientation scheme. The reflection symmetry of the plume forms around the symmetry axis of a flow field (e.g. I_1 aligns with the symmetry axis of the plume). Plume swaying occurs since the plume between the neighbouring apertures has the same symmetry as the underlying flow field. The apertures of these flows are located at the opposite side of the hot plume basis, close to the hot boundary. The controller promotes the formation of a plume around such a symmetry axis to further direct heat transport. Prolonged continuous circulation can result in cold spots as seen above. The goal of the behavioural transition from $\mathcal{T}_1$ to $\mathcal{T}_2$ becomes clear from Figure 4.10. The controller heats the cold spots, which were left inside $\mathcal{T}_1$, inside $\mathcal{T}_2$. Rapid switching of u_1 and, simultaneously, the intermittent reduction of inputs u_2 and u_3 directs heat into the cold spot left during $\mathcal{T}_1$. The rapid flow reversals observed in $\mathcal{T}_2$ result in similar swaying of the merged plume as seen in $\mathcal{T}_1$. However, the hot "core" of the plume moves closer to the domain boundary inside $\mathcal{T}_2$ compared to $\mathcal{T}_1$. This is caused by the intermittent reduction of either u_2 or u_3, observed in Figure 4.5c, combined with the activation of u_1. The reduction of u_2 (or u_3) results in reduces fluid circulation such that

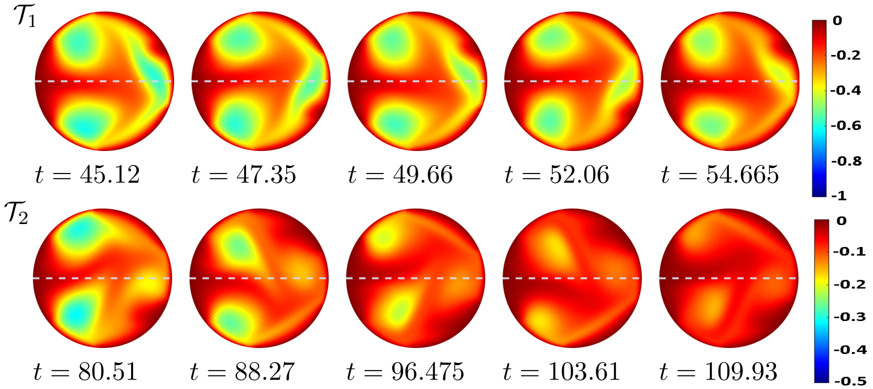

Figure 4.10: Evolution of the transient temperature field associated with time windows shown in Figure 4.8a. Top row associated with Figure 4.8b (blue: $\min(\widetilde{T}) = -1$; red: $\max(\widetilde{T}) = 0$; dashed line: reflection axis $\mathcal{I}_1$) and bottom row associated with Figure 4.8c (blue: $\min(\widetilde{T}) = -0.5$; red: $\max(\widetilde{T}) = 0$; dashed line: reflection axis $\mathcal{I}_1$).

The above suggests that indefiniteness of $\boldsymbol{Q}_i$ is vital for controller operation in this work. Positive (or negative) definiteness of $\boldsymbol{Q}_i$ would force the controller to circulate fluid in only a single direction. To see this, observe that $u_i(t)$ in (4.29) can only be positive (negative) for a positive (negative) definite $\boldsymbol{Q}_i$. This would inhibit the formation of large merged plumes for effective fluid heating (i.e. flows can then only circulate in a *single* direction and thus the controller is unable to form large merged plumes between apertures). Furthermore, symmetries play a crucial role in heating with both controllers. RAMs with an odd number of apertures can align merged hot plumes with the symmetry axes of flow fields that can then be used to direct heat from this plume into cold spots. Both controllers use this possibility to target cold spots inside the fluid. This suggests that an odd number of apertures promotes that ability of the controllers to direct heat. Further investigation is required and should include a RAM with six apertures. Such a RAM contains the symmetry axes of a RAM with two and three apertures.

4.5.4 Sensitivity of plume formation

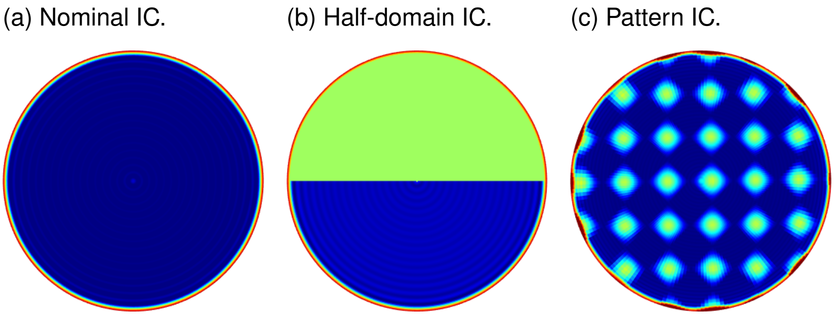
(a) Nominal IC.
(b) Half-domain IC.
(c) Pattern IC.

Figure 4.11: The (a) nominal initial transient temperature field $\widetilde{T}(\boldsymbol{x},0) = -1$, the (b) initial temperature field where half of $\mathcal{D}$ is heated (to $\widetilde{T}(\boldsymbol{x},0) = -0.5$) and (c) the patterned initial temperature field with localized hot spots (at $\widetilde{T}(\boldsymbol{x},0) = 0.5\,(\max\,(\sin\,(6\pi x),0) + \max\,(\cos\,(6\pi y),0)) - 1$) for the RAM.

Section 4.5.3 revealed that the controller produces a hot plume between neighbouring apertures to effectively boost heating. However, plume formation was only studied for a uniformly cold fluid. Heating behaviour can thus potentially change if other ICs are presented to the controller. Heating behaviour of open-loop flow control by a conventional periodic reorientation scheme (see (4.31)) is investigated here as well. Such open-loop methods (e.g. like conventional periodic reorientation schemes) are widely adopted for fluid heating. For "optimal" heating these methods require *a priori* parameter tuning. Fluid heating rates are thus also susceptible to perturbations as a result (e.g. to erroneous model parameters or perturbations in the ICs). Therefore, fluid heating is studied for perturbed ICs next. The results can provide insight into the sensitivity of the plume formation behaviour observed in Section 4.5.3.

The ICs during the analysis are shown in Figure 4.11. Part of the fluid is already heated in the first perturbation. Figure 4.11b shows a temperature field with a cold bottom and hot top half. Temperatures in the top half are halfway towards heating (i.e. $\widetilde{T}(\boldsymbol{x},0) = -0.5$). The second perturbation introduces local "hot spots" in the fluid as shown in Figure 4.11c. These hot spots follow a pattern described by $\widetilde{T}(\boldsymbol{x},0) = 0.5\,(\max\,(\sin\,(6\pi x),0) + \max\,(\cos\,(6\pi y),0)) - 1$. This perturbed IC is henceforth referred to as a patterned IC. ICs with such patterned scalar distributions can be studied to determine the sensitivity of transport enhancements [110, 5].

Figure 4.12a,b show the inputs from the quadratic controller in response to the ICs in Figure 4.11. A comparison between the inputs in Figure 4.12b and Figure 4.6d reveals that the quadratic controller exhibits similar actuation behaviour for the perturbed ICs as for the nominal IC (i.e. neighbouring flows circulate fluid be-

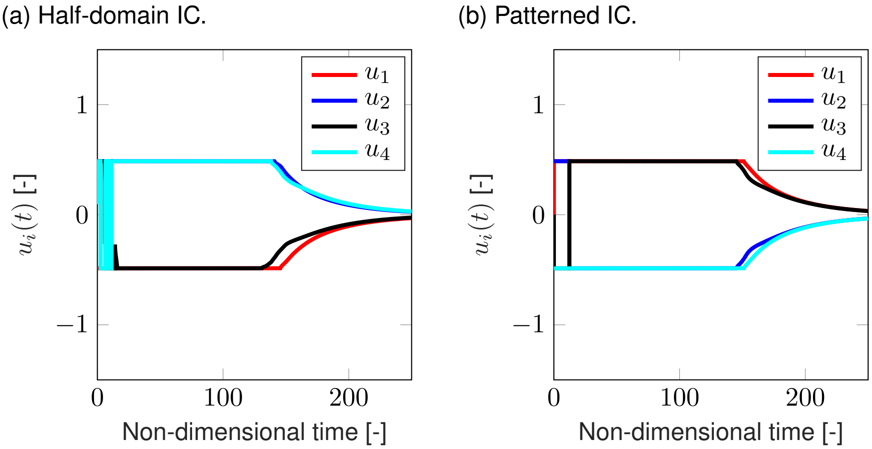

Figure 4.12: Time evolution of u_i for (a) the half-domain and (b) the patterned heat perturbation of the ICs for the quadratic controller on a RAM with four apertures ($I = 4$) with advection-dominated transport at $Pe = 10^3$.

tween them). Moreover, a similar pattern in the inputs can be observed, albeit for different inputs (e.g. input u_3 in Figure 4.12b shows almost the same behaviour as input u_2 in Figure 4.6d). However, input behaviour in response to the half-domain IC in Figure 4.12b differs significantly from the behaviour in Figure 4.6d. Namely, both u_3 and u_4 show switching behaviour similar to the behaviour observed for a RAM with three aperture (see Figure 4.6c). The results in Figure 4.12 reveal that the quadratic controller adapts the inputs based on the presented IC. This clarifies the utility of a closed-loop flow controller over a conventional open-loop periodic reorientation scheme; namely the adaptation of the fluid flow in response to perturbations and/or noise.

The snapshots, associated with the inputs in Figure 4.12, are shown in Figure 4.13 to investigate the response of the flow controller to the ICs in Figure 4.11 on the transient temperature field evolution. The flow controller opts for opposing fluid circulation between neighbouring apertures regardless of the IC. Plumes initially emanate from different locations from the boundary. Figure 4.13 shows that he initial plume emanates from the bottom left, top right, and bottom right parts of the fluid domain for the nominal, half-domain and patterned IC, respectively. As a result, hot plumes arise between different neighbouring apertures to ensure fast fluid heating. The mechanism leading to this thermal plume formation is investigated for the nominal IC in the previous section. The response of the quadratic controller on a RAM with four apertures differs only slightly from those studied in Section 4.5.3. For example, the inputs u_1 and u_2, in response to the nominal IC, circulate the fluid in the same direction as u_4 and u_3, respectively. This means that the first and second aperture circulate the fluid in the direction that aids the development of the hot plume. Fluid circulation by u_1 and u_2 reverses after an initial transient resulting in another hot plume forming between these two neighbouring apertures. The same behaviour is observed for the perturbed ICs in Figure 4.13. To determine the difference in fluid heating behaviour, associated with the transient temperature snapshots in Figure 4.13, heating rates are investigated next. The heating rate of a periodic reorientation scheme in Figure 4.11 is also studied.

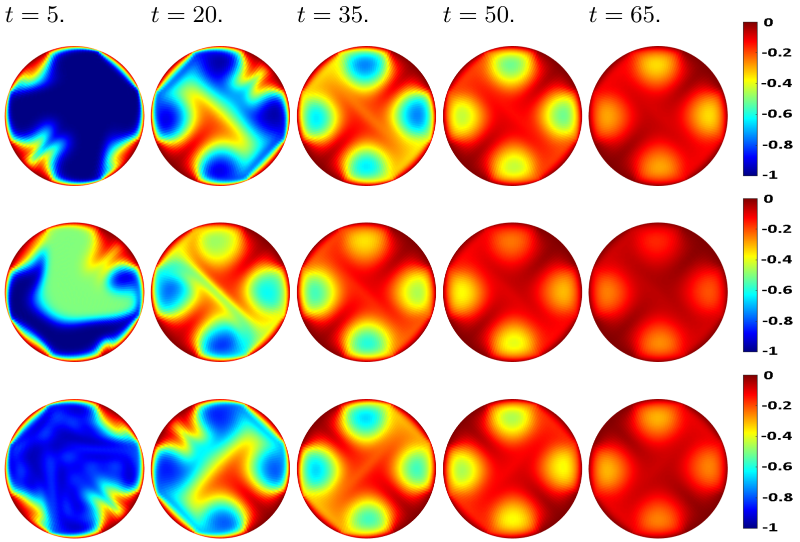

Figure 4.13: Evolution of transient temperature fields for quadratic feedback on a RAM with four apertures in response to the nominal IC (top row), the half-domain IC (middle row) and the patterned IC (bottom row) (blue: $\min(\widetilde{T}) = -1$; red: $\max(\widetilde{T}) = 0$; closed curves: streamlines).

The periodic reorientation scheme is investigated for the same perturbed ICs as the controller. This allows for a comparison between both methods of heating. The periodic scheme in (4.31) activates apertures for a time span τ. Here, an optimal activation time τ, optimized for $Pe = 10^3$ and the nominal IC shown in Figure 4.11a, is adopted from Lester et al. [109]. Numerical simulation of a RAM with four apertures with $Pe = 10^3$ reveals a local optimum for $\tau \approx 25$. This activation time – and likewise the activation sequence – is not necessarily optimal for other initial conditions. Consequently, changing the ICs can result in different heating times (e.g. due to suboptimal τ). This sensitivity, inherent to open-loop flow control, can be reduced by opting for closed-loop control instead.

The response to both perturbations is shown in Figure 4.14. Heating by continuous circulation of a single flow is shown for comparison. Heating rates for

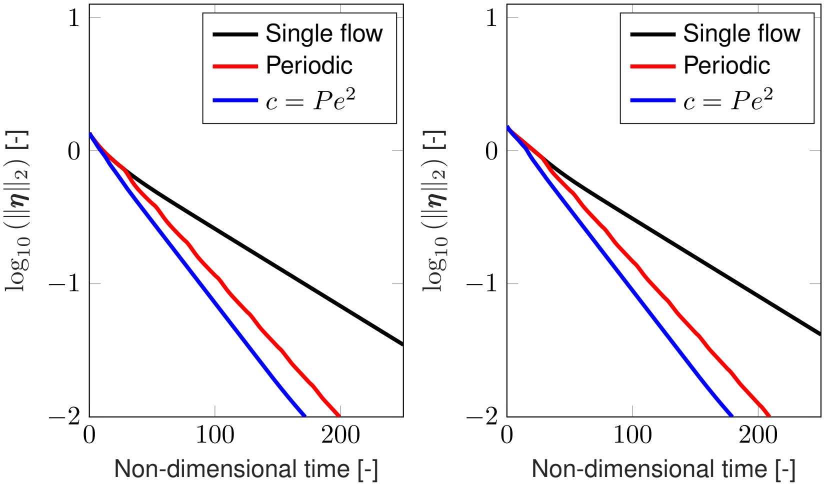

(b) Patterned IC.

(a) Half-domain IC.

Figure 4.14: Time evolution of $\|\boldsymbol{\eta}\|_2$ for (a) the half-domain and (b) the patterned heat perturbation of the ICs for the quadratic controller and the periodic reorientation scheme on a RAM with four apertures ($I = 4$) with advection-dominated transport at $Pe = 10^3$.

the first perturbation are shown in Figure 4.14a. Heating accelerates with a single flow for the perturbed IC compared to the nominal one. The threshold is reached in 300.6 dimensionless time units. This is an increase of 6.9 % with respect to heating for the nominal IC. Figure 4.14a shows that heating with the periodic scheme falls between the other two flow forcing methods. The fluid is heated in 176.2 time units with the periodic scheme, an acceleration of 7.7 % compared to the 191 units for the nominal IC. The controller further reduces this “time” to 149.8 time units. Similar heating behaviour is observed for the patterned IC in Figure 4.14b. Heating slightly decelerates for the patterned IC compared to the perturbed IC in Figure 4.11b. The controller reaches the threshold in 157.4 time units. Whereas the periodic scheme sufficiently heats the fluid in 185.6 time units. This is a decrease of 5.1 % and 5.3 % in the heating rates obtained by the controller and the periodic scheme compared to results in 4.14a, respectively.

The accelerated heating is partly caused by the added heat due to the perturbations. Here, the heating rates of the controller and the periodic scheme are compared to those obtained by continuous circulation by a single flow. Results show that the periodic scheme and the controller boost heating rates compared to a single flow by an average of 41 % and 49 %, respectively. The controller thus consistently outperforms both the periodic scheme and single flow for the ICs considered here. Heating rates obtained by the controller are accelerated by at least 13.2 % with respect to the periodic scheme, regardless of the IC. Moreover, transient temperature field snapshots reveal that the quadratic controller adopts similar plume formation behaviour for the ICs considered here. This shows that plume formation behaviour, analysed in Section 4.5.3, has at least some resilience to perturbed ICs.

4.6 Conclusions and discussion

In this chapter we investigated performance and sensitivity of a two nonlinear control methodologies to accelerate scalar transport. The presented control methodology relies on a spectral decomposition of the advection-diffusion equation in the Laplacian eigenfunctions on a circular plane. The infinite dimensional system is captured by a compact finite dimensional bilinear state-space description. State feedback control of bilinear systems can become problematic when the inputs vanish, which effectively results in the system becoming uncontrolled. However, heating of an initially cold fluid combined with the second law of thermodynamics ensures that the origin is only passed when the fluid reaches the boundary temperature and is homogeneous. The challenge considered in this work is to ensure that the stable heat transport system reaches the origin as fast as possible. The real-time control of the scalar field involves designing the inputs such that the decay rate of a generic Lyapunov function or “thermal energy” is minimized.

We proposed two control methods that minimize the decay rate: a bang-bang controller and a nonlinear quadratic feedback controller. Heat transport from the hot boundary is significantly improved resulting in substantially accelerated heating rates compared to mere diffusion. Both controllers also significantly accelerate the heating rates compared to continuous fluid circulation depending on the number of flows and the controller tuning. Fluid heating rates are comparable with those accomplished with the adaptive reorientation controller presented in chapters 2 and 3. The bang-bang controller shows high-frequency behaviour, which is undesirable for real-time actuation. The quadratic feedback controller is less restrictive compared to the bang-bang controller, which comes at a sacrifice of heating rate improvement. However, rapid switching is significantly reduced during control with the quadratic controller as a consequence. In addition, the rapid switching with the quadratic controller is predominantly confined to the initial stages of control.

Numerical results reveal that plume formation, by circulating the fluid in opposite directions between apertures, seems to form a key characteristic for effective heat-transfer from the hot boundary (in)to the fluid. This makes the proposed methods tailor-made for flow control of scalar transport in i) the presence of significant diffusion and ii) the absence of a boundary condition that can directly influencing the scalar field, e.g., a adjustable boundary temperature. Numerical simulations show that the advantages of the quadratic controller to heat the fluid also appears to hold for higher Péclet numbers than studied here. Furthermore, heating rates obtained with the quadratic controller are compared to a conventional open-loop periodic reorientation scheme for perturbed initial conditions. The flow field activation time of this periodic scheme is locally optimized for an unperturbed initial condition. Results show that the quadratic controller consistently outperforms the periodic scheme for both the unperturbed and perturbed initial conditions. Moreover, the quadratic controller circulates the fluid in opposite directions to effectively heat the fluid regardless of the initial conditions considered here. This shows that the aforementioned plume formation behaviour possesses some resilience towards perturbations. The degree of resilience and robustness against perturbations in general requires further research though.

Future work will be focussed on experimental investigation of the results for both the bang-bang controller and the quadratic controller. Further research efforts will be focussed on the design and implementation of an observer to reconstruct the spectral decomposition from discrete sensor data. This leads the way to the implementation of both controllers in a practical device.

CHAPTER 5

Numerical feasible model and field estimation for scalar transport

Abstract - *Transport of scalar quantities (such as heat and/or chemical species) by reorienting fluid flows is fundamental to the effective operation of various industrial applications, ranging from resource extraction by subsurface reservoir flows to processing of foodstuffs or chemicals. Fluid flows typically consist of the periodic reorientation of a laminar base flow in either space or time in these applications (e.g. implemented by baffles or pump schemes). Dedicated closed-loop flow control based on the scalar field can significantly boost fluid heating. However, practical application of dedicated closed-loop flow control for scalar transport is often inhibited by the unavailability of the complete scalar field. In this chapter an estimator (or observer) is developed that can rapidly reconstruct the scalar field based on discrete sensor data. The estimator is implemented on a scalar transport problem that is representative for the applications of interest; heating of an initially cold fluid surrounded by a hot boundary by stirring. Field estimation is posed as an optimal estimation problem to design a Luenburger estimator. The estimation accuracy is investigated numerically for heat transport governed by mere diffusion, the base flow and a periodic flow. Results show rapid and accurate field reconstruction is feasible and therefore help in developing dedicated closed-loop flow control and enhance transport in practice.*

Supplementary material to this chapter is provided in Appendices D, E, F and G.

5.1 Introduction

Scalar transport (of heat and/or mass) is a key element to various industrial/medical processes. Scalar transport is indispensable during, for example, manufacturing of ingredients/products in the foodstuffs industry [101, 102] or the polymer industry [111]. It also plays a vital role during resource extraction from underground oil/gas/thermal reservoirs [112] or chemical species mixing in the pharmaceutical industry [113]. Accelerating scalar transport can potentially result in faster and/or more (energy) efficient operation of the abovementioned applications. Recent research has shown that dedicated control strategies can significantly enhance scalar transport [25, 55]. Thereby potentially reducing the time and/or (material) cost of operating/manufacturing an application/product. The practical application of dedicated control strategies requires the complete scalar field in order to function. However, the scalar field is often only partially available through a finite set of sensors. The estimation of the scalar field based on discrete sensor data is therefore essential to boost transport in real-time.

The estimation the scalars can be performed by a state estimator. The term "state estimator" is interchangeable with the term "state observer" – well-known in the control community – in this thesis. However, state estimator is used throughout this thesis. Various techniques are available for state reconstruction or estimation in lumped parameter models, where the state evolution is governed by a relatively small set of ordinary differential equations (ODEs) (i.e. the number of states $n \sim \mathcal{O}(10)$). Heating of a two dimensional ($2D$) cold fluid by a hot boundary is studied in this work as a representative case study of the above applications. The scalar quantities considered here (and in the applications of interest) depend on both space *and* time. As a consequence, the evolution of these quantities is typically modelled/captured by partial differential equations (PDEs). State estimation for ($2D$) distributed parameter models, whose evolution is typically governed by PDEs, has received significantly less attention than state estimation in lumped parameter models, where the state evolution is governed by a small set ODEs [114]. Numerous numerical schemes can be employed to discretize the ($2D$) PDE resulting in a set of ODEs (e.g. see books [78, 115]). Typically, a large state dimension n is required to perform accurate numerical simulations (i.e. the number of states $n \sim \mathcal{O}(10^4)$). This renders most state estimation techniques developed for ODEs too time-consuming for real-time scalar field estimation. Nonetheless various design methods have been developed for estimators based on the (extended) Kalman or Luenburger filter [42, 37, 34, 38], the backstepping method [116, 40] or nonlinear/robust estimator design [31, 32, 117]. However, most estimator designs for $2D$ PDEs are investigated theoretically and/or numerically. Moreover, studies of estimators in practice are mostly restricted to a single dimension in space. Thus far, the estimator presented by Lausterer et al. [42] remains one of the few practical studies of scalar field estimation in two dimensions.

This chapter aims to contribute to the existing literature in several ways. First, practical application of dedicated closed-loop flow control for boosting scalar transport is often inhibited by the unavailability of the complete scalar field. Hence, developing a scalar field estimator cab aid the practical adoption of flow controllers in industry. Second, scalar field reconstruction can aid in real-time detection of malfunctions that result from faults in, e.g., sensors or actuators during the operation of industrial applications [26]. Malfunction detection requires a good estimate of a relevant transport measure that adequately captures the operational performance of the application in question. Rapid reconstruction can therefore help develop dedicated closed-loop flow control and enhance transport in practice. Third, research into field reconstruction of $2D$ systems described by PDEs has, to the author's best knowledge, mostly dealt with their theoretical development. The work in this chapter therefore distinguishes itself from other studies on state estimators in $2D$ PDEs in [42, 116, 40, 34, 118, 117] by applying the developed scalar field estimator on a practically realizable system; the RAM. The field estimator, developed in this chapter, is experimentally investigated in Chapter 6 on the experimental RAM.

This chapter is structured as follows. In Section 5.2, the model and resulting system description we use for the reconstruction of a scalar field is presented. In Section 5.3, we present the methods that are used to identify model parameters, place sensors and design the scalar field estimator. In Section 5.4, we numerically investigate field reconstruction performance of a representative case study. Several key transformations of the model are implemented before it is used for parameter identification and state estimation. These model transformations, together with their presentation in this chapter, estimator design and numerical simulations are indicated in Figure 5.1. Finally, conclusions and recommendations for further development are presented in Section 5.5.

5.2 Scalar transport in Stokes flows

5.2.1 Experimental configuration

An experimental setup, known as the $2D$ Rotated Arc Mixer (RAM) [17], is considered here. Figure 5.2 shows the experimental $2D$ RAM in more detail. The RAM consists of a fluid container encircled by an annulus, a thermal camera and controller (see $1-3$ in Figure 5.2a). The fluid is contained inside a $2D$ circular domain $\mathcal{D}$, which is surrounded by a hot boundary $\partial\mathcal{D}$ at a constant temperature T_∞. The estimation of scalar transport is studied by considering fluid heating of an initially cold fluid at temperature T_0.

The observed fluid container contains multiple apertures of arc-length Δ as shown in Figure 5.2a. The apertures are covered by belts, which can move tangentially along the boundary by actuating a belt-pulley assembly. Radial tensioners prevents leaking at the belt aperture interfaces. Fluids inside the container are heated by a hot boundary $\partial\mathcal{D}$ (see Figure 5.2b). The boundary $\partial\mathcal{D}$ is heated by circulating a water-glycerol mixture through the annulus. Temperatures inside the annulus are sampled with four standard PT100 sensors and fed back to a thermal

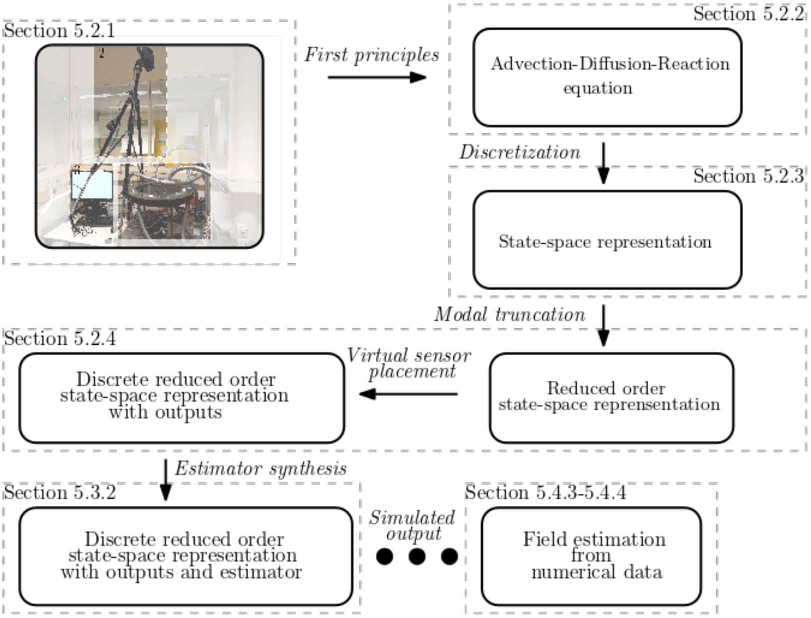
Section 5.2.1
First principles
Section 5.2.2
Advection-Diffusion-Reaction equation
Discretization
Section 5.2.3
State-space representation
Modal truncation
Section 5.2.4
Discrete reduced order state-space representation with outputs
Virtual sensor placement
Reduced order state-space reprensentation
Estimator synthesis
Section 5.3.2
Discrete reduced order state-space representation with outputs and estimator
Simulated output
Section 5.4.3-5.4.4
Field estimation from numerical data

Figure 5.1: A flow chart with an outline of Chapter 5 showing, in particular, the various models introduced throughout this chapter.

bath. The thermal bath (Thermal Scientific Haake Bath K41) uses the average annulus temperature to enforce a *constant* temperature inside the annulus. The thermal bath enforces an annulus temperature T_∞ that is $10°C$ higher than T_0. However, fluid temperatures inside the thermal bath are at T_0 at the beginning of each experiment. Fluids inside the annulus thus undergo a brief transient period of heating before reaching the required T_∞. Fluid heating inside $\mathcal{D}$ occurs as long as $T_0 < T_\infty$. Experiments are initialized *after* temperatures inside the annulus reach T_∞ (i.e. to within $0.05\ °C$).

Temperature fields are obtained in the experimental RAM by a thermal camera (see 2 in Figure 5.2a). The thermal camera (FLIR T650SC [119]) captures infrared irradiation emitted and/or reflected by the fluid and the surroundings. The camera heats up during the experiments to a temperature above the ambient temperature during the experiment. This means the camera also emits infrared irradiation itself. Heating of the camera during experiments can thus potentially influence the measured temperature field. The camera is therefore placed under an angle at the elevated position as shown in Figure 5.2a. Such placement provides a mostly unobstructed view of the container without reflecting infrared irradiation generated by the camera. However, the camera placement results in image distortions on top of any regular lens distortions (e.g. the circular boundary $\partial\mathcal{D}$ becomes an ellipse). Temperature fields are therefore processed by purpose built

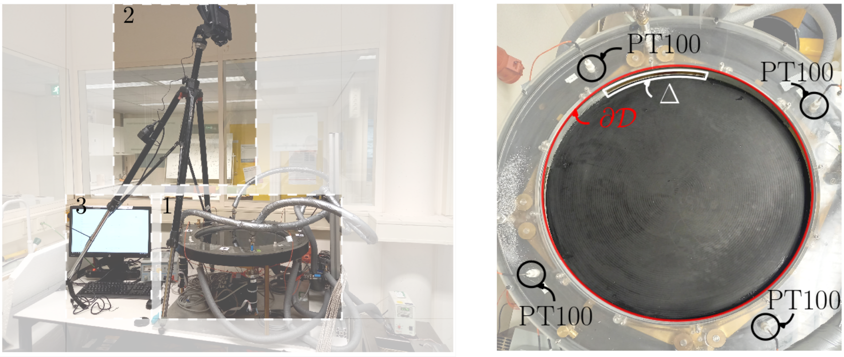

(a) Experimental setup

(b) Top view.

Figure 5.2: The (a) configuration of the experimental RAM with the fluid container (1), the thermal camera (2) and the controller (3). Top view (b) of the container from the perspective of the thermal camera.

software to compensate for both camera and lens distortions. Post-processed temperature fields will be used in both parameter identification and a comparative study to gauge field estimation quality in Section 5.4. Finally, a set of regular J-type thermal couples – with five-point calibration – is included for the measurement of the ambient temperature T_a. The initial and boundary temperatures – important for normalization – can thus be measured independently. The initial temperature T_0 is sampled at the start of each experiment. Both ambient temperature sensor and thermal camera are queried to obtain T_0 (e.g. $T_a(0) \equiv T_0$).

Experiments in this work use similar experimental settings as presented by Baskan et al. [17]. Again, the layered fluid consists of a bottom layer with a water-glycerol mixture and a top layer of silicone-oil. This inhibits bottom contact such that three-dimensional flow effects are negligible and fluid flows can be considered two-dimensional. Bottom and top layer thickness are changed, with respect to Baskan et al. [17], to $0.006\ m$ and $0.004\ m$, respectively. The increased layer thickness of the water-glycerol mixture ensures horizontal levelling of the RAM is less stringent. The thermal camera, ambient sensor and thermal bath are all sampled *and* operated at a maximum sampling frequency of $1/30$ Hz. Other experimental settings, that influence heat and mass transport in the experimental RAM, are shown Table 5.1.

5.2.2 Heat transport model and configuration

Figure 5.3a shows a schematic configuration of the top-view observed with thermal camera in the experimental RAM in Figure 5.3b. The experimental RAM has a single open surface, which is used to measure the fluid temperature $T(\boldsymbol{x}, t)$ with

Table 5.1: Fluid properties and configuration measures relevant to experiments.

Parameter	**Magnitude**	**Unit**
Aperture Δ	$\pi/4$	rad
Radius R	0.25	m
Sample time T_s	30	s
Density silicon-oil ρ_o	970	kg/m^3
Density mixture $\rho_m{}^\dagger$	1186	kg/m^3
Kinematic viscosity silicon-oil ν_o	0.01	m^2/s
Kinematic viscosity mixture $\nu_m{}^\dagger$	$21.88 \cdot 10^{-6}$	m^2/s

†: Calculated at $21\ °C$ for mixture with $0.33\ L$ water and $0.67\ L$ glycerol based on method in [120].

a thermal camera. A fluid flow is induced by viscous drag due to a moving boundary segment (of arclength Δ). The fields associated with these moving segments reduce to a Stokes flow under strongly laminar flow conditions (i.e. negligible inertia and rapid fluid response). Figure 5.3b shows the flow field induced by a single moving segment, which is henceforth referred to as the base flow.

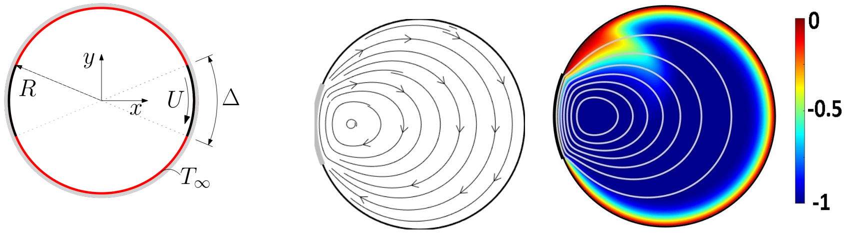
(a) Configuration.

(b) Flow 1.

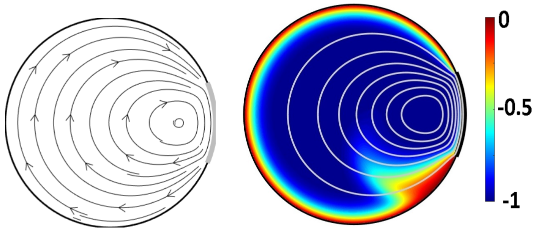
(c) Flow 2.

Figure 5.3: The (a) configuration of a boundary heated fluid, (b) the induced base flow (left) and a typical associated temperature field (right) and (c) the reoriented flow (left) and a typical associated temperature field (right) due to wall motion U at the aperture.

Scalar transport inside the container is “driven” by two mechanisms, i.e., i) diffusion (or conduction) and ii) advection (or convection). Such transport is typically modelled by the well-known advection-diffusion-reaction equation (ADRE) as

$$\frac{\partial T(\boldsymbol{x},t)}{\partial t} = -\boldsymbol{v}(\boldsymbol{x},t)\cdot\boldsymbol{\nabla}T(\boldsymbol{x},t) + Pe^{-1}\Delta T(\boldsymbol{x},t) + f\left(\boldsymbol{x},t\right), \tag{5.1}$$

where T the temperature field, $\boldsymbol{v}$ the fluid flow field, $\Delta = \boldsymbol{\nabla}^2$ the Laplace operator, Pe the Péclet number, $\boldsymbol{x} \in \mathcal{D}$ the position vector and $t \in \mathbb{R}_0^+$ non-dimensional time. Heating by diffusion and advection both serve to transport heat (in)to the fluid inside the container. The sink term $f\left(\boldsymbol{x},t\right)$ in (5.1) models convective heat losses at the open fluid-ambient interface. This heat loss to the ambient is known to significantly impact long-term heating behaviour in the experimental RAM [17].

Fluids are in direct contact with the surrounding air in the experimental RAM (shown in Figure 5.2a). Contact between the fluid and environment introduces heat loss that can influence the temperature field $T(\boldsymbol{x},t)$ as a result. This heat loss at the fluid-environment interface can be substantial for long experiments [17]. The ambient heat loss can be described as a sink term by

$$f(\boldsymbol{x},t) = \kappa(\boldsymbol{x})\left(T_a(t) - T(\boldsymbol{x},t)\right), \tag{5.2}$$

where $\kappa(\boldsymbol{x})$ a (convective) heat transfer coefficient and $T_a(t)$ the ambient temperature. Heat will thus be lost to the environment if the *local* fluid temperature exceeds the ambient temperature (i.e. $T_a(t) < T(\boldsymbol{x},t)$). The heat transfer coefficient $\kappa(\boldsymbol{x})$ is spatially dependent, because the convective heat loss to the environment is not necessarily the same everywhere. However, modelling a spatially dependent $\kappa(\boldsymbol{x})$ requires *a priori* knowledge of any ambient flow conditions. The spatial and temporal dependency of both the heat transfer coefficient is assumed negligible. The accuracy of these assumptions are examined further in Section 5.4.1.

The flow field $\boldsymbol{v}$ in (5.1) is considered solenoidal as mass is conserved and density is independent of T inside the container (i.e. the considered flow fields are divergence-free and satisfy $\boldsymbol{\nabla}\cdot\boldsymbol{v} = 0$). We consider sufficiently slow flow velocities and negligible fluid inertia so that the flow field approaches the Stokes limit and instantaneously starts upon activation of the aperture. Fluid flows are induced by I moving boundary segments of arc-length Δ resulting in

$$\boldsymbol{v}_i(\boldsymbol{x},t)|_{\partial\mathcal{D}} = \begin{cases} U_i\boldsymbol{e}_\theta & \text{if}|\theta-(i-1)\Theta| \leq \Delta/2 \\ 0 & \text{otherwise} \end{cases}, \tag{5.3}$$

where $\boldsymbol{e}_\theta$ the tangential unit vector, U_i the non-dimensional velocity of the moving boundary segment and i the aperture. In this work, a RAM with two apertures ($I = 2$), which can each induce a fluid flow, is considered. The activation of a moving boundary segment at either one of these apertures results in the flow fields and temperature fields shown in figures 5.3b and 5.3c. Here, only a single moving boundary segment can be activated for an activation time τ. In this work, flows are (de)activated for a total activation time τ_{tot} where $\tau_{tot} = \mathcal{T}\tau$ for $\mathcal{T} > 0$

samples. Flows are activated according to an “orientation scheme” $u(t)$ where $u(t) \in \mathcal{U}$ with $\mathcal{U} = \{u_0, u_1, \ldots, u_n\}$. For example, $u(t) \in \mathcal{U}$ with the orientation scheme $\mathcal{U} = \{1, 2, 0\}$ consecutively activates flows $\boldsymbol{v}_1$, $\boldsymbol{v}_2$ and no flows. Both apertures can only circulate the fluid in clockwise direction (i.e. $U_1 = U_2 = U \neq 0$). As a result, $\boldsymbol{v}_2$ differs from the base flow $\boldsymbol{v}_1$ by a mere reorientation Θ. Both moving boundary segments are considered stationary for $i \equiv 0$ (i.e. thus resulting in $\boldsymbol{v}_i(\boldsymbol{x}, t) = \boldsymbol{0}$). An analytical expression for the resulting (normalized) flow field $\boldsymbol{v}_i$ in the RAM is available as presented by Hwu et al. [70].

The ADRE in (5.1) including ambient heat loss, according to (5.2), can be expressed as

$$\begin{aligned} \frac{\partial \widetilde{T}(\boldsymbol{x}, t)}{\partial t} &= \left(-\boldsymbol{v}_i(\boldsymbol{x}) \cdot \boldsymbol{\nabla} + Pe^{-1}\Delta - \kappa\right) \widetilde{T}(\boldsymbol{x}, t) + \kappa \widetilde{T}_a(t) \\ &= \mathcal{A}^{(i)}\left(\boldsymbol{x}\right) \widetilde{T}(\boldsymbol{x}, t) + \kappa \widetilde{T}_a(t) \end{aligned}, \tag{5.4}$$

where $\widetilde{T}(\boldsymbol{x}, t) \equiv \left(T(\boldsymbol{x}, t) - T_0\right) / \left(T_0 - T_\infty\right) - 1$ the normalized *transient* temperature field and $\widetilde{T}_a \equiv \left(T_a - T_0\right) / \left(T_0 - T_\infty\right) - 1$ the normalized ambient temperature. Here, operator $\mathcal{A}^{(i)}\left(\boldsymbol{x}\right)$ is time invariant as long as only a single Stokes flow $\boldsymbol{v}_i$ is activated *or* deactivated at a time. The superscript i indicates whether heat transport includes advection due to an induced fluid flow ($i \neq 0$) or merely consists of diffusion ($i = 0$).

Incorporating the heat loss term (5.2) in (5.4) simultaneously i) influences the operator $\mathcal{A}^{(i)}$ (i.e. heat transfer coefficient κ influences $\mathcal{A}^{(i)}$) and ii) introduces a constant heating rate in (5.4). The term containing the normalized ambient temperature in (5.4) results in an inhomogeneous steady-state (or equilibrium) temperature field. Local differences between the temperature field and the ambient temperature determine the deviation of the temperature field from an otherwise homogeneous temperature field at T_∞. The inhomogeneous steady-state deviates from the boundary temperature for any $T_a \neq T_\infty$.

Model parameters rely on the configuration of the considered thermal flow system. Parameters relevant for the RAM are given by [17]

$$Pe = \frac{R^2}{\alpha T_c}, \quad \tau = \frac{\xi T_s}{T_c}, \tag{5.5}$$

where T_c the characteristic time scale, R the radius of the container, α the thermal diffusivity of the fluid, τ the non-dimensional activation time and T_s the sampling time. Here ξ represents a time scaling factor which, following the results from Baskan et al. [69], is used to match the model with the experiments. The scaling factor is assumed unknown since the layer thickness in the experiments in this thesis deviates form those in the experiments by Baskan et al. [69]. The heat transfer coefficient κ and thermal diffusivity α are also unknown in this work and these parameters, together with ξ, will be estimated in Section 5.3.1. Hence, the thermal characteristics of both the ambient environment and the silicone oil can deviate with respect to previous work (see Section 5.2.1). The characteristic time scale T_c represents either the advection time scale or the diffusion time scale when heat transport is driven by a flow or mere diffusion. They are defined as either $T_c = R/U$ or $T_c = R^2/\alpha$, respectively.

5.2.3 State-space representation of heating

The operator $\mathcal{A}^{(i)}$ in (5.4) is spatially dependent due to the introduction of both flow and diffusion. Real-time computation of $\widetilde{T}$ requires a spatial (and temporal) discretization of (5.4) though. Standard numerical computation schemes (e.g. FVM or FEM) can be used to discretize the PDE in (5.4) on an, in principle, arbitrary discrete grid $\boldsymbol{D}$. As a result of discretization, heat transport on $\boldsymbol{D}$ is described by a set of ODEs of the form

$$\frac{\mathrm{d}\widetilde{\boldsymbol{T}}(t)}{\mathrm{d}t} = \boldsymbol{A}^{(i)}(\boldsymbol{U}, Pe, \kappa)\widetilde{\boldsymbol{T}}(t) + \kappa\boldsymbol{b}\widetilde{T}_a(t), \tag{5.6}$$

where $\boldsymbol{U}^\dagger = \begin{bmatrix} U_1 & U_2 \end{bmatrix}$ represents the velocity vector with the velocities of each moving boundary segment that induces a fluid flow according to (5.3), $\widetilde{\boldsymbol{T}}^\dagger(t) = \begin{bmatrix} \widetilde{T}(\boldsymbol{x}_1, t) & \cdots & \widetilde{T}(\boldsymbol{x}_N, t) \end{bmatrix}$ the vector with N nodal transient temperatures on the discrete grid $\boldsymbol{D}$, $\boldsymbol{A}^{(i)}$ the state matrix that represents the discretized version of $\mathcal{A}^{(i)}$ and $\boldsymbol{b}$ the "input" vector that incorporates the effect of $\widetilde{T}_a$. The fluid flow (or absence thereof) influences the state matrix $\mathcal{A}^{(i)}$ by altering the heating dynamics and the normalized ambient temperature acts as an uncontrolled *constant* input in (5.6). Both the state matrix $\boldsymbol{A}^{(i)}$ and the input vector $\boldsymbol{b}$ depend on the employed discretization scheme and are linear time-invariant (LTI) in the RAM either with or without fluid flow. Heat-transport without any fluid flow is governed by both diffusion *and* the heat-loss term according to (5.1). Heat-transport without any fluid flow is referred to as mere diffusion henceforth in this chapter. This slight abuse of terminology serves to better clarify the fundamental difference between the heat transport mechanisms in the models used throughout this chapter. In addition, both $\boldsymbol{A}^{(i)}$ and $\boldsymbol{b}$ explicitly depend on κ and the state matrix also depends explicitly on α when a flow is present (i.e. through the Péclet number). This explicit dependence of $\boldsymbol{A}^{(i)}$ on these parameters is henceforth omitted for notational convenience. Reorientations of flow fields by Θ result in the same reorientation by Θ of $\boldsymbol{A}^{(i)}$ under current conditions (i.e. the considered Stokes flows only differ from each other by a reorientation angle of Θ). This reorientation is captured by a reorientation matrix $\boldsymbol{R}_\Theta$ resulting in matrices of the form

$$\boldsymbol{A}^{(i)} = \boldsymbol{R}_\Theta^{(i-1)}\boldsymbol{A}^{(1)}\boldsymbol{R}_\Theta^{(1-i)}, \tag{5.7}$$

where $i = 1, 2$ and $\boldsymbol{R}_\theta^{-1} = \boldsymbol{R}_\theta^\dagger$.

The finite dimensional relation in (5.6) is convenient as it resembles a "classical" LTI state-space representation upon viewing the normalized ambient temperature and fluid flow(s) as inputs. Here, either a single (reoriented) flow is activated at a time or all flows are deactivated (i.e. heat transport is governed by mere diffusion) for a time span of τ. Time span τ represents the non-dimensional discrete sampling time of the system according to (5.5). The similarity of (5.6) with the well-known LTI state-space representation means that solutions can be described by [121]

$$\widetilde{\boldsymbol{T}}(t) = \boldsymbol{P}^{(i)}(t_0, t)\widetilde{\boldsymbol{T}}(t_0) + \int_{t_0}^{t} \kappa \boldsymbol{P}^{(i)}(\xi, t)\boldsymbol{b}\widetilde{T}_a(t)\mathrm{d}\xi. \tag{5.8}$$

The solution integral of (5.8) for a *constant* normalized ambient temperature $\widetilde{T}_a(t)$ can be simplified to

$$\left[\int_{t_k}^{t_{k+1}} \kappa \boldsymbol{P}^{(i)}(t_k, \zeta)\boldsymbol{b}\mathrm{d}\zeta\right] \widetilde{T}_a(t_k) = \kappa \left(\boldsymbol{P}^{(i)}\left(t_k, t_{k+1}\right) - \boldsymbol{I}\right) \left(\boldsymbol{A}^{(i)}\right)^{-1} \boldsymbol{b}\widetilde{T}_a(t_k), \tag{5.9}$$

if $\widetilde{T}_a(t)$ is assumed constant at $\widetilde{T}_a(t_k)$ throughout the time interval $t \in [t_k, t_{k+1}]$. The resulting simplification of (5.8) for a *piece-wise constant* normalized ambient temperature $\widetilde{T}_a(t)$ is thus given by

$$\widetilde{\boldsymbol{T}}(t_{k+1}) = \boldsymbol{P}_{\tau}^{(i)}\widetilde{\boldsymbol{T}}(t_k) + \boldsymbol{B}_{\tau}^{(i)}\widetilde{T}_a(t_k), \tag{5.10}$$

where $\boldsymbol{P}_{\tau}^{(i)} = \boldsymbol{P}^{(i)}(t_k, t_{k+1})$ and $\boldsymbol{B}_{\tau}^{(i)} = \boldsymbol{B}^{(i)}(t_k, t_{k+1})$ for $k \geq 0$ are introduced for notational convenience. The matrices in (5.10) can thus be described by

$$\boldsymbol{P}_{\tau}^{(i)} = e^{\boldsymbol{A}^{(i)}\tau} = \boldsymbol{R}_{\Theta}^{(i-1)} e^{\boldsymbol{A}^{(1)}\tau} \boldsymbol{R}_{\Theta}^{(1-i)}, \quad \boldsymbol{B}_{\tau}^{(i)} = \kappa \left(\boldsymbol{P}_{\tau}^{(i)} - \boldsymbol{I}\right) \left(\boldsymbol{A}^{(i)}\right)^{-1} \boldsymbol{b}. \tag{5.11}$$

Relation (5.11), arising from (5.7), is a key enabler to construct a numerically efficient model for fast state estimation with (switching) multiple flows as will be shown in Section 5.3.

Solution (5.10) describes scalar transport by either steady Stokes flow(s), e.g. for $\boldsymbol{U} = \begin{bmatrix} U & 0 \end{bmatrix}$, or by diffusion, i.e. with $\boldsymbol{U} = \begin{bmatrix} 0 & 0 \end{bmatrix}$, on the discrete grid $\boldsymbol{D}$. This grid is the discrete counterpart of $\mathcal{D}$, which can, without loss of generality, be chosen arbitrarily. Here, the points in the grid correspond to pixels of the thermal images obtained with the thermal camera (see Section 5.2.1). Nodal temperatures in $\widetilde{\boldsymbol{T}}(t)$ thus correspond to the individual pixels in the thermal image. Hence the thermal camera provides “full” access to the temperature field $\widetilde{\boldsymbol{T}}(t)$. Numerical solutions for $\widetilde{\boldsymbol{T}}$ in (5.10) approach the solution $\widetilde{T}$ in (5.4) for $N \rightarrow \infty$.

5.2.4 Model reduction of the state-space representation

In a practical application, the temperature field is measured with a finite amount of sensors that sample the field at discrete locations. Access to the “full state” $\widetilde{\boldsymbol{T}}(t)$ is therefore severely restricted. Placing sensors at the same location as some nodes in $\boldsymbol{D}$ results in

$$\boldsymbol{y}(t) = \boldsymbol{C}\widetilde{\boldsymbol{T}}(t), \tag{5.12}$$

where the output matrix $\boldsymbol{C} \in \mathbb{R}^{p\times N}$ only contains non-zero elements at p locations inside $\boldsymbol{D}$ such that $y_i(t) = T(\boldsymbol{x}_i, t)$. Some nodal temperatures on $\boldsymbol{D}$ will serve as "virtual" sensors for the state estimator in Section 5.4 (i.e. only some entries of $\boldsymbol{T}(\boldsymbol{x}, t)$ are considered measured). The outputs in (5.12) are thus measured at fixed sensor positions here. Access to the complete temperature field via the thermal camera enables the quantitative analysis of this state estimator by comparing the reconstructed fields, estimated solely based on the outputs in (5.12), to the measured fields (also in Section 5.4).

Relations (5.10)-(5.12) describe the thermal flow system as a discrete state-space representation. Such a representation is useful to i) perform system identification, ii) reduce the model for computational efficiency and iii) develop an accurate field estimator. For equidistant sampling with sampling "time" τ, (5.10)-(5.12) are also linear and time-invariant. Relation (5.11) shows that input matrix $\boldsymbol{B}_\tau^{(i)}$ also relies on the activated flow i. In Chapter 6, $\boldsymbol{U}$ is considered either constant or periodic. In the latter case, relations (5.8)-(5.12) describe a discrete hybrid system where the impact of the *uncontrolled* input $\widetilde{T}_a$ on heat transport depends on the activated (or deactivated) flow i.

Models using regular spatial discretization schemes – resulting in systems of the form (5.10)-(5.12) – can have a large amount of states. The state-space representation in (5.10)-(5.12) consists of as many states as there are spatial nodes in the discrete grid. Numerical implementation of (5.6) requires a relatively dense grids for sufficiently accurate simulations though (i.e. containing $N \gtrsim \mathcal{O}(10^4)$ elements for the RAM [55]). As a result, the state matrix $\boldsymbol{A}^{(i)}$ contains N^2 elements. The large dimension of the state matrix $\boldsymbol{A}^{(i)}$ results in long computation times. Fast computation of $\widetilde{\boldsymbol{T}}_k$ by a low-dimensional model ensures rapid numerical computation in real-time, which is especially important upon incorporating state estimation in model based closed-loop control.

Therefore, the dimension of the state matrix is reduced by reducing the considered number of modes in the modal decomposition of $\boldsymbol{A}^{(i)}$. The reduced model captures the evolution of the transient temperature field $\widetilde{\boldsymbol{T}}$ by truncating the Perron-Frobenius operator $\boldsymbol{P}_\tau^{(i)}$ to M modes – with $M \ll N$ – as shown in Lensvelt et al. [55]. This reduction boosts the computational efficiency of (5.10)-(5.12) such that $\widetilde{\boldsymbol{T}}$ can be rapidly obtained. Relation (5.11) reveals that the truncation of $\boldsymbol{P}_\tau^{(i)}$ can be obtained by simply reorienting the truncation of $\boldsymbol{P}_\tau^{(1)}$ associated with the base flow. The discrete operator $\boldsymbol{A}^{(i)}$ is decomposable in an eigenvector-eigenvalue decomposition according to [55]

$$\boldsymbol{A}^{(i)} = \boldsymbol{V}^{(i)}\boldsymbol{\Lambda}^{(i)}\left(\boldsymbol{V}^{(i)}\right)^{-1}, \quad \boldsymbol{V}^{(i)} = \boldsymbol{R}_\Theta^{(i-1)}\boldsymbol{V}^{(1)}, \tag{5.13}$$

where the eigenvectors in $\boldsymbol{V}^{(i)}$ and eigenvalues $\boldsymbol{\Lambda}^{(i)}$ of $\boldsymbol{A}^{(i)}$ represent the eigenvalue-eigenfunctions pairs of the Perron-Frobenius operator on the discrete grid $\boldsymbol{D}$. Moreover, observe that the eigenvalues are invariant to reorientation in the RAM such that $\boldsymbol{\Lambda}^{(i)} = \boldsymbol{\Lambda}^{(1)}$ [16]. The higher order modes of the advection-diffusion operator typically become progressively more stable, viz. $Re(\lambda_m) \leq 0$ becomes smaller as m increases [122]. The *constant* heat transfer coefficient κ has no influence on this property. Therefore, it is assumed here that eigenvalues in (5.13) are ordered such that $Re(\lambda_1) \geq \ldots \geq Re(\lambda_N)$.

Fast and accurate simulations requires including a sufficient number of eigenvalues and eigenvectors (or thermal "eigenmodes"). Various methodologies are available for model reduction (e.g. see review by Besselink et al. [123]). However, ordering of the eigenvalues makes a separation into fast and slow thermal modes well suited for the ADRE. The M slowest eigenvalues are retained in the model by introducing a transformation matrix of the form

$$\widetilde{\boldsymbol{T}}(t_k) \approx \boldsymbol{G}^{(i)}\boldsymbol{\alpha}^{(i)}(t_k), \qquad \boldsymbol{G}^{(i)} = \begin{bmatrix}\boldsymbol{V}_1^{(i)} & \cdots & \boldsymbol{V}_M^{(i)}\end{bmatrix}. \tag{5.14}$$

where the definition of $\boldsymbol{V}^{(i)}$ leads to the following relations

$$\boldsymbol{G}^{(i)} = \boldsymbol{R}_\Theta^{i-1}\boldsymbol{G}^{(1)}, \quad \left(\boldsymbol{G}^{(i)}\right)^+ = \left(\boldsymbol{G}^{(1)}\right)^+ \boldsymbol{R}_\Theta^{1-i}, \tag{5.15}$$

and $(\quad)^+$ represents the well-known Moore-Penrose pseudoinverse used to "invert" $\boldsymbol{G}^{(i)}$. The inversion is used to determine the instantaneous spectral coefficients $\boldsymbol{\alpha}^{(i)}(t_k)$ from the temperature field $\widetilde{\boldsymbol{T}}(t_k)$ according to (5.14). The introduction of $\boldsymbol{G}^{(i)}$ means that (5.8)-(5.12) can be rewritten, by employing the pseudoinverse $\left(\boldsymbol{G}^{(i)}\right)^+$, as

$$\begin{aligned} \boldsymbol{\alpha}^{(i)}(t_{k+1}) &= \widetilde{\boldsymbol{A}}^{(i)}\boldsymbol{\alpha}^{(i)}(t_k) + \widetilde{\boldsymbol{B}}^{(i)}\widetilde{T}_a(t_k) \\ \boldsymbol{y}(t_k) &= \widetilde{\boldsymbol{C}}^{(i)}\boldsymbol{\alpha}^{(i)}(t_k) \end{aligned}, \tag{5.16}$$

with matrices defined as

$$\widetilde{\boldsymbol{A}}^{(i)} = \left(\boldsymbol{G}^{(i)}\right)^+ \boldsymbol{P}_\tau^{(i)}\boldsymbol{G}^{(i)} \quad \widetilde{\boldsymbol{B}}^{(i)} = \left(\boldsymbol{G}^{(i)}\right)^+ \boldsymbol{B}_\tau^{(i)}, \quad \widetilde{\boldsymbol{C}}^{(i)} = \boldsymbol{C}\boldsymbol{G}^{(i)}, \tag{5.17}$$

The above is analogous to a Rayleigh-Ritz reduction procedure used in vibration theory [124].

5.3 Estimation of scalar transport

5.3.1 Parameter identification of scalar transport

Field estimation relies on the ability of a model to accurately describe the physical behaviour of a system. Table 5.1 and (5.5) reveal that ξ, α and κ need to be estimated. These parameters need to be (locally) structurally identifiable from the measured outputs in order to get such an estimate. A dynamical system – like (5.10)-(5.11) – is called identifiable if the model parameters, captured in $\boldsymbol{\theta}$, can be *uniquely* determined from the input(s) and the measured output(s) [125, 126] (i.e. $\boldsymbol{U}(t)$, $\widetilde{T}_a$ and $\boldsymbol{y}(t)$ uniquely determine $\boldsymbol{\theta}$). Moreover, a system structure is locally structurally identifiable if and only if, for some set of model parameters $\boldsymbol{\theta}$ in close proximity to some $\boldsymbol{\theta}^*$, the output(s) satisfy $\boldsymbol{y}|_{\boldsymbol{\theta}=\boldsymbol{\theta}_1} \equiv \boldsymbol{y}|_{\boldsymbol{\theta}=\boldsymbol{\theta}_2}$ for $\boldsymbol{\theta}_1 \equiv \boldsymbol{\theta}_2$ and some admissible input(s) [126]. A *sufficient* condition to guarantee that parameters are (locally) structurally identifiable is when the output sensitivity matrix is full rank [126]. Note that parameters can still be identifiable even though the output sensitivity matrix is rank deficient [125]. Nonetheless, satisfying the rank condition on the output sensitivity matrix provides a *guarantee* that the model parameters are consistently and uniquely estimated. Availability of the "full" temperature field with the thermal camera means the output encompasses the entire field $\widetilde{\boldsymbol{T}}(t)$. This means that $\boldsymbol{C} = \boldsymbol{I}$ in (5.12) such that $\boldsymbol{y}(t_k) = \widetilde{\boldsymbol{T}}(t_k)$. The output sensitivity matrix for K snapshots is defined as [125]

$$\boldsymbol{S}^{K-1}(\boldsymbol{\theta}) = \begin{bmatrix} \frac{\partial \widetilde{\boldsymbol{T}}(t_0)}{\partial \theta_1} & \vdots & \frac{\partial \widetilde{\boldsymbol{T}}(t_0)}{\partial \theta_p} \\ \vdots & \ddots & \vdots \\ \frac{\partial \widetilde{\boldsymbol{T}}(t_{K-1})}{\partial \theta_1} & \vdots & \frac{\partial \widetilde{\boldsymbol{T}}(t_{K-1})}{\partial \theta_p} \end{bmatrix}, \tag{5.18}$$

where $\boldsymbol{\theta}$ contains the unknown model parameters. For diffusion both α and ξ show up in τ and thus the columns of $\boldsymbol{S}^{K-1}$ differ by a mere constant (i.e. these parameters are indistinguishable from the output). This means that α and ξ cannot be estimated simultaneously for heat transport by mere diffusion. Therefore, only κ and α are estimated for heat transport by mere diffusion since only these parameters are relevant in that case. Hence, $\boldsymbol{\theta}^\dagger = \begin{bmatrix}\xi & \alpha & \kappa\end{bmatrix}$ and $\boldsymbol{\theta}^\dagger = \begin{bmatrix}\alpha & \kappa\end{bmatrix}$ for the experiment with the base flow and with mere diffusion, respectively. The columns of $\boldsymbol{S}^{K-1}$ can be derived from (5.10) by taking the derivatives where the initial state $\widetilde{\boldsymbol{T}}(t_0)$ is available from the thermal camera. The definition $\boldsymbol{P}_\tau^{(i)}$ in (5.11) inhibits a direct analytical computation of (5.18) for all model parameters in $\boldsymbol{\theta}$. A (partial) numerical computation of the output sensitivity matrix and the derivatives, as presented in Appendix D, is therefore pursued here.

Identification of $\boldsymbol{\theta}$ for the set of ODEs in (5.10)-(5.11) is performed by the minimisation of a model error. Parameter identification in the ADRE is formulated as a least-square problem in time according to

$$J(\boldsymbol{\theta}^*) = \text{arg}\min_{\boldsymbol{\theta}} \sum_{k=1}^{N_T} \widetilde{J}(\boldsymbol{\theta}, t_k), \quad \text{subject to} \quad Re\left(\lambda\left(\widetilde{\boldsymbol{A}}^{(i)}\right)\right) < 0, \tag{5.19}$$

where N_T the amount temperature field snapshots and $\boldsymbol{\theta}^*$ the local minimizer of (5.19). An explicit stability constraint is included in (5.19) to enforce stability during the optimization of J for $\kappa < 0$. This constraint enforces stable eigenvalues in $\boldsymbol{\Lambda}^{(i)}$. Parameter identification on the experiments (in Section 5.4.1) converged faster if $\kappa < 0$ is allowed. Such values for the (convective) heat transfer coefficient imply that heat is added, rather than lost, by convection to the ambient environment. Parameter estimates with $\kappa < 0$ are disregarded though, since such estimates are inconsistent with physics. The model error $\widetilde{J}$ is defined as the L^2 norm between the measured and estimated temperature fields on $\mathcal{D}$. The integral, required to calculate the L^2 norm, is approximated by an area weighed summation on the discrete grid $\boldsymbol{D}$ resulting in a model error as

$$\widetilde{J}(\boldsymbol{\theta}, t_k) = \boldsymbol{\varepsilon}^\dagger(t_k)\boldsymbol{F}\boldsymbol{\varepsilon}(t_k), \qquad \boldsymbol{\varepsilon}(t_k) \equiv \widehat{\boldsymbol{T}}(t_k) - \widetilde{\boldsymbol{T}}(t_k), \tag{5.20}$$

where $\widehat{\boldsymbol{T}}(t_k)$ and $\widetilde{\boldsymbol{T}}(t_k)$ the measured and estimated nodal temperature vectors on $\boldsymbol{D}$, respectively. The matrix $\boldsymbol{F}$ contains the surface area of each node in $\boldsymbol{D}$. The elements of $\boldsymbol{F}$ can be readily obtained for any grid by straightforward linear algebra operations.

Model parameters $\boldsymbol{\theta}$ are estimated by directly optimizing (5.19). The relationship between (5.19) and (5.18) follows from the analysis of a Taylor series expansion around $\boldsymbol{\theta}^*$. The analysis serves to justify the choice of $J(\boldsymbol{\theta})$ in (5.22). Temperature snapshots $\widetilde{\boldsymbol{T}}(t_k)$ evolve according to (5.10) and their evolution therefore depends on $\boldsymbol{\theta}$ (see the discussion below (5.6) and the matrices in (5.11)). The Taylor series expansion of $\widetilde{\boldsymbol{T}}(t_k)$ around $\boldsymbol{\theta}^*$ results in [126]

$$\widetilde{\boldsymbol{T}}(t_k) \approx \widetilde{\boldsymbol{T}}(t_k)\Big|_{\boldsymbol{\theta}^*} + \boldsymbol{S}^{K-1}(\boldsymbol{\theta}^*)\Delta\boldsymbol{\theta}, \quad \Delta\boldsymbol{\theta} = \boldsymbol{\theta} - \boldsymbol{\theta}^*, \tag{5.21}$$

where $\boldsymbol{S}^{K-1}(\boldsymbol{\theta})$ the output sensitivity matrix in (5.18). The substitution of (5.21) into $J(\boldsymbol{\theta})$ reveals a quadratic relationship between $J(\boldsymbol{\theta})$ and $\Delta\boldsymbol{\theta}$ of the form

$$J(\boldsymbol{\theta}) \approx \Delta\boldsymbol{\theta}^\dagger \boldsymbol{H}\Delta\boldsymbol{\theta} + 2\boldsymbol{f}^\dagger\Delta\boldsymbol{\theta} + c, \tag{5.22}$$

with matrices and constants defined as

$$\begin{aligned} \boldsymbol{H} &= \left(\boldsymbol{S}^{K-1}\right)^\dagger \boldsymbol{W}\boldsymbol{S}^{K-1}, \quad \boldsymbol{f} = (\boldsymbol{Y} - \boldsymbol{Z})^\dagger \boldsymbol{W}\boldsymbol{S}^{K-1}, \\ c &= -2\boldsymbol{Z}^\dagger\boldsymbol{W}\boldsymbol{Y} + \boldsymbol{Y}^\dagger\boldsymbol{W}\boldsymbol{Y} + \boldsymbol{Z}^\dagger\boldsymbol{W}\boldsymbol{Z}, \quad \boldsymbol{W} = \begin{bmatrix} \boldsymbol{F} & & \\ & \ddots & \\ & & \boldsymbol{F} \end{bmatrix} \end{aligned} \tag{5.23}$$

where $\boldsymbol{Y}^\dagger = \left[\widetilde{\boldsymbol{T}}^\dagger(t_0) \quad \cdots \quad \widetilde{\boldsymbol{T}}^\dagger(t_{K-1}))\right]\Big|_{\boldsymbol{\theta}^*}$ and $\boldsymbol{Z}^\dagger = \left[\widehat{\boldsymbol{T}}^\dagger(t_0) \quad \cdots \quad \widehat{\boldsymbol{T}}^\dagger(t_{K-1})\right]$. The quadratic form of $J(\boldsymbol{\theta})$ in (5.22) shows that the optimization problem according to (5.22) has a minimum provided that the output sensitivity matrix is full rank. Relation (5.22) in principle only applies in close proximity to $\boldsymbol{\theta}^*$ though. This means that the aforementioned observation only apply locally. Error (5.19) can be minimised by a variety of iterative optimization methods [127]. Here, numerical solutions to (5.19) are obtained by a gradient-based optimization using a interior-point method.

5.3.2 Synthesis of scalar field estimator

The presented estimator synthesis will initially concentrate on the reconstruction of $\widetilde{\boldsymbol{T}}$ when heat transport is solely "driven" by a single flow i. The presented estimator synthesis method also applies to heat transport by mere diffusion ($i = 0$). Restricting the synthesis to a single flow i is motivated by the observation that the pair $(\widetilde{\boldsymbol{C}}^{(i)}, \widetilde{\boldsymbol{A}}^{(i)})$ can be obtained from $(\widetilde{\boldsymbol{C}}^{(1)}, \widetilde{\boldsymbol{A}}^{(1)})$ by a mere reorientation of $\boldsymbol{G}^{(1)}$ according to (5.15). Under certain conditions, the estimator design for flow i is the same as the estimator designed for the base flow $i = 1$. This will be shown below.

For an estimator to estimate $\boldsymbol{\alpha}(t_k)$ – and by extension $\widetilde{\boldsymbol{T}}(t_k)$ – the system (5.14)-(5.17) needs to be observable. A state-space system is observable if the initial condition at t_0 can be determined from the time history of both the inputs and the outputs for any time t_1 with $t_1 > t_0$ [54]. For (5.14)-(5.17) this means that the initial transient temperature field $\widetilde{\boldsymbol{T}}(t_0)$ can be determined from the evolution of both the normalized ambient temperature $\widetilde{T}_a$, the fluid flow(s) i and the outputs in $\boldsymbol{y}(t)$. With the inputs known, observability of the initial conditions solely depends on the pair $(\widetilde{\boldsymbol{C}}^{(i)}, \widetilde{\boldsymbol{A}}^{(i)})$ [121]. The observability of the pair $(\widetilde{\boldsymbol{C}}^{(i)}, \widetilde{\boldsymbol{A}}^{(i)})$ can be investigated by various methods [121]. Here, the Popov-Belevitch-Hautus test is used for its computational efficiency [128]. To satisfy the Popov-Belevitch-Hautus rank test, $\widetilde{\boldsymbol{C}}^{(i)}$ needs to be such that the matrix pair $(\widetilde{\boldsymbol{C}}^{(i)}, \widetilde{\boldsymbol{A}}^{(i)})$ yields

$$\text{rank}\left(\begin{bmatrix}\widetilde{\boldsymbol{A}}^{(i)} - \lambda\boldsymbol{I}\\ \widetilde{\boldsymbol{C}}^{(i)}\end{bmatrix}\right) = M, \tag{5.24}$$

for all $\lambda \in \mathbb{C}$. The matrix $\widetilde{\boldsymbol{A}}^{(i)} - \lambda\boldsymbol{I}$ can only lose rank if and only if λ is an eigenvalue of $\widetilde{\boldsymbol{A}}^{(i)}$. Therefore, it suffices to merely consider (5.24) for the eigenvalues of $\widetilde{\boldsymbol{A}}^{(i)}$. Eigenvalues that satisfy (5.24) are called *observable* and eigenvalues that fail to satisfy (5.24) are called *unobservable*. The pair $(\widetilde{\boldsymbol{C}}^{(i)}, \widetilde{\boldsymbol{A}}^{(i)})$ is called detectable if all the *unobservable* eigenvalues are asymptotically stable. The eigenvalues of the ADRE become progressively more stable the higher the order of the mode [122]. Moreover, eigenvalues associated with the eigenmodes of the ADRE are stable regardless whether scalar transport is driven by a flow or mere diffusion. This implies that any *unobservable* eigenvalue of $\widetilde{\boldsymbol{A}}^{(i)}$ is always stable. Hence, (5.24) is always satisfied for the system matrices in (5.17) and, consequently, system (5.16) is always detectable. Temperature field reconstruction from discrete sensor data with an estimator is thus possible for properly chosen sensor locations. However, the rate at which a sufficiently accurate state estimate can be obtained depends on the estimator's design.

For the design of the temperature field estimator, a state-space system – like (5.16) – needs to be detectable. For such a system, a state estimator will ensure that the state estimate $\overline{\boldsymbol{T}}$ always converges on $\widetilde{\boldsymbol{T}}$. Numerous implementations are available for the implementation of a state estimator, e.g., high-gain (Luenburger) estimators [75] or (extended) Kalman filtering [54]. The normalized ambient temperature $\widetilde{T}_a$ is measured with a set of thermal couples (see Section 5.2.1). Therefore, all the inputs in (5.16) are available during an experiment. This makes full state estimation with a Luenburger estimator well-suited in this work since only $\boldsymbol{\alpha}^{(i)}(t_k)$ is unknown.

The implementation of a Luenburger estimator can be summarized as follows. Consider the estimated state-space system, analogous to (5.16), given by

$$\begin{aligned}\overline{\boldsymbol{\alpha}}^{(i)}(t_{k+1}) &= \widetilde{\boldsymbol{A}}^{(i)}\overline{\boldsymbol{\alpha}}^{(i)}(t_k) + \widetilde{\boldsymbol{B}}^{(i)}\widetilde{T}_a(t_k) + \boldsymbol{L}^{(i)}(\boldsymbol{y}(t_k) - \overline{\boldsymbol{y}}(t_k)),\\ \overline{\boldsymbol{y}}(t_k) &= \widetilde{\boldsymbol{C}}^{(i)}\overline{\boldsymbol{\alpha}}^{(i)}(t_k)\end{aligned} \tag{5.25}$$

where $\overline{(.)}$ indicates the estimate and $\boldsymbol{L}^{(i)}$ the Luenburger estimator gain matrix. Relation (5.25) shows that the estimator injects a weighted output error to correct the estimated state evolution. The evolution of the state estimation error $\boldsymbol{e}^{(i)}(t_k) = \overline{\boldsymbol{\alpha}}^{(i)}(t_k) - \boldsymbol{\alpha}^{(i)}(t_k)$ follows from its substitution into (5.25) resulting in error dynamics as

$$\boldsymbol{e}^{(i)}(t_{k+1}) = \left(\widetilde{\boldsymbol{A}}^{(i)} - \boldsymbol{L}^{(i)}\widetilde{\boldsymbol{C}}^{(i)}\right)\boldsymbol{e}^{(i)}(t_k). \tag{5.26}$$

Measuring the normalized ambient temperature means that $\widetilde{T}_a(t_k)$ vanishes from the error dynamics in (5.26). Accurate estimation thus relies on gain matrix $\boldsymbol{L}^{(i)}$ rendering the error dynamics (5.26) stable. State estimation for discrete system (5.16) requires that closed-loop eigenvalues of the estimators are inside the unit circle (i.e. $\left|\lambda\left(\left(\widetilde{\boldsymbol{A}}^{(i)} - \boldsymbol{L}^{(i)}\widetilde{\boldsymbol{C}}^{(i)}\right)\right)\right| < 1$. Rapid estimation occurs if these eigenvalues are inside a circle with radius $1/o$ for $o > 1$ [129]. In such case, the estimated state converges to the actual state as the error converges to zero (i.e. $\|\boldsymbol{e}_k^{(i)}\|_2 \to 0$ for $k \to \infty$ resulting in $\overline{\boldsymbol{\alpha}}_k \equiv \boldsymbol{\alpha}_k$ for large k). For detectable systems a gain matrix $\boldsymbol{L}^{(i)}$ that ensures asymptotic stability can always be designed. However, $\boldsymbol{L}^{(i)}$ can only influence the observable eigenvalues of the pair $(\widetilde{\boldsymbol{C}}^{(i)}, \widetilde{\boldsymbol{A}}^{(i)})$. As a consequence, the convergence rate of the estimation error $\|\boldsymbol{e}_k\|_2$ will depend on the slowest eigenvalue of $\widetilde{\boldsymbol{A}}^{(i)} - \boldsymbol{L}^{(i)}\widetilde{\boldsymbol{C}}^{(i)}$. Hence, sensor placement should ensure that the state estimator is able to influence/adjust the slowest observable eigenvalues of the pair $(\widetilde{\boldsymbol{C}}^{(i)}, \widetilde{\boldsymbol{A}}^{(i)})$. Sensor placement – viz. the design of $\boldsymbol{C}$ in (5.12) – should thus render the slowest eigenvalues of $\widetilde{\boldsymbol{A}}^{(i)}$ observable as they determine the maximum attainable decay rate of the estimation error (see Section 5.3.3).

The gain matrix $\boldsymbol{L}^{(i)}$ can be designed by employing the duality between detectability/observability and stabilizability/controllability [130]. The duality between control and estimation suggests that standard control techniques can be employed to develop the estimator. Here a standard discrete linear quadratic regulator (LQR) is used to obtain $\boldsymbol{L}^{(i)}$ since the algorithm is more convenient to work with for large system matrices than other methods in `MATLAB` (e.g. pole placement with `place`). The design method is briefly summarized here. The discrete LQR problem minimizes a quadratic cost-function given by [131]

$$J = \sum_{k=0}^{\infty} \left(\boldsymbol{\alpha}_k^{\dagger} \boldsymbol{Q} \boldsymbol{\alpha}_k + \boldsymbol{y}_k^{\dagger} \boldsymbol{R} \boldsymbol{y}_k \right), \tag{5.27}$$

where $\boldsymbol{R}$ a positive definite matrix and $\boldsymbol{Q}$ a positive semidefinite matrix. For a detectable system the estimator gain matrix $\boldsymbol{L}^{(i)}$ that minimizes (5.27) can be determined as

$$\boldsymbol{L}^{(i)} = \left(\boldsymbol{R} + \widetilde{\boldsymbol{C}}^{(i)} \boldsymbol{X}_i (\widetilde{\boldsymbol{C}}^{(i)})^{\dagger} \right)^{-1} (\widetilde{\boldsymbol{C}}^{(i)} \boldsymbol{X}_i (\widetilde{\boldsymbol{A}}^{(i)})^{\dagger}), \tag{5.28}$$

where $\boldsymbol{X}_i$ the positive definite solution to the discrete algebraic Riccati equation (DARE) given by [131]

$$\begin{aligned} \boldsymbol{X}_i =& \widetilde{\boldsymbol{A}}^{(i)} \boldsymbol{X}_i (\widetilde{\boldsymbol{A}}^{(i)})^{\dagger} \\ &- (\widetilde{\boldsymbol{A}}^{(i)} \boldsymbol{X}_i (\widetilde{\boldsymbol{C}}^{(i)})^{\dagger})(\boldsymbol{R} + \widetilde{\boldsymbol{C}}^{(i)} \boldsymbol{X}_i (\widetilde{\boldsymbol{C}}^{(i)})^{\dagger})^{-1}(\widetilde{\boldsymbol{C}}^{(i)} \boldsymbol{X}_i (\widetilde{\boldsymbol{A}}^{(i)})^{\dagger}) + \boldsymbol{Q}. \end{aligned} \tag{5.29}$$

Relations (5.28)-(5.29) suggest that the computation of the gain matrix $\boldsymbol{L}^{(i)}$ requires solving the DARE for each flow i. However, choosing an output matrix which is invariant under reorientation (i.e. $\boldsymbol{C} = \boldsymbol{C}\boldsymbol{R}_{\Theta}^{i-1}$) renders both (5.29) and (5.28) invariant under rotation as well. To see this, observe that rotation invariance of the output matrix means that $\widetilde{\boldsymbol{C}}^{(i)} = \widetilde{\boldsymbol{C}}^{(1)}$. Moreover, the state matrix $\widetilde{\boldsymbol{A}}^{(i)} = \widetilde{\boldsymbol{A}}^{(1)}$ by definition (i.e. this follows from (5.17) since $\boldsymbol{\Lambda}^{(i)} = \boldsymbol{\Lambda}$ in (5.13)). Hence, designing the estimator for the pair $(\widetilde{\boldsymbol{C}}^{(1)}, \widetilde{\boldsymbol{A}}^{(1)})$ is the same as designing the estimator for the pair $(\widetilde{\boldsymbol{C}}^{(2)}, \widetilde{\boldsymbol{A}}^{(2)})$. As a consequence, state estimation with the gain matrix designed for the base flow ($i = 1$) can also be applied to perform state estimation for the reoriented flows ($i > 1$) (i.e. $\boldsymbol{L}^{(1)} = \boldsymbol{L}^{(i)}$). A mathematical derivation of the above discussion is presented in Appendix E.

In Chapter 6 a state estimator will be presented that estimates the field in the presence of a periodic flow. The flow consists of the periodic activation of flows according to $u(t) \in \mathcal{U}$ for reorientation scheme $\mathcal{U} = \{1, 2, 1, \ldots\}$. According to (5.16)-(5.17), the (periodic) switching of flows inevitably leads to a reorientation of the eigenmodes that describe the relevant heating dynamics (i.e. heat transport by flows 1 and 2 is expressed in $\boldsymbol{G}^{(1)}$ and $\boldsymbol{G}^{(2)}$, respectively). As a result, the error dynamics for the periodic activation of flows is described by

$$\begin{aligned}\boldsymbol{\varepsilon}(t_{k+1}) = \boldsymbol{G}^{(2)}(\widetilde{\boldsymbol{A}}^{(2)} - \boldsymbol{L}^{(2)}\widetilde{\boldsymbol{C}}^{(2)}) \left(\boldsymbol{G}^{(2)}\right)^{+} \cdot \\ \cdot \boldsymbol{G}^{(1)}(\widetilde{\boldsymbol{A}}^{(1)} - \boldsymbol{L}^{(1)}\widetilde{\boldsymbol{C}}^{(1)}) \left(\boldsymbol{G}^{(1)}\right)^{+} \boldsymbol{\varepsilon}(t_k).\end{aligned} \tag{5.30}$$

The matrix product $\left(\boldsymbol{G}^{(2)}\right)^{+}\boldsymbol{G}^{(1)}$ describes the transition (or saltation) from heat transport driven by flow 1 to heat transport driven by flow 2 and is also referred to as a saltation matrix [106]. For an output matrix that is invariant under reorientation, the error dynamics in (5.30) can be simplified to

$$\begin{aligned}\boldsymbol{\varepsilon}(t_{k+1}) &= \boldsymbol{R}_{\Theta}^{2} \left(\boldsymbol{R}_{\Theta}^{\dagger}\boldsymbol{G}^{(1)} \left(\widetilde{\boldsymbol{A}}^{(1)} - \boldsymbol{L}\widetilde{\boldsymbol{C}}^{(1)}\right) \left(\boldsymbol{G}^{(1)}\right)^{+}\right)^{2} \boldsymbol{\varepsilon}(t_k), \\ &= \boldsymbol{A}_{per}^{2}\boldsymbol{\varepsilon}(t_k),\end{aligned} \tag{5.31}$$

where $\boldsymbol{R}_{\Theta}^{I} = \boldsymbol{I}$ [132] and $\boldsymbol{L}^{(i)} = \boldsymbol{L}$ based on the discussion following after (5.29) (see Appendix F for derivation of (5.31)). For the state estimator to estimate the temperature field in a periodic flow the error dynamics in (5.31) need to be stable. Hence, the gain matrix $\boldsymbol{L}$ needs to ensure that the eigenvalues of $\boldsymbol{A}_{per}$ in (5.31) are inside the unit circle. However, computation of $\boldsymbol{A}_{per}$ and its eigenvalues typically require long computation times due to its dimension (i.e. $\boldsymbol{A}_{per} \in \mathbb{C}^{N \times N}$). Here, the stability of the error dynamics for the switching system is gauged by investigating whether ample time is spent to estimate temperature fields before switches occur (i.e. dwell-time between switches should be sufficiently large to ensure $\|\boldsymbol{\varepsilon}(t)\|_2$ decays [133]). For a periodic flow with a period of N_T time, this requires that, e.g., $\|\boldsymbol{\varepsilon}(t_{kN_T})\|_2 \geq \|\boldsymbol{\varepsilon}(t_{(k+1)N_T})\|_2$.

The size of the state-space and the number of inputs considered here is large. This allows for a very large number of possible choices for the weighing matrices $\boldsymbol{Q}$ and $\boldsymbol{R}$. Following a "classical" simplification (e.g. see Kwakernaak and Sivan [134]), the complexity of $\boldsymbol{Q}$ and $\boldsymbol{R}$ is reduced by considering them diagonal. This structure allows for a single diagonal entry of $\boldsymbol{Q}$ or $\boldsymbol{R}$ to influence a *single* mode or output in (5.27) (used in Section 6.2), respectively. The diagonal entries of $\boldsymbol{Q}$ and $\boldsymbol{R}$ are considered the same unless stated otherwise. Such a choice results in a further simplification of the weighing matrices to

$$\boldsymbol{Q} = q\boldsymbol{I}, \quad \boldsymbol{R} = r\boldsymbol{I}, \tag{5.32}$$

where $q, r > 0$. Relation (5.32) simplifies the interpretation of (5.27) significantly. Namely, increasing q – or, equivalently, decreasing r – penalizes the state – or the output – more in (5.27) (i.e. increasing q puts more emphasize on the state $\boldsymbol{\alpha}$ in (5.27) compared to the outputs). Further simplification of (5.29) – or (5.28) for that matter – by using the simplified weighing matrices in (5.32) is not necessarily feasible/insightful, since $\widetilde{\boldsymbol{C}}^{(i)} = \boldsymbol{C}\boldsymbol{G}^{(i)}$ is a dense matrix. This dependence of the output matrix on the eigenmodes prevents a further simplification of either (5.29) or (5.28) (e.g. through diagonalization of (5.29)). Nonetheless, substituting (5.32) in (5.29) combined with (5.17) reveals that solution $\widetilde{\boldsymbol{X}}_i$ of (5.29) is determined by

$$\begin{aligned}\widetilde{\boldsymbol{X}}_i =& \widetilde{\boldsymbol{A}}^{(i)} \widetilde{\boldsymbol{X}}_i (\widetilde{\boldsymbol{A}}^{(i)})^\dagger \\ &- (\widetilde{\boldsymbol{A}}^{(i)} \widetilde{\boldsymbol{X}}_i (\widetilde{\boldsymbol{C}}^{(i)})^\dagger)(\boldsymbol{I} + \widetilde{\boldsymbol{C}}^{(i)} \widetilde{\boldsymbol{X}}_i (\widetilde{\boldsymbol{C}}^{(i)})^\dagger)^{-1} (\widetilde{\boldsymbol{C}}^{(i)} \widetilde{\boldsymbol{X}}_i (\widetilde{\boldsymbol{A}}^{(i)})^\dagger) + \frac{q}{r}\boldsymbol{I}.\end{aligned} \tag{5.33}$$

where $\boldsymbol{X}_i = r\widetilde{\boldsymbol{X}}_i$. Hence, the tuning of $\boldsymbol{Q}$ with respect to $\boldsymbol{R}$ – with matrices according to (5.32) – through adjusting q/r determines the contribution of the states $\boldsymbol{\alpha}$ to (5.27) *relative* to the contribution of the outputs in (5.27).

5.3.3 Sensor placement methodology

A key step to accurate state estimation is proper input/output selection [135]. Attention is focussed on output selection, viz. sensor placement, since actuators are already selected in the RAM. The analysis in Section 5.3.2 reveals two important conditions for sensor placement in a system with reoriented flows:

i) Sensors should be placed such that $\boldsymbol{C}$ is invariant under reorientation (see discussion after (5.29)).

ii) Sensors should render the lower order modes observable.

Condition i) can significantly reduce computation times required to obtain $\boldsymbol{L}^{(i)}$, which becomes especially important upon including a larger number of flows. To meet condition i) the following approach is followed to place p sensors for $I = 2$ flows. The first $\lfloor p/I \rfloor$ sensors are optimally placed for state estimation with heat transport governed by the base flow ($i = 1$). Eigenmodes for the reoriented flow ($i = 2$) differ by at most a reorientation. Optimal sensor locations for the reoriented flow can thus also be obtain by a mere reorientation. The optimal locations for the base flow are rotated by Θ and serve as the location for the second $\lfloor p/I \rfloor$ sensors. The process continues until all $I\lfloor p/I \rfloor$ are placed.

Condition ii) follows from the observation that (5.24) can only confirm whether an eigenvalue is observable or not. For example, multiple sensor locations can render the same eigenvalue observable. However, (5.24) provides no means to determine which location is optimal. A large variety of criteria can be optimized to obtain proper sensor locations (i.e. proper in the sense of a selected criterion). Sensor placement techniques are available that optimize the modelling error [136], minimize error dynamics [137], maximize modal observability [138] or optimize Gramian-based selection [139]. These techniques focus on the infinite dimensional PDE and rely on the absence of either advection or diffusion during sensor placement. Here, sensor placement needs to ensure that sensors enable accurate state estimation with an estimator (developed in Section 5.3.2) in the presence of both advection and diffusion. Field estimation/reconstruction from measurements requires knowledge of each eigenmode to do so, since the model in (5.16) consists of spectral coefficients. Therefore, sensor placement for optimal modal observability, following a modified version of the approach presented by Armaou and Demetriou [138], is considered here. The method is preferred here as it also explicitly minimizes the effect of spill-over from higher-order modes during estimation. Spill-over effects can, inadvertently, cause instability and/or noise amplification and are thus important to consider during sensor placement.

The considered sensor placement method, maximizes the cumulative observability of the low-order modes under the spatial H_2 norm. A key criterion in this method is that dynamic behaviour can be described by a finite set of eigenmodes. The transfer function $\boldsymbol{H}^{(1)}(s)$ describing this behaviour can be determined by taking the Laplace transform of (5.6) which, combined with (5.14), results in

$$\begin{aligned}\widetilde{\boldsymbol{T}}(s) &= -\boldsymbol{G}^{(1)}\left(s\boldsymbol{I}-\boldsymbol{\Lambda}\right)^{-1}\left(\boldsymbol{G}^{(1)}\right)^{+}\widetilde{\boldsymbol{T}}(0)+\kappa\boldsymbol{G}^{(1)}\left(s\boldsymbol{I}-\boldsymbol{\Lambda}\right)^{-1}\left(\boldsymbol{G}^{(1)}\right)^{+}\boldsymbol{b}\widetilde{T}_a(t),\\ &\approx -\boldsymbol{G}^{(1)}\left(s\boldsymbol{I}-\boldsymbol{\Lambda}\right)^{-1}\widetilde{\boldsymbol{\alpha}}(0)+\kappa\boldsymbol{G}^{(1)}\left(s\boldsymbol{I}-\boldsymbol{\Lambda}\right)^{-1}\left(\boldsymbol{G}^{(1)}\right)^{+}\boldsymbol{b}\widetilde{T}_a(t),\\ &= -\boldsymbol{H}^{(1)}(s)\widetilde{\boldsymbol{\alpha}}(0)+\kappa\boldsymbol{H}^{(1)}(s)\left(\boldsymbol{G}^{(1)}\right)^{+}\boldsymbol{b}\widetilde{T}_a(t), \qquad (5.34)\end{aligned}$$

such that

$$H^{(1)}_{nm}(s) = G^{(1)}_{nm}\left(s-\lambda^{(1)}_m\right)^{-1}. \qquad (5.35)$$

Transfer function $H^{(1)}_{nm}(s)$ describes the behaviour between mode m and an output sampled with a sensor placed at $\boldsymbol{x}_n \in \boldsymbol{D}$. The H_2 norm of the transfer function $H^{(i)}_{nm}(s)$ in (5.40) has an analytical expression given by

$$\begin{aligned}\|H^{(1)}_{nm}(s)\|_{H_2} &= \left(\frac{1}{2\pi}\int_{-\infty}^{\infty}\left|H^{(1)}_{nm}(j\omega)\right|^2 \mathrm{d}\omega\right)^{1/2},\\ &= \left(\frac{D^{(1)}_{nm}}{2|Re(\lambda_m)|}\right)^{1/2}, \end{aligned} \qquad (5.36)$$

where $D^{(1)}_{nm} = \left(Re\left(V^{(1)}_{nm}\right)\right)^2 + \left(Im\left(V^{(1)}_{nm}\right)\right)^2$. Relation (5.36) can be interpreted as the time domain norm of a system's response to a unit impulse [54]. In essence, investigating heating of a cold fluid by a hot boundary can be viewed as studying the step-response. Hence, evaluation (5.36) for sensor placement is well-suited for the fluid heating system at hand. The relative spatial modal observability of each mode m in (5.40) is defined for flow 1 as [138]

$$N^{(1)}_{nm} = \frac{\|H^{(1)}_{nm}(s)\|_{H_2}}{\max\limits_{n}\|H^{(1)}_{nm}(s)\|_{H_2}} \times 100\%, \qquad (5.37)$$

where $\|.\|_{H_2}$ indicates the H_2 norm [140] and $s = j\omega \in \mathbb{C}$ with ω the angular frequency and $j = \sqrt{-1}$. The elements $N^{(1)}_{nm}$ thus express the relative observability of a mode m from an output with a sensor at $\boldsymbol{x}_n \in \boldsymbol{D}$. High (low) values for $N_{nm}^{(1)}$ indicate that a sensor at $\boldsymbol{x}_n$ is more (less) sensitivity to the mode m according to (5.37). Relation (5.36) thus suggests that (5.37) represents the ratio between a mode's spatial magnitude at $\boldsymbol{x}_n$ with respect to its peak spatial magnitude (i.e. $N_{nm}^{(1)} = \left(D_{nm}^{(1)} / \max\limits_{n} D_{nm}^{(1)}\right)^{1/2}$). To maximize the modal observability of the first p modes in (5.40) and, simultaneously, minimize the spill-over effects of the remaining $M-p$ higher order modes, the following condition, adopted from Armaou and Demetriou [138], is optimized

$$\text{arg}\max_{n^*}\left(S_n^{(1)} - \omega_s L_n^{(1)}\right), \quad \text{for } N_{nm}^{(1)} \geq \beta, \tag{5.38}$$

where n^* the optimal sensor location at $\boldsymbol{x}_{n^*}$, β an observability threshold, ω_s a weighing function and

$$S_n^{(1)} = \frac{\sqrt{\sum\limits_{m=1}^{m=p} \|H_{nm}^{(1)}(s)\|_{H_2}^2}}{\max\limits_{n}\sqrt{\sum\limits_{m=1}^{m=p} \|H_{nm}^{(1)}(s)\|_{H_2}^2}}, \quad L_n^{(1)} = \frac{\sqrt{\sum\limits_{m=p+1}^{m=M} \|H_{nm}^{(1)}(s)\|_{H_2}^2}}{\max\limits_{n}\sqrt{\sum\limits_{m=p+1}^{m=M} \|H_{nm}^{(1)}(s)\|_{H_2}^2}}. \tag{5.39}$$

The ratios $S_n^{(1)}$ and $L_n^{(1)}$ represent the cumulative modal observability of the p lower order modes and $M-p$ higher order modes observed from a sensor placed at $\boldsymbol{x}_n \in \boldsymbol{D}$, respectively. Following the optimization of (5.38), the mth sensor is placed at $\boldsymbol{x}_{n^*}$ (i.e. the mth row of $\boldsymbol{C}$ consists of zeros and contains a one in the n^* column). The optimization is repeated until all $\lfloor p/I \rfloor$ sensors are placed.

The placement of sensor m at a location $\boldsymbol{x}_n$ inhibits placement of another sensor with a certain proximity (e.g. due to the dimensions of the sensor). This is incorporated in the optimization (5.38) by excluding a set of grid points surrounding the placed sensors. Sensor locations inside a circle with radius r surrounding location $\boldsymbol{x}_n$ are excluded from the optimization in (5.38). Here, two times the *normalized* diameter of a regular thermocouple is considered an appropriate radius (i.e. a non-dimensional distance of $r \approx 1.6 \cdot 10^{-5}$). Both the state matrix $\widetilde{\boldsymbol{A}}^{(i)}$ and the output matrix $\widetilde{\boldsymbol{C}}^{(i)}$ reorient, due to transformation matrix $\boldsymbol{G}^{(i)}$ in (5.14), as a consequence of the activated flow i. Hence optimal sensor locations will depend on the activated flow as well. In the considered sensor placement method, sensors are placed based on the eigenmodes associated with heat transport following the activation of the base flow $i = 1$ (i.e. described by columns of $\boldsymbol{G}^{(1)}$). The sensors for other flows (i.e. $i > 1$) in the system are placed at reorientations of these locations. Placed sensors are considered immovable and thus remain fixed at their location $\boldsymbol{x}_n$ regardless of the (de)activated fluid flow (i.e. according to $\boldsymbol{C}$ in (5.12)). Part of the placed sensors will therefore always be (sub)optimally placed for state estimation if the above procedure is followed. Moreover, the above-mentioned placement approach renders all sensors suboptimally placed for state estimation in the absence of flow (i.e. eigenmodes associated with mere diffusion differs by more than a reorientation from the eigenmodes associated with the base flow). This can result in suboptimal performance of the field estimator in the absence of flow. However, results show that state estimation is relatively insensitive to the suboptimal sensor placement in the absence of flow as opposed to state estimation in the presence of flow (see Chapter 6). Therefore, sensors are place solely on eigenmodes associated with the base flow.The weighted residual ω_s in (5.38) can be used to reduce spill-over effects of higher order modes in the optimization. Here including the residual has, regardless of any nontrivial weight, been found to have little influence on optimal sensor placement. Finally, relations (5.35) through (5.39) are readily obtained on the discrete grid $\boldsymbol{D}$.

To examplify the physical interpretation of the optimization in (5.38), consider the simplified situation when $\widetilde{T}_a = 0$ for $i = 1$. In that case, the response of (5.14)-(5.17) to a non-trivial initial condition $\boldsymbol{\alpha}^{(1)}(0)$ – viz. a cold fluid – can be expressed as

$$Y_n^{(1)}(s) = \boldsymbol{C}_n \widetilde{\boldsymbol{V}}^{(1)} \left(s\boldsymbol{I} - \widetilde{\boldsymbol{\Lambda}}^{(1)} \right)^{-1} \boldsymbol{\alpha}^{(1)}(0) = \sum_{m=1}^{m=M} H_{nm}^{(1)}(s)\alpha_m^{(1)}(0), \tag{5.40}$$

where $\boldsymbol{\alpha}^{(i)}(0) \neq \boldsymbol{0}$ in order for heating to occur in the RAM and n such that $\boldsymbol{x}_n \in \boldsymbol{D}$ for $n \in \{1, ..., N\}$. The output vector $\boldsymbol{C}_n$ consists of zeros, where only a single element is non-zero. The effect of placing sensors according to (5.38) can be gauged from (5.40). Maximizing (5.38) for the first p modes results in the "amplification" of the associated initial conditions in (5.40) relative to the $M - p$ higher order modes. A similar observation, albeit less straightforward in its interpretation, follows for $\widetilde{T}_a(t) \neq 0$.

Figure 5.4 shows the 48 sensor locations for the advective-diffusive eigenmodes with model parameters presented in Table 5.2. The observability of the eigenmodes are deemed acceptable when $\beta = 0.95$. The first 24 optimal sensor locations, following the minimization of (5.38), are indicated by white squares in Figure 5.4. The second 24 sensors, following a reorientation of the optimal sensor locations for the base flow, are indicated by black circles in Figure 5.4. The cyan crosses in Figure 5.4 indicate the sensor location that maximizes the observability of the shown mode (viz. the cyan cross in Figure 5.4(a) indicates the n-th sensor that maximizes $N_{m,n}^{(1)}$ for $m = 1$).

Figure 5.4 reveals that sensors are placed in or close to the maxima (or minima) of the respective eigenmode. Sensor placement is confined to a smaller region of the flow domain for eigenmodes with flow. Lensvelt et al. [55] showed that heat transport in the RAM primarily occurs in close proximity to an activated aperture. Sensor placement in the vicinity of the aperture therefore makes physical sense since most of the relevant heating dynamics occurs there.

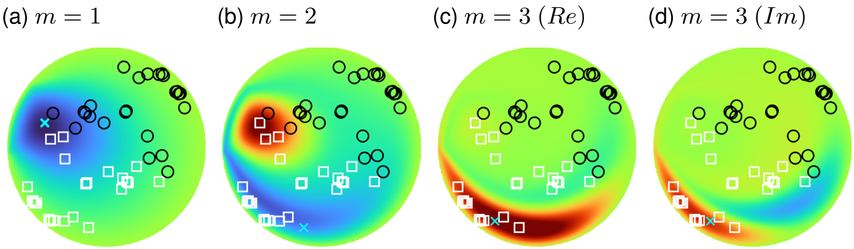

Figure 5.4: The first four dominant modes associated with the base flow ($i = 1$) of the RAM. Parameters used to obtain optimal sensor locations are adopted from Table 5.2. White squares: optimal sensor locations for the base flow ($i = 1$); black circles: optimal sensor location for reoriented flow; cyan crosses: optimal sensor for mode m.

5.4 Comparative analysis

In this section, results of estimated and experimentally obtained temperature fields are compared. The analysis consists of three distinctive parts. First, parameters in (5.5), required for numerical simulation, are obtained from experiments based on the identification procedure presented in Section 5.3.1. Next, these parameters are used to place sensors inside the fluid container of the RAM. Sensor placement with the base flow and by mere diffusion according to results in Section 5.3.3 is investigated here as well. Finally, sensor locations and model parameters are used to obtain state estimators. A comparison is made between both the estimated and measured fields to investigate the accuracy of state estimation.

5.4.1 Parameter identification

Experiments can last extremely long for the RAM as Péclet numbers decrease. Thermal experiments are limited to a fixed time of three hours to ensure practical feasibility. As a result of long experiment times, experiments have been performed at different times and/or days. This can result in different behaviour for the ambient temperatures as the absolute ambient temperature can differ per experiment. Its normalisation in (5.4) ensures that ambient temperatures are comparable across experiments. Therefore, ambient temperatures are normalised by the minimal and maximal temperatures, respectively, T_0 and T_∞, and are *measured* during each experiment with a set of thermocouples. The thermocouples are placed close to the open surface in RAM (see Figure 5.2b) without obstructing the thermal camera's view (i.e. bottom right corner in 1 in Figure 5.2a).

Figure 5.5 shows the measured normalized ambient temperatures $\widetilde{T}_a$ for two different experiments (i.e. for the base flow ($i = 1$) and for mere diffusion ($i = 0$)). The normalized ambient temperatures $\widetilde{T}_a$ fluctuates in time. However, the average normalized ambient temperature, denoted by $\mu(\widetilde{T}_a(t))$, deviates by less than

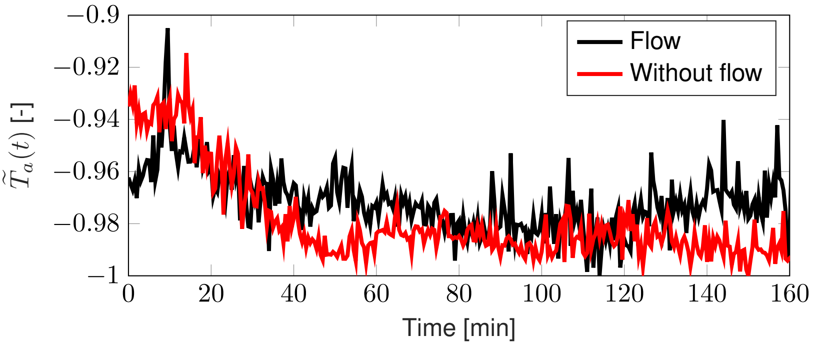

Figure 5.5: Evolution of the normalized ambient temperature measured surrounding to RAM for two different experiments used for parameter identification. Heat transport is driven by the base flow (black) or by mere diffusion (red).

1 % between experiments. The low variability of $\mu(\widetilde{T}_a(t))$ between experiments suggests that both the ambient conditions and the measurement of $\widetilde{T}_a$ are consistent. The standard deviation of the normalized ambient temperature, denoted by $\sigma(\widetilde{T}_a(t))$, is at most 2 % (i.e. $\sigma(\widetilde{T}_a(t)) \approx 0.02$ in Figure 5.5). This implies that $\widetilde{T}_a$ can be viewed as a time-independent constant input in (5.10)-(5.11). However, numerical simulations reveal that even small deviations in the input $\widetilde{T}_a$ between experiments can potentially have a large impact on the quality of field estimation. Moreover, Figure 5.5 shows that the normalized ambient temperature is skewed towards the start of the experiment (i.e. $\mu(\widetilde{T}_a(t))$ changes only slightly *after* 60 minutes of sampling $\widetilde{T}_a(t)$ in experiments). In addition, obtaining a real-time measurement of the *average* normalized ambient temperature takes a long time compared to the duration of an experiment (i.e. sufficient samples of $\widetilde{T}_a$ need to be measured before an accurate average is obtained). Hence, $\mu(\widetilde{T}_a(t))$ needs to be determined *a posteriori*. As a consequence, $\widetilde{T}_a$ is assumed constant during the parameter identification procedure.

Model parameters are estimated according to (5.19) based on experiments with either the base flow or mere diffusion. The base flow ($i = 1$) circulates the fluid in clockwise direction for a belt-speed $U = 0.004\ m/s$ (see Figure 5.3b). To determine identifiability of $\boldsymbol{\theta}$, (5.18) is evaluated for heat transport with the base flow and by mere diffusion. Numerical evaluation of (5.18) reveals that $\boldsymbol{S}^{K-1}$ is only full rank for mere diffusion in the considered parameter span. Therefore, $\boldsymbol{\theta}$ is guaranteed to be theoretically structurally identifiable in (5.10)-(5.11) for mere diffusion. The minimization of (5.19) for experiments with the base flow requires further analysis though. In addition, numerical solutions to a least-square problem – like (5.19) – can converge to a set of parameters that are only locally optimal [141]. Different numerical solutions to (5.19) can, e.g., indicate the presence multiple optima [141] or the presence of numerical errors [127]. The optimization is therefore started from different initial guesses for $\boldsymbol{\theta}^*$. The relative proximity of the obtained parameter estimates gives information about the optimality of the parameters (e.g. close proximity of these parameter estimates implies the same optimum is found). The close proximity of the residuals $J(\boldsymbol{\theta}^*)$ implies that the found optimum is unique. Numerically estimated parameters $\boldsymbol{\theta}^*$ are shown in Table 5.2.

Table 5.2: Numerically estimated $\boldsymbol{\theta}^*$ based on the optimization according to (5.19) for an the experiment with mere diffusion ($i = 0$) and the base flow ($i = 1$) with belt speed $U = 0.004\ m/s$.

Parameter	$\alpha\ [m^2/s]$	κ	ξ
Diffusion ($i = 0$)	$3.3 \cdot 10^{-7}$	45.1	$-$
Base flow ($i = 1$)	$1.0 \cdot 10^{-6}$	0.052	0.36

Thermal diffusivity is estimated at a consistently higher than the theoretical value with pure silicone oils (or polydimethylsiloxane (PDMS)) for the experiment with the base flow. The parameter identification method in (5.19) identifies a thermal diffusivity coefficient in the experiment with flow comparable to those presented in Baskan et al [17]. Moreover, the estimated value is significantly elevated compared to values typically found for pure silicone oils (or PDMS) [142]. However, the parameters in Table 5.2 reveal that the estimated thermal diffusivity is estimated 66 % lower for the experiment with mere diffusion. This difference is caused by the characteristic time-scales used to non-dimensionalize (5.1). As a consequence, ξ and α are indistinguishable in the output and are thus estimated together (see Appendix D). The factor $\alpha/\xi \approx 9.25 \cdot 10^{-7}\ m^2/s$ – where ξ and α estimated for the experiment with, respectively, the base flow and mere diffusion – is close to the thermal diffusivity estimated for the base flow though. Hence, the parameter identification method consistently overestimates α by the same factor. As a result, the estimated Péclet number is much lower than observed in previous experiments (i.e. $Pe = 10^4$ in Baskan et al. [17]). The silicon oil used in this work differs from the oil used in experiments by Baskan et al. [17]. The consistent overestimate of α combined with the model's agreement with experiments suggests that the overestimate in α could have been caused by impurities in the oil rather than significant model error (see Section 5.4.2 for details).

The estimated heat transfer coefficient for experiments with the base flow and mere diffusion differ significantly. Note however that the values of κ in Table 5.2 are valid for different non-dimensionalizations (see Section 5.2.2). Taking into account the difference between these non-dimensionalizations, reveals a deviation of 21 % between the ratio of estimated heat transfer coefficients and its expected theoretical value based on the estimated parameters in Table 5.2 (i.e. $\kappa_0/\kappa_1 \approx 854$ differs by 21 % from the equivalent $UR/(\alpha_0/\xi_1) \approx 1.08 \cdot 10^3$ where "0" and "1" indicate the model parameters for mere diffusion and the base flow in Table 5.2, respectively). A large value for κ indicates a large impact of ambient heat loss on the overall heat transport inside the fluid. This can be understood from (5.10)-(5.12) as follows. The introduction of a heat-loss term according to (5.2) results in eigenvalues as

$$\left.\widetilde{\mathbf{\Lambda}}^{(i)}\right|_{\kappa\neq 0} = -\kappa\boldsymbol{I} + \left.\widetilde{\mathbf{\Lambda}}^{(i)}\right|_{\kappa=0}, \tag{5.41}$$

for $i = 0, 1, 2$. The eigenvalues in (5.41) show that the loss term adds an additional *negative* real part to the eigenvalues of the Perron-Frobenius operator without heat loss. The additional term results in accelerated heat transport compared to heat transport without ambient heat loss (i.e. $\kappa = 0$). Moreover, (5.8) reveals that input $\widetilde{T}_a$ acts, scaled by κ, on the transient temperature field $\widetilde{\boldsymbol{T}}$. This implies that input $\widetilde{T}_a$ has a larger impact on $\widetilde{\boldsymbol{T}}$ for larger κ. The estimated parameters thus suggest implies that fluid heating in the RAM is more susceptible to heat loss in the absence of a fluid flow.

The scaling factor is estimated at $\xi = 0.36$ for the experiment with the base flow. The estimated scaling factor is considerably lower than the $\xi = 0.86$ presented by Baskan et al. [69]. They introduced the scaling factor ξ to compensate for weak $3D$ effects resulting in a local departure from a full $2D$ Stokes flow in the RAM. The largest deviation between the experimentally and numerically obtained flow fields is found close to the activated aperture. The notable difference with the experiments in this work and in Baskan et al. [69] are the experimental settings. Here, the belt speed is reduced from $U = 0.005$ m/s to $U = 0.004$ m/s and the silicon oil (glycerol-water) layer thickness is reduced (increased) to 0.004 m (0.006 m) versus 0.005 m to ensure proper alignment (see the discussion above Table 5.1). The changes in experimental settings directly influence the fluid flow close to the aperture. Namely, the reduction in layer thickness of the glycerol-water mixture can result in additional $3D$-effects that influence the flow field. Additionally, the scaling factor ξ captures the deviation of the experimental and numerical temperature field evolution. Hence, ξ accounts for more than just deviations in the flow field (e.g. deviations due to a heat loss term with a non-homogeneous heat-transfer coefficient).

5.4.2 Predictive ability of the model

The model in (5.10)-(5.12) needs to be able to accurately predict fluid heating in order to, eventually, be included in a control loop. Accurate prediction of transient behaviour is key for fast prediction in closed-loop. In addition, close resemblance of temperature fields from the model with those from the experiments is essential for good performance of the field estimator in Chapter 6 (i.e. state estimation is namely dependent on accurate measurements *and* an accurate predictive model). This warrants a closer examination of temperature field snapshots to assess the accuracy of the model.

Figure 5.6 shows temperature field snapshots for both the experiments (top row) and model (bottom row) for mere diffusion. Snapshots show qualitative agreement of the temperature fields between model and experiments. Axisymmetry of the temperature field is preserved even though i) thermal images require image distortion compensation (e.g. to compensate for lens distortions) and ii) local variation of the heat conduction coefficient in the annulus (e.g. at the belt-aperture interface). Furthermore, temperatures are slightly lower in the model compared to the experiments at the core of the fluid domain (i.e. around $x = y = 0$). Despite the abovementioned deficiencies, numerical prediction by (5.10)-(5.12) is accurate enough to capture heating.

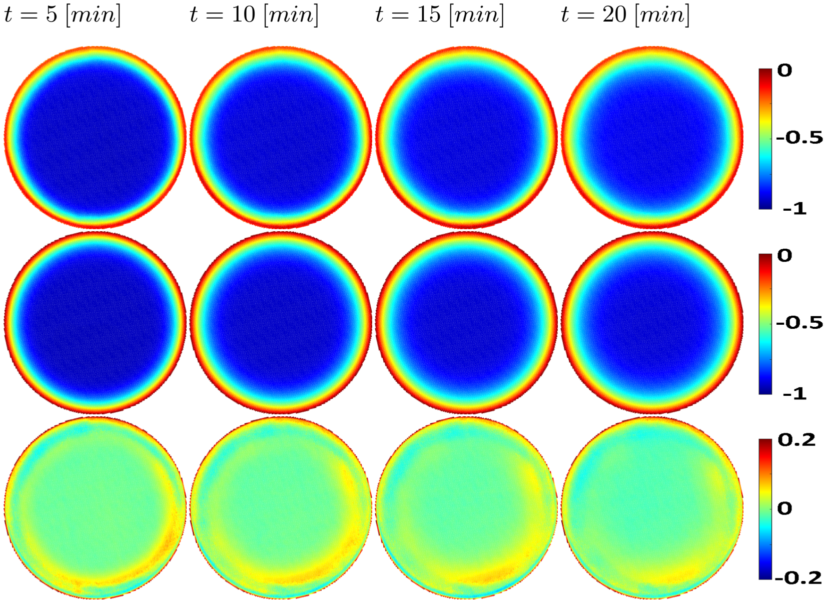

Figure 5.6: Measured (top row) and numerical (middle row) temperature snapshots (blue: $\min(\widetilde{T}) = -0.5$; red: $\max(\widetilde{T}) = 0$) combined with the error (bottom row) (blue: $\min(\varepsilon) = -0.2$; red: $\max(\varepsilon) = 0.2$) between them for a RAM with mere diffusion ($i = 0$). Model parameters used during numerical simulation are taken from Table 5.2.

Figure 5.7 shows temperature field snapshots between the experiments (top row) and model (bottom row) with the base flow. Constant belt motion of 0.004 m/s at one of the available apertures induces a fluid flow. This fluid flow eventually produces the hot plume observed in Figure 5.7. The model shows qualitatively similar heating to the experiments with flow. However, the plume formed in the numerical simulation is better developed and is thus easier to discern than in the experiments. A ”cold” spot can be observed in close proximity to the activated aperture in both the numerical simulation and experiment, which is encircled by the hot plume as time progress. This cold spot is more distinct for the numerical simulation than in the experiment. However, the discrepancy diminishes as time progresses and the fluid heats up.

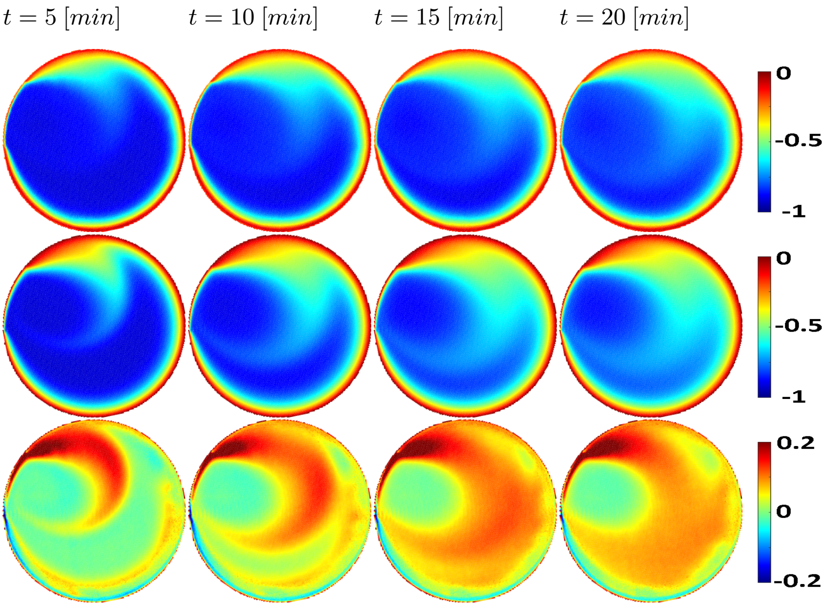

Figure 5.7: Measured (top row) and numerical (middle row) temperature snapshots (blue: $\min(\widetilde{T}) = -1$; red: $\max(\widetilde{T}) = 0$) combined with error (bottom row) (blue: $\min(\boldsymbol{\varepsilon}) = -0.2$; red: $\max(\boldsymbol{\varepsilon}) = 0.2$) between them for the base flow with belt speed $U = 0.004\ m/s$ ($i = 1$). Model parameters used during numerical simulation are taken from Table 5.2.

The model's capacity to capture a cost-function, that accurately describes fluid heating, is studied next. The cost-function that accurately captures fluid heating is defined as [55]

$$J_2(t) = \frac{1}{\pi}\int_{\mathcal{D}} \widetilde{T}^2(\boldsymbol{x},t)\mathrm{d}^2\boldsymbol{x} \approx \frac{1}{\pi}\sum_{i=1}^{N} \widetilde{T}^2(\boldsymbol{x}_i,t)\Delta A_i = \frac{1}{\pi}\widetilde{\boldsymbol{T}}^{\dagger}(t)\boldsymbol{A}\widetilde{\boldsymbol{T}}(t). \tag{5.42}$$

The cost-function in (5.42) is successfully used in numerical simulations to boost fluid heating in the RAM [55]. Hence, accurate predictions of the scalar field – and thus also the cost-function – with the model will prove vital to replicate these results in practice. The cost-function $J_2(t)$ is shown in Figure 5.8 for both experiments and model. Based on Figure 5.8 the model captures the qualitative behaviour fairly accurately. The model where heat transport is driven by the base flow or mere diffusion both show similar exponential decay of J_2 compared to their respective experiments in Figure 5.8(a) and Figure 5.8(b). Moreover, heat transport by mere diffusion is captured especially well. A relatively small error is observed between the cost-function of the model and experiments at steady-state in the absence of any flow. This steady-state error in Figure 5.8a is comparable in magnitude to the steady-state error in Figure 5.8b. However, the cost-function J_2 is consistently underestimated for the model with the base flow throughout the entire time window, whereas it is overestimated by the model for mere diffusion only at the end of the time window. The model for mere diffusion captures transient behaviour quantitatively better than “steady-state” behaviour in the considered time span.

(a) $u = 0$

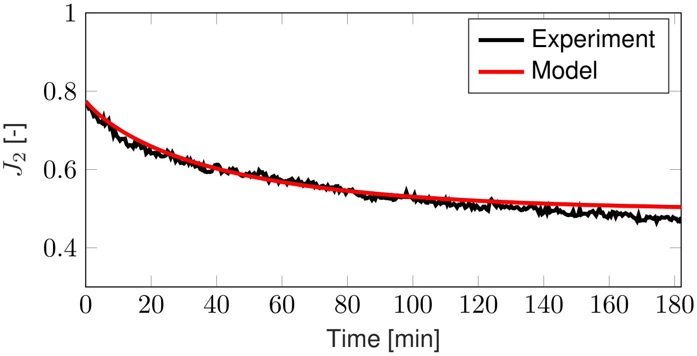

(b) $u \neq 0$

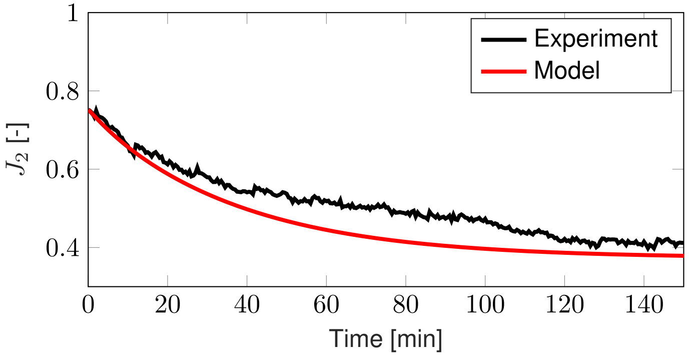

Figure 5.8: The cost-function $J_2(t)$ for different experiments and model (5.10)-(5.12) with parameters from Table 5.2 as a result of heating (a) by mere diffusion and (b) with the base flow.

5.4.3 Numerical field estimation

In this subsection the estimator, presented in Section 5.3.2, is investigated numerically. Numerical field estimation is investigate for heat transport driven by a fluid flow and by mere diffusion in sections 5.4.3.1 and 5.4.3.2, respectively. Field estimation is performed with an estimator gain $\boldsymbol{L}$ designed on the sensor placement presented in Section 5.3.3. Note that this sensor placement is suboptimal for heat transport by mere diffusion, since sensors are optimally placed in Section 5.3.3 for detectability in the presence flow. The output vector $\widehat{\boldsymbol{y}}$ – used for field estimation in (5.25) – is generated by a standard FVM code [143]. The output vector and transient temperature fields obtained from the FVM code are henceforth referred to as the nominal output (vector) and nominal transient temperature fields, respectively. The truncated model used in (5.25) is constructed using the spectral method presented by Lester et al. [16].

5.4.3.1 Numerical field estimation by mere diffusion

Field estimation is performed on a truncated state-space model according to (5.25). The number of eigenmodes considered in $\boldsymbol{G}^{(i)}$ determine the accuracy temperature field according to (5.14). The effect of the number of considered eigenmodes on the field estimation is investigated by evaluating field estimation accuracy for different M.

Numerical results from the field estimator for heat transport by mere diffusion are shown in the top row of Figure 5.9. The second and the fourth row of Figure 5.9 show the estimation error in the transient temperature field for $M = 500$ and $M = 1000$, respectively. Peak estimation errors are $\boldsymbol{\varepsilon}(t) \approx 0.1$ and $\boldsymbol{\varepsilon}(t) \approx 0.07$ for $\boldsymbol{G}^{(0)}$ with $M = 500$ and $M = 1000$ eigenmodes, respectively. Both field estimation errors show similar oscillations throughout $\boldsymbol{D}$. These oscillations are a result of the model truncation presented in Section 5.2. They are reminiscent of the Gibbs phenomenon. The high frequency eigenmodes – present in the numerically "measured" $\widehat{\boldsymbol{y}}$ – cannot be captured exactly by the lower order modes considered during field estimation in (5.25). Based on Figure 5.9, the error appears to decrease as more eigenmodes are considered in field estimation with (5.25). Hence, increasing M diminishes the impact of the Gibbs phenomenon. Moreover, errors seem largely confined to close proximity of the boundary for $M = 1000$. Beside the number of modes M, the evolution of the field estimation error $\boldsymbol{\varepsilon}$ depends on the design of $\boldsymbol{L}$ as well. The estimator design depends on both weighing functions $\boldsymbol{Q}$ and $\boldsymbol{R}$ according to (5.32). Therefore, the evolution of the estimation error for different q/r tunings is investigated further.

Figure 5.10 shows the numerical result of field estimation for different ratios q/r with weighing matrices $\boldsymbol{Q}$ and $\boldsymbol{R}$ according to (5.32). In Figure 5.10, field esimation is performed for $M = 500$ eigenmodes (indicated by the solid lines) as well as for $M = 1000$ eigenmodes (indicated by the dashed lines). Figure 5.10 reveals that increasing the number of eigenmodes in $\boldsymbol{G}^(i)$ significantly improves field estimation regardless of the ratio q/r used to design the state estimator. Figure 5.10b shows that high values for q/r have little impact on improving field estimation accuracy. However, increasing the state's cost penalization in (5.27) is found to slightly decrease the accuracy in field estimation for the q/r considered

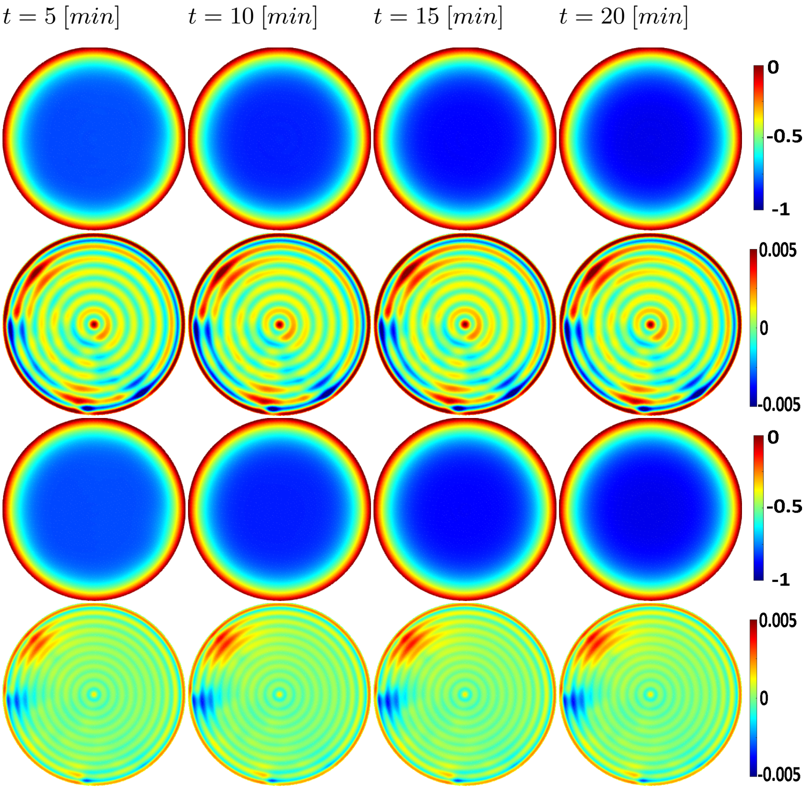

Figure 5.9: Estimated transient temperature snapshots for heat transport by mere diffusion with $M = 500$ (first row) and $M = 1000$ (third row) eigenmodes in (5.14) (blue: $\min(\widetilde{T}) = -1$; red: $\max(\widetilde{T}) = 0$). Error with $M = 500$ (second row) and $M = 1000$ (fourth row) eigenmodes between the estimated and nominal transient temperature fields (blue: $\min(\boldsymbol{\varepsilon}) = -0.005$; red: $\max(\boldsymbol{\varepsilon}) = 0.005$). Model parameters used during numerical simulation are taken from Table 5.2.

in Figure 5.10b. Decreasing q/r serves to improve the field estimation accuracy for any number of eigenmodes considered here. The effect is more pronounced for a smaller number of eigenmodes (i.e. changing $\boldsymbol{R}$ has a larger impact on $\widetilde{J}$ for $M = 500$ than for $M = 1000$).

From the numerical results it can be concluded that considering $M = 1000$ eigenmodes results in sufficiently accurate estimation of heat transport by mere diffusion. The above analysis reveals no clear preference for a certain choice of ratio q/r. Closer examination of Figure 5.10 revealed that $q/r < 1$ is slightly preferential to boost estimation performance here. The apparent invariance of $\widetilde{J}$ to changes in q/r in Figure 5.10 is caused by the relatively large number of eigenmodes considered during estimation for mere diffusion. For such large numbers

(a) Small q/r.

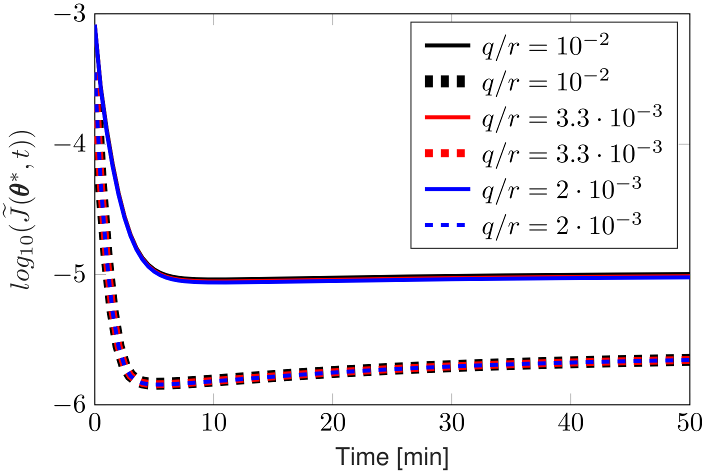

(b) Large q/r.

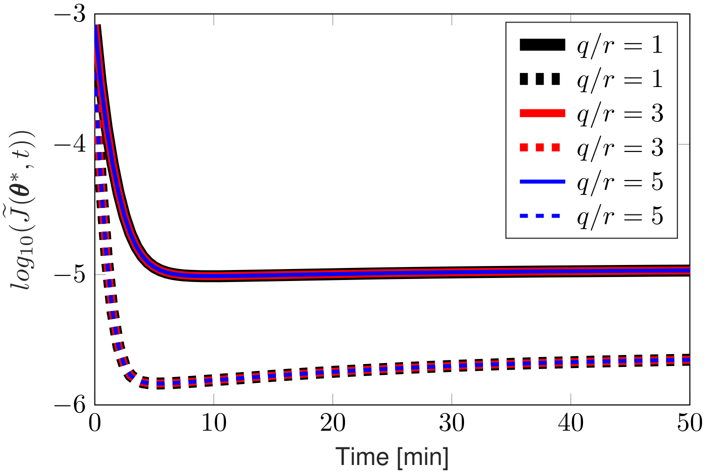

Figure 5.10: The cost-function $\widetilde{J}(\boldsymbol{\theta}^*, t)$ for small (a) q/r and (b) large q/r with parameters from Table 5.2 as a result of heating. Field estimation with only the first $M = 500$ dominant eigenmodes are represented by solid lines. Estimation with $M = 1000$ eigenmodes is represented by dashed by dashed lines.

of eigenmodes (i.e. $M \geq 500$), the ICs at the start of the estimation process – obtained from the nominal IC with (5.14) – are already close to the nominal ICs. This results in the observed rapid convergence and in the apparent invariance of $\widetilde{J}$ for changes in q/r observed in Figure 5.10. Note, however, the ratio influences the weighing matrices that determine gain matrix $\boldsymbol{L}$ and thus determine the amplification of noise during estimation (e.g. amplification of measurement noise or perturbed ICs). The state estimator is evaluated in the absence of noise though. In Chapter 6, the state estimator is investigated further for experimental measurements and thus includes the presence of noise.

5.4.3.2 Numerical field estimation for the base flow

Numerical field estimation for heat transport driven by the base flow is investigated for various M. Transient temperature field estimation is performed on the sensors placed in Section 5.3.3. As (some) sensors are suboptimally placed (i.e. according to the methodology in Section 5.3.3) they can potentially influence field estimation accuracy. Therefore, the impact of sensor placement on the field estimation accuracy is investigated as well. The effect of sensor placement used to design $\boldsymbol{L}^{(1)}$ is investigated in Appendix G. Field estimation for the base flow is performed on the truncated state-space model (5.25). Transient temperatures fields $\widetilde{\boldsymbol{T}}$ for heat transport driven by the base flow are again generated by a standard FVM code [143].

The number of eigenmodes considered in $\boldsymbol{G}^{(i)}$ determines the accuracy of the temperature field according to (5.14). Field estimation is performed with an estimator gain matrix $\boldsymbol{L}^{(i)}$ designed on the sensors placed in Section 5.3.3. The base flow is rescaled compared to the parameter estimation in Section 5.4.1 by decreasing the belt speed from $U = 0.004\ m/s$ to $U = 0.001\ m/s$. Rationale for this rescaling of the base flow is that the experimental settings for field estimation in Chapter 6 differ from those used during the parameter identification in Section 5.4.1. Rescaling of U results in a lower Pe according to (5.5). This means that the eigenmodes in $\boldsymbol{G}^{(i)}$ change with respect to those considered during sensor placement in Section 5.4.1. As a consequence, the sensors are suboptimally placed for field estimation with heat transport driven by the base flow. The changes in the eigenmodes by altering Pe can be quite substantial (e.g. see Lester et al. [109]). However, numerical results show that rescaling U yields only slightly different eigenmodes than those used to place the sensors in Section 5.3.3.

Transient temperature field snapshots for heat transport driven by the base flow are shown in the top row of Figure 5.11. The middle and the bottom row of Figure 5.11 show snapshots of the estimation error for field estimation with $\boldsymbol{G}^{(1)}$ consisting of $M = 500$ and $M = 1000$ eigenmodes, respectively. Peak estimation errors are found at $\boldsymbol{\varepsilon}(t) \approx 0.11$ and $\boldsymbol{\varepsilon}(t) \approx 0.09$ for field estimation with $M = 500$ and $M = 1000$ eigenmodes, respectively. Figure 5.11 reveals that the maximum field estimation error occurs in close proximity to the aperture edges. Based on Figure 5.11, the error in the temperature field estimate decreases as more eigenmodes are considered during field estimation according to (5.25). Beside the number of modes M, the evolution of the field estimation error $\boldsymbol{\varepsilon}$ depends on the design of $\boldsymbol{L}^{(1)}$ as well. The estimator design depends on both weighing functions $\boldsymbol{Q}$ and $\boldsymbol{R}$ according to (5.32). Therefore, the evolution of the estimation error for different q/r tunings is investigated further.

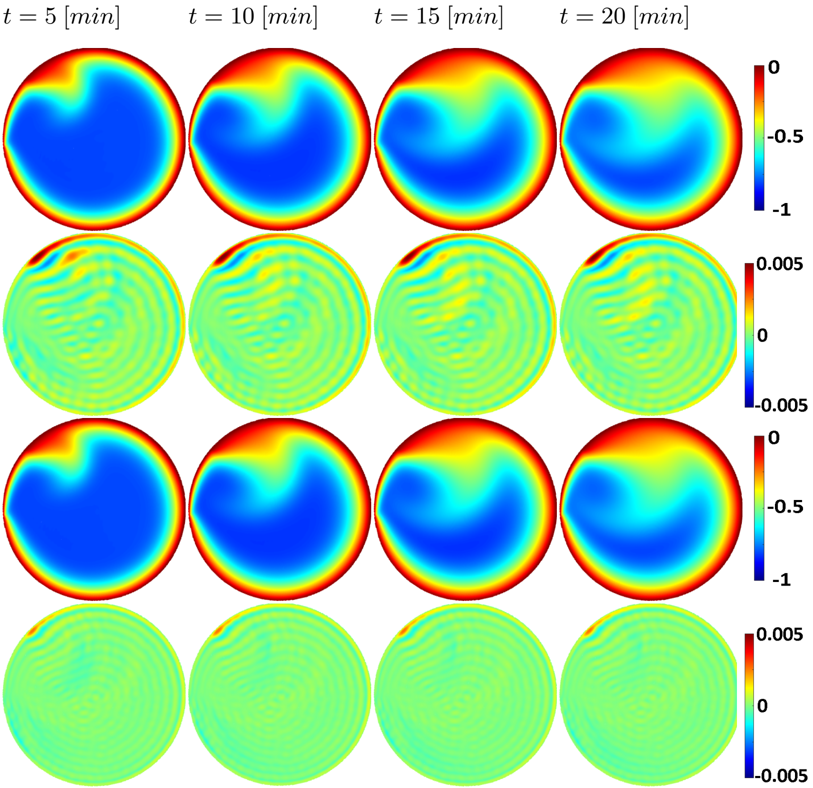

Figure 5.11: Estimated transient temperature snapshots for heat transport driven by the base flow with $M = 500$ (first row) and $M = 1000$ (third row) eigenmodes in (5.14) (blue: $\min(\widetilde{T}) = -1$; red: $\max(\widetilde{T}) = 0$). Error with $M = 500$ (second row) and $M = 1000$ (fourth row) eigenmodes between the estimated and nominal transient temperature fields (blue: $\min(\boldsymbol{\varepsilon}) = -0.005$; red: $\max(\boldsymbol{\varepsilon}) = 0.005$). Model parameters used during numerical simulation are taken from Table 5.2.

Figure 5.12 shows the field estimation error $\widetilde{J}$ for various weighing functions. The solid and dashed lines indicate field estimation for $\boldsymbol{G}^{(1)}$ with $M = 500$ and $M = 1000$ eigenmodes, respectively. Figure 5.12b reveals that heavier penalization of the state – by increasing q/r in (5.27) – results in amplification of the field estimation error $\widetilde{J}$ for $M = 500$. Increasing the number of eigenmodes in $\boldsymbol{G}^{(1)}$ decreases the field estimation error significantly as can be seen in Figure 5.12a,b. Moreover, the initial oscillations in $\widetilde{J}$ observed at the beginning of field estimation significantly diminish for $M = 1000$ compared to $M = 500$. In addition, increasing q/r has less impact on the estimation error following this initial transient for $M = 1000$. Figure 5.12a reveals that increasing the output penalization – by decreasing q/r in (5.27) – results in improved field estimation accuracy for the weighing functions considered. Moreover, field estimation errors are smallest when $M = 1000$ eigenmodes are considered during estimation. Additionally, the initial transient oscillation of $\widetilde{J}$ observed for large q/r in Figure 5.12b is absent for small q/r in Figure 5.12a. Comparing Figure 5.12a with Figure 5.12b reveals that the steady-state error also decreases for small q/r. Similar behaviour has already been observed for field estimation for mere diffusion. Based on these results, it is concluded that a small q/r is preferential for field estimation with heat transport driven the base flow as well.

Numerical results show that considering a large number of eigenmodes is key to accurate field estimation of heat transport for the base flow. Considering $M = 500$ eigenmodes is sufficient to guarantee a small error $\widetilde{J}$. However, peak estimation errors in the transient field are sufficiently minimized by considering $M = 1000$ or more eigenmodes. Hence, $M = 1000$ eigenmodes are considered in experimental field estimation of the transient temperature field for the base flow in Chapter 6. Moreover, the results also suggests that decreasing q/r minimizes the field estimation error significantly.

5.5 Conclusions and discussion

The present study aims to contribute to the detection of scalar transport in (re-orienting) fluid flows. To this end a dedicated scalar field estimator is developed that systematically reconstructs the transient temperature field by estimating the contribution of the "dominant" eigenmodes based on a discrete set of thermal sensors to capture heating of a cold fluid via a hot boundary in a representative case study. Field reconstruction is considered for two heat transport mechanisms that are commonly encountered in industry; transport by i) only diffusion or ii) both advection and diffusion. In practice, however, a third transport mechanism is present, i.e., a scalar sink in the form of a reaction term. Here, a case-study is investigated where convective heat loss to the ambient environment encompasses this scalar sink. The ambient heat loss results in the presence of a non-homogeneous scalar field at steady-state. The detection strategy relies on the reconstruction of so-called "dominant" eigenmodes, which have been shown essential for the accurate description of scalar transport. The sensors and the thereupon developed field estimator are, respectively, placed and designed based on these eigenmodes as well. The considered scalar transport dynamics therefore play a crucial role in accurately reconstructing the dominant eigenmodes and, as a consequence, the scalar field.

A Luenburger state estimator is developed by posing the detection problem as a linear quadratic regulator (LQR) problem. Numerical analysis shows that the estimator is able to accurately reconstruct/estimate the scalar field. The estimator is able to capture the scalar field accurately in the absence of fluid flow even

(a) Small q/r.

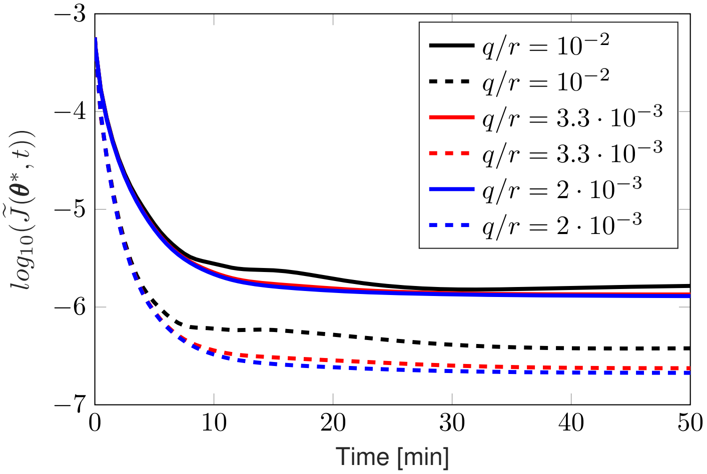

(b) Large q/r.

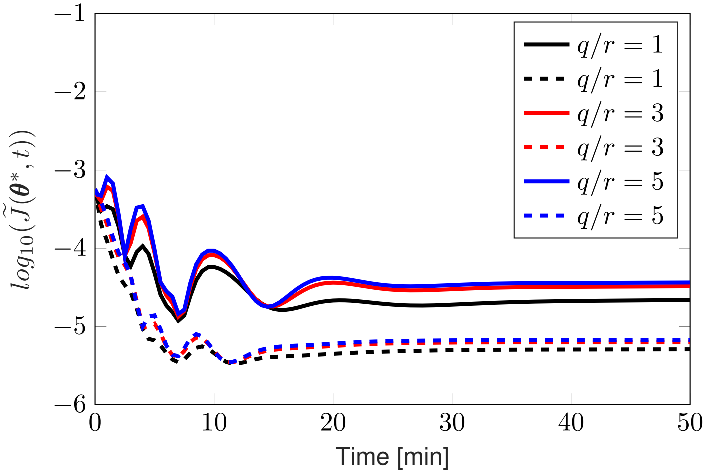

Figure 5.12: The cost-function $\widetilde{J}(\boldsymbol{\theta}^*, t)$ for (a) small q/r and (b) large q/r with parameters from Table 5.2 as a result of heating. Field estimation with only the first $M = 500$ dominant eigenmodes are represented by solid lines. Estimation with $M = 1000$ eigenmodes is represented by dashed lines.

after only a rudimentary tuning of the weighing matrices. Similar results have been found for scalar field estimation in the presence of the base flow. Moreover, numerical results reveal that putting less emphasize on the outputs during the design of the estimator gain matrix leads, in general, to reduced estimation errors.

In addition, retaining a sufficient number of eigenmodes is crucial to attain low estimation errors during state reconstruction (i.e. here $M = 1000$ eigenmodes suffices for the case study). In Chapter 6, the estimators developed in this chapter will be investigated further on the basis experimental results.

Future efforts will, first, be focussed on further analysis of the estimator's (stability) properties in open-loop heating strategies with multiple flows and, second, on closed-loop flow control where the scalar field is fed back to achieve rapid fluid heating. Future studies should aim to improve parameter identification by incorporating data-driven models based, for example, on Dynamic Mode Decomposition.

CHAPTER 6

Experimental estimation of scalar transport

Abstract - *The feedback flow controllers presented in this thesis require the complete instantaneous scalar field to operate. However, the scalar field is usually only partially available through a finite number of sensors. To reconstruct the scalar field from the discrete set of sensor data, a field estimator is developed in Chapter 5. The developed estimator is investigated on a representative case-study: the RAM. Numerical results in Chapter 5 show that the estimator is able to accurately reconstruct scalar fields for heat transport governed by mere diffusion or a single Stokes flow. In this chapter, the estimators ability to reconstruct the scalar field from experimental sensor data is investigated. Field estimation is – like in Chapter 5 – investigated on the RAM with heat transport governed by mere diffusion and a single Stokes flow. The estimator is also investigated for heat transport driven by an open-loop periodic flow. The estimated scalar fields show a close resemblance with the experimentally measured ones. Moreover, results show close agreement between a measured cost-function, which is shown relevant for fluid heating in Chapter 2, and its estimate. The accurate estimation of this measure is key to be able to apply the estimator with feedback flow controllers in a closed-loop in practice.*

The contents of this chapter forms the basis for: R. Lensvelt, M.F.M. Speetjens and H. Nijmeijer, “Experimental estimation of scalar transport”, in preparation, 2023.

6.1 Introduction

In Chapter 5, a field estimator has been developed that reconstructs the scalar field from a finite number of sensors. The estimator has been numerically investigated on a heat-transfer case-study known as the RAM. Numerical results revealed that the estimator is able to capture the temperature field accurately for heat transport driven by both the base flow and by mere diffusion (i.e. with a small spatially averaged error). However, the outputs, used for field estimation by the estimator, were obtained from a *numerical* model in Chapter 5. Any (measurement) noise, e.g. introduced by sensors, were absent during the estimation. Accurate estimation in the presence of noise is vital for any real-time application of the estimator in closed-loop flow control (i.e. as presented in Chapter 1). In this chapter, the analysis of the estimators, presented in Chapter 5, is extended. The estimators from Chapter 5 are exposed to experimental measurements to investigate the estimator's ability to accurately reconstruct the scalar field in practice. This extension is summarized in Figure 6.1.

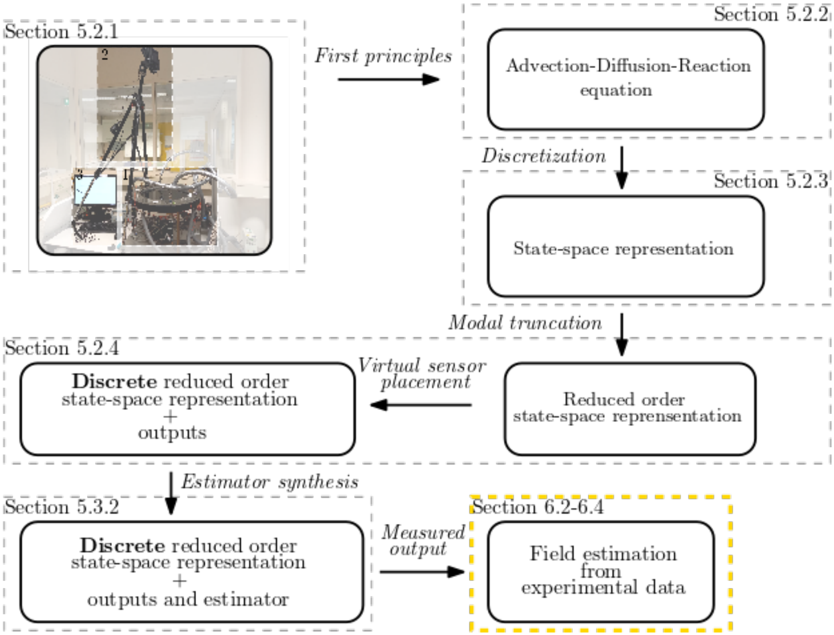
Section 5.2.1
First principles
Section 5.2.2
Advection-Diffusion-Reaction equation
Discretization
Section 5.2.3
State-space representation
Modal truncation
Section 5.2.4
Discrete reduced order state-space representation + outputs
Virtual sensor placement
Reduced order state-space reprensentation
Estimator synthesis
Section 5.3.2
Discrete reduced order state-space representation + outputs and estimator
Measured output
Section 6.2-6.4
Field estimation from experimental data

Figure 6.1: A flow chart showing the link between the estimator presented in Chapter 5 showing the novel elements of Chapter 6 in yellow.

The field estimators in this chapter are investigated on *different* experimental data sets than those used during the parameter identification in Section 5.4.1. The same experimental settings are used during experiments as presented in Section 5.2.1. Moreover, the model parameters in Table 5.2 and Table 5.1 are used to synthesize $\boldsymbol{L}^{(i)}$ in the estimator (5.25). Experiments initialize as soon as the temperature difference between the initial temperature field T_0 and the boundary temperature T_∞ in the annulus reaches $10\ ^\circ C$. The virtual sensors are placed based on the discrete Perron-Frobenius eigenmodes of the base flow and reoriented flow for $U = 0.004\ m/s$ (see Figure 5.4 in Section 5.3.3). Field estimation in the presence of only the base flow and the periodic flow is investigated for $U = 0.001\ m/s$ – like in Section 5.4.3.2 – and for $U = 0.004\ m/s$, respectively. Hence, they are suboptimally placed for scalar field estimation with heat transport governed by mere diffusion and the base flow. The estimators in this chapter are designed on all the available sensors. Moreover, the weighing matrices $\boldsymbol{Q}$ and $\boldsymbol{R}$ have the same structure as in (5.32) unless stated otherwise. The estimator gain matrix $\boldsymbol{L}^{(i)}$ is tuned with ratio q/r in (5.33) for weighing matrices according to (5.32).

Similar to Chapter 5, experimental field estimation is studied for heat transport driven by mere diffusion and by the base flow in Section 6.2 and Section 6.3, respectively. Flows reorient sequentially in the conventional periodic reorientation scheme and the closed-loop flow controller presented in Chapter 2. Therefore, the response of the estimator to periodic reorientation is investigated in this chapter as well. Estimation of the scalar field from experimental data in the presence of a periodic flow is investigated in Section 6.4. This section is intended as a prelude to the real-time application of closed-loop flow control. Finally, conclusions and recommendations are presented in Section 6.5.

6.2 Field estimation for mere diffusion

Transient temperature field estimation is first investigated for heat transport governed by mere diffusion. Figure 6.2 presents snapshots of the measured fields and the estimated fields in the top and bottom row, respectively. Two measurement errors are immediately noticeable in the measured temperature fields. First, departures from an axisymmetric field can be observed in close proximity to the boundary. These perturbations are caused by a small leakage at the belt-aperture interface. As a result, a small amount of the hot glycerol-water mixture in the annulus leaks into the container throughout the experiment. Second, a hot spot can be observed inside the fluid domain (encircled in snapshot at $t = 13\ [min]$ in Figure 6.2). The hot spot is caused by the positioning of the thermal camera, which locally heats up the fluid through infrared irradiation. Heat from the thermal camera adds an additional source term to (5.1), which can alter the evolution of the transient temperature field $\widetilde{T}$. The effect of this disturbance on the evolution of $\widetilde{T}$ is investigated before field estimation is performed. The overall evolution of the transient temperature snapshots appears unaffected by the irradiation from the thermal camera though. A visual inspection of the last *measured* snapshot in Figure 6.2 (top row) reveals that the thermal camera is almost indistinguishable in the transient temperature field. Observe that the total energy added to the fluid (by energization) is captured by its instantaneous energy content, which is defined as [55]

$$J_1(t) = \frac{1}{\pi}\int_{\mathcal{D}} \widetilde{T}^2(\boldsymbol{x},t)\mathrm{d}^2\boldsymbol{x}. \tag{6.1}$$

A comparison between the experiments presented here and in Section 5.4.1 is made based on $J_1(t)$. This comparison reveals that both experiments, with heat-transport driven by mere diffusion, have a maximum and time-averaged deviation in $J_1(t)$ of 22.6 % and 7 % (i.e. $J_1(t)$ is maximally 22.6 %, and on average 7 %, higher for the experiment considered in this section). Note, however, that the transient ambient temperature $\widetilde{T}_a(t)$ in the experiment in this section is slightly elevated as well. Hence, part of the higher energy content can also be attributed to a reduction in heat loss. For the abovementioned reasons, the experiment with heat transport governed by mere diffusion is still considered for analysis here.

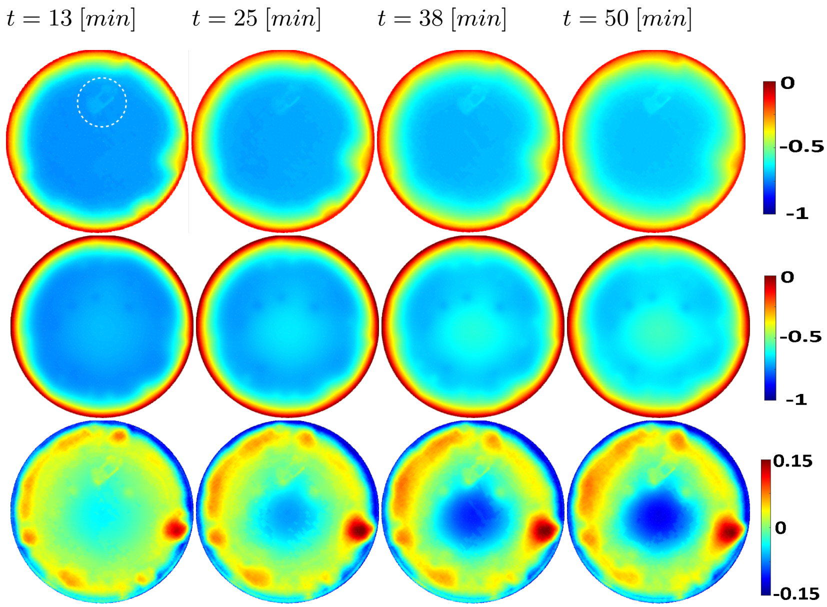

Figure 6.2: Measured (top row) and estimated (middle row) transient temperature snapshots (blue: $\min(\widetilde{T}) = -0.5$; red: $\max(\widetilde{T}) = 0$) for a RAM with heat-transport governed by mere diffusion ($i = 0$). The error between the transient fields is shown in the bottom row (blue: $\min(\boldsymbol{\varepsilon}) = -0.15$; red: $\max(\boldsymbol{\varepsilon}) = 0.15$). The estimator is designed for weighing matrices in (6.2) with model parameters presented in Table 5.2 and $q_{11} = 2 \cdot 10^3$.

Here, slightly altered weighing matrices, with respect to those in (5.32), are considered as

$$\widetilde{\boldsymbol{Q}} = \begin{bmatrix} \widetilde{q}_{11} & & & \\ & 1 & & \\ & & \ddots & \\ & & & 1 \end{bmatrix}, \qquad \boldsymbol{R} = \boldsymbol{I}, \tag{6.2}$$

to design the estimator gain matrix $\boldsymbol{L}^{(0)}$ as well. The rationale behind the weighing matrix $\widetilde{\boldsymbol{Q}}$ in (6.2) is that it puts, depending on the choice of $\widetilde{q}_1 1$, more emphasis on the first mode in (5.27). Here, this first mode represents the slowest eigenmode for heat transport driven by mere diffusion. As a result, the estimator exerts more effort to ensure $e_1^{(0)}(t_{k+1})$ in (5.26) converges faster on 0. Figure 6.3 shows the estimation error $\widetilde{J}$ for different tunings of the weighing matrices $\widetilde{\boldsymbol{Q}}$ and $\boldsymbol{Q}$ with $\boldsymbol{R} = \boldsymbol{I}$ (i.e. $r = 1$ in (5.32)).

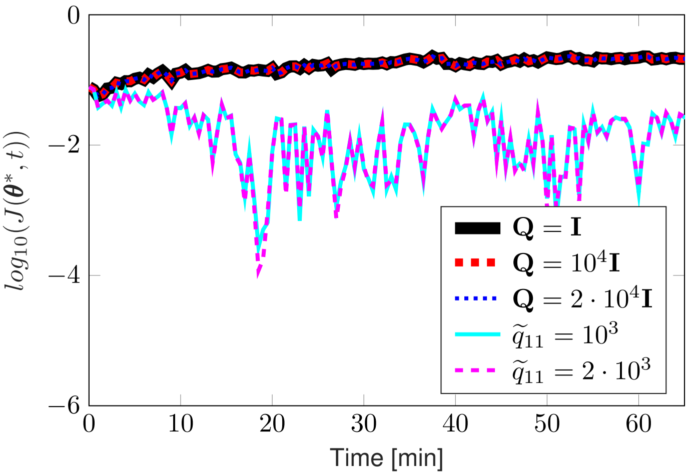

Figure 6.3: The estimation error $\widetilde{J}$ for different weighing matrices $\widetilde{\boldsymbol{Q}}$ and $\boldsymbol{Q}$ with $\boldsymbol{R} = \boldsymbol{I}$ for a RAM with heat-transport driven by mere diffusion. The employed estimator is designed based on (5.28) with parameters in Table 5.2.

Some notable discrepancies can be observed in the estimated fields in Figure 6.2. Localized cold spots can be observed that coincide with the sensor locations from Section 5.3.3. These spots are, most probably, caused by (local) noise amplification by the estimator. Moreover, a large hot spot can be observed at the center of the fluid domain. The matrices in (6.2) put a heavier penalization on the first mode in (5.27). As a result, the estimator gain matrix $\boldsymbol{L}^{(0)}$ responds faster and stronger to the contribution of the first eigenmode to the estimated transient temperature field. This results in the observed hot spot. Peak estimation errors occur in close proximity of the hot boundary. These peak errors are caused by the thermal camera's positioning (i.e. viewing the fluid under an angle obscures part of the temperature field). Errors stay below $\max \varepsilon \approx 0.23$ throughout the experiment though. Estimator designs for different weighing matrices are investigated to gauge the effect of tuning q and q_{11} in (5.32) and (6.2), respectively, on transient temperature field estimation in practice.

Figure 6.3 shows that $\widetilde{J}$ remains mostly unchanged for changed q in (5.32) (i.e. changes in $\widetilde{J}$ are very small). Similar behaviour is found for small $q \ll 1$ as well. These results are not shown here for brevity. However, heavier penalization of only the first mode in (5.27) can be seen to significantly decrease the estimation error $\widetilde{J}$ in Figure 6.3. The estimation accuracy for an estimator designed with weighing matrices in (6.2) is significantly improved compared to those designed with weighing matrices in (5.32). This result implies that not all states and outputs in (5.27) are of equal importance to the accuracy of the estimator. The result also suggests that tuning each diagonal entry in $\boldsymbol{Q}$ (or equivalently $\boldsymbol{R}$) could further improve the estimation accuracy. These results also suggest that a heat transport model for mere diffusion should accurately describe the slowest eigenmodes to achieve accurate scalar field estimation.

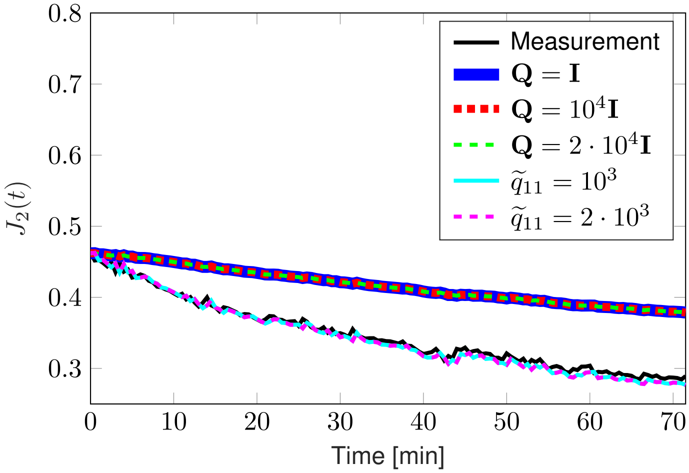

Figure 6.4: The measured and estimated cost-functions J_2 for different weighing matrices $\widetilde{\boldsymbol{Q}}$, $\boldsymbol{Q}$ and $\boldsymbol{R}$ for a RAM without flow. The employed estimator is designed based on (5.28) with parameters in Table 5.2.

The ability of the estimator to reconstruct $J_2(t)$ in (5.42) is investigated next. An accurate estimate of cost-function $J_2(t)$ is essential to the incorporation the estimator into a closed-loop flow controller for boosting fluid heating (e.g. see Chapter 2). Results of field estimation for different weighing matrices, with heat-transport driven by mere diffusion, are shown in Figure 6.4. Figure 6.4 reveals only a small deviation between the measured and estimated cost-function for an estimator designed on the weighing matrices in (6.2). A maximum deviation of only 5.8 % is observed between the estimated and measured cost-function for $\widetilde{q}_{11} = 2 \cdot 10^3$. Moreover, the result in Figure 6.3 suggests that a (local) optimum for $\widetilde{q}_{11}$ exists since $\widetilde{J}$ is underestimated by the estimator for $\widetilde{q}_{11} = 2 \cdot 10^3$ and overestimated for $\widetilde{q}_{11}$. This indicates that optimization of the *individual* diagonal elements in $\widetilde{\boldsymbol{Q}}$ can improve the transient field estimation for heat transport driven by mere diffusion. The ability of the estimator to reconstruct the transient temperature field when heat transport is driven by the base flow is investigated next.

6.3 Field estimation for the base flow

Field estimation for heat transport driven by the base flow is investigated next. Snapshots of the transient temperature field are shown in Figure 6.5. Both the measured (top row) and estimated (middle row) fields are shown. The estimated temperature fields show significantly less agreement with the measured fields than previously observed for field estimation with heat-transport driven by mere diffusion. Key to capturing the heating dynamics in the RAM is the accurate estimation of the plume as a result of fluid flows. This hot plume in the estimated fields shows some resemblance with the measured fields in Figure 6.5. However, as time progresses the plume in the estimated transient fields develops further into the domain than the plume for the measured field. Peak estimation errors can reach upto $\max(\boldsymbol{\varepsilon}) \approx 0.26$ upon starting state estimation for $q/r = 2 \cdot 10^{-3}$. This can clearly be seen in the error between the measured and estimated temperature fields. Peak estimation errors decay to as low as $\max(\boldsymbol{\varepsilon}) \approx 0.19$ as time progresses. These errors primarily occur in close proximity to the hot boundary and are caused by a small detection mismatch of the hot boundary following the application of the purpose built camera distortion compensation software (i.e. the hot boundary is detected slightly too large in the thermal image and the thermal camera observes the RAM under an angle). Nonetheless the field estimator is able to capture the transient temperature field remarkably accurate for a significant reduction in the number of modes (i.e. $M \ll N$).

Moreover, localized hot and cold ripples surround the hot plume that are reminiscent of the Gibbs phenomenon. The Gibbs phenomenon occurs if the number of modes considered is to low to capture high frequent (or fast) dynamics. The observed ripples (or striations) and differences in evolution between measured and estimated hot plume could thus indicate modelling error. These errors can be understood from the observation that $3D$ effects alter the fluid flow field compared to the theoretical flow field [12]. A different flow field will result in different eigenmodes in (5.13) and will, as a consequence, result in a different model (5.16) through (5.14). Moreover, the heat transfer coefficient κ is not necessarily constant. Local heat losses in the field depend on both the ambient air flow and the (transient) temperature field and are, thus, space dependent. This coefficient is assumed constant in Section 5.2.2 and, through (5.2), determines the convective heat losses from the RAM to the environment. A spatially varying κ will introduce local difference in heat loss and would result in a change of the eigenmodes in (5.13) as well. However, agreement of the transient temperature field in sections 5.4.1 and 6.2 suggests that these effects are minimal. These striations can also be the result of noise amplification by the estimator, since high estimator gains can inhibit noise attenuation [54].

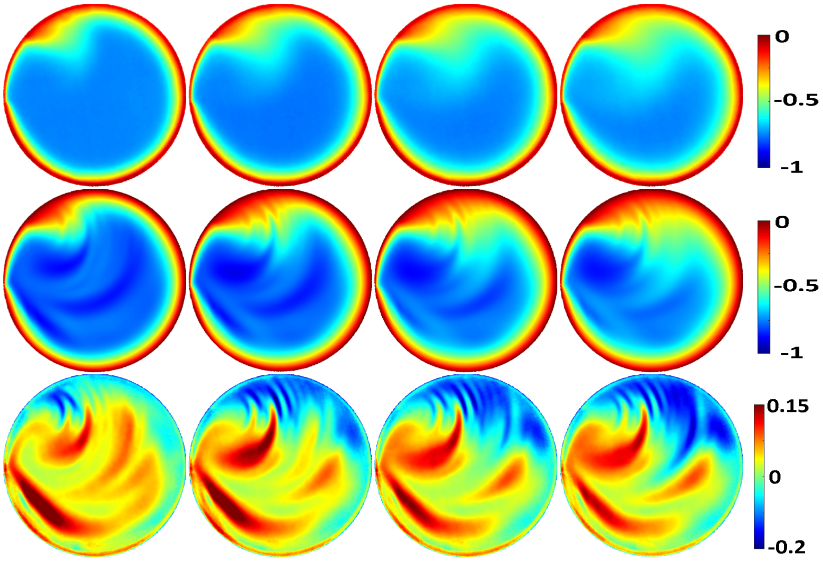
(a) $t = 30\ [min]$ (b) $t = 60\ [min]$ (c) $t = 90\ [min]$ (d) $t = 120\ [min]$

Figure 6.5: Measured (top row) and estimated (middle row) temperature snapshots (blue: $\min(\widetilde{T}) = -1$; red: $\max(\widetilde{T}) = 0$) with the error (blue: $\min(\boldsymbol{\varepsilon}) = -0.15$; red: $\max(\boldsymbol{\varepsilon}) = 0.2$) between them (bottom row) for a RAM with a rescaled base flow at $0.001\ m/s$. Model parameters used during estimator design in Table 5.2.

The estimation error $\widetilde{J}$ is therefore investigated for different weighing functions $\boldsymbol{Q}$ (or $\boldsymbol{R}$). The weighing matrices used to synthesize $\boldsymbol{L}^{(1)}$ can be found in (5.32). Hence, $\boldsymbol{L}^{(1)}$ is determined by the ratio q/r according to (5.33). The effect of estimator tuning on the evolution of the field estimation error $\widetilde{J}$ is of particular interest. The estimation error in (5.20) is a measure for the "energy" left in the mismatch between measured and estimated transient fields. It thus directly represents the mismatch in fluid heating between the measured and estimated system. Results are shown in Figure 6.6 for a base flow rescaled with $U = 0.001\ m/s$. Figure 6.6 shows that the estimator estimates the transient temperature field relatively accurately based on experimental measurements. Transient temperature fields are captured especially well at the start of the experiment. Nonetheless, the error $\widetilde{J}$ is orders of magnitude *larger* in the experiments than observed in Section 5.4.3.2.

This increased error compared to the numerical estimation results is caused by a variety of measurement noise and model error(s) as explained above. Furthermore, it should be noted that the used model is an approximation of heat transport in the RAM and, therefore, unmodelled dynamics can have a significant impact on the accuracy of scalar field estimation. Observe that decreasing q/r minimizes $\widetilde{J}$ significantly at the start of experiment. Conversely, increasing q/r results in an increase of $\widetilde{J}$. The field estimation error therefore responds in the same fashion for changing weighing functions as previously observed in Section 5.4.3.2. However, tuning based on $\widetilde{J}$ is challenging due to the presence of (measurement) noise, model mismatch and model inaccuracies. However, the “steady-state” estimation error is minimized most among the considered weighing functions between the considered ratios q/r. This suggests an optimal setting for q/r. To gauge the estimator’s ability to be used in a closed-loop flow control, the cost-function J_2 in (5.42) is investigated.

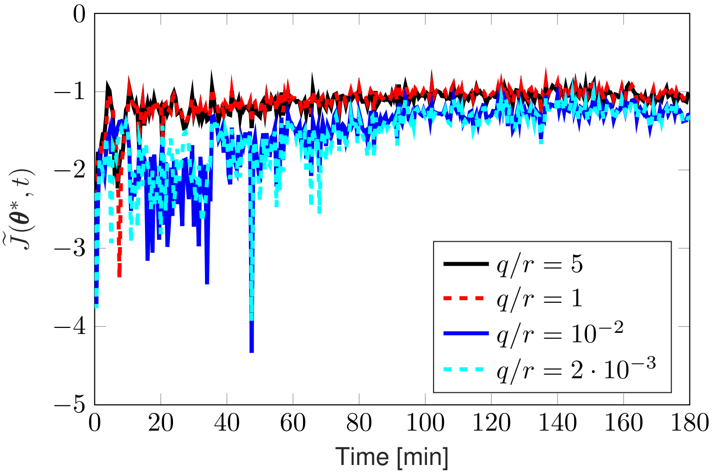

Figure 6.6: The estimated error $\widetilde{J}$ for different q/r on a RAM where heat transport is driven by a rescaled base flow at $0.001\ m/s$. The employed estimator is designed based on (5.28) with parameters in Table 5.2.

A significant mismatch between measured and estimated J_2 is observed at the early stage of estimation in Figure 6.6. The resulting error is significantly amplified upon increasing q/r. Heavier penalization of the outputs by increasing q/r decreases this initial amplification. The transient error in the state estimate rapidly declines as time progresses following this initial amplification. Furthermore, the higher gains appear to amplify the initial mismatch between estimated and measured cost-function. The peak mismatch, observed in Figure 6.6 directly after initialization, appears directly related to the increase of q/r. The increase of q/r results in heavier penalization of the state in (5.27) and results in higher gains in the estimator gain matrix $\boldsymbol{L}^{(1)}$. The estimator overcompensates, which results in the observed "overshoot" (i.e. peak error of J_2). The steady-state offset between estimated and measured cost-functions initially decrease as q/r penalizes the outputs in (5.27) more (i.e. the difference between measured and estimated J_2 decreases at the end of the window as q/r decrease). Eventually, higher output penalization also results in an increasing mismatch at steady-state. This can be observed upon comparing the estimated and measured cost-functions for small q/r in Figure 6.7. A different response is observed for large q/r in Figure 6.7. Heavier state penalization in (5.27) always appears to result in a deterioration of the steady-state field estimate for the considered q/r.

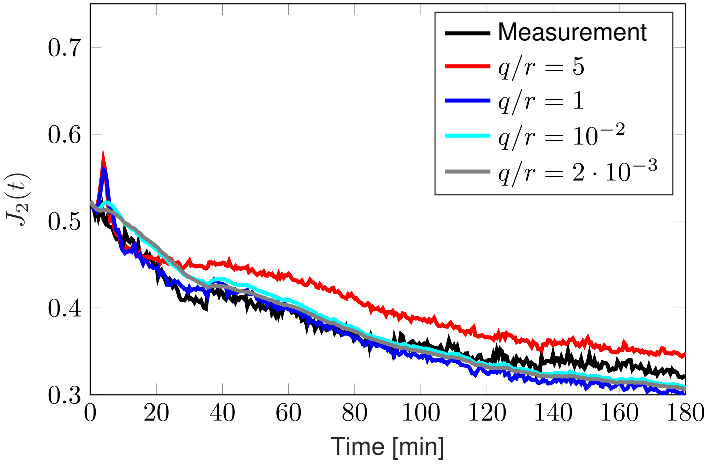

Figure 6.7: The measured and estimated cost-functions J_2 for different q/r for a RAM with a rescaled base flow at $0.001\ m/s$. The employed estimator is designed based on (5.28) with parameters in Table 5.2.

The presented results suggest that tuning of the gain matrix $\boldsymbol{L}^{(1)}$ should primarily concentrate on decreasing q/r. The presented results show that a *relative* relaxation of state penalization in (5.27) – through the decrease of q/r – results in a better overall estimate of J_2 and $\widetilde{J}$. The above analysis suggests that the design of $\boldsymbol{L}^{(1)}$ – by choosing q/r – is also dependant on the time-scale relevant for estimation. For example, estimation of the initial transient field is less important in thermal flow systems with constant flow (de)activation than in a system with dynamic flow (de)activation. In a thermal system with constant flow (de)activation, ample "time" is available to estimate the steady-state field. Accurate estimation of the steady-state field is less important to thermal systems with rapid switching between multiple flows though. Rationale behind this is that the estimation error $\widetilde{J}$ is primarily caused by switching between the multiple flows (see Section 6.4). Hence, minimizing the initial estimation error $\widetilde{J}$ is more important if the time between switches (or dwell-time) is small. The proposed estimator is intended to be included into a closed-loop heating strategy (e.g. with the estimated scalar field fed back to a flow controller as presented in Chapter 2 and [55]). Therefore, accurate steady-state estimates are less relevant than capturing the initial transient. The application of $\boldsymbol{L}^{(i)}$ to estimate the transient field for a periodic flow is studied next.

6.4 Field estimation for a periodic flow

The activation of multiple fluid flows and the possibility to switch between them requires the development of multiple state estimators (see Section 5.3.2). The fluid flows in the RAM differ by at most a reorientation (see Section 5.2.2), which is inherited by the eigenmodes in (5.14). Placing the sensors such that the output matrix is invariant reorientation allows for the straightforward design of $\boldsymbol{L}^{(i)}$ on the base flow alone (i.e. $\boldsymbol{L}^{(i)} = \boldsymbol{L}^{(1)}$). Here, transient temperature field estimation is investigated for a periodic flow. The flow follows a reorientation scheme $u(t)$ that periodically activates either the base flow ($i = 1$) or the reorientated flow ($i = 2$). Fluid flows are activated for 31 minutes during experiments on the RAM (or the aperture activation time $\tau_{tot} = 11$ time-units). This activation time, combined with $Pe \approx 10^3$, maximizes fluid heating with the considered periodic flow [16]. Note that the numerical results in Chapter 3 show that, for these parameters, heating rates attained with the adaptive reorientation scheme and the periodic reorientation scheme closely resemble each other. Experiments are initialized at the base flow ($i = 1$) as soon as the boundary temperature reaches its setpoint. Estimators are designed for different q/r on all available sensors (i.e. based on the reasoning in Section 6.3). Care should be taken in tuning the estimator gain matrix $\boldsymbol{L}^{(1)}$ though (see the discussion directly below (5.26)). The estimator should be granted ample “time” to estimate the scalar field between reorientations (i.e. the dwell-time should be sufficiently large).

Figure 6.8 presents snapshots of the measured fields and the estimated fields in the top and middle row, respectively. The error between these fields is shown in the bottom row. The snapshots reveal the transient temperature fields are estimated especially well at the start of the experiment. Moreover, the estimated hot plumes show qualitative agreement with those in the measured temperature fields. Some notable discrepancies are present though. Most noticeable is the hotter “base” of the plume in the estimated fields compared to the measured fields. In addition, striations can be observed throughout the domain in the estimated field. These striations are again reminiscent of the Gibbs phenomenon and are most clearly visible in the vicinity of the plumes and the colder parts of the domain. They introduce local hot and cold ripples inside the domain. Their relative magnitudes diminish between switches as time progresses. To quantify the accuracy of the estimator, the estimation error $\widetilde{J}$ is investigated next.

Figure 6.9 shows the estimation error between measured and estimated transient temperature fields for various q/r. Figure 6.9 reveals that heavier penal-

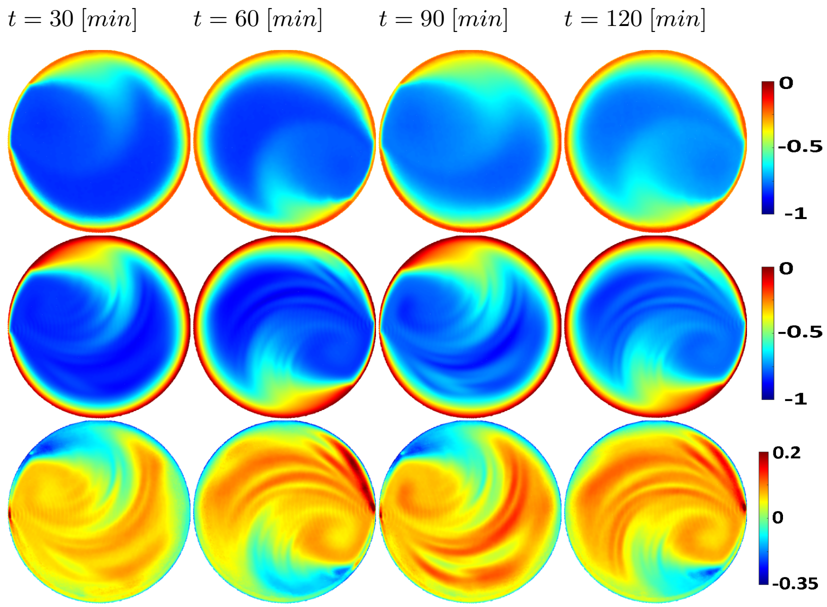

Figure 6.8: Measured (top row) and estimated (middle row) transient temperature snapshots (blue: $\min(\widetilde{T}) = -1$; red: $\max(\widetilde{T}) = 0$) with the error (blue: $\min(\boldsymbol{\varepsilon}) = -0.35$; red: $\max(\boldsymbol{\varepsilon}) = 0.2$) between them (bottom row) for a RAM with a periodic flow with a belt-speed of $0.004\ m/s$. Model parameters in Table 5.2 and $q/r = 2 \cdot 10^{-3}$ used during estimator design.

ization of the state – by increasing q/r – results in deteriorating state estimates. Large peaks can be observed in the estimation error as well. These peaks occur directly after the flow reorients and they are caused by the change in eigenmodes as a result of flow reorientation. An investigation of the transient temperature field reveals that an insufficient number of eigenmodes is retained to capture the scalar field immediately following the reorientation. Moreover, maximum peaks are observed directly following the reorientation from the base flow ($i = 1$) to the reoriented flow ($i = 2$). The reorientations between flows in the periodic flow can be thought of as discrete jumps in system dynamics. As a result of these jumps, all eigenmodes in the system are excited (i.e. similar to a step-response). The system (5.16) is detectable and sensors are placed such that the slowest eigenmodes are at least observable. Hence, rapid decay of the error after the jump is due to the rapid decay rate of the higher order modes. Penalizing the output more in (5.27) – by decreasing q/r – serves to diminish these large estimation peaks directly following a switch. This can be observed in Figure 6.9. Estimation errors are significantly lower throughout the entire experiment for lower q/r compared to the errors for higher q/r in Figure 6.9. Heavier penalization of the output by decreasing q/r shows improved convergence of the error dynamics on the origin.

Again, calculation of the (maximum) eigenvalues of $\boldsymbol{A}_{per}$ is hampered by the dimension of the matrix. Hence, the estimation error after a single period is investigated (i.e. $\widetilde{J}$ is sampled every 63 minutes). Periods are indicated by dashed gray lines in Figure 6.9. The exact moment of switching for the estimator designed with weighing matrices in (5.32) for $q/r = 2 \cdot 10^{-3}$ is indicated in Figure 6.9 by black-green circles. Figure 6.9 shows that the sampled estimation error decreases after each period. This is an indication that the estimator's have ample dwell-time to sufficiently estimate the state before another flow reorientation occurs.

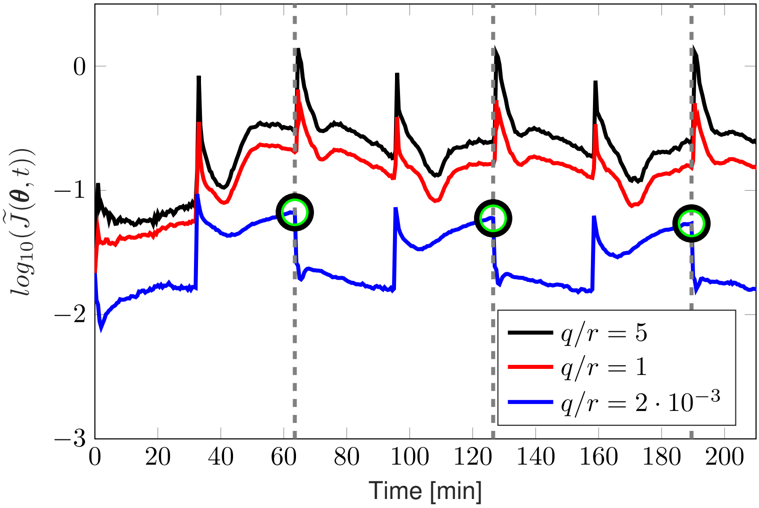

Figure 6.9: The estimatiod error $\widetilde{J}$ for different gains (a) $\boldsymbol{Q}$ and (b) $\boldsymbol{R}$ for a RAM with a periodic flow with a belt-speed of $0.004\ m/s$. The errors $\widetilde{J}$ sampled after a period (indicated by dashed gray lines) for $q/r = 2 \cdot 10^{-3}$ are indicated with black-green circles. The employed estimators are designed based on (5.28) with parameters in Table 5.2.

To investigate the estimation accuracy for output-based closed-loop flow control we investigate the ability to estimate the cost function $J_2(t)$. Figure 6.10 shows the measured and estimated cost functions for various q/r. Figure 6.10 reveals that the field estimator accurately estimates $J_2(t)$ for any q/r in the first 31 minutes (or 11 time units). Subsequent reorientation of flows results in poor estimates for the cost function for high q/r though. Increasing q/r actually deteriorates the cost-function estimate rather than improve it. Figure 6.10 also reveals that the discrepancy between the measured cost-function and the estimated cost-function is significantly smaller for smaller q/r compared to larger q/r. Moreover, decreasing q/r improves the estimate of the cost-function in the periodic flow. An optimal value appears to exists as results show that increasing q/r (i.e. beyond $q/r = 2 \cdot 10^{-3}$) further deteriorates the estimate of $J_2(t)$. Hence, optimal performance by the field estimator requires the optimization of q/r for each flow.

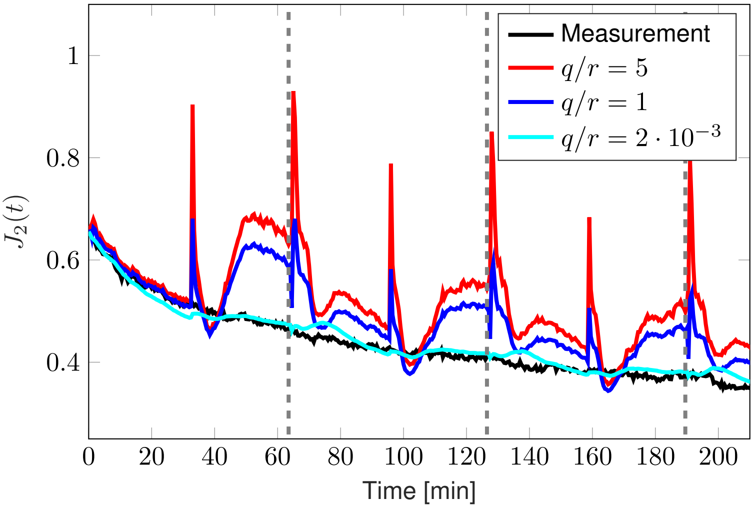

Figure 6.10: The measured and estimated cost-functions J_2 for different gains (a) $\boldsymbol{Q}$ and (b) $\boldsymbol{R}$ for a RAM with a periodic flow with a belt-speed $U = 0.004\ m/s$. The period is indicated with dashed gray lines ans the estimators are designed based on (5.28) with parameters in Table 5.2.

6.5 Conclusions and discussion

The present study investigates the accuracy of scalar field estimation in practice. To this end the scalar estimator is experimentally investigated on the representative heat-transfer problem studied throughout this thesis; the RAM. Field estimation accuracy is – as done numerically in Chapter 5 – investigated for scalar transport driven by mere diffusion and the base flow. As a prelude to output-based closed-loop flow control, the estimators accuracy is investigated for a conventional periodic flow as well.

The Luenburger state estimators studied here are synthesized by posing the detection problem as a linear quadratic regulator problem with diagonal weighing matrices. Experimental analysis shows that the estimator is able of accurately reconstructing/estimating the scalar field in such a case. The estimator can capture the scalar field accurately with scalar transport driven by mere diffusion only after rudimentary tuning of the weighing matrices (i.e. emphasizing only the first mode instead of all considered eigenmodes). Field estimates prove considerably more challenging in the presence of fluid flows though. Field estimates are considerably less accurate, but the estimator is able to capture the important heating measure fairly accurately. The estimation of this measure is essential to i) monitor the instantaneous “state of fluid heating and ii) enable heating acceleration by output-based closed-loop flow control. Field estimation accuracy of the estimator is further investigated for an experiment with a periodically reorienting fluid flow as well. Results reveal close agreement between the measured and the estimated scalar fields, which results in close agreement between the estimated heating measure and the measured heating measure as well. Finally, the weighing matrices should put more emphasize on the output to minimize peak estimation errors with the developed estimator.

Future efforts should, first, be focused on noise attenuation for heat transport in the RAM. Such an analysis will prove vital insights into the estimator’s accuracy in an industrial setting (e.g. heat loss to the environment is far better controlled there). Tuning of the weighing matrices is of particular interest to this analysis (e.g. by tuning the diagonal entries of the weighing matrices). Second, estimation accuracy of the estimators should be evaluated when sensors for (partial) scalar field measurement are directly placed in the fluid. Such placement can potentially significantly alter scalar transport, i.e., by altering the fluid flow, and thus deteriorate the estimation accuracy with the current models. Finally, research should focus on closed-loop flow control where outputs are measured by sensors placed inside the fluid are fed back to achieve rapid fluid heating.

CHAPTER 7

Conclusions and recommendations

Scalar transport by (reoriented) fluid flows is a key feature in various (industrial) applications ranging from, e.g., viscous mixing of polymers and foodstuffs via process intensification and underground resource extraction by subsurface flows to microfluidic heating/cooling in small-scale circuitry. Rapid scalar transport can have significant benefits. For example, rapid scalar transport results in a more effective operation of these applications. Hence, this lowers the energy expenditure of applications, to achieve the same target. Heat transport (in fluids) accounts for a large portion of the energy used by both industry and private consumers. Boosting heat transport by fluid stirring can thus potentially lead to lower energy usage. Therefore, this thesis is focussed around the main question:

- How to stir a fluid to heat it up as quickly as possible?

In this thesis, a heat-transfer system known as the Rotated Arc Mixer (RAM) is studied. Fluid stirring is achieved in the RAM by reorienting Stokes flows and heat transport occurs in the presence of i) a non-adiabatic boundary condition, and ii) significant diffusion. These features make the RAM representative as a case-study for the systems of interest to this thesis. The principal objective of this thesis is to gain theoretical and experimental insight into the design of closed-loop flow forcing controllers that can boost scalar transport by stirring. The intermediate objectives related to this principal objective are:

Objective 1. Gain insights into heating dynamics that can be used to structurally boost fluid heating in practice.

Objective 2. Develop a flow forcing controller that significantly enhances fluid heating in the presence of both diffusion and a non-adiabatic boundary condition.

Objective 3. Develop a method that is able to accurately capture/reconstruct the scalar field from discrete sensor data in practice.

The conclusions regarding the main question – and related objectives – are summarized here.

7.1 Conclusions

Chapter 2 is focused on objectives 1 and 2. A dedicated flow-control strategy is developed in Chapter 2 (i.e. “adaptive flow reorientation”) that systematically determines the “best” flow reorientation for the fast heating of a cold fluid via a hot boundary in the RAM.

The control strategy is founded on an in-depth analysis of the dynamics of heating in fluid flows. This exposes fluid deformation as the “thermal actuator” via which the flow affects the heat transfer. The link between former and latter is non-trivial, though. Fluid deformation may, depending on its orientation relative to the temperature gradient, both enhance and diminish local heat exchange between fluid parcels. Moreover, enhanced heat transfer promotes local thermal homogenisation and, by reducing temperature gradients, thus effectively counteracts itself. This fundamental “conflict” between local heat transfer and thermal homogenisation tends to restrict the beneficial impact of flow to short-lived episodes following a flow’s activation. The impact of fluid deformation on the global fluid heating is primarily confined to the direct proximity of the moving boundary that drives the flow. Fluid deformation in the flow interior only plays a secondary role in this process due to its relative weakness compared to said regions. These insights imply that incorporation of the thermal behaviour is essential for effective flow-based enhancement strategies and efficient fluid mixing, the conventional approach adopted in industry for this purpose, is potentially sub-optimal.

Global heating encompasses two concurrent processes, i.e. increasing energy content (“energising”) and thermal homogenisation, and this fundamentally differentiates the current problem from the thermal homogenisation in adiabatic systems usually considered in related studies. Moreover, this notion yields the relevant metrics for the global dynamics and thus enables formulation of the control problem as the minimisation of a dedicated cost function that naturally emerges from the dynamic analyses and adequately incorporates both processes. This facilitates step-wise determination of the “best” flow reorientation from predicted future evolutions of actual intermediate states and, in tandem with an efficient predictor, paves the way to (real-time) regulation of scalar transport by flow control in practical applications. Key enablers for this predictor are i) the property that flow reorientations carry over to the temperature field ii) a compact reduced-order model for the Perron-Frobenius evolution operator that rapidly maps initial to final temperature fields for each step duration and flow reorientation.

Performance analyses reveal that adaptive flow reorientation significantly accelerates the fluid heating throughout the considered parameter space and thus is superior over conventional periodic schemes (designed for efficient fluid mixing) both in terms of consistency and effectiveness. Fluid heating is accelerated in the RAM by at least 14% everywhere and 24% or more in large areas. Process enhancement of this magnitude on other (industrial) applications would constitute a dramatic reduction in energy and (potentially also) resource consumption. The controller in fact breaks with conventions by, first, never selecting these periodic schemes and, second, achieving the same superior performance for all flow conditions irrespective of whether said mixing occurs. The controller typically achieves this superiority by creating an essentially heterogeneous situation comprising of thermal plumes that extend from the hot wall into the cold(er) interior and are driven by two alternating and counter-rotating circulations. The performance analyses furthermore substantiate the primary and secondary roles of fluid deformation near the driving boundary segments and in the flow interior, respectively, in the heating enhancement by the flow.

Chapter 3 extends the analysis of the reorientation schemes found with the dedicated control approach from Chapter 2. This chapter is focused on further gaining insights into fast fluid heating and is thus concentrated on objective 2. Fluid heating is investigated for a large span of realistic fluid and flow properties. Fluid is merely allowed to circulate in a single direction to emulate existing fluid flow configuration of existing fluid mixing/heating applications widely adopted in industry. Hence, fluid stirring with adaptive flow reorientation is constrained during the optimization in this chapter compared to Chapter 2. Numerical results show that adaptive flow reorientation yields a systematic improvement over a large span of these parameters. Moreover, numerical results reveal improved resilience against parameter variations with the reorientation schemes, found with the dedicated controller from Chapter 2, while simultaneously ensuring faster heating. Reorientation schemes achieve these two facets by either i) (slightly) altering the conventional periodic reorientation scheme or ii) introducing an aperiodic transient to an otherwise periodic reorientation scheme.

In Chapter 4, performance and sensitivity of a general nonlinear control methodology to accelerate scalar transport is investigated. This chapter is also focused on objective 1 and 2. The presented control methodology relies on a spectral decomposition of the advection-diffusion equation of the Laplacian eigenfunctions on a circular plane. The infinite dimensional system is approximated by a compact finite dimensional bilinear state-space description. The real-time control of the scalar field involves designing the inputs such that the decay rate of a generic Lyapunov function or “thermal energy” is minimized. In Chapter 4, two flow control methods, that minimize this decay rate, are proposed: a bang-bang controller and a nonlinear quadratic feedback controller. Heat transport from the hot boundary is significantly improved resulting in substantially accelerated heating rates compared to mere diffusion. Both controllers are found to significantly accelerate the heating rates compared to continuous fluid circulation depending on the number of flows and the controller tuning. The bang-bang controller shows high-frequency behaviour during control, which is undesirable for real-time actuation. The inputs of the nonlinear quadratic feedback controller are proportional with the temperature field due to its quadratic feedback and are, therefore, less restrictive than the inputs of the bang-bang controller. However, this comes at a sacrifice of heating rate improvement. However, rapid switching is significantly reduced during control with the nonlinear controller as a consequence.

Heating rates with the nonlinear controller are compared to a conventional open-loop periodic reorientation scheme for perturbed initial conditions. Results show that the nonlinear controller consistently outperforms the periodic scheme for both the unperturbed and perturbed initial conditions. Moreover, plume formation, by circulating the fluid in opposite directions between apertures, seems to form a key characteristic for this effective heat transfer from the hot boundary (in)to the fluid. Namely, both flow controllers circulate the fluid in opposing directions between neighbouring fluid flow fields and effectively heat the fluid. This fluid flow behaviour possesses some resilience towards perturbations, since resulting plumes are formed regardless of the initial conditions considered here. The fluid circulation behaviour is similar to the behaviour observed in Chapter 2. The key difference between this behaviour and the flow forcing behaviour observed in Chapter 4 is that both flow controllers *simultaneously* circulate the fluid resulting in a hot plume. The consistently improved heating rates by similar fluid flow behaviour makes the proposed methods – or at least the resulting fluid circulation behaviour – tailor-made for practical applications of flow control to boost heat transport in i) the presence of significant diffusion and ii) the absence of a boundary condition that can directly influence the scalar field, e.g., an adjustable boundary temperature.

In Chapter 5, a method for the detection of scalar transport in a fluid from a set of sensors that discretely sample the field is presented. This chapter is thus focused on the third objective of this thesis. To this end, a dedicated scalar field estimator is developed that systematically reconstructs the transient temperature field by estimating the contribution of the “dominant” eigenmodes based on a discrete set of thermal sensors to capture heating of a cold fluid via the hot boundary in the RAM. The detection strategy relies on the reconstruction of so-called “dominant” eigenmodes, which have been shown essential for the accurate description of scalar transport in Chapter 2. The sensors and the thereupon developed field estimator are, respectively, placed and designed based on these eigenmodes as well. The considered scalar transport dynamics therefore play a crucial role in accurately reconstructing the dominant eigenmodes and the scalar field. A Luenburger state estimator is developed by posing the detection problem as a (dual) linear quadratic regulator problem. Numerical analysis shows that the estimator is capable of accurately reconstructing the scalar field.

In Chapter 6, the field estimator – developed in Chapter 5 – is investigated on an experimental version of the RAM as well. Results show that the estimator is able to capture the scalar field accurately in the absence of any fluid flow even after only rudimentary tuning and poor sensor placement. Field estimates prove considerably more challenging in the presence of fluid flows though. Field estimates are considerable less accurate. However, the estimator is able to capture the fluid heating measure, used by the flow controllers in this thesis, quite accurately. Field estimation accuracy of the estimator is further investigated on a periodically reorienting fluid flow as well. Results reveal close agreement between the measured and the estimated transient fields resulting in close proximity of the estimated heating measure to the measured heating measure.

7.2 Recommendations

Several suggestions for future research and development arise. These are as follows.

Fluid stirring by reorienting Stokes flows is a key feature in many industrial flow systems, which can be utilized to boost scalar transport. Boosting heat-transfer from a non-adiabatic boundary condition in(to) a fluid by reorienting Stokes flows has therefore been studied on the RAM as a case-study throughout this thesis. The RAM is experimentally realisable and admits laboratory studies both on (chaotic) advection and thermal transport. However, industrial applications typically have complexer geometries and operate under more challenging conditions than explored for the RAM. In principle, the flow controllers developed in this thesis can be applied to more complex cases as well. Hence, the flow controllers developed in this thesis should be studied on systems other than the RAM to determine the generality of their fluid heating performance.

The dedicated flow control-strategy, developed in Chapter 2, shows great promise to improve fluid mixing/heating in the RAM. However, applications of this flow controller have largely been theoretical and numerical throughout this thesis. Implementation of the flow controller on the experimental RAM in a preliminary study – not part of this thesis – suggests that results translate to practice as well [144]. Ongoing research should be focussed on ascertaining the robustness of the fluid heating enhancement by the developed controller in practice. This leads the way to the industrial application of these type of dedicated flow controllers.

Both the dedicated flow controller and scalar field estimator in, respectively, Chapter 2 and Chapter 4 rely on the eigenmodes associated with the base flow. The methods in those chapters rely on a scalar transport model to obtain the eigenmodes of the Perron-Frobenius operator, e.g., from CFD software. The modelling effort to obtain the eigenmodes can become exceedingly cumbersome for geometries/systems complexer than the RAM considered in this thesis, though.

Moreover, the identification of model parameters to obtain the eigenmodes can incur significant computational overhead for such geometries/systems. Data-driven models such as, e.g., Dynamic Mode Decomposition (DMD) could provide an alternative that minimize both the modelling and numerical efforts to obtain these eigenmodes. Future work could concentrate on a data-driven approach to rapidly obtain the eigenmodes for both flow control and scalar field detection.

The numerical analyses in Chapter 3 have revealed that a slight adaptation of existing periodic reorientation schemes can already significantly improve heating rates in the RAM. These results are obtained with adaptive flow reorientation on a RAM with three possible flow reorientations. A further analysis of the adaptive reorientation approach for perturbed system conditions, e.g., a perturbed initial condition, is also required though. Such further analyses might reveal tuning guidelines to improve heating/mixing rates for (a)periodic reorientation schemes in existing applications without the need for any major (mechanical) overhauls.

The bang-bang controller and nonlinear quadratic feedback controller developed in Chapter 4 were studied for a single Péclet number. Hence, fluid heating performance for these controllers for different fluid and flow parameters are unknown. Exceeding stiffness for larger Péclet numbers might result in long simulation times. Preliminary numerical simulations show that the advantage of the nonlinear quadratic controller, to boost fluid heating, also holds for higher Péclet numbers than studied in this thesis. Fluid heating performance of the nonlinear quadratic feedback controller should be investigated further in future studies to determine generality of fluid heating performance with these flow controllers.

The flow controllers developed in Chapter 2 and Chapter 4 have both exposed a similar plume forming mechanism that effectively boosts fluid heating on the RAM (i.e. circulating fluids between neighbouring apertures). This fluid heating phenomenon is shown to have some degree of resilience against perturbations for the nonlinear quadratic feedback controller. Moreover, (a)periodic and opposing circulation between neighbouring apertures occurred throughout the large parameter span studied in Chapter 2. Future research should study if this methodology of fluid circulation also results in enhanced heat transport for fluid flow systems with other geometries/operating conditions than the RAM. If so, the mechanism represents an opportunity to improve heating/mixing rates in existing applications without major (mechanical) alterations.

Scalar field estimation is studied in Chapter 5 for heat-transport driven without flow, the base flow and a periodic flow. The scalar field was estimated especially accurately when heat-transport inside the fluid is driven by a periodic flow. Moreover, the developed scalar field estimators captured the heating measure, presented in Chapter 2, sufficiently accurate regardless of these flow fields. The estimation of this measure is essential to; i) monitor the evolution of fluid heating and ii) enable fluid heating with closed-loop flow controllers based on the scalar field. Closed-loop flow control with feedback based on a reconstructed/estimated scalar field requires a more rigorous study of the estimator's (stability) properties than examined in this thesis. Future efforts should therefore concentrate on closed-loop flow control where a scalar field, estimated on a finite sensor set, is fed back.

In Chapter 5, the scalar field is estimated from a finite number of ”virtual” sensors that discretely sample the scalar field from a thermal image in this thesis. A thermal image is generally unavailable in existing applications and thus sensors need to be placed inside the fluid to locally gauge the fluid temperature in practice (e.g. placing thermal couples inside the fluid flow). Placing sensors inside the fluid can potentially alter the fluid flow field, e.g., due to vortex shedding, and thus, as a result, disturb the development of the scalar field. This can potentially significantly influence field estimation accuracy. Moreover, the sensor placement method used in this thesis is based on the thermal eigenmodes associated with the base flow, which does not account for (parametric) noise directly. In addition, poor sensor placement can result in (additional) measurement noise if sensors are placed in the wake formed upstream of a sensor. Future research of the estimators should theoretically and experimentally study the impact of the sensors on both the scalar field evolution and its estimation.

APPENDIX A

Evolution of metric J_1

The evolution of metric J_1 according to (2.33) is governed by

$$\begin{aligned}\frac{dJ_1}{dt} &= \int_{\mathcal{D}} \frac{\partial \widetilde{T}^2}{\partial t} d^2\mathbf{x} = 2\int_{\mathcal{D}} \widetilde{T}\frac{\partial \widetilde{T}}{\partial t} d^2\mathbf{x} \\ &\overset{(2.3)}{=} -2\int_{\mathcal{D}} \widetilde{T}\,\mathbf{v}\cdot\boldsymbol{\nabla}\widetilde{T} d^2\mathbf{x} - 2\int_{\mathcal{D}} \widetilde{T}\,\boldsymbol{\nabla}\cdot\widetilde{\mathbf{q}} d^2\mathbf{x}.\end{aligned} \tag{A.1}$$

The leading term on the RHS of (A.1) admits reformulation as

$$\begin{aligned}\int_{\mathcal{D}} \mathbf{v}\cdot(\widetilde{T}\boldsymbol{\nabla}\widetilde{T}) d^2\mathbf{x} = \int_{\mathcal{D}} \mathbf{v}\cdot\boldsymbol{\nabla}(\widetilde{T}^2/2) d^2\mathbf{x} \overset{\boldsymbol{\nabla}\cdot\mathbf{v}=0}{=} \int_{\mathcal{D}} \boldsymbol{\nabla}\cdot\left(\mathbf{v}T^2/2\right) d^2\mathbf{x} \\ \int_{\Gamma} \mathbf{v}\cdot\mathbf{n}\widetilde{T}^2/2ds = 0,\end{aligned} \tag{A.2}$$

due to $\mathbf{v}\cdot\mathbf{n} = 0$ and $\widetilde{T} = 0$ on Γ. The trailing term on the RHS of (A.1) admits reformulation as

$$\begin{aligned}\int_{\mathcal{D}} \widetilde{T}\,\boldsymbol{\nabla}\cdot\widetilde{\mathbf{q}} d^2\mathbf{x} &= \int_{\mathcal{D}} \boldsymbol{\nabla}\cdot(\widetilde{T}\widetilde{\mathbf{q}}) d^2\mathbf{x} - \int_{\mathcal{D}} \widetilde{\mathbf{q}}\cdot\boldsymbol{\nabla}\widetilde{T} d^2\mathbf{x} \\ &= \int_{\Gamma} \widetilde{\mathbf{q}}\cdot\mathbf{n}\widetilde{T} ds - \int_{\mathcal{D}} \widetilde{\mathbf{q}}\cdot\boldsymbol{\nabla}\widetilde{T} d^2\mathbf{x} \\ &= -\int_{\mathcal{D}} \widetilde{\mathbf{q}}\cdot\boldsymbol{\nabla}\widetilde{T} d^2\mathbf{x},\end{aligned} \tag{A.3}$$

due to $\widetilde{T} = 0$ on Γ. Substitution of (A.2) and (A.3) into (A.1) yields

$$\frac{dJ_1}{dt} = 2\int_{\mathcal{D}} \widetilde{\mathbf{q}}\cdot\boldsymbol{\nabla}\widetilde{T} d^2\mathbf{x}. \tag{A.4}$$

as simplified evolution equation for metric J_1.

APPENDIX B

Laplacian eigenfunctions

The eigenfunction-eigenvalue problem of the Laplacian operator as $\Delta\phi_\ell\left(\boldsymbol{x}\right) = \lambda_\ell\phi_\ell\left(\boldsymbol{x}\right)$ on a circular domain results in eigenfunctions of the form [16]

$$\phi_\ell\left(\boldsymbol{x}\right) = \sqrt{\frac{2}{\pi}}\frac{J_\ell\left(\alpha_\ell r\right)}{J_{\ell+1}\left(\alpha_\ell\right)}\begin{cases}\frac{1}{\sqrt{2}} & \text{if } \ell \in \Sigma_0,\\ \cos\left(\ell\theta\right) & \text{if } \ell \in \Sigma_1,\\ \sin\left(\ell\theta\right) & \text{if } \ell \in \Sigma_2,\end{cases} \tag{B.1}$$

with $J_k\left(\alpha_\ell r\right)$ the kth-order Bessel function of the first kind, α_ℓ the ℓth zero of the kth-order Bessel function of the first kind and Σ_0, Σ_1 and Σ_2 index sets required for ordering.

APPENDIX C

Well-posedness of the bang-bang controller

Discrete switching events in a continuous (closed-loop) system can make obtaining numerical solutions difficult if not impossible (e.g. due to infinitely many switches in a finite time [145]). Well-posedness, that is existence and uniqueness of solution trajectories, of these hybrid system needs to be examined. This chapter examines well-posedness of the bang-bang controller presented in Section 4.3.4.1. In Section C.1 relevant concepts and definitions for the well-posedness analysis are introduced. Moreover concepts are introduced in the context of the bang-bang controller. Their theoretical treatment is therefore neither exhaustive nor rigorous here. A more formal and comprehensive background on hybrid automatons, on which this section is based, can be found in Lygeros [146], and Lygeros et al. [147]. Finally, well-posedness of the bang-bang controller for two flows is analysed in Section C.2.

C.1 Hybrid automaton definitions

Hybrid automata are continuous dynamical systems that contain discrete switching events. A hybrid automaton A consists of a collection of sets such that $A = (Q, H, f, Init, Dom, E, G, R))$. These sets are defined, in order, as:

i) The set $Q = \{q_1, q_2, \ldots\}$ contains all discrete modes of operation of the hybrid automaton.

ii) The set H represents the continuous state of the automaton and thus consist of $H = \mathbb{R}^K$ according to (4.5).

iii) The vector field $\boldsymbol{f}_i(\cdot,\cdot) : Q \times H \to \mathbb{R}^n$ associated with discrete state i.

iv) The set $Init \subset Q \times H$ contains all possible combinations of states from which the automaton can be initialized (i.e. combination of discrete and continuous states).

v) The domain $Dom(\cdot) : Q \to P(H)$ assigns continuous states to the discrete states in Q.

vi) The set $E \subset Q \times Q$ contains the edges along which the system "transitions" between discrete states.

vii) The set $G(\cdot) : E \to P(H)$ consists of guard condition that, if true, "triggers" the transition between discrete states.

viii) The reset map $R(\cdot,\cdot) : E \times H \to P(H)$ establishes the relationship between continuous states before and after an event.

The power set $P(H)$ refers to the set of all subsets of H. The combination of q and $\boldsymbol{\eta}$ defines the state of the hybrid automaton A (i.e. $(q, \boldsymbol{\eta}) \in Q \times H$). The definitions presented below are directly adopted from Lygeros [146].

Definition C.1 (Lygeros [146], Definition 4.1). *A state $(\tilde{q}, \tilde{\boldsymbol{\eta}}) \in Q \times H$ of a hybrid automaton A is called reachable if there exists a finite execution (τ, q, x) ending in $(\tilde{q}, \tilde{\boldsymbol{\eta}})$, i.e. $\tau = \{[\tau_i, \tau_i']\}_0^N$, $N < \infty$, and $(q_N(\tau_N'), \boldsymbol{\eta}_N(\tau_N')) = (\tilde{q}, \tilde{\boldsymbol{\eta}})$.*

Definition C.1 formally states that the $(\tilde{q}, \tilde{\boldsymbol{\eta}})$ can be reached by the automaton within a finite amount of time steps starting at τ_i. The set of all these reachable states is defined as $Reach$. The set of states for which *continuous* state evolution is impossible is defined as $Trans$.

Definition C.2 (Lygeros [146], Definition 4.2). *A hybrid automaton H is called non-blocking if for all initial $(\tilde{q}, \tilde{\boldsymbol{\eta}}) \in Init$ there exists an infinite execution starting at $(\tilde{q}, \tilde{\boldsymbol{\eta}})$. It is called deterministic if for all initial states $(\tilde{q}, \tilde{\boldsymbol{\eta}}) \in Init$ there exists at most one maximal execution starting at $(\tilde{q}, \tilde{x})$.*

Non-blocking automata, according to Definition C.1, are in essence assured to have a state trajectory. If the automaton is simultaneously deterministic, then the state trajectory converging on $(\tilde{q}, \tilde{\boldsymbol{\eta}})$ is also unique. The abovementioned definitions are important to show existence and uniqueness of a state trajectory. Two important Lemmas are presented here that, if satisfied, ensure the existence and uniqueness of a state trajectory.

Lemma C.1: (Lygeros [146], Lemma 4.1). *A hybrid automaton A, is non-blocking if for all $(\tilde{q}, \tilde{\boldsymbol{\eta}}) \in Reach \cap Trans$, there exists $\tilde{q}' \in Q$ such that $(\tilde{q}, \tilde{q}') \in E$ and $\tilde{\boldsymbol{\eta}} \in G(\tilde{q}, \tilde{q}')$. If A is deterministic, then it is non-blocking if and only if this* *condition holds.*

Hybrid automatons that satisfy Lemma C.1 have continuous and discrete states that are well-defined. In other words, for a non-blocking hybrid automaton it is ensured that a state trajectory exists for all $(\tilde{q}, \tilde{\boldsymbol{\eta}}) \in Init$. Moreover this trajectory is unique if Lemma C.2 is satisfied.

Lemma C.2 (Lygeros [146], Lemma 4.2). *A hybrid automaton, A, is deterministic if and only if for all $(\tilde{q}, \tilde{\boldsymbol{\eta}}) \in Reach$*

i) *if $\tilde{\boldsymbol{\eta}} \in G(\tilde{q}, \tilde{q}')$ for some $(\tilde{q}, \tilde{q}') \in E$, then $(\tilde{q}, \tilde{\boldsymbol{\eta}}) \in Trans$;*

ii) *if $(\tilde{q}, \tilde{q}') \in E$ and $(\tilde{q}, \tilde{q}'') \in E$ with $\tilde{q}' \neq \tilde{q}''$ then $\tilde{\boldsymbol{\eta}} \neq G(\tilde{q}, \tilde{q}') \cap G(\tilde{q}, \tilde{q}')'$; and,*

iii) *if $(\tilde{q}, \tilde{q}') \in E$ and $\boldsymbol{\eta} \in G(\tilde{q}, \tilde{q}')$ then $R(\tilde{q}, \tilde{q}', \tilde{\boldsymbol{\eta}}) = \{\tilde{\boldsymbol{\eta}}'\}$, i.e. the set contains a single element, $\tilde{\boldsymbol{\eta}}'$.*

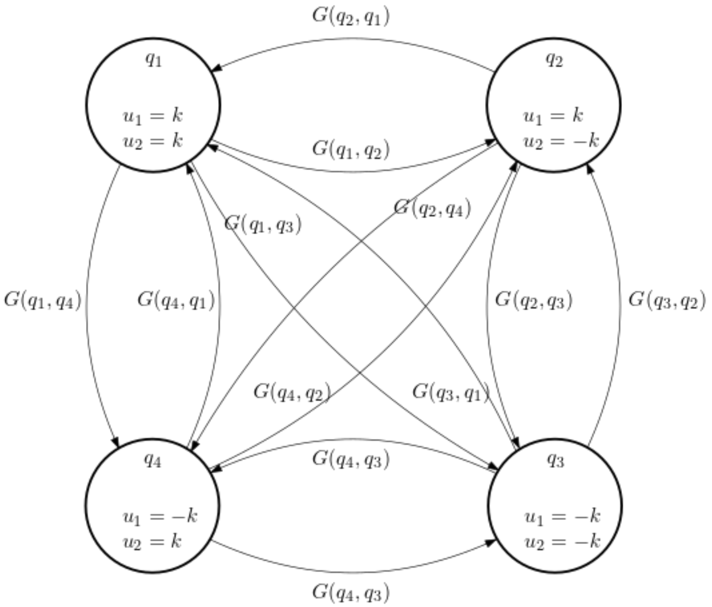

Figure C.1: Hybrid automaton for heating by bang-bang control of a RAM with two apertures ($I = 2$).

By satisfying both Lemmas one is assured that an unique state trajectory exists. Zeno-type behavior, i.e., infinitely many switches in finite time, might still be part of the system behaviour despite it being well-posed though. Proving the absence/presence of Zeno-type behavior with closed-loop flow control of the RAM is considered beyond the scope of this work however.

Table C.1: Table with guard conditions regulating the discrete transition between modes for bang-bang control of a RAM with two apertures ($I = 2$).

Mode	q_1	q_2	q_3	q_4
q_1	-	$G(q_1, q_2) = \{\boldsymbol{\eta} \in H \mid \Sigma_1 \leq 0 \wedge \Sigma_2 \geq 0\}$	$G(q_1, q_3) = \{\boldsymbol{\eta} \in H \mid \Sigma_1 \geq 0 \wedge \Sigma_2 \leq 0\}$	$G(q_1, q_4) = \{\boldsymbol{\eta} \in H \mid \Sigma_1 \geq 0 \wedge \Sigma_2 \geq 0\}$
q_2	$G(q_2, q_1) = \{\boldsymbol{\eta} \in H \mid \Sigma_1 \leq 0 \wedge \Sigma_2 \leq 0\}$	-	$G(q_2, q_3) = \{\boldsymbol{\eta} \in H \mid \Sigma_1 \geq 0 \wedge \Sigma_2 \geq 0\}$	$G(q_2, q_4) = \{\boldsymbol{\eta} \in H \mid \Sigma_1 \geq 0 \wedge \Sigma_2 \leq 0\}$
q_3	$G(q_3, q_1) = \{\boldsymbol{\eta} \in H \mid \Sigma_1 \leq 0 \wedge \Sigma_2 \geq 0\}$	$G(q_3, q_2) = \{\boldsymbol{\eta} \in H \mid \Sigma_1 \geq 0 \wedge \Sigma_2 \leq 0\}$	-	$G(q_3, q_4) = \{\boldsymbol{\eta} \in H \mid \Sigma_1 \geq 0 \wedge \Sigma_2 \leq 0\}$
q_4	$G(q_4, q_1) = \{\boldsymbol{\eta} \in H \mid \Sigma_1 \geq 0 \wedge \Sigma_2 \leq 0\}$	$G(q_4, q_2) = \{\boldsymbol{\eta} \in H \mid \Sigma_1 \leq 0 \wedge \Sigma_2 \leq 0\}$	$G(q_4, q_3) = \{\boldsymbol{\eta} \in H \mid \Sigma_1 \leq 0 \wedge \Sigma_2 \geq 0\}$	-

Switching functions are defined as $\Sigma_i = \boldsymbol{\eta}^\dagger \boldsymbol{Q}_i \boldsymbol{\eta}$ for $i = 1, 2$.

C.2 Analysis of the bang-bang controller

Here, heating by bang-bang control of a RAM with two apertures ($I = 2$) is considered. Heating with the bang-bang controller can be represented by the hybrid automaton shown in Figure C.1. Discrete states in Figure C.1 are characterized by the fluid circulation direction implemented with the bang-bang controller in (4.24). The four discrete states, associated with bang-bang control on a RAM with two apertures, are designated as:

q_1: clockwise circulation by $u_1 = k$ and $u_2 = k$.

q_2: clockwise and counter-clockwise circulation by $u_1 = k$ and $u_2 = -k$.

q_3: clockwise and counter-clockwise circulation by $u_1 = -k$ and $u_2 = k$.

q_4: counter-clockwise circulation by $u_1 = -k$ and $u_2 = -k$.

The aforementioned four discrete modes thus form set $Q = \{q_1, q_2, q_3, q_4\}$. The hybrid automaton in Figure C.1 transitions between each discrete state if the relevant guard condition $G(q_i, q_j)$ is triggered. Possible edges along which transitions can occur are $E = \{(q_i, q_j)\}$ with $i, j \in \{1, \ldots, 4\}$. Notable exceptions are self-loops defined by $G(q_i, q_i)$. No transition to a different discrete state occurs if such loops are triggered. The guard conditions in Figure C.1 are based on the switching functions of (4.24). These switching functions are defined as $\Sigma_1 = \boldsymbol{\eta}^\dagger \boldsymbol{Q}_1 \boldsymbol{\eta}$ and $\Sigma_2 = \boldsymbol{\eta}^\dagger \boldsymbol{Q}_2 \boldsymbol{\eta}$. Table C.1 presents all guard condition associated with the automaton in Figure C.1. Finally, the continuous state is independent of the discrete state in the sense that the reset map is defined as $R(q_i, q_j, \boldsymbol{\eta}) = R(q_j, q_i, \boldsymbol{\eta}) = \{\boldsymbol{\eta}\}$.

The reachable set and set where continuous evolution of the state $\boldsymbol{\eta}$ is impossible are defined by

$$Reach := Q \times H, \qquad Trans := Trans_1 \cup Trans_2 \cup Trans_3 \cup Trans_4, \tag{C.1}$$

respectively. The sets $Trans_i$ are associated with each discrete state q_i of the automaton and are given by

$$\begin{aligned}
Trans_1 = &\{q_1\} \times \big\{\boldsymbol{\eta} \in \mathbb{R}^K \big| \\
&\quad \Sigma_1 > 0 \wedge \Sigma_2 \le 0 \vee \Sigma_1 \le 0 \wedge \Sigma_2 > 0 \vee \Sigma_1 > 0 \wedge \Sigma_2 > 0\}, \\
Trans_2 = &\{q_2\} \times \big\{\boldsymbol{\eta} \in \mathbb{R}^K \big| \\
&\quad \Sigma_1 > 0 \wedge \Sigma_2 \ge 0 \vee \Sigma_1 \le 0 \wedge \Sigma_2 < 0 \vee \Sigma_1 > 0 \wedge \Sigma_2 < 0\}, \\
Trans_3 = &\{q_3\} \times \big\{\boldsymbol{\eta} \in \mathbb{R}^K \big| \\
&\quad \Sigma_1 < 0 \wedge \Sigma_2 \ge 0 \vee \Sigma_1 \ge 0 \wedge \Sigma_2 < 0 \vee \Sigma_1 < 0 \wedge \Sigma_2 < 0\}, \\
Trans_4 = &\{q_4\} \times \big\{\boldsymbol{\eta} \in \mathbb{R}^K \big| \\
&\quad \Sigma_1 < 0 \wedge \Sigma_2 \le 0 \vee \Sigma_1 \ge 0 \wedge \Sigma_2 > 0 \vee \Sigma_1 < 0 \wedge \Sigma_2 > 0\}.
\end{aligned} \tag{C.2}$$

Continuous evolution of $\boldsymbol{\eta}$ is inhibited when switching functions Σ_1 and Σ_2 satisfy the guard condition. The sets $Trans_i$ thus capture logical impossibilities. For example, $Trans_1$ expresses that in state q_1 at least one of the two switching functions exceeds zero. This implies that either $G(q_1, q_2)$, $G(q_1, q_3)$ or $G(q_1, q_3)$ in Table C.1 is triggered. Hence continuous evolution according to discrete state q_1 is impossible by its definition. The intersection of $Reach$ and $Trans$ as

$$\begin{aligned}
Reach \cap Trans = &\{q_1\} \times \big\{\boldsymbol{\eta} \in \mathbb{R}^K \big| \; \Sigma_1 \le 0 \wedge \Sigma_2 \le 0\} \\
&\cup \{q_2\} \times \big\{\boldsymbol{\eta} \in \mathbb{R}^K \big| \; \Sigma_1 \ge 0 \wedge \Sigma_2 \le 0\} \\
&\cup \{q_3\} \times \big\{\boldsymbol{\eta} \in \mathbb{R}^K \big| \; \Sigma_1 \ge 0 \wedge \Sigma_2 \ge 0\} \\
&\cup \{q_4\} \times \big\{\boldsymbol{\eta} \in \mathbb{R}^K \big| \; \Sigma_1 \le 0 \wedge \Sigma_2 \ge 0\}
\end{aligned}, \tag{C.3}$$

describes the set where continuous evolution of the $\boldsymbol{\eta}$ is possible.

To show that closed-loop bang-bang control possesses a unique state trajectory, both Lemma C.1 and Lemma C.2 need to be satisfied. To this end, consider the set of initial conditions defined as

$$Init = \{q_1, q_2, q_3, q_4\} \times \{\boldsymbol{\eta} \in H | \quad \|\boldsymbol{\eta}\|_2 \neq 0\}. \tag{C.4}$$

The considered set $Init$ consists of any fluid that is still cold compared to the boundary temperature (i.e. $\|\boldsymbol{\eta}\|_2 = 0$ means the fluid is uniformly heated at T_∞). Take any $\tilde{q} = q_i$ and $\tilde{\boldsymbol{\eta}}$ such that $\|\boldsymbol{\eta}\|_2 \neq 0$ and $(\tilde{q}, \tilde{\boldsymbol{\eta}}) \in Init$. According to (C.3) this naturally means that $(\tilde{q}, \tilde{\boldsymbol{\eta}}) \in Reach \cap Trans$ for $i = 1, \ldots, 4$ since $Init \equiv Reach \cap Trans$. Moreover, for any $\tilde{q}' = q_j$ one find an edge such that $(\tilde{q}, \tilde{q}') \in E$ and subsequently $\tilde{\boldsymbol{\eta}} \in G(\tilde{q}, \tilde{q}')$. The above shows that the bang-bang controller on a RAM with two apertures ($I = 2$) is non-blocking according to Lemma C.1. In other words, continuous state evolution can occur regardless of the initial heat distribution in the fluid.

Consider a state $(\tilde{q}, \tilde{\boldsymbol{\eta}}) \in Reach$ with $\tilde{q} = q_i$ as above. From Table C.1 and (C.2) it can thus be observed that condition i) of Lemma C.2 holds for any $\tilde{q}' \neq q_i$. To show condition ii) of Lemma C.2 holds, consider $\tilde{q} = q_1$ combined with $\tilde{q}' \neq \tilde{q}''$ according to Table C.1. The intersection between the different guard conditions are given by:

i) $G(q_1, q_2) \cap G(q_1, q_3) = \left\{ \boldsymbol{\eta} \in \mathbb{R}^K \middle| \, \Sigma_1 = 0 \wedge \Sigma_2 = 0 \right\};$

ii) $G(q_1, q_2) \cap G(q_1, q_4) = \left\{ \boldsymbol{\eta} \in \mathbb{R}^K \middle| \, \Sigma_1 = 0 \wedge \Sigma_2 \geq 0 \right\};$

iii) $G(q_1, q_3) \cap G(q_1, q_4) = \left\{ \boldsymbol{\eta} \in \mathbb{R}^K \middle| \, \Sigma_1 \geq 0 \wedge \Sigma_2 = 0 \right\}.$

The intersections in ii) and iii) are both subsets of $Trans_1$. Therefore, $\tilde{\boldsymbol{\eta}} \notin G(q_1, q_2) \cap G(q_1, q_4)$ and $\tilde{\boldsymbol{\eta}} \notin G(q_1, q_3) \cap G(q_1, q_4)$ by definition. Moreover, $\Sigma_i = 0$ means that $\tilde{\eta} \in \mathcal{N}(\boldsymbol{Q}_i)$ for $i = 1, 2$ where $\mathcal{N}(\cdot)$ denotes the null-space of a matrix (i.e. $\mathcal{N}(\boldsymbol{X}) = \left\{ \boldsymbol{b} \in \mathbb{R}^K | \boldsymbol{X}\boldsymbol{b} = \boldsymbol{0} \text{ for all } \boldsymbol{b} \neq \boldsymbol{0} \right\}$). The intersection i) can thus only occur if the null-spaces of matrices $\boldsymbol{Q}_i$ are equivalent or the fluid is completely heat (i.e. $\mathcal{N}(\boldsymbol{Q}_1) \equiv \mathcal{N}(\boldsymbol{Q}_2)$ or $\tilde{\boldsymbol{\eta}} \equiv \boldsymbol{0}$). The null-spaces only align when $\Theta \equiv 0$ for the chosen $\boldsymbol{P}_4$ in Section 4.3 such that $\boldsymbol{v}_1 \equiv \boldsymbol{v}_2$. A similar result, following an analogous analysis of guard condition intersections, is found by considering $\tilde{q} = q_2$ or $\tilde{q} = q_3$. Therefore, condition ii) of Lemma C.2 is satisfied almost everywhere as $\tilde{\boldsymbol{\eta}} \in G(\tilde{q}, \tilde{q}') \cap G(\tilde{q}, \tilde{q}'')$ (viz. if and only if the fluid is not homogeneously heated resulting in $\tilde{\boldsymbol{\eta}} = \boldsymbol{0}$). Finally, condition iii) in Lemma C.2 is automatically satisfied by the definition of the reset map. This means that Lemma C.2 is satisfied. The above shows that closed-loop heating with the bang-bang controller is both non-blocking and deterministic. As a results bang-bang control is well-posed in forward time. State trajectories of the closed-loop therefore exist and are unique as long as the fluid is still (partially) cold. The above presented analysis is generalisable to bang-bang control with more than two flows as well. However, analysis for more flows is omitted for the sake of brevity (e.g. a RAM with I apertures will lead to an automaton with 2^I discrete states).

APPENDIX D

Local identifiability of model parameters

The output sensitivity matrix (5.18) uses the derivatives of (5.10)-(5.11) with respect to $\boldsymbol{\theta}^\dagger = \begin{bmatrix}\xi & \alpha & \kappa\end{bmatrix}$ or $\boldsymbol{\theta}^\dagger = \begin{bmatrix}\alpha & \kappa\end{bmatrix}$ for heat transport in the absence of any flow ($i = 0$) or the base flow ($i = 1$), respectively. The output sensitivity matrix $\boldsymbol{S}$ in (5.18) is numerically constructed in a similar fashion for both (i.e. derivatives with respect to α and κ follow from the same relations presented below). Therefore, derivatives of (5.10)-(5.11) are only derived for the base flow. The derivatives of (5.10)-(5.11) can be expressed as

$$\frac{\partial \widetilde{\boldsymbol{T}}(t_k)}{\partial \theta_j} = \frac{\partial}{\partial \theta_j} \left(\boldsymbol{P}_\tau\right)^k \widetilde{\boldsymbol{T}}(t_0) + \frac{\partial}{\partial \theta_j} \left(\sum_{\ell=0}^{k} \left(\boldsymbol{P}_\tau\right)^{k-\ell-1} \boldsymbol{B}_\tau \widetilde{T}_a(t_\ell) \right), \tag{D.1}$$

where superscript i is omitted for the sake of notational convenience. The derivatives in (D.1) with respect to ξ can be readily obtained as

$$\begin{aligned} \frac{\partial \left(\boldsymbol{P}_\tau\right)^k}{\partial \xi} &= k \frac{T_s}{T_c} \boldsymbol{A} \left(\boldsymbol{P}_\tau\right)^{k-1}, \\ \frac{\partial \left(\boldsymbol{P}_\tau\right)^{k-\ell-1} \boldsymbol{B}_\tau}{\partial \xi} &= \kappa \frac{T_s}{T_c} \boldsymbol{A} \left(\boldsymbol{P}_\tau\right)^{k-\ell-1} \left((k-\ell) \boldsymbol{I} - (k-\ell-1) \boldsymbol{P}_\tau^{-1} \right) \boldsymbol{A}^{-1} \boldsymbol{b}, \end{aligned} \tag{D.2}$$

The derivative of $\widetilde{\boldsymbol{T}}$ with respect to ξ thus has an analytical expression according to (D.2). Observe that both α and κ occur in the exponent of $\boldsymbol{P}_\tau$ (see (5.11) and (5.6)). Therefore, the output derivatives with respect to α and κ are computed numerically. The numerical calculation of these derivatives can lead to long computation times. Diagonalisation of $\boldsymbol{A}$ (and likewise $\boldsymbol{P}_\tau$) according to (5.13) reduces the numerical computation time significantly. The derivative of $\boldsymbol{P}_\tau$ with respect to θ_j can be obtained as

$$\frac{\partial\left(\boldsymbol{P}_\tau\right)^k}{\partial\theta_j}=\frac{\partial\boldsymbol{V}}{\partial\theta_j}\widetilde{\boldsymbol{\Lambda}}^k\boldsymbol{V}^{-1}+k\boldsymbol{V}\frac{\partial\widetilde{\boldsymbol{\Lambda}}}{\partial\theta_j}\widetilde{\boldsymbol{\Lambda}}^{k-1}\boldsymbol{V}^{-1}-\boldsymbol{V}\widetilde{\boldsymbol{\Lambda}}^k\boldsymbol{V}^{-1}\frac{\partial\boldsymbol{V}}{\partial\theta_j}\boldsymbol{V}^{-1}\quad, \tag{D.3}$$

where $\widetilde{\boldsymbol{\Lambda}}=e^{\boldsymbol{\Lambda}\tau}$ and $\frac{\partial\boldsymbol{V}^{-1}}{\partial\theta_j}=-\boldsymbol{V}^{-1}\frac{\partial\boldsymbol{V}}{\partial\theta_j}\boldsymbol{V}^{-1}$. This latter property for $\frac{\partial\boldsymbol{V}^{-1}}{\partial\theta_j}$ follows immediately by solving $\frac{\partial\boldsymbol{V}\boldsymbol{V}^{-1}}{\partial\theta_j}=\boldsymbol{0}$. The derivative of the trailing terms in (D.1) are determined by

$$\frac{\partial\left(\boldsymbol{P}_\tau\right)^\ell\boldsymbol{B}_\tau}{\partial\theta_j}=\frac{\partial\left(\boldsymbol{P}_\tau\right)^\ell}{\partial\theta_j}\boldsymbol{B}_\tau+\left(\boldsymbol{P}_\tau\right)^\ell\frac{\partial\boldsymbol{B}_\tau}{\partial\theta_j}, \tag{D.4}$$

and

$$\begin{aligned}\frac{\partial\boldsymbol{B}_\tau}{\partial\theta_2}&=-\kappa\frac{R^2}{\alpha^2T_c}\left(\frac{\partial\boldsymbol{V}}{\partial\theta_2}\boldsymbol{\Lambda}^{-1}\boldsymbol{V}^{-1}+\boldsymbol{V}\frac{\partial\boldsymbol{\Lambda}^{-1}}{\partial\theta_2}\boldsymbol{V}^{-1}-\boldsymbol{V}\boldsymbol{\Lambda}^{-1}\boldsymbol{V}^{-1}\frac{\partial\boldsymbol{V}}{\partial\theta_2}\boldsymbol{V}^{-1}\right),\\ \frac{\partial\boldsymbol{B}_\tau}{\partial\theta_3}&=\left(\boldsymbol{P}_\tau-\boldsymbol{I}\right)\boldsymbol{A}^{-1}\boldsymbol{b}\\ &\quad+\kappa\left(\frac{\partial\boldsymbol{V}}{\partial\theta_3}\boldsymbol{\Lambda}^{-1}\boldsymbol{V}^{-1}+\boldsymbol{V}\frac{\partial\boldsymbol{\Lambda}^{-1}}{\partial\theta_3}\boldsymbol{V}^{-1}-\boldsymbol{V}\boldsymbol{\Lambda}^{-1}\boldsymbol{V}^{-1}\frac{\partial\boldsymbol{V}}{\partial\theta_3}\boldsymbol{V}^{-1}\right).\end{aligned} \tag{D.5}$$

Numerical computation of (D.5) to construct (5.18) with (numerical) derivatives in (D.4) reveals that $\boldsymbol{\theta}$ is locally structurally identifiable in the absence of any flow for the parameters in Table 5.2. Numerical computation of (D.5) to construct (5.18) with (numerical) derivatives in (D.2) and (D.4) reveals that $\boldsymbol{\theta}$ is locally structurally *un*identifiable for the base flow for the parameters in Table 5.2.

APPENDIX E

Reorientation invariance of the discrete algebraic Ricatti equation

The state estimator for the base flow ($i = 1$) is described by

$$\begin{aligned} \boldsymbol{L}^{(1)} &= \left(\boldsymbol{R} + \widetilde{\boldsymbol{C}}^{(1)}\boldsymbol{P}_1(\widetilde{\boldsymbol{C}}^{(1)})^\dagger\right)^{-1}(\widetilde{\boldsymbol{C}}^{(1)}\boldsymbol{P}_1(\widetilde{\boldsymbol{A}}^{(1)})^\dagger), \\ &= \left(\boldsymbol{R} + \boldsymbol{C}\widetilde{\boldsymbol{G}}^{(1)}\boldsymbol{P}_1(\boldsymbol{C}\widetilde{\boldsymbol{G}}^{(1)})^\dagger\right)^{-1}(\boldsymbol{C}\widetilde{\boldsymbol{G}}^{(1)}\boldsymbol{P}_1(\widetilde{\boldsymbol{A}}^{(1)})^\dagger), \end{aligned} \tag{E.1}$$

with the matrix $\boldsymbol{X}_1$ the positive definite solution to the discrete algebraic Riccati equation (DARE) given by [131]

$$\begin{aligned} \boldsymbol{X}_1 = &\widetilde{\boldsymbol{A}}^{(1)}\boldsymbol{X}_1(\widetilde{\boldsymbol{A}}^{(1)})^\dagger \\ &- (\widetilde{\boldsymbol{A}}^{(1)}\boldsymbol{X}_1(\widetilde{\boldsymbol{C}}^{(1)})^\dagger)(\boldsymbol{R} + \widetilde{\boldsymbol{C}}^{(1)}\boldsymbol{X}_1(\widetilde{\boldsymbol{C}}^{(1)})^\dagger)^{-1}(\widetilde{\boldsymbol{C}}^{(1)}\boldsymbol{X}_1(\widetilde{\boldsymbol{A}}^{(1)})^\dagger) + \boldsymbol{Q}, \end{aligned} \tag{E.2}$$

where $\boldsymbol{R}$ a positive definite matrix and $\boldsymbol{Q}$ a positive (semi)definite matrix. Likewise, a similar state estimator can be obtained for flow i described by

$$\boldsymbol{L}^{(i)} = \left(\boldsymbol{R} + \widetilde{\boldsymbol{C}}^{(i)}\boldsymbol{X}_i(\widetilde{\boldsymbol{C}}^{(i)})^\dagger\right)^{-1}(\widetilde{\boldsymbol{C}}^{(i)}\boldsymbol{X}_i(\widetilde{\boldsymbol{A}}^{(i)})^\dagger), \tag{E.3}$$

with the matrix $\boldsymbol{X}_i$ the positive definite solution to the discrete algebraic Riccati equation (DARE) given by

$$\begin{aligned}\boldsymbol{X}_i =& \widetilde{\boldsymbol{A}}^{(i)} \boldsymbol{X}_i (\widetilde{\boldsymbol{A}}^{(i)})^\dagger \\ &- (\widetilde{\boldsymbol{A}}^{(i)} \boldsymbol{X}_i (\widetilde{\boldsymbol{C}}^{(i)})^\dagger)(\boldsymbol{R} + \widetilde{\boldsymbol{C}}^{(i)} \boldsymbol{X}_i (\widetilde{\boldsymbol{C}}^{(i)})^\dagger)^{-1}(\widetilde{\boldsymbol{C}}^{(i)} \boldsymbol{X}_i (\widetilde{\boldsymbol{A}}^{(i)})^\dagger) + \boldsymbol{Q}.\end{aligned} \tag{E.4}$$

The combination of (5.7), (5.15) and (5.15) results in the following observation

$$\begin{aligned}\widetilde{\boldsymbol{A}}^{(i)} &= \left(\boldsymbol{G}^{(i)}\right)^+ \boldsymbol{X}_\tau^{(i)} \boldsymbol{G}^{(i)} = \left(\boldsymbol{G}^{(1)}\right)^+ \boldsymbol{R}_\Theta^{1-i} \boldsymbol{X}_\tau^{(i)} \boldsymbol{R}_\Theta^{i-1} \boldsymbol{G}^{(1)}, \\ &= \left(\boldsymbol{G}^{(1)}\right)^+ \boldsymbol{X}_\tau^{(1)} \boldsymbol{G}^{(1)} = \widetilde{\boldsymbol{A}}^{(1)},\end{aligned} \tag{E.5}$$

and reorientation invariance of $\boldsymbol{C} = \boldsymbol{C}\boldsymbol{R}_\Theta^{i-1}$ implies that

$$\widetilde{\boldsymbol{C}}^{(i)} = \boldsymbol{C}\boldsymbol{R}_\Theta^{i-1}\boldsymbol{G}^{(1)} = \widetilde{\boldsymbol{C}}^{(1)}. \tag{E.6}$$

Hence the substitution of both (E.5) and (E.6) in (E.4) reveals that both (E.4) and (E.2), which suggests that $\boldsymbol{X}_i = \boldsymbol{X}_1$. As a consequence, (E.3) and (E.1) express the same state estimator (i.e. $\boldsymbol{L}^{(i)} = \boldsymbol{L}^{(1)}$ following the substitution of (E.5), (E.6) and $\boldsymbol{X}_i = \boldsymbol{X}_1$ in (E.3)).

APPENDIX F

Error dynamics for a periodic flow

Here the estimation error dynamics for a periodic flow are investigated. The periodic flow activates fluid flows in the RAM according to $u(t) \in \mathcal{U}$ for the reorientation scheme $\mathcal{U} = \{1, 2, 1, \ldots\}$. The error dynamics after to subsequent flow activations thus reads as

$$\begin{aligned}\boldsymbol{\varepsilon}(t_{k+1}) = \boldsymbol{G}^{(2)}(\widetilde{\boldsymbol{A}}^{(2)} - \boldsymbol{L}^{(2)}\widetilde{\boldsymbol{C}}^{(2)}) \left(\boldsymbol{G}^{(2)}\right)^{+} \\ \boldsymbol{G}^{(1)}(\widetilde{\boldsymbol{A}}^{(1)} - \boldsymbol{L}^{(1)}\widetilde{\boldsymbol{C}}^{(1)}) \left(\boldsymbol{G}^{(1)}\right)^{+} \boldsymbol{\varepsilon}(t_k).\end{aligned} \tag{F.1}$$

The definition of transformation matrices $\boldsymbol{G}^{(2)}$ and $\boldsymbol{G}^{(1)}$, in (5.15), leads to a saltation matrix as

$$\boldsymbol{G}^{(2)} = \boldsymbol{R}_{\Theta}\boldsymbol{G}^{(1)}, \quad \left(\boldsymbol{G}^{(2)}\right)^{+} \boldsymbol{G}^{(1)} = \left(\boldsymbol{G}^{(1)}\right)^{+} \boldsymbol{R}_{\Theta}^{-1}\boldsymbol{G}^{(1)}, \tag{F.2}$$

where $\boldsymbol{R}_{\Theta}^{-1} = \boldsymbol{R}_{\Theta}^{\dagger}$. The substitution of (F.2) results in

$$\begin{aligned}\boldsymbol{\varepsilon}(t_{k+1}) = \boldsymbol{R}_{\Theta}\boldsymbol{G}^{(1)}(\widetilde{\boldsymbol{A}}^{(2)} - \boldsymbol{L}^{(2)}\widetilde{\boldsymbol{C}}^{(2)}) \left(\boldsymbol{G}^{(1)}\right)^{+} \boldsymbol{R}_{\Theta}^{\dagger} \\ \boldsymbol{G}^{(1)}(\widetilde{\boldsymbol{A}}^{(1)} - \boldsymbol{L}^{(1)}\widetilde{\boldsymbol{C}}^{(1)}) \left(\boldsymbol{G}^{(1)}\right)^{+} \boldsymbol{\varepsilon}(t_k).\end{aligned} \tag{F.3}$$

which, with $\boldsymbol{L}^{(i)} = \boldsymbol{L}$ according to results in Appendix E, results in

$$\boldsymbol{\varepsilon}(t_{k+1}) = \boldsymbol{R}_{\Theta}^{2} \left(\boldsymbol{R}_{\Theta}^{\dagger}\boldsymbol{G}^{(1)} \left(\widetilde{\boldsymbol{A}}^{(1)} - \boldsymbol{L}\widetilde{\boldsymbol{C}}^{(1)}\right) \left(\boldsymbol{G}^{(1)}\right)^{+}\right)^{2} \boldsymbol{\varepsilon}(t_k). \tag{F.4}$$

Finally, using $\boldsymbol{R}_\Theta^I = \boldsymbol{I}$ [132] for $I = 2$, results in

$$\boldsymbol{\varepsilon}(t_{k+1}) = \left(\boldsymbol{R}_\Theta^\dagger \boldsymbol{G}^{(1)} \left(\widetilde{\boldsymbol{A}}^{(1)} - \boldsymbol{L}\widetilde{\boldsymbol{C}}^{(1)} \right) \left(\boldsymbol{G}^{(1)} \right)^+ \right)^2 \boldsymbol{\varepsilon}(t_k), \tag{F.5}$$

APPENDIX G

Impact sensor placement on field estimation for the base flow

This chapter considers the impact of sensor placement on field estimation in the presence of the base flow. In Section 5.3.3, sensors are placed based on the eigenmodes associated with both the base flow *and* the reoriented flow with $U = 0.004\ m/s$ for the model parameters in Table 5.2. Any number of these sensors (or outputs) can be used to design the estimator gain matrix $\boldsymbol{L}^{(i)}$ according to Section 5.3.2. The choice of the sensors used by the estimator determines $\widetilde{\boldsymbol{C}}^{(i)}$ and thus the design of gain matrix $\boldsymbol{L}^{(i)}$. Based on the methodology presented in Section 5.3.2, two obvious choices are available; i) select the first $\lfloor p/I \rfloor$ outputs (i.e. first $\lfloor p/I \rfloor$ rows of $\boldsymbol{C}$) to design $\boldsymbol{L}^{(1)}$ or ii) select *all* outputs placed in Section 5.3.3 to design $\boldsymbol{L}^{(1)}$. In the former option, sensors are placed based on the eigenmodes associated with heat transport driven by the base flow. Hence, the first $\lfloor p/I \rfloor$ sensors are optimally placed for estimation of the base flow. In the latter option, the second $\lfloor p/I \rfloor$ sensors are placed optimally for the eigenmodes associated with the base flow (i.e. they are optimally placed for the reoriented flow). As a result, a part of these sensors will always be suboptimally placed to estimate the transient temperature field (i.e. the first $\lfloor p/I \rfloor$ sensors – indicated by the squares in Figure 5.4 – are suboptimally placed for the reoriented flow).

Numerical field estimation is investigated for a rescaled base flow at $U = 0.001\ m/s$ with $M = 1000$ eigenmodes. As a consequence, Pe decreases and results in topological changes of the eigenmodes associated with the base flow. This implies that all sensors are suboptimally placed for field estimation in the rescaled base flow (i.e. sensors were placed based on eigenmodes with a larger Pe in Section 5.3.3). Nonetheless, the estimation accuracy is investigated when all sensors or only the first $\lfloor p/I \rfloor$ placed sensors are used during field estimation of the base flow. Rescaling of the base flow from $U = 0.004\ m/s$ to $U = 0.001$ m/s – yielding a smaller Pe – can result in a topological change of the (dominant) eigenmodes (e.g. see results in Reference [109]). However, topological changes for the lower order modes are relatively small for the considered Pe. Numerical analysis (i.e. placing sensors based on the rescaled base flow) reveals that the eigenmodes, and as consequence the optimal sensor placement, only substantially change for the higher order modes. Hence, sensor placement remains unaltered in the analysis with respect to the placement presented in Section 5.3.3.

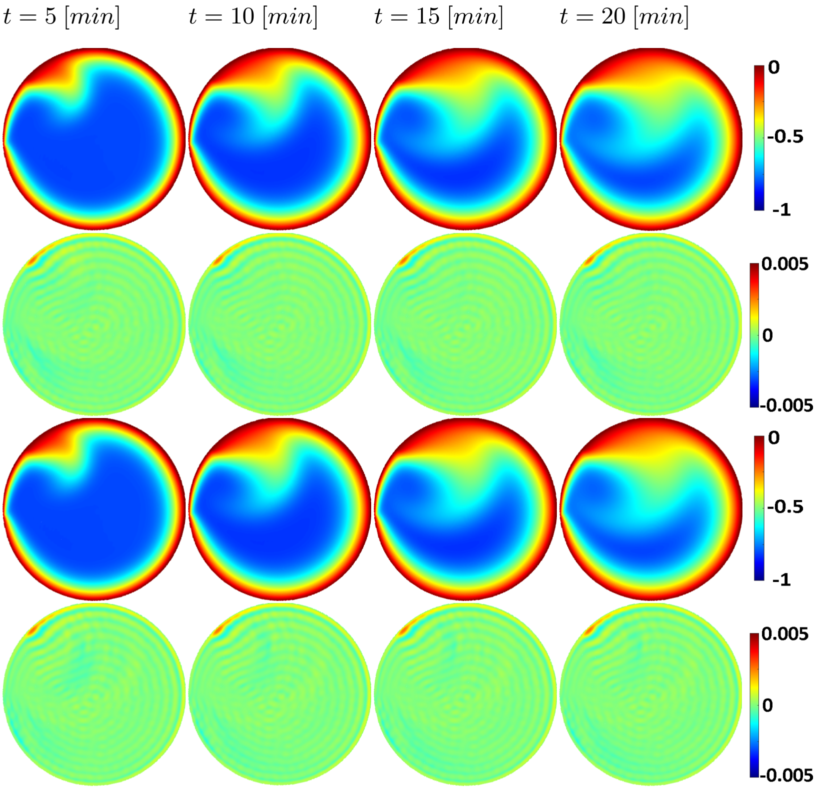

Figure G.1: Estimated transient temperature snapshots (first and third row) and error between estimated and nominal transient temperature snapshots (second and fourth row) for the base flow with estimation based on first $\lfloor p/I \rfloor$ sensors (top two rows) and all sensors (bottom two rows). Parameters during simulations are adopted from Table 5.2 with $M = 1000$ eigenmodes.

Figure G.1 shows snapshots of the nominal transient temperature field in the

(a) Small q/r.

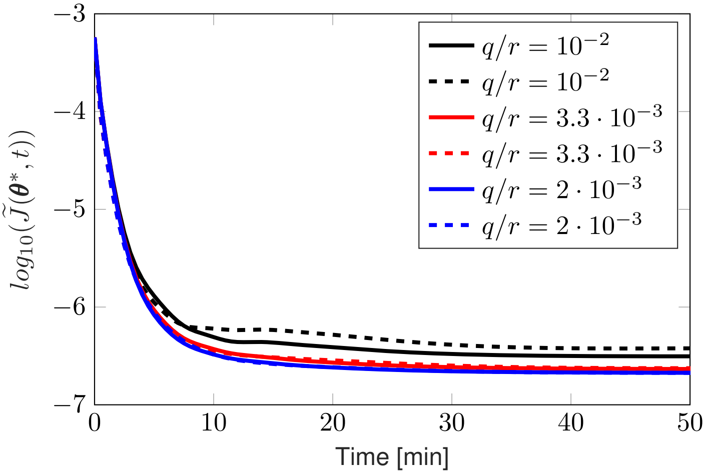

(b) Large q/r.

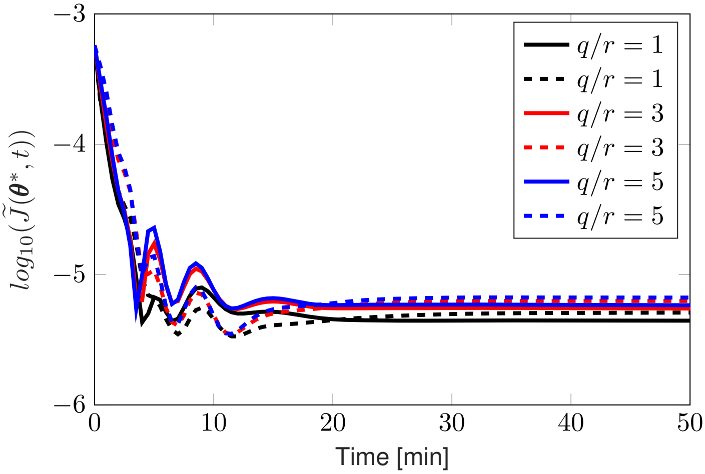

Figure G.2: The cost-function $\widetilde{J}(\boldsymbol{\theta}^*, t)$ for the base flow with (a) small q/r and (b) large q/r. Field estimation on only the first 24 sensors are represented by solid lines. Estimation with all sensors is represented by dashed lines. Parameters during simulations are adopted from Table 5.2 with $M = 1000$ eigenmodes.

top row. The middle and bottom row in Figure G.1 show snapshots where, respectively, the first $\lfloor p/I \rfloor$ sensors and all p sensors are used for field estimation of the base flow. Figure G.1 reveals no quantitatively and qualitatively differences if the estimator is designed on estimation for either half or all sensors. The second $\lfloor p/I \rfloor$ sensors are suboptimally placed for field estimation of the base flow (i.e. they are placed based on $\boldsymbol{G}^{(2)}$ rather than $\boldsymbol{G}^{(1)}$). This suboptimal placement means that the higher-order modes can potentially (negatively) influence the lower-order modes. This is commonly referred to as the spill-over effect [107]. However, spill-over effects appear to be limited/negligible regardless of the suboptimal placement.

The effect of ratio q/r on the evolution of the field estimation error is shown in Figure G.2. The dashed and solid lines in Figure G.2 indicate results where field estimation is performed with all sensors and only the first $\lfloor p/I \rfloor$ sensors, respectively. Figure G.2 reveals that $\widetilde{J}$ is smaller at steady-state if only the first $\lfloor p/I \rfloor$ sensors are used during estimation. This improved steady-state estimation accuracy for a smaller number of sensors occurs irrespective of the q/r tuning. Notably different behaviour of the estimation error is observed in the initial transient in Figure G.2a compared to Figure 5.12b (i.e. in the first 10 minutes). The oscillations of $\widetilde{J}$ – observed in the first 10 minutes in Figure G.2a – diminish if also the suboptimally placed sensors are included during estimation. The estimation error becomes larger for estimation based on all sensors as time progresses though (i.e. field estimation errors with the estimation based on all sensors becomes larger than those based on the first $\lfloor p/I \rfloor$ sensors). Moreover, larger q/r result in an increase of the field estimation error regardless which sensors are used here. The behaviour of the error for a larger q/r is consistent with the behaviour observed in Section 5.4.3.2. A similar observation holds for decreasing q/r. Figure G.2b reveals that a small q/r minimizes the estimation error $\widetilde{J}$ most. Moreover, for $q/r \ll 1$ there is no distinguishable difference between estimation based on the first $\lfloor p/I \rfloor$ or all sensors. Therefore, it is concluded that a small q/r preferential to boost estimation accuracy.

The numerical results presented above show that considering all sensors instead of only the first $\lfloor p/I \rfloor$ sensors during field estimation has only a small detrimental effect on the field estimation error. Moreover, proper tuning of $\boldsymbol{R}$ can mostly counteract the differences in $\widetilde{J}$ observed between estimation of the base flow based on all or the first half of the available sensors. However, estimation errors are smallest immediately following base flow activation (i.e. in the initial transient) for estimation based on all sensors in $\boldsymbol{C}$. This low estimation error becomes especially important for successful field estimation in rapidly switching (periodic) flows. Hence, all sensors should be used for (experimental) field estimation of the base flow and the periodic flow. Observe that the invariance of the sensor position to rotation is still preserved for such an output matrix (i.e. $\boldsymbol{C}\boldsymbol{R} = \boldsymbol{C}$).

Bibliography

[1] IEA, “Renewables 2019: Analysis and forecast to 2024.” `https://iea.blob.core.windows.net/assets/a846e5cf-ca7d-4a1f-a81b-ba1499f2cc07/Renewables_2019.pdf`. Accessed online 01-09-2022.

[2] D. B. Todd, “Mixing of highly viscous fluids, polymers, and pastes,” in *Handbook of Industrial Mixing*, ch. 16, pp. 987–1025, Wiley-Blackwell, 2004.

[3] L. Erwin, “Mixing,” in *Encyclopedia of Polymer Science and Technology*, Encyclopedia of Polymer Science and Technology, John Wiley & Sons, Inc., 2011.

[4] P. Tabeling, *Introduction to microfluidics*. Oxford University Press, 2005.

[5] O. Gubanov and L. Cortelezzi, “Towards the design of an optimal mixer,” *Journal of Fluid Mechanics*, vol. 651, pp. 27–53, 2010.

[6] M. Bayareh, M. N. Ashani, and A. Usefian, “Active and passive micromixers: A comprehensive review,” *Chemical Engineering and Processing - Process Intensification*, vol. 147, no. 107771, 2020.

[7] J. Chen and F. Jiang, “Designing multi-well layout for enhanced geothermal system to better exploit hot dry rock geothermal energy,” *Renewable Energy*, vol. 74, pp. 37–48, 2015.

[8] K. Guo, H. Li, and Z. Yu, “In-situ heavy and extra-heavy oil recovery: A review,” *Fuel*, vol. 185, pp. 886 – 902, 2016.

[9] M. F. M. Speetjens, S. Varghese, and R. R. Trieling, “Lagrangian approach to analysis and engineering of two generic transport problems in enhanced subsurface flows,” *Journal of Contaminant Hydrology*, vol. 224, no. 103482, 2019.

[10] A. N. Piscopo, R. M. Neupauer, and D. C. Mays, “Engineered injection and extraction to enhance reaction for improved in situ remediation,” *Water Resources Research*, vol. 49, no. 6, pp. 3618–3625, 2013.

[11] L. Huo, G. Liu, X. Yang, Z. Ahmad, and H. Zhong, "Surfactant-enhanced aquifer remediation: Mechanisms, influences, limitations and the countermeasures," *Chemosphere*, vol. 252, no. 126620, 2020.

[12] Ö. Baskan, M. F. M. Speetjens, G. Metcalfe, and H. J. H. Clercx, "Experimental and numerical parametric analysis of a reoriented duct flow," *European Journal of Mechanics - B/Fluids*, vol. 57, pp. 1–14, 2016.

[13] Roto-art. `https://www.roto-art.nl/`. Accessed online 16-12-2022.

[14] S. van Pelt, A. J. H. Frijns, and J. M. J. den Toonder, "Microfluidic magnetic bead conveyor belt," *Lab on a Chip*, vol. 17, no. 22, pp. 3826–3840, 2017.

[15] R. DiPippo, *Geothermal Power Plants: Principles, Applications, Case studies and Environmental Impact*. Butterworth-Heinemann: Elsevier, 2016.

[16] D. R. Lester, M. Rudman, G. Metcalfe, and H. M. Blackburn, "Global parameteric solutions of scalar transport," *Journal of Computational Physics*, vol. 227, pp. 3032–57, 2008.

[17] Ö. Baskan, M. F. M. Speetjens, G. Metcalfe, and H. J. H. Clercx, "Experimental and computational study of scalar modes in a periodic laminar flow," *International Journal of Thermal Sciences*, vol. 96, pp. 102–118, 2015.

[18] H. Aref, J. R. Blake, M. Budišić, S. S. S. Cardoso, J. H. E. Cartwright, H. J. H. Clercx, K. El-Omari, U. Feudel, R. Golestanian, E. Gouillart, G. F. van Heijst, T. S. Krasnopolskaya, Y. Le Guer, R. S. MacKay, V. V. Meleshko, G. Metcalfe, I. Mezić, A. P. S. de Moura, O. Piro, M. F. M. Speetjens, R. Sturman, J. Thiffeault, and I. Tuval, "Frontiers of chaotic advection," *Reviews of Modern Physics*, vol. 89, p. 121, 2017.

[19] J. M. Ottino, *The kinematics of Mixing: Stretching, Chaos, and Transport*. Cambridge University Press, 1989.

[20] M. F. M. Speetjens, G. Metcalfe, and M. Rudman, "Lagrangian transport and chaotic advection in three-dimensional laminar flows," *Applied Mechanics Reviews*, vol. 73, p. 030801, 2021.

[21] M. Liu, F. J. Muzzio, and R. L. Peskin, "Quantification of mixing in aperiodic chaotic flows," *Chaos, Solitons & Fractals*, vol. 4, no. 6, pp. 869–893, 1994.

[22] D. R. Lester, G. Metcalfe, and M. Rudman, "Control mechanisms for the global structure of scalar dispersion in chaotic flows," *Physical Review E*, vol. 90, p. 022908, 2014.

[23] B. R. Noack, "Optimal mixing in recirculation zones," *Physics of Fluids*, vol. 16, no. 4, pp. 867–888, 2004.

[24] L. Cortelezzi, A. Adrover, and M. Giona, “Feasibility, efficiency and transportability of short-horizon optimal mixing protocols,” *Journal of Fluid Mechanics*, vol. 597, pp. 199–231, 2008.

[25] V. S. Dolk, M. Lauret, D. J. Antunes, P. D. Anderson, and W. P. M. H. Heemels, “A switched system approach to optimize mixing of fluids,” *IFAC-PapersOnLine*, vol. 51, pp. 31–36, 2018.

[26] P. M. Frank, “Enhancement of robustness in observer-based fault detection,” *International Journal of Control*, vol. 59, no. 4, pp. 955–981, 1994.

[27] Bernard, P, V. Andrieu, and D. Astolfi, “Observer design for continuous-time dynamical systems,” *Annual Reviews in Control*, vol. 53, pp. 224–248, 202.

[28] A. Smyshlyaev and M. Krstić, “Backstepping observers for a class of parabolic PDEs,” *Systems & Control Letters*, vol. 54, pp. 613–625, 2005.

[29] D. Zhang, S. X. Tang, and S. J. Moura, “State and disturbance estimator for unstable reaction-advection-diffusion PDE with boundary disturbance,” in *2019 Proceedings of the SIAM Conference on Control and its Applications (CT)*, pp. 67–74, 2019.

[30] S. J. Moura and H. K. Fathy, “Optimal boundary control & estimation of diffusion-reaction PDEs,” in *Proceedings of the 2011 American Control Conference*, pp. 921–928, 2011.

[31] M. J. Balas, “Nonlinear state estimation and feedback control of nonlinear and bilinear distributed parameter systems,” *Journal of Dynamic Systems, Measurement, and Control*, vol. 102, pp. 78–83, 1981.

[32] F. Eleiwi and T. M. L. Kirati, “Nonlinear observer-based lyapunov boundary control of distributed heat transfer mechanisms for membrane distillation plant,” *Journal of Process Control*, vol. 47, pp. 78–86, 2016.

[33] F. Eleiwi and T. M. Laleg-Kirati, “Observer-based perturbation extremum seeking control with input constraints for direct-contact membrane distillation process,” *International Journal of Control*, vol. 91, no. 6, pp. 1363–1375, 2018.

[34] T. Gunder, A. Sehlinger, R. Skoda, and M. Mönningmann, “Sensor placement for reduced-order model-based observers in hydraulic fluid machinery,” in *IFAC PapersOnline*, vol. 51, pp. 414–419, 2018.

[35] T. John, M. Guay, N. Hariharan, and S. Naranayan, “Pod-based observer for estimation in navier-stokes flow,” *Computers and Chemical Engineering*, vol. 34, pp. 965–975, 2010.

[36] H. Bounit and H. Hammouri, “Observers for infinite dimensional bilinear systems,” *European Journal of Control*, vol. 3, pp. 325–339, 1997.

[37] H. Bounit and A. Idrissi, “Regular bilinear systems,” *Journal of Mathematical Control and Information*, vol. 22, pp. 26–57, 2005.

[38] M. A. Demetriou, “Reduced order observer of finite dimensional radiative-conductive heat transfer systems,” in *2018 Annual American Control Conference (ACC)*, pp. 931–936, 2018.

[39] T. Egorova, “Plume estimation using static gynamic formations of unmanned aerial vehicles,” in *2016 IEEE 55th Conference on Decision and Control (CDC)*, pp. 2270–2275, 2016.

[40] L. Jadachowski, T. Meurer, and A. Kugi, “Backstepping observers for linear PDEs on higher-dimensional spatial domains,” *Automatica*, vol. 51, pp. 85–97, 2015.

[41] Á. Veress and J. Rohács, “Application of finite volume method in fluid dynamics and inverse design based optimization,” in *Finite Volume Method - Powerful Means of Engineering Design*, ch. 1, pp. 3–34, IntechOpen Publishing, 2012.

[42] G. K. Lausterer, W. H. Ray, and H. R. Martens, “Real time distributed parameter state estimation applied to a two dimensional heated ingot,” *Automatica*, vol. 14, pp. 335–344, 1978.

[43] P. V. Danckwerts, “The definition and measurement of some characteristics of mixtures,” *Applied Scientific Research, Sections A*, vol. 3, no. 4, pp. 279–296, 1952.

[44] G. Mathew, I. Mezić, and L. Petzold, “A multiscale measure for mixing,” *Physica D: Nonlinear Phenomena*, vol. 211, pp. 23–46, 2005.

[45] C. R. Doering and J. L. Thiffeault, “Multiscale mixing efficiencies for steady sources,” *Physical Review E*, vol. 74, p. 025301, 2006.

[46] D. D’Alessandro, M. Dahleh, and I. Mezić, “Control of mixing in fluid flow: A maximum entropy approach,” in *IEEE Trans. Autom. Control*, vol. 44, pp. 1852–1863, 1999.

[47] T. A. Shaw, J. L. Thieffeault, and C. R. Doering, “Stirring up trouble: Multiple-scale mixing measures for steady scalar sources,” *Physica D*, vol. 231, no. 2, pp. 143–164, 2007.

[48] A. Sharma and N. Gupte, “Control methods for problems of mixing and coherence in chatoic maps and flows,” *Pramana - Journal of Physics*, vol. 48, no. 4, pp. 231–248, 1997.

[49] A. Vikhansky, “Enhancement of laminar mixing by optimal control methods,” *Chem. Engng Sci.*, vol. 57, pp. 2719–2725, 2002.

[50] A. Balogh, O. M. Aamo, and M. Krstić, “Optimal mixing enhancement in 3-D pipe flow,” *IEEE Transactions on Control Systems Technology*, vol. 13, pp. 27–41, 2005.

[51] P. Ashwin, M. Nicol, and N. Kirkby, “Acceleration of one-dimensional mixing by discontinuous mappings,” *Physica A*, vol. 310, pp. 347–363, 2002.

[52] D. Rothstein, E. Henry, and J. P. Gollub, “Persistent patterns in transient chaotic fluid mixing,” *Nature*, vol. 13, no. 2, pp. 502–507, 2003.

[53] K. El-Omari and Y. Le Guer, “Thermal chaotic mixing of power-law fluids in a mixer with alternately rotating walls,” *Journal of Non-Newtonian Fluid Mechanics*, vol. 165, p. 641651, 2010.

[54] S. Skogestad and I. Postlethwaite, *Multivariable feedback control: Analysis and design*. Wiley-Interscience, 2001.

[55] R. Lensvelt, M. F. M. Speetjens, and H. Nijmeijer, “Fast fluid heating by adaptive flow reorientation,” *International Journal of Thermal Sciences*, vol. 180, p. 107720, 2022.

[56] R. Lensvelt, M. F. M. Speetjens, and H. Nijmeijer, “Heat-transfer enhancement by adaptive reorientation of flow fields,” in *5th Thermal and Fluids Engineering Conference (TFEC)*, pp. 411–420, 2020.

[57] R. Lensvelt, M. F. M. Speetjens, and H. Nijmeijer, “Rapid thermalization by adaptive flow reorientation,” *Journal of Physics: Conference Series*, pp. 1–4, 2021.

[58] R. Lensvelt, M. F. M. Speetjens, and H. Nijmeijer, “Lyapunov-based temperature regulation by flow reorientation,” in *19th European Control Conference (ECC21)*, European Union Control Association (EUCA), 2021.

[59] K. El-Omari and Y. Le Guer, “Alternate rotating walls for thermal chaotic mixing,” *International Journal of Heat and Mass Transfer*, vol. 53, pp. 123–134, 2010.

[60] O. Gubanov and L. Cortelezzi, “On the cost efficiency of mixing optimization,” *Journal of Fluid Mechanics*, vol. 692, pp. 112–136, 2011.

[61] G. Mathew, I. Mezić, S. Grivopoulos, U. Vaidya, and L. Petzold, “Optimal control of mixing in Stokes fluid flows,” *Journal of Fluid Mechanics*, vol. 580, p. 261281, 2007.

[62] W. Liu, “Mixing enhancement by optimal flow advection,” *International Journal of Heat and Mass Transfer*, vol. 47, pp. 624–638, 2008.

[63] I. J. Couchman and E. C. Kerrigan, "Control of mixing in a Stokes fluid flow," *Journal of Process Control*, vol. 20, pp. 1103–1115, 2010.

[64] Z. Lin, J. L. Thiffeault, and C. R. Doering, "Optimal stirring strategies for passive scalar mixing," *Journal of Fluid Mechanics*, vol. 675, pp. 465–476, 2011.

[65] E. Lunasin, Z. Lin, A. Novikov, A. Mazzucato, and C. R. Doering, "Optimal mixing and optimal stirring for fixed energy, fixed power, or fixed palenstrophy flows," *Journal of Mathematical Physics*, vol. 53, no. 115611, 2012.

[66] D. P. G. Foures, C. P. Caulfield, and P. J. Schmid, "Optimal mixing in two-dimensional plane Poiseuille flow at finite Péclet number," *Journal of Fluid Mechanics*, vol. 748, p. 241277, 2014.

[67] W. Hu, "Boundary control for optimal mixing by Stokes flows," *Applied Mathematics and Optimization*, vol. 78, p. 201217, 2018.

[68] M. F. Eggl and P. J. Schmid, "Mixing enhancement in binary fluids using optimised stirring strategies," *Journal of Fluid Mechanics*, vol. 899, p. A24, 2020.

[69] Ö. Baskan, M. F. M. Speetjens, G. Metcalfe, and H. J. H. Clercx, "Direct experimental visualization of the global hamiltonian progression of two-dimensional lagrangian flow topologies from integrable to chaotic state," *Chaos*, vol. 25, no. 103106, 2015.

[70] T. Y. Hwu, D. L. Young, and Y. Y. Chen, "Chaotic advections for Stokes flows in circular cavity," *Journal of Engineering Mechanics*, vol. 123, no. 8, pp. 774–782, 1997.

[71] M. G. Trefry, D. R. Lester, G. Metcalfe, A. Ord, and K. Regenauer-Lieb, "Toward enhanced subsurface intervention methods using chaotic advection," *Journal of Contaminant Hydrology*, vol. 127, no. 1, pp. 15–29, 2012.

[72] P. Chadwick, *Continuum Mechanics: Concise Theory and Problems*. Dover books on physics, Dover Publications, 1999.

[73] X. Z. Tang and A. H. Boozer, "A Lagrangian analysis of advection-diffusion equation for a three-dimensional chaotic flow," *Physics of Fluids*, vol. 11, no. 6, pp. 1418–1434, 1999.

[74] E. Kreyszig, H. Kreyszig, and E. J. Norminton, *Advanced Engineering Mathematics*. Hoboken, NJ: Wiley, tenth ed., 2011.

[75] H. K. Khalil, *Nonlinear Systems*. Pearson Education, 2014.

[76] E. F. Camacho and C. B. Alba, *Model Predictive Control*. Advanced Textbooks in Control and Signal Processing, Springer London, 2013.

[77] J.-P. Corriou, *Process Control: Theory and Applications*. Springer International Publishing, 2018.

[78] J. W. Thomas, *Numerical Partial Differential Equations: Finite Difference Methods*. Springer, New-York, 1994.

[79] A. G. G. Toh, Z. P. Wang, C. Yang, and N. T. Nguyen, “Engineering microfluidic concentration gradient generators for biological applications,” *Microfluidics and Nanofluidics*, vol. 16, pp. 1–14, 2014.

[80] C. Y. Lee, W. T. Wang, C. C. Liu, and L. M. Fu, “Passive mixers in microfluidic systems: A review,” *Chemical Engineering Journal*, vol. 288, pp. 146–160, 2016.

[81] L. J. Alvarez-Vazquez, F. J. Fernandez, and A. Martinez, “Analysis of a time optimal control problem related to the management of a bioreactor,” *ESAIM: Control, Optimisation and Calculus of Variations*, vol. 17, pp. 722–748, 2011.

[82] A. Datta, D. Sanyal, A. Agrawal, and A. K. Das, “A review of liquid flow and heat transfer in microchannels with emphasis to electronic cooling,” *Sadhana*, vol. 44, pp. 1–32, 2019.

[83] D. D’Alessandro, M. Dahleh, and I. Mezic, “Control of mixing in fluid flow: A maximum entropy approach,” *IEEE Transactions on Automatic Control*, vol. 44, pp. 1852–1863, 1999.

[84] Y. Ou and E. Schuster, “On the stability of receding horizon control of bilinear parabolic PDE systems,” in *49th IEEE Conference on Decision and Control (CDC)*, (Atlanta, USA), pp. 851–857, IEEE Control Systems Society (CSS), December 15-17,2010.

[85] E. H. Zerrik and H. E. Boukhari, “Constrained optimal control for a class of semilinear infinite dimensional systems,” *Journal of Dynamics and Control systems*, vol. 24, pp. 65–81, 2018.

[86] S. Yahyaoui and M. Ouzahra, “Quadratic optimal control and feedback stabilization of bilinear systems,” *Optimal Control Applications and Methods*, vol. 42, pp. 878–890, 2021.

[87] M. Krstić and A. Smyshlyaev, “Adaptive control of pdes,” *Annual Reviews in Control*, vol. 32, pp. 149–160, 2008.

[88] S. Koga, R. Vázquez, and M. Krstić, “Backstepping control of the stefan problem with flowing liquid,” *2017 American Control Conference (ACC)*, pp. 1151–1156, 2017.

[89] Z. Ren, C. Xu, Z. Zhou, Z. Wu, and T. Chen, “Boundary stabilization of a class of reactionadvectiondiffusion systems via a gradient-based optimization approach,” *Journal of the Franklin Institute*, vol. 356, pp. 173–195, 2019.

[90] E. C. Quintero and F. Jurado, “Boundary control for a certain class of reaction-advection-diffusion system,” *Mathematics*, vol. 8, p. 1854, 2020.

[91] M. Ouzahra, “Stabilisation of infinite-dimensional bilinear systems using a quadratic feedback control,” *International Journal of Control*, vol. 82, pp. 1657–1664, 2009.

[92] E. H. Zerrik and M. O. Sidi, “Regional controllability for infinite-dimensional bilinear systems: approach and simulations,” *International Journal of Control*, vol. 84, no. 12, pp. 2108–2116, 2011.

[93] M. Slemrod, “Stabilization of bilinear control systems with applications to nonconservative problems in elasticity,” *SIAM Journal of Control and Optimization*, vol. 16, no. 1, pp. 131–141, 1978.

[94] J. M. Ball, J. E. Marsden, and M. Slemrod, “Controllability for distributed bilinear systems,” *SIAM Journal of Control and Optimization*, vol. 20, no. 4, pp. 575–579, 1982.

[95] M.-S. Chen, “Exponential stabilization of a constrained bilinear system,” *Automatica*, vol. 34, pp. 989–992, 1998.

[96] M. Ouzahra, “Exponential stabilization of unstable bilinear systems in finite and infinite dimensional spaces,” *IEEE Transactions on Automatic Control*, vol. 14, 2015.

[97] H. Bounit and H. Hammouri, “Feedback stabilization for a class of distributed semilinear control systems,” *Nonlinear analysis*, vol. 37, pp. 953–969, 1999.

[98] M. Ouzahra, “Exponential and weak stabilization of constrained bilinear systems,” *SIAM Journal of Control and Optimization*, vol. 48, pp. 3962–3974, 2010.

[99] L. Berrahmoune, “A note on admissbility for unbounded bilinear control systems,” *Bulletin of the Belgian Mathematical Society - Simon Stevin*, vol. 16, pp. 193–204, 2009.

[100] D. L. Elliot, *Bilinear Control Systems*. Springer, 1st ed., 2009.

[101] G. Metcalfe and D. R. Lester, “Mixing and heat transfer of highly viscous food products with a continuous chaotic duct flow,” *Journal of Food Engineering*, vol. 95, pp. 21–29, 2009.

[102] Z. Berk, “Mixing,” in *Food Process Engineering and Technology*, ch. 7, pp. 193–216, Elsevier Science, 2013.

[103] C. Scherer and S. Weiland, “Linear matrix inequalities in control,” April 2020.

[104] B. Brogliato, R. Lozano, B. Maschke, and O. Egeland, *Dissipative systems analysis and control: Theory and applications*. Springer Nature Switzerland AG, 2020.

[105] E. H. Zerrik, A. A. Aadi, and R. Larhrissi, “Regional stabilization for a class of bilinear systems,” *IFAC PapersOnLine*, vol. 50, no. 1, pp. 4540–4545, 2017. 20th IFAC World Congress.

[106] R. I. Leine and H. Nijmeijer, *Dynamics and bifurcations of non-smooth mechanical systems*. Springer, 1st ed., 2004.

[107] M. J. Balas, “Active control of flexible systems,” *Journal of optimization theory and applications*, vol. 25, no. 3, pp. 415–436, 1978.

[108] O. V. Popovych, A. Pikovsky, and B. Eckhardt, “Abnormal mixing of passive scalars in chaotic flows,” *Physical Review E*, vol. 75, p. 036308, 2007.

[109] D. R. Lester, G. Metcalfe, and M. Rudman, “Complete parametric scalar dispersion,” in *Proceedings of SPIE: Complex Systems II*, vol. 6802, pp. 122–132, 2008.

[110] O. Gubanov and L. Cortelezzi, *Sensitivity of mixing optimization to the geometry of the initial scalar field*. Springer, 2009.

[111] O. Gorodetskyi, M. F. M. Speetjens, P. D. Anderson, and M. Giona, “Analysis of the advectiondiffusion mixing by the mapping method formalism in 3d open-flow devices,” *AICHE Journal*, vol. 60, no. 1, pp. 387–407, 2014.

[112] H. I. Essaid, B. A. Bekins, and I. M. Cozzarelli, “Organic contaminant transport and fate in the subsurface: Evolution of knowledge and understanding,” *Water Resources Research*, vol. 51, pp. 4861–4902, 2015.

[113] M. M. Alvarez, J. M. Zalc, T. Shinbrot, P. E. Arratia, and F. J. Muzzio, “Mechanisms of mixing and creation of structure in laminar stirred tanks,” *AICHE Journal*, vol. 48, no. 10, pp. 2135–2148, 2002.

[114] I. F. Y. Tello, A. van de Wouwer, and D. Coutinho, “A concise review of state estimation techniques for partial differential equation systems,” *Mathematics*, vol. 9, no. 3180, pp. 1–15, 2021.

[115] D. A. Kopriva, *Implementing spectral methods for partial differential equations: Algorithms for scientists and engineers*. Springer, New-York, 2009.

[116] R. Vazquez, E. Schuster, and M. Krstić, “Magnetohydrodynamic state estimation with boundary sensors,” *Automatica*, vol. 44, pp. 2517–2527, 2008.

[117] M. Benosman and J. Borggaard, “Data-driven robust state estimation for reduced-order models of 2D boussinesq equations with parametric uncertinties,” *Computers and Fluids*, vol. 214, p. 104773, 2021.

[118] M. Ghattassi, M. Boutayeb, and J. R. Roche, “Reduced order observer of finite dimensional radiative-conductive heat transfer systems,” *SIAM Journal of Control and Optimization*, vol. 56, no. 4, pp. 2485–2512, 2018.

[119] T. FLIR, “Support for FLIR T630sc.” https://www.flir.com/products/t630sc/, July 2022.

[120] A. Volk and C. J. Kähler, “Density model for aqueous glycerol solutions,” *Experiments in Fluids*, vol. 59, no. 75, pp. 1–4, 2018.

[121] J. P. Hespanha, *Linear systems theory*. Princeton University Press, 2018.

[122] M. Giona, A. Adrover, S. Cerbelli, and V. Vitacolonna, “Spectral properties and transport mechanisms of partially chaotic bounded flows in the presence of diffusion,” *Physical Review Letters*, vol. 92, p. 114101, 2004.

[123] B. Besselink, U. Tabak, A. Lutowska, N. van de Wouw, H. Nijmeijer, D. J. Rixen, M. E. Hochstenbach, and W. H. A. Schilders, “A comparison of model reduction techniques from structural dynamics, numerical mathematics and systems and control,” *Journal of Sound and Vibration*, vol. 332, pp. 4403–4422, 2013.

[124] J. J. Thomsen, *Vibration and Stability: Advanced theory, analysis, and tools*. Springer-Verlag, 2003.

[125] J. D. Stigter and J. Molenaar, “A fast algorithm to assess local structural identifiability,” *Automatica*, vol. 58, pp. 118–124, 2015.

[126] H. Miao, X. Xia, A. S. Perelson, and H. Wu, “On identifiability of nonlinear ode models and applications in viral dynamics,” *SIAM review*, vol. 53, no. 1, pp. 3–39, 2011.

[127] M. T. Heath, “Optimization,” in *Scientific Computing*, ch. 6, pp. 256–308, McGraw-Hill, 2005.

[128] R. W. van Gils, *Feedback stabilisation of pool-boiling systems: for application in thermal management schemes*. PhD thesis, Technische Universiteit Eindhoven, 2012.

[129] H. S. Tharp, “Optimal pole-placement in discrete systems,” *IEEE Transactions on automatic control*, vol. 37, no. 5, pp. 646–648, 2008.

[130] B. Friedland, *Control system design: an introduction to state-space methods*. United States of America, New York: Dover Publications, 2005.

[131] E. D. Sontag, "Optimality: Value function," in *Mathematical Control Theory: Deterministic Finite Dimensional Theory*, ch. 8, pp. 347–396, Springer, 1998.

[132] M. F. M. Speetjens, G. Metcalfe, and M. Rudman, "Topological mixing study of non-newtonian duct flows," *Physics of Fluids*, vol. 18, no. 103103, 2006.

[133] A. Heydari, "Optimal switching with minimum dwell time constraint," *Journal of the Franklin Institute*, vol. 354, pp. 4498–4518, 2017.

[134] H. Kwakernaak and R. Sivan, "Optimal linear state feedback control systems," in *Linear optimal control systems*, ch. 3, pp. 193–327, Wiley Inerscience, 1972.

[135] M. van de Wal and B. de Jager, "A review of methods for input/output selection," *Automatica*, vol. 37, pp. 487–510, 2001.

[136] M. A. Demetriou, "Sensor selection and static output feedback of parabolic pdes via state feedback kernel partitioning using modification of voronoi tessellations," in *2017 American Control Conference*, pp. 2497–2503, 2017.

[137] M. A. Demetriou, "Robust sensor location optimization in distributed parameter systems using functional observers," in *44th IEEE Conference on Decision and Control and European Control Conference*, pp. 7187–7192, 2005.

[138] A. Armaou and M. A. Demetriou, "Optimal actuator/sensor placement for linear parabolic PDEs using spatial $\mathcal{H}_2$ norm," *Chemical Engineering Science*, vol. 61, pp. 7351–7367, 2006.

[139] U. Vaidya, R. Rajaram, and S. Dasgupta, "Actuator and sensor placement in linear advection pde," in *50th IEEE Conference on Decision and Control and European Control Conference*, pp. 5395–5400, 2011.

[140] S. O. R. Moheimani, D. Halim, and A. J. Fleming, "Spatial norms and model reduction," in *Spatial Control of Vibration: Theory and Experiments*, ch. 3, pp. 45–66, World Scientific, 2003.

[141] P. Y. Papalambros and D. J. Wilde, "Optimization models," in *Principles of optimal design*, ch. 1, pp. 1–43, Cambridge University Press, 2003.

[142] J. E. Mark, "Poly(dimethylsiloxane)," in *Polymer Data Handbook*, ch. 89, pp. 539–561, Oxford University Press, 2009.

[143] M. E. Geurts, "Fast heat transfer by smart flow control," Master's thesis, Technische Universiteit Eindhoven, 2019.

[144] R. de Nooijer, “Enhanced heat transfer by smart flow control: Experimental analysis,” Master’s thesis, Technische Universiteit Eindhoven, 2021.

[145] K. H. Johansson, M. Egerstedt, J. Lygeros, and S. S. Sastry, “On the regularization of zeno hybrid automata,” *Systems & Control Letters*, vol. 38, pp. 141–150, 1999.

[146] J. Lygeros, “Lecture notes on hybrid systems,” February 2004.

[147] J. Lygeros, K. H. Johansson, S. N. Simić, J. Zhang, and S. Sastry, “Dynamical properties of hybrid automata,” *IEEE transactions on Automatic Control*, vol. 48, no. 1, pp. 2–17, 2003.

List of publications

Peer-reviewed journal articles related to thesis

- R. Lensvelt, M.F.M. Speetjens., and H. Nijmeijer, “Fast fluid heating by adaptive flow reorientation,” in *International Journal of Thermal Sciences*, 180:1-34, 2022.

- R. Lensvelt, M.F.M. Speetjens., and H. Nijmeijer, “Experimental estimation of scalar transport,” in *preparation*, 2023.

Other peer-reviewed journal articles

- R. Lensvelt, R.H.B. Fey., R.M.C. Mestrom and H. Nijmeijer, “Design and numerical analysis of an electrostatic energy harvester with impact for frequency up-conversion,” in *Journal of Computational and Nonlinear Dynamics*, 15(5):1-8, 2020.

Peer-reviewed articles in conference proceedings

- R. Lensvelt, M.F.M. Speetjens., and H. Nijmeijer, (2020) *“Heat-transfer enhancement by adaptive reorientation of flow fields,”* in *Proceedings 5th Thermal and Fluids Engineering Conference (TFEC)*, 5-8 April 2020, New-Orleans, Louisiana, USA.

- R. Lensvelt, M.F.M. Speetjens., and H. Nijmeijer, (2020) “Lyapunov-based temperature regulation by flow reorientation,” in *European Control Conference (ECC21)*, 29 June - 2 July 2021, Rotterdam, Zuid-Holland, The Netherlands.

- R. Lensvelt, M.F.M. Speetjens., and H. Nijmeijer, (2021) “Rapid thermalization by adaptive flow reorientation,” in *Journal of Physics: Conference Series*, 2116, 012114.

- R. Lensvelt, M.F.M. Speetjens., and H. Nijmeijer, (2019) “Enhanced scalar transport through switched boundary conditions,” in *Book of Abstracts of the 38th Benelux Meeting on Systems and Control*, Lommel, Belgium.

Dankwoord

Onderzoek staat nooit op zichzelf. Daar is dit proefschrift geen uitzondering op. Op deze plaats wil ik daarom een aantal mensen bedanken voor hun bijdrage.

Allereerst wil ik om mijn promotoren bedanken voor de mogelijkheid om dit onderzoek uit te voeren. Henk, bedankt voor de “opvoeding”. De subtiliteit waarmee je haarscherp kunt duidelijk maken waar de zwakke plekken in een verhaal zitten blijft me nog steeds verbazen. Bedankt voor de mogelijkheid om mijn kennis van zowel dynamica als regeltechniek aan te scherpen.

Michel, bedankt dat je me altijd gestimuleerd hebt om autonoom te werken. Hoewel dat niet altijd even gemakkelijk ging (e.g. de befaamde “hack” van 2019) was jouw kritisch blik uiterst waardevol om het wiskundige konijnen gat te vermijden en/of scherpe formulaties op papier te krijgen. Ik heb hier enorm veel van geleerd en ga onze wekelijkse vergaderingen missen.

Additionally, I would like to thank the chair Patrick Anderson and the committee members Herman Clerx, Marco de Baar, Bendiks-Jan Boersma and Martin Guay for the time and effort they spent reading my dissertation and participating in my defense.

Hoewel GEM-Z 2.128 slechts een tijdelijke kantoor zou zijn, ben ik blij dat ik permanent op de tweede vloer ben gebleven. Ik wil graag alle leden van de Energy Technology groep bedanken met wie ik het genoegen heb gehad om samen te werken. Bedankt voor de vele koffietjes en/of lunches Ruben, Mengting, Koen, Shahin, Shravan, Gijs, Camila, Jaimy, Mohammad and Shima. Max, bedankt voor de leestip (!) aan de start van deze onderneming en de humor gedurende. Luca, thanks for the conversations and technical tips on programming. Mauro, the many office excursions, occasional (dino) battle tricks and gym excursions were a delight.

Naast mijn collega’s op de tweede vloer wil ik ook graag al mijn (part-time) collega’s van de kelder bedanken. Brandon, Wouter, Wouter, Sebastian, Erik en Nathan, bedankt voor de fijne samenwerking op het gebied van regeltechniek. Rob, bedankt voor het advies om een promotie te doen en de gesprekken voor, na en tijdens Dynamica. Sajad and Igor, thanks for the many conversations about politics, friction models and/or cows. Daniël, bedankt voor de vele discussie omtrent niet-lineare regeltechniek, de advectie-diffusie vergelijking en (de grote favouriet) communisme. Het was me een genoegen. Geertje, Linda en Marjan, bedankt voor de hulp met andere zaken rondom het promoveren.

Naast de nodige theorie en simulaties bevat dit proefschrift ook de nodige (zwaarbevochten) experimentele resultaten. Freek en Gerald, bedankt voor de initiële hulp en uitleg bij het opstarten van de experimentele opstelling. Irene en Sjoukje, bedankt voor het regelen van de administratieve taken rondom de verplaatsing van de opstelling. Jaap, zonder jouw hulp had ik met deze opstelling nooit “goede” experimentele resultaten gekregen. Bedankt daarvoor!

Koen, bedankt voor de uitleg over lange afstand lopen en de hardloopsessies tijdens corona. De halve marathon met Viktor was me anders nooit gelukt. Op het gebied van sporten mogen ook de vele (eenmalige) gym buddies zeker niet ontbreken. Brandon, Roeland, Rinus, Ricky, Robert en Paul, jullie aanwezigheid maaktte de vele trainingen een stuk gezelliger.

Ricky, Rinus en Timo ik heb genoten van de vele gesprekken onder het genot van menige koffietje, biertje en/of whiskeytje. Rinus en Ricky, bedankt voor de vele (balkon) gesprekken over spiritualiteit, politiek, economie, (regel)techniek, ethiek, etc., hulp bij verhuizingen en uitdagingen in de sportschool! De burgerlijke activiteiten van de voormalige “Computerenisleuk” groep waren een welkome afleiding van het harde gecomputer Thomas en Ton. Bedankt daarvoor!

Mirella and Emanuele, thank you for pushing beyond my comfort zone. Davide and Alesandra, thanks for the great conversations and even better pizze. Thanks for the dinners when Tamara left town, Sepideh and Breandán.

Ik wil mijn paranimfen in het bijzonder bedanken. Het is een lange, en soms vreemde, reis geweest van het skatepark tot de universiteit, Roboto. Mooi dat je erbij bent! Van ons kleine bastion der werktuigbouwkundigen tot het volwassen leven. Bedankt voor de gezelligheid daar(na), Stijn en Laura!

Verder wil ik mijn familie bedanken voor hun geduld gedurende deze gehele academische onderneming. Pa en ma, jullie no nonsense aanpak en ontelbare adviezen liggen aan de basis van dit onderzoek. De vele weekenden op de fabriek hebben me geleerd om vastberaden doelen na te streven. Paul, Tom en Chayenne bedankt voor de afleiding na het werken aan dit onderzoek. Martien en Angela, bedankt voor de mogelijkheid om mijn eigen pad te kunnen uitstippelen. Vorrei anche ringraziare la mia famiglia allargata a Ferla per il supporto. Grazie Nuccio, Francesca e Layla.

Finally, I would like to thank the most important person to me: Tamara. Without your unwavering support during the many worries, trying moments and midnight coding/running sessions I do not known how I would have finished this work. Thank you for the many fun adventures outside work and during our travels abroad. That more may follow soon! I am grateful you set foot in my office and happy that I decided not to wait to answer your question. Thank you for the love and support during this journey.

Ruud Lensvelt
Eindhoven, April 2023

About the author

Ruud Lensvelt was born on August 22, 1989, in Oosterhout, the Netherlands. After finishing Atheneum at Dongemond College in Raamsdonksveer, the Netherlands, he studied Mechanical Engineering with a minor in Embedded Systems at the Eindhoven University of Technology, in the Netherlands. In 2017 he obtained his MSc-degree in Systems & Control within the Dynamics & Control group. His graduation project on the design of an electrostatic vibration energy harvester was performed under the supervision of Rob Fey, Rob Mestrom and Henk Nijmeijer.

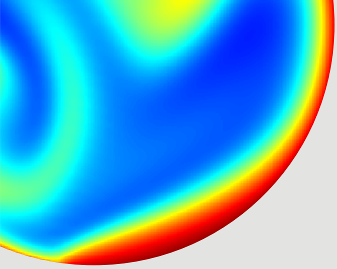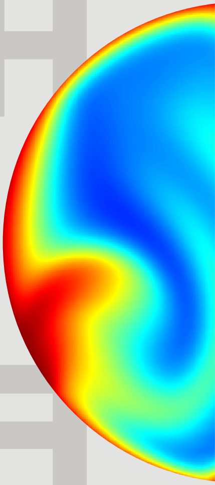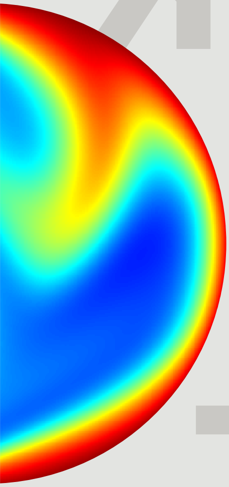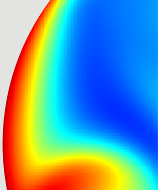In February 2018 he started his PhD research in the Dynamics & Control group and in the Energy Technology group at the Department of Mechanical Engineering of the Eindhoven University of Technology under the supervision of Henk Nijmeijer and Michel Speetjens. Between 2019 and 2021 he was part of the Faculty Council of the Department of Mechanical Engineering at the Eindhoven University of Technology. This research was supported by the Dutch Research Council (NWO) as part of the ‘Computational Sciences for Energy for Energy Research’ (CSER). The main results of this research or summarized in this thesis.